Alma Mater Studiorum – Università di Bologna

DOTTORATO DI RICERCA IN

Ingegneria Elettronica, delle Telecomunicazioni e Tecnologie dell'Informazione

Ciclo XXV

Settore Concorsuale di afferenza: 09/F1

Settore Scientifico disciplinare: ING-INF/02

SILICON PHOTONICS INTEGRATED CIRCUITS FOR FLEXIBLE OPTICAL SYSTEMS

Presentata da: **PIERO ORLANDI**

Coordinatore Dottorato Prof. **Alessandro Vanelli Coralli**

Relatore Prof. **Paolo Bassi**

Esame finale anno 2014

SILICON PHOTONICS INTEGRATED CIRCUITS FOR FLEXIBLE OPTICAL SYSTEMS

PIERO ORLANDI

A Thesis submitted for the degree of

Doctor of Philosophy (PhD)

DEI - Dept. of Electrical, Electronic and Information Engineering
University of Bologna

2014

To my parents

"Hear the rime of the ancient mariner
See his eye as he stops one of three
Mesmerises one of the wedding guests
Stay here and listen to the nightmares of the sea ...
... Driven south to the land of the snow and ice
To a place where nobody's been " ...

The Rime of the Ancient Mariner - Steve Harris - Iron Maiden

"Day after day, day after day,
We stuck, nor breath nor motion;
As idle as a painted ship
Upon a painted ocean.
Water, water, every where,
And all the boards did shrink;
Water, water, every where,
Nor any drop to drink."

The Rime of the Ancient Mariner - Samuel Taylor Coleridge

"The curse it lives on in their eyes
The mariner wished he'd die ...
... And by the light of the moon
He prays for their beauty not doom ...
... Then the spell starts to break
The albatross falls from his neck
Sinks down like lead into the sea
Then down in falls comes the rain."

The Rime of the Ancient Mariner - Steve Harris - Iron Maiden

"He went like one that hath been stunned,
And is of sense forlorn:
A sadder and a wiser man,
He rose the morrow morn."

The Rime of the Ancient Mariner - Samuel Taylor Coleridge

PUBLICATIONS

Journal Papers

P. Orlandi, C. Ferrari, M.J. Strain, A. Canciamilla, F. Morichetti, M. Sorel, P. Bassi and A. Melloni, "Reconfigurable silicon filter with continuous bandwidth tunability," Optics Letters, vol. 37, no. 5, pp. 3669 – 3671 (2012).

P. Orlandi, F. Morichetti, M.J. Strain, M. Sorel, A. Melloni and P. Bassi, "Tunable silicon photonics directional coupler driven by a transverse temperature gradient," Optics Letters, vol. 38, no. 6, pp. 863 – 865 (2013).

P. Orlandi, F. Morichetti, M.J. Strain, M. Sorel, A. Melloni and P. Bassi, "Photonic integrated filter with widely tunable bandwidth," Journal of Lightwave Technology, vol 32, no. 5, pp. 897 – 907 (2014).

Conferences

P. Orlandi, M. Gnan, Samarelli A., G. Bellanca, R.M. De La Rue, M. Sorel and P. Bassi, "Modeling of Racetrack Resonator with Grating Assisted Coupling," In 18th International Workshop on Optical Waveguide Theory and Numerical Modelling (OWTNM 2010). Cambridge, UK, 9 – 10 April 2010.

Samarelli A., M. Sorel, R.M. De La Rue, A. Melloni, P. Orlandi, M. Gnan and P. Bassi, "Grating Assisted Coupling in Microring Resonators," In 15th European Conference on Integrated Optics (ECIO 2010). Cambridge, UK, 7 – 9 April 2010.

P. Orlandi, M. Gnan, Samarelli A., G. Bellanca, R.M. De La Rue, M. Sorel and P. Bassi, "Accoppiatori Assistiti da Reticolo Associati a Risuonatori ad Anello," Atti della XVIII Riunione Nazionale di Elettromagnetismo (RINEM 2010), Post39, Benevento, Italy, September 6 – 10, 2010.

Velha P. , P. Orlandi, M. Gnan, P. Bassi, Samarelli A., M. Sorel, M.J. Strain, and R.M. De La Rue, "Microring Resonator with Wavelength Selective Coupling in SOI," Proceedings of the 8th IEEE International Conference on Group IV Photonics (GFP 2011), pp. 281 – 283, London, United Kingdom, 14 – 16 September 2011.

A. Canciamilla, C. Ferrari, M. Mattarei, F. Morichetti, S. Grillanda, A. Melloni, M.J. Strain, M. Sorel, P. Orlandi and P. Bassi, "A variable delay integrated receiver for differential phase-shift keying optical transmission systems," Proceedings of the 16th European Conference on Integrated Optics (ECIO 2012), pp. 44 – 45, Sitges, Barcelona, Spain, 18 – 20 April 2012.

P. Orlandi, P. Bassi, C. Ferrari, A. Canciamilla, F. Morichetti, A. Melloni, M.J. Strain and M. Sorel, "Tunable bandwidth optical filter in SOI," Proceedings of the 16th European Conference on Integrated Optics (ECIO 2012), pp. 40 – 41, Sitges, Barcellona, Spain, 18 – 20 April 2012.

P. Orlandi, M.J. Strain, C. Ferrari, A. Canciamilla, F. Morichetti, A. Melloni, P. Bassi and M. Sorel, "Bandwidth-tunable optical filters in silicon photonics," Proceedings of Conference on Laser and Electro-Optics (CLEO 2012), OSA, paper CTu2A.5. San Jose, California, 6 – 11 May 2012.

F. Morichetti, A. Canciamilla, S. Grillanda, P. Orlandi, Malaguti S., M.J. Strain, M. Sorel, G. Bellanca, P. Bassi and A. Melloni, "SAPPHIRE: A generic foundry platform for silicon photonics," Atti della XIX Riunione Nazionale di Elettromagnetismo (RINEM 2012), pp. 410 – 413, Rome, 10 – 14 September 2012.

P. Orlandi, F. Morichetti, M.J. Strain, M. Sorel, A. Melloni and P. Bassi, "Compact Tunable Directional Couplers in SOI," Proceedings of Conference on Laser and Electro-Optics (CLEO 2013), OSA, paper JTu4A.51. San Jose, California, 9 – 14 June 2013.

A. Melloni, F. Morichetti, P. Orlandi, P. Bassi, M.J. Strain and M. Sorel, "Signal Processing Subsystems for Optical Interconnects," Invited paper, Proceedings of Conference on Laser and Electro-Optics Pacific Rim (CLEO Pacific Rim 2013), paper ThO3 – 1Kyoto, Japan, 30 June –4 July 2013.

M.J. Strain, P. Orlandi, C. Lacava, F. Morichetti, A. Melloni, P. Bassi, I. Cristiani and M. Sorel, "Silicon micro-ring resonators with tunable Q-factor for ultra-low power parametric signal generation," In Conference on Laser and Electro-Optics (CLEO/EUROPE 2012), Munich, Germany, 12 – 16 May 2013.

ABSTRACT

This doctoral dissertation deals with the design and the characterization of novel reconfigurable silicon-on-insulator (SOI) devices able to filter and route optical signals on-chip. The design is carried out through circuit simulations based on basic circuit elements (Building Blocks, BBs) in order to prove the feasibility of an approach allowing to move the design of Photonic Integrated Circuits (PICs) toward the system level.

PICs can play a key role to realize power efficient and cost effective solutions for future flexible optical networks and data interconnect. CMOS compatibility and large integration scale make SOI one of the most promising material to accomplish these tasks. The high cost to access photonic integrated technologies represents however an issue to pursue this aim. Moreover, single device performance are usually optimized but system level evaluations are rarely performed. The concepts of generic foundry and BB based circuit simulations for the design are rapidly emerging as a solution to reduce the costs and increase the circuit complexity.

To validate this approach to the design of PICs, the development of some of the most important BBs for the realization of optical integrated circuits is carried out first: Straight/bent waveguides, directional couplers, Bragg gratings and Grating Assisted Couplers (GACs). They are modelled and characterized evidencing performance variability due to fabrication tolerances. A novel BB is also designed and realized: a coupler with tunable power splitting ratio, enabling fabrication tolerances counteraction and devices reconfiguration. This BB is demonstrated to be a valuable alternative to the most common solution employed in literature, being more compact and providing lower losses.

Two novel reconfigurable multi-element PICs, based on the previously defined BBs, are then investigated: a narrow linewidth single mode resonator and a passband filter with a widely tunable bandwidth. Extensive circuit simulations are performed in order to determine the devices potentials and limits. Suitable working points are then selected evaluating the impact of fabrication tolerance effects.

The narrow linewidth single mode resonator is presented first. This device is based on two GACs in a ring resonator (RR) configuration. This solution enhances the GAC selectivity and limits the resonance range of the RR. It is shown that a trade-off between performance, resonance bandwidth and device footprint has to be performed. The device could be employed to realize reconfigurable add-drop de/multiplexers. Sensitivity with respect to fabrication tolerances and spurious effects is however observed.

The passband filter with a widely tunable bandwidth is then analysed. This filter is based on an unbalanced Mach-Zehnder interferometer loaded with a pair of RRs. The device is shown to have valuable performance in comparison with the most recent devices presented in literature at a reduced control complexity. Moreover, the device is demonstrated to be robust to fabrication tolerances and nonlinear effects. These properties, together with bit error rate measurements, have confirmed its applicability as functional element for the realization of future flexible network systems.

The behaviour of the realised multi-element PICs as a function of their component parts is shown to be in agreement with the simulated one thus demonstrating both the viability and the potentials of an approach based on standardized circuit elements for the design of complex PICs.

CONTENTS

ABSTRACT xi

INTRODUCTION 1

Aim of the work . . . 2

Thesis Outline . . . 2

1 THESIS BACKGROUND 5

1.1 Reconfigurable Photonic Integrated Circuits for Flexible Optical Systems . . . 5

1.2 Materials . . . 7

1.2.1 Silicon-on-Insulator . . . 8

1.3 A Building Block based approach to the design . . . 10

1.4 SOI devices fabrication . . . 13

1.5 Standard measurement setup . . . 16

1.6 Summary . . . 20

2 BASIC BUILDING BLOCKS 21

2.1 The Waveguide . . . 21

2.1.1 Straight waveguide . . . 21

2.1.2 Bends . . . 24

2.2 Directional Couplers . . . 27

2.2.1 Model . . . 27

2.2.2 Characterization . . . 29

2.3 Ring Resonator . . . 31

2.3.1 All–pass Filter . . . 32

2.3.2 Add–drop Filter . . . 36

2.4 Mach-Zehnder Interferometer . . . 39

2.5 Conclusions . . . 42

3 A NOVEL BUILDING BLOCK: A TUNABLE COUPLER 45

3.1 Introduction . . . 45

3.2 The Tunable Coupler . . . 46

3.2.1 Geometry and Functionality . . . 46

3.2.2 Design . . . 47

3.3 Fabricated Devices . . . 51

3.3.1 Characterization . . . 51

3.3.2 Heater position and Coupler gap . . . 54

3.3.3 Performance . . . 55

3.4 Conclusions . . . 58

4 BRAGG GRATINGS AND GRATING ASSISTED COUPLERS 59

4.1 Introduction . . . 59
4.2 Bragg gratings . . . 59
4.2.1 Geometry and Model . . . 60
4.2.2 Linear characterization . . . 61
4.2.3 Considerations on the Grating design through the CMT . . . 71
4.2.4 Conclusions . . . 74
4.3 Grating Assisted Couplers . . . 75
4.3.1 Functionality and Modelling . . . 75
4.3.2 Characterization . . . 79
4.3.3 Conclusions . . . 84
4.4 Conclusions . . . 84
5 RING RESONATORS WITH GRATING ASSISTED COUPLERS 85
5.1 Introduction . . . 85
5.2 Functionality . . . 86
5.3 Narrow-linewidth Single Mode Resonator . . . 88
5.3.1 Numerical approach to the GAC-RING design . . . 90
5.3.2 Single Resonance Design . . . 93
5.3.3 Spurious effects minimization . . . 99
5.3.4 Fabricated devices performance . . . 102
5.4 Conclusions . . . 110
6 TUNABLE BANDWIDTH FILTER 113
6.1 Introduction . . . 113
6.2 Filter Functionality . . . 114
6.3 Filter Design . . . 118
6.3.1 RRs Coupling Coeffcient . . . 119
6.3.2 Robustness against fabrication tolerance effects . . . 121
6.3.3 MZI Input/Output Couplers . . . 123
6.3.4 Loss Effects . . . 127
6.3.5 Flat Passband . . . 128
6.4 Group Delay and Dispersion . . . 131
6.5 Fabricated Devices . . . 133
6.5.1 Thermal Tuning and Fitting . . . 134
6.5.2 Performance . . . 136
6.5.3 Design versus Experiments . . . 140
6.5.4 RRs Coupling Coefficient Disorder Effects . . . 141
6.5.5 Comparison with the state of the art . . . 142
6.5.6 Full Control via Tunable Couplers . . . 144
6.5.7 Multiple Bandwidths Simultaneous Tuning . . . 146
6.5.8 Impairments due to nonlinear effects . . . 149
6.5.9 BER measurements . . . 151
6.6 Conclusions . . . 154

CONCLUSIONS AND FUTURE WORKS 155
A COUPLED MODE THEORY 157
A.1 Lorentz's reciprocity theorem . . . 157
A.2 Coupled Mode Equations . . . 158
A.3 Fourier analysis of periodic perturbations . . . 163
A.4 Directional Coupler . . . 166
A.5 Bragg grating . . . 169
A.6 Grating Assisted Coupler . . . 175
B TUNABLE BANDWIDTH FILTER 179
B.1 Tunable Bandwidth Filter Transfer Functions . . . 179

BIBLIOGRAPHY 182
LIST OF FIGURES 200
LIST OF TABLES 211
ACRONYMS 213
ACKNOWLEDGEMENTS 216

INTRODUCTION

> Think about how one could re-partition the server platform if CPU and memory modules could be separated. Also think about the system advantages of optically connecting a CPU to memory that is no longer constrained by electrical limitations. Think about how data centres could be redesigned with optical links instead of big, heavy copper cables; the cooling benefits alone would be significant. Think of all the data that exists in the cloud of the internet, and the future ability to access it at high speed over fibre links. Think about future high-resolution displays, 3D televisions and movies that require high-bandwidth connections. All of these could significantly benefit from high-volume, low-cost optical communications, and this is what we are trying to achieve with integrated silicon photonics.
>
> Dr. Mario Paniccia, Director of Photonics Research at Intel Labs [1]

The development of low cost, energy efficient and reconfigurable photonic integrated circuits (PICs) represents one of the key elements to process and transport the constantly increasing data flow of modern times, from on chip interconnects to flexible telecom networks.

Power management is becoming in fact a growing issue for multicore platforms as the number of cores increases to optimize the computation capability. The substitution of standard global interconnects with optical integrated circuits able to route signals inside the chip could offer higher bandwidths and larger interconnection density with reduced power consumption. But, increasing the computation capability enhances problems related to electrical interfaces that cannot scale at the same rate. The only way to increase the bandwidth is to increase power, reduce range and add sophisticated signal processing which in turn brings to more power dissipation. Optical interfaces are then envisaged as one of the most promising solution to overcome this bottleneck for chip to chip and board to board data links.

At the same time, the growth of cloud-based services is driving the rise of larger and larger data centres. In these networks the demand for higher communication speed and longer reach is constantly growing. Optical communication links through low cost photonic integrated circuits can, also in this case, significantly reduce power dissipation and costs.

Finally, the rise in computational and storage capabilities impacts also on long-haul communication systems. The network traffic is constantly increasing and larger capacities are required (i.e. 1 Tbit/s per optical channel is foreseen for 2020). A flexible network that can be managed and reconfigured via software is seen as one

of the viable solution to efficiently allocate the spectral resources. The capacity requirements can in fact vary in time and space depending on the used service and on the devices position. Low cost per bit reconfigurable photonic integrated circuits could enable this paradigm offering cost effective solutions for the adaptive routing and processing of optical signals.

Many technological platforms have been investigated and solutions proposed. However, the sustainable growth of the PICs market has been mainly limited by the classical application oriented approach to the design. This led to a situation where the costs are still too high and system level evaluation of complex circuits is rarely performed. The paradigm of shared access foundries and optical design based on circuit simulations with certified basic elements (building blocks, BBs) is rapidly emerging as a solution to the aforementioned problem.

AIM OF THE WORK

Within the presented scenario, this doctoral dissertation is focused on the validation of the BB based approach for the design of PICs using the silicon-on-insulator (SOI) platform. The high level of integration as well as its intrinsic compatibility with standard CMOS processes has in fact driven the interest and the efforts of the scientific community and of the major microelectronic companies toward the exploitation of the SOI material. In this framework, new basic BBs have been developed and the circuit approach has been exploited to design higher complexity devices based on the aforementioned BBs, taking into account fabrication tolerance effects on their performance. In particular, novel solutions to filter and route optical signals on chip are proposed and investigated. Their successful design, fabrication and characterization will demonstrate the viability of the employed approach.

THESIS OUTLINE

The dissertation is structured as follows:

In Chapter 1, the concepts presented in this Introduction are discussed. Then, the fabrication technique employed to realize the SOI devices designed during this doctoral work is briefly presented. Finally, the standard characterization setup employed to characterize the aforementioned devices is described.

In Chapter 2, the functionality, the models and the characteristic parameters of straight/bent waveguides and directional couplers (DCs) are presented. These three elements represent the first basic set of BBs necessary for the realization of optical integrated circuits. Fundamental devices such as ring resonators (RRs) and Mach-Zehnder Interferometers (MZIs) can be realized with the aforementioned BBs. Being the novel devices presented in this dissertation based on these elements, models and functionalities of RRs and MZIs are then also illustrated.

In Chapter 3, a novel BB to extend the first set defined in the previous Chapter is developed. The device is a directional coupler with a power splitting ratio that can be tuned through a transverse temperature gradient induced by a laterally shifted integrated heater. The tuning mechanism exploits the thermally induced phase velocity mismatch between the coupled modes of the silicon waveguides. In order to maximize the tuning range and reduce electric power consumption, the position of the integrated heater and the waveguide design are optimized through systematic 2D thermo-optical simulations. The measured performance is shown to be in agreement with simulations, demonstrating how asynchronous devices with an intrinsic phase mismatch can provide a more power efficient tuning. The presented device offers a more compact and lower losses solution with respect to that usually employed in literature.

In Chapter 4, other two BBs are characterized in order to allow the development of complex circuits with more functionalities. The first part of the Chapter deals with Bragg gratings. The model based on the Coupled Mode Theory (CMT) is presented first. The model parameters are then obtained through the so called 'cavitometric' technique. A technique employed to retrieve the transmission and reflection spectra of the realized devices. In order to estimate with higher accuracy the grating reflection losses, a technique based on the evaluation of the measured reflection group delay is then proposed showing encouraging results. In the second part of the Chapter, the modelling and the characterization of Grating Assisted Couplers (GACs) are carried out. The model parameters are obtained through systematic measurements, highlighting the performance variability of the devices between different fabrication runs.

In Chapter 5, the first multi-element PIC designed with the previously defined circuit elements is presented. The device is a RR with GACs at the input/ouput coupling sections. The wavelength selective functionality of the GAC allows in principle for the realization of a single mode resonator. The analysed geometry would allow for the realization of Wavelength Division Multiplexing (WDM) de/multiplexers more compact than that based on GACs and not limited by the free spectral range as that based on RRs. Extensive circuit simulations are carried out showing that a trade-off between desired filter bandwidth, footprint and performance is required. Optimized GACs geometries are employed in order to reduce possible spurious effects. The design tool employed allowed an estimation of the device behaviour that was proven by the reported experimental results. In order to improve the device performance with respect to that obtained and add a degree of flexibility, an increase in the control circuit complexity is shown to be mandatory.

In Chapter 6, the second multi-element PIC designed through the BB based approach, a novel bandpass filter with widely tunable bandwidth, is investigated. The filter architecture is based on an unbalanced Mach-Zehnder interferometer loaded with a pair of ring resonators. Wide bandwidth tunability while preserving a good

filter off-band rejection can be achieved by controlling the resonant frequency of the rings. Design rules are provided that take into account fabrication tolerances as well as propagation losses variability. The device is shown to be robust to this variations and good agreement between measurements and circuit simulations is observed. Valuable performance compared to the most recent SOI tunable filters presented in literature has been obtained with a reduced number of actuators. Furthermore, the use of the tunable coupler BB developed in Chapter 3 allows a more flexible shaping of the filter spectral response. The sensitivity with respect to nonlinear effects is carefully investigated. Operation over a wavelength spectrum of 20 nm is demonstrated. The impact of the presented filter over a modulated optical signal is also evaluated. Bit error rate (BER) measurements as well as eye diagrams evaluations show that when signal degradation is detected this is mainly due to sideband filtering rather than dispersion. These characteristics make the device suitable for channel subset selection in flexible WDM systems.

Finally, the conclusions about the results achieved in the present work are drawn in the last chapter together with considerations on future activity that could follow from the present research.

1

THESIS BACKGROUND

This thesis focuses on the BB based approach for the design of multi-element PICs. Such approach will be investigated, both illustrating its philosophy and designing, fabricating and characterizing new types of reconfigurable devices. Performance variability of the BBs due to unavoidable fabrication tolerances effects will be taken into account in the design stage of the multi-element PICs. Finally, the successful comparison between measured and expected performance will show the viability of the approach followed for the design. The results that will be presented have been obtained in the framework of the Italian Project Shared Access Platform to PHotonic Integrated REsources (SAPPHIRE) [2].

The motivations for the development of PICs with spectral characteristics that can be flexibly changed are illustrated first. An overview on the materials that can be used for the realization of these devices is then given, focusing in particular on that exploited during this work: silicon-on-insulator (SOI). After, the philosophy and the advantages of the BB based approach to the design of PICs are illustrated. Finally, the fabrication technique and the standard characterization setup used to realize and characterize the devices during this work are presented.

1.1 RECONFIGURABLE PHOTONIC INTEGRATED CIRCUITS FOR FLEXIBLE OPTICAL SYSTEMS

Capacity, cost and power efficiency are the keywords representing the challenges of future communication systems, regardless the distance to be reached. Higher capacity and higher power efficiency are constantly required to keep up with the continuous growth of the network traffic and computation capability. Performance of individual processors as well as the fastest supercomputers have shown a 10 factor increase every 4 years, the total amount of stored data a factor 10 increase every 5 years and, taking for example the network traffic in North America, a factor 100 increase in 10 years [3]. In this scenario, low cost per bit and reconfigurable Photonic Integrated Circuits (PICs) are addressed as one of the most promising solution to process and transport this increasing data flow with power and cost efficiency.

At chip level, power management is one of the main issues that is increasingly limiting the ability of processing information. Interconnections inside and outside the chip give the dominant contribution to power dissipation [4]. Consequently, the need to limit this figure while improving performance led to multicore solutions rather than just upscaling clock rates. However, as the number of cores increases, classical interconnects are again becoming critical when the lengths to cover become greater than few millimiters. Additionally, the chip input/output interfaces cannot scale at the same rate of the processing capabilities, representing then an increasingly more stringent limitation. CMOS compatible integrated optics can then offer a solution to these problems by substituting classical interconnections. Optical interfaces employing Wavelength Division Multiplexing (WDM) and on-chip global interconnect employing Optical Networks on Chip (ONoC) [5, 6] can increase the bandwidth while reducing power dissipation. Note that ONoC systems must also be reconfigurable so that routing protocols can be changed on request.

Moving to short range communications, the realization of transparent optical data links are also envisaged to become the future solution for data centres and High Performance Computing Systems (HPCS) [7]. Cost and interface bottleneck issues could be in fact tackled down through optical interfaces and switching fabrics enabling pervasive parallel computing.

As to long-haul systems, optical communications are unchallenged for the transmission of large amounts of data. For most of the last decade, the rapid growth of systems capacity thanks to WDM led to a situation where signals were carried with low spectral efficiency. The available capacity exceeded in fact the network requests. The adoption of advanced modulation formats to achieve higher spectral efficiencies was then driven by the constant growth of network traffic requirements. Nowadays it is foreseen that the bit-rate per single optical channel should reach 1 Tbit/s in 2020 to satisfy this increasing demand [3]. Reaching capacities beyond 100 Gbit/s poses however hard challenges for the current technology. The International Telecommunication Union (ITU) standard 50 GHz channel spacing grid will in fact not likely fit bitrates beyond 100 Gbit/s. Both telecom and datacom industries are considering now 400 Gbit/s as the next standard data rate and forcing it to fit in the current grid by adopting a modulation format with higher spectral efficiency would only allow short transmission distances. Moreover, the capacity requirements of the network can rapidly vary in time and space due to the widespread diffusion of mobile devices and the presence of many diverse services. Consequently, in order to efficiently manage the spectral resources for this increasing and diverse capacity demands, the concept of Elastic Optical Networking (EON) [8] has been developed. This paradigm, also referred as gridless networking in the following of the thesis, is based on a grid that is no more fixed but flexible. The optical fibre bandwidth is divided into slots having central frequencies spaced by 6.25 GHz and available widths of 12.5 GHz. A subset of the slot widths and central frequencies can be then

selected depending on the application. This would allow to efficiently accommodate different bit-rate and modulation formats within the transmission spectrum. In this view, variable bit-rate transceivers, as well as flexible wavelength selective switches that can be controlled and reconfigured via software are required. Integrated optical solutions can potentially offer low cost per bit and the required flexibility [9].

The possibility to variate the spectral characteristics of the devices is then fundamental in view of the realization of future flexible optical systems (i.e. where bandwidth or routing requirements of the incoming signals might vary) but not only. When realizing complex system on chip, an active control is of key importance to counteract the effects of mutual interaction between different devices. Moreover, the control on the device functionality allows to counteract unavoidable fabrication tolerance effects.

1.2 MATERIALS

Up to now, the importance of reconfigurable PICs development have been highlighted. In order to realize these circuits, many different materials (such as GaAs, InP, $LiNbO_3$, Si, etc ...) can be exploited. This variety is motivated by the need for different waveguiding, electrooptic, emissive and detection capabilities to realize the required functionalities. Among all, the silicon platform gained more and more attention during the years [10–12]. This increasing interest was mainly due to the possible exploitation of the microeletronic industry capabilities to produce low cost PICs for mass-market applications.

Different materials can be employed to realize optical waveguides on the silicon platform: silica-on-silicon, silicon-on-silicon, silicon oxynitride (SiON), silicon nitride (Si_3N_4) and silicon-on-insulator SOI [10]. One of the most important parameters that has to be taken into account when choosing a technology is the refractive index contrast between the core and the cladding $\Delta n = (n_{core} - n_{cladding})/n_{cladding}$ [13]. The higher the index contrast, the higher the light confinement. When light is more confined, the maximum waveguide dimensions allowing single mode operations are reduced as well as the bending losses for a fixed radius. A larger integration scale can be then achieved. This property is of great interest for two main reasons: higher yield and optoelectronic integration. Increasing the index contrast brings however some drawbacks. The smaller the cross section of the waveguide core, the higher the sensitivity to fabrication tolerances. High resolution fabrication techniques are then required. For sub-micrometer cross sectional dimensions, waveguide sidewall perturbations of only few nanometers can in fact produce remarkable issues: large scattering losses, large backreflections and polarization conversion.

Despite these drawbacks, the possibility to realize single mode waveguides with sub-micrometre sized cross sections and micrometre sized bend radius led toward high index contrast technologies. In particular, SOI, showing the highest index con-

trast (i.e. $\Delta n \approx 1.4$) received great attention from the scientific community as well as from major players of the microelectronic industry [14–17] and several thousands of elements on a single chip can be now realized [18]. In the next subsection some of the most important features of this technology will be then reviewed.

1.2.1 *Silicon-on-Insulator*

Waveguiding in SOI is achieved by the means of the index difference between the silicon core ($n_{Si} \approx 3.5$) and the SiO_2 cladding ($n_{SiO_2} \approx 1.5$). This difference allows the realization of single mode waveguides with core widths ranging from about 400 to 500 nm and core heights from about 200 to 300 nm. The strong light confinement allows also the realization of micrometer sized bend radii. Resonators with curvature radius of 1 μm have been in fact demonstrated [19]. However, in order to reduce bending losses $R > 5$ μm is usually taken into account when designing complex passive devices.

Bulk silicon is transparent from wavelengths larger than 1.1 μm to the far infrared. This property makes it suitable for waveguiding in the second and third telecom windows (i.e. around 1.3 and 1.5 μm). State of the art values for the losses of deep etched 500×220 nm^2 waveguides are 2.4 dB/cm [20] and 1 dB/cm [21], obtained respectively with Deep Ultraviolet (DUV) and Electron beam (Ebeam) lithography. The impact of this high value on the device performance is however mitigated by the reduced device size allowed by SOI.

The transparency of silicon at telecom wavelengths avoided the possibility to realize an important device for optoelectronics circuits, the photodetector. However, advancement in the epitaxial growth of germanium on silicon allowed the realization of large 3 dB bandwidth waveguide coupled photodetectors [22].

SOI waveguides have a high aspect ratio, consequently, the device response is different for transverse electric (TE) and transfer magnetic (TM) polarized light. The devices geometry has then to be optimized for either one of the two polarizations.

The small cross sectional area of SOI waveguides makes difficult to realize butt coupling with optical fibres at the chip input/output section. To increase the coupling efficiency, inverse tapers and grating couplers are the most common structures employed. Inverse tapers are realized by narrowing down to few tens of nanometers the width of the silicon waveguide. The tapered wire is typically coated with a polymer cladding having cross sectional dimensions of few μm^2. The propagating mode is then tapered adiabatically from the SOI to the polymer waveguide. This allows for a better match between the fibre modes and the guided modes at the chip output. Grating couplers are instead periodic structures coupling the waveguide mode out of the chip plane. These structures allow then the testing of the devices directly on the wafer. A feature that is of interest when mass production is the aim. Inverse tapers instead, requiring the chip cleaving, can be suitable for research pur-

poses when just few chips are produced. With polarized input light, high levels of coupling efficiencies have been demonstrated for both techniques [23, 24].

In order to reconfigure the device spectral characteristic, the most common electrooptic effects used in compound semiconductors cannot be exploited in silicon. For example, the linear electro-optic effect (Pockels) is not present due to the centrosymmetric crystal structure of silicon [11]. This limitation has been overcome through the exploitation of the free-carrier dispersion effect by realizing p-i-n or p-n junctions [25]. Free carriers concentration in the silicon waveguide can be varied by forward or reverse biasing the junction. When increasing the carrier concentration, a reduction of the silicon effective index can be obtained. This results in a blue shift of the realized device spectral characteristic. Although nanosecond response times can be achieved [26], the fabrication technique can be complex [25]. Moreover, exploiting the free-carrier plasma-dispersion effect can also induce a loss increase [11]. The control of the device spectral behaviour through this effect should be then employed just when fast responses are required. For example, when realizing high speed modulators [25].

The devices reconfiguration can be also performed by exploiting the thermo-optic effect. By inducing a temperature variation ΔT, a variation in the refractive index Δn proportional to ΔT is induced. It holds that $\Delta n = K_T \Delta T$, where K_T is the so called thermo-optic coefficient. For silicon $K_{T_{Si}} = 1.86e^{-4}\ K^{-1}$ while for SiO_2 $K_{T_{SiO_2}} \approx 10^{-5}\ K^{-1}$ [27]. Increasing the device temperature it is then possible to induce a positive phase shift to the propagating modes, which translate into a rigid red shift of the device spectral response. The fabrication of heaters controlling the devices temperature is much easier than that required to exploit the free-carrier plasma dispersion effect. Metal strips on top of the chip overcladding, producing Joule heating, can be in fact realized with standard lift-off techniques. The thickness of the overcladding is usually designed in order to have negligible losses of the guided modes in the metal sections [28,29]. This choice represents then a suitable solution to realize lossless and easy to fabricate controls of the devices spectral behaviour. For this reason, during this work, the thermo-optic effect have been exploited to perform the devices reconfiguration. More details on the heaters geometry is then given in Section 1.4, where the exploited fabrication technique is described. The thermo-optic effect has typically slow response times due to the slow heat diffusion process in silicon-on-insulator substrates. Best optimized devices show response times in the order of a few microseconds [28]. A reduction of this figure can be obtained by directly heating the silicon core layer and employing pulsed excitation. By the means of these techniques, response times below 100 ns have been demonstrated [30, 31].

Another important property of SOI that must be underlined is its nonlinear behaviour. The tight confinement of light together with the large Kerr coefficient makes SOI a suitable material for the exploitation of nonlinear effects to process op-

tical signals [32]. Especially in structures that enhances the light matter interaction such as photonic crystals and resonators. At wavelengths used in optical communication networks, the sum of the energies from two photons is sufficient to excite an electron across the indirect band-gap of silicon. The generation of free carriers related to this two photon absorption (TPA) is an important nonlinear effect that can be detrimental for both the exploitation of nonlinear effects and the linear operation of the devices. The focus of this work is on devices designed to operate in the linear regime. In this case, nonlinear extralosses and distortion of the device behaviour due to TPA related effects have to be carefully evaluated.

Finally, the silicon indirect bandgap avoids the possibility of efficient light generation and amplification on-chip. This is one of the major differences between the presented material and other III-V compounds such as InP and GaAs. Light sources are a fundamental component for on-chip interconnects, and is an active field of research [33]. For longer communication ranges the near term solution is based on lasers placed in external packages and coupled to the SOI chip.

The realization of low-loss waveguides together with the advancement in coupling, modulating, processing and detect light on a SOI chip allowed for the exploitation of this platform for commercial purposes. At the time of writing this doctoral dissertation Luxtera have already commercialized SOI based circuits (i.e. Active Optical Cables) and majors like Intel and ST Microelectronics are at the R&D stage [14, 16].

However, the access cost to photonic integrated technologies is still too high also for silicon photonics. This usually results in great investments for still relatively small markets. Looking for example at the InP platform, many groups have demonstrated during the years PICs of increasing complexity and sophistication. Most of these circuits have not been successfully commercialized [34]. One of the possible solutions to this problem, as it will be illustrated in the next section, is to develop a building block based approach to the design of PICs through the exploitation of shared access technological platforms.

1.3 A BUILDING BLOCK BASED APPROACH TO THE DESIGN

The classical approach used to design and realize PICs can be called as 'application oriented'. The technological processes are in fact finely adapted to the user and the specific application. This led to and extreme fragmentation of resources, affecting the cost of photonic products. Costs that nowadays are still too high to fully exploit the potentials of photonics in many application areas. In addition, the discussed approach implies optical designers with an all level knowledge of the design chain sketched in Fig. 1.1: from the technology to the circuit level, passing through electromagnetic simulations.

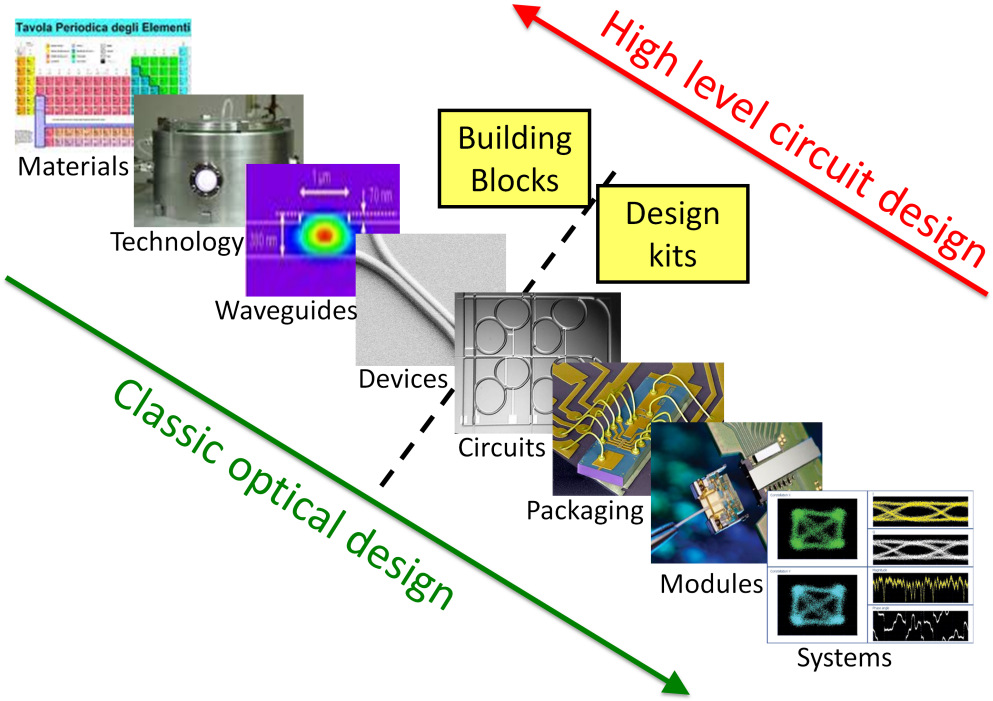

Figure 1.1.: PIC design flows: Classical optical design (green arrow) and Building Block based design (High level circuit design, red arrow).

This design flow makes difficult the realization of complex multi-element circuits as well as the realization of system level evaluations. Numerical techniques such as FDTD and BPM can have a high level of accuracy but, due to their computational weight and time requirements, can hardly be employed for the performance evaluation and design of high complexity circuits. Moreover, the simulated structures are supposed to be ideal. In real devices, the impact of fabrication tolerances lead to backreflections, polarization rotations and variability of the device characteristic parameters that can affect the final performance. For example, in Section 2.2 it will be shown that a power splitting device, widely employed to realize photonic circuits, can show normalized power coupling values of about 10% lower than expected. Moreover, nominally identical couplers can show a 10% variability in the coupling with respect to the expected value. Following the classical optical design approach, this information has to be retrieved with dedicated fabrication runs before approaching the realization of the desired complex device. This increases the costs as well as the project timings. The classical optical design can be then successfully employed to obtain high performing devices but can hardly be exploited for the realization of systems with increasing complexity.

A possible solution to overcome the underlined problems is an approach, demonstrated successful for electronics and microwave systems, that relies on two concepts: generic foundry and Building Blocks.

The generic foundry model is based on multiproject wafers runs organized by the foundry that aggregates different designs of several users. This scheme allows for the sharing of the same technology and the related costs between all the users [35]. The design of complex PICs is then based just on standardized circuit elements (building blocks, BBs) performing guaranteed and certified functions within the limits of the selected technological process. The BBs are basic elements of optical integrated circuits such as straight and bent waveguides, directional couplers, Bragg gratings, etc... The functionalities of these devices are expressed through their scattering or transfer matrix, enabling circuit level simulations. A complex device can be then simulated with a circuit simulator that combines the scattering matrices of the various BBs. The BBs optimization is performed just once through electromagnetic simulations and device characterization. All the informations, such as expected values and variability of the BB model parameters, are then collected and inserted in the design kits (DKs [36]), made available to circuit designers. All the users can benefit from the information collected during years of characterization and focus on the realization of complex systems on a chip. Moreover, the performance of complex devices such as, for example, multi-element filters, can be evaluated considering unavoidable process variabilities. The design of the aforementioned filter can be firstly carried out using one of the available synthesis technique [37–39]. A selection of the more robust architecture can be then performed through circuit simulations and statistical evaluations. The described conditions allow the design of complex and reliable circuits with reduced computational time.

To the knowledge of the author, at least three European projects EuroPIC, Paradigm and Helios [40–42], have been activated to create the necessary infrastructures for the application of the generic foundry model. In particular, in the framework of the projects EuroPIC and Paradigm, a first validation of the BB based approach to the design of PICs has been recently demonstrated on the InP technological platform [43]. The Helios project focuses instead on silicon technology and the optoelectronic integration on a CMOS platform. Some of the Helios project partners have adopted the circuit model approach originally initiated by the ePIXnet Network of Excellence [44]. Even in North America it is possible to find generic foundries, an example of which is Opsis [45], a silicon photonics foundry. Within this picture, several young "design houses" were born in Northern Europe around those foundries that accepted this new paradigm.

Within this growing scenario, the Italian Project SAPPHIRE [2] aims to bring the concepts discussed in this Section in Italy, via the realization and the management of a SOI shared access platform. A platform based on the James Watt Nanofabrication Centre foundry at the University of Glasgow. One of the partners involved in this project, the Photonics Devices Group at the Politecnico di Milano, developed a strong collaboration with the optoelectronic group at the University of Glasgow in the framework of the European Project SPLASH [46]. Apart from many scientifically

relevant results on 'slow light' devices, one of the outcomes of this collaboration was the systematic characterization and modelling of some of the most important passive SOI BBs. The project SAPPHIRE inherited all the knowledge collected during the SPLASH project and is based on the circuit simulator Aspic [47]. The technological platform is developed for TE polarized fields and devices working in linear regime. The maximum on chip power in order to work in this regime was set to 5 dBm.

As previously introduced, the fabrication technique employed to realize BBs and filters presented in this work was developed at the James Watt Nanofabrication Centre (JWNC) by the Optoelectronics Group of the University of Glasgow. The processes and the machines used to fabricate SOI devices are detailed in [29, 48, 49] and will be briefly reviewed in the following Section.

1.4 SOI DEVICES FABRICATION

The SOI material is produced by SOITEC [50, 51] and the wafer is composed of three layers. The top one is made of silicon and will become the guiding core of the optical waveguides. The typical nominal thickness is of 220 nm. The core layer lies on a 2 µm thick buried oxide (BOX) SiO2 substrate. This thickness allows negligible leakage losses in the bottom layer made of bulk silicon crystals. This layer is about 700 µm thick and gives mechanical stability to the wafer. The fabrication process employed to define waveguides on the SOI material is based on two main steps (see Fig. 1.2): hard mask definition (resist spinning, patterning and development); silicon etching.

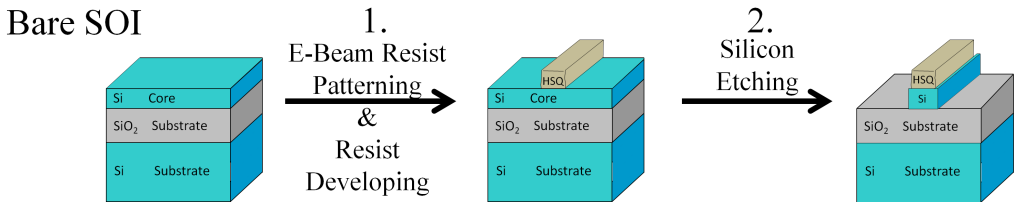

Figure 1.2.: Sketch of the process sequence employed for SOI devices fabrication.

The negative tone resist employed to realize the hard mask is HSQ (Hydrogen SilsesQuioxane), a spin-on glass material that consists of silicon, oxygen and hydrogen atoms that are initially disposed in a three-dimensional cage fashion [52]. A nominal 200 nm thick film is obtained on the top layer of the chip by spinning for 60 seconds and subsequently baking for 2 minutes at 90 °C a 1 : 1 dilution of HSQ in MIBK (Methyl Isobutyl Ketone). A sequential writing lithographic technique using an electron beam is then employed to pattern the processed resist. The machine employed to perform the Ebeam lithography is the Vistec VB6-UHR-EWF. The chosen resolution is of 1 nm which brings to a 1×1 mm^2 writing field dimensions (i.e.

the area that can be patterned without mechanical movements of the machine). To realize SOI waveguides the resist film is patterned with a *Beam Spot Size* of 4 nm and a *Beam Step Size* of 2 nm. Moreover, the Ebeam tool employed implements both proximity corrections and stitching errors compensations. When energy is applied on the resist film, the hydrogen atoms of HSQ are displaced to form a three-dimensional network structure more similar to that of silica [53]. The exposed region has a different level of reactivity with TMAH (Tetra-Methyl-Ammonium Hydroxide) [54] which is used, at 25% concentration in water, as a developer. The unexposed soluble areas are then removed during the development.

Once the hard mask has been defined, the pattern is transferred into the silicon layer through a dry etching technique: Inductively Coupled Plasma (ICP) Reactive Ion Etching (RIE) with SF_4-CF_8 gases. The silicon etching is provided by chemical reactions between F^+ radicals and the silicon layer as well as by ion acceleration. This mixed chemical/physical etching process, together with the passivation effect of the C_4F_8 gas, can produce a strong anisotropic etching. This property is fundamental for the realization of waveguides with vertical sidewalls.

The described process allows for the realization of high quality, state of the art passive SOI devices. In Fig. 1.3a the Scanning Electron Microscope (SEM) images of the fabricated waveguide cross section shows near-vertical sidewalls with an angle of 87°. This property is fundamental in view of the matching between simulations and realized devices properties.

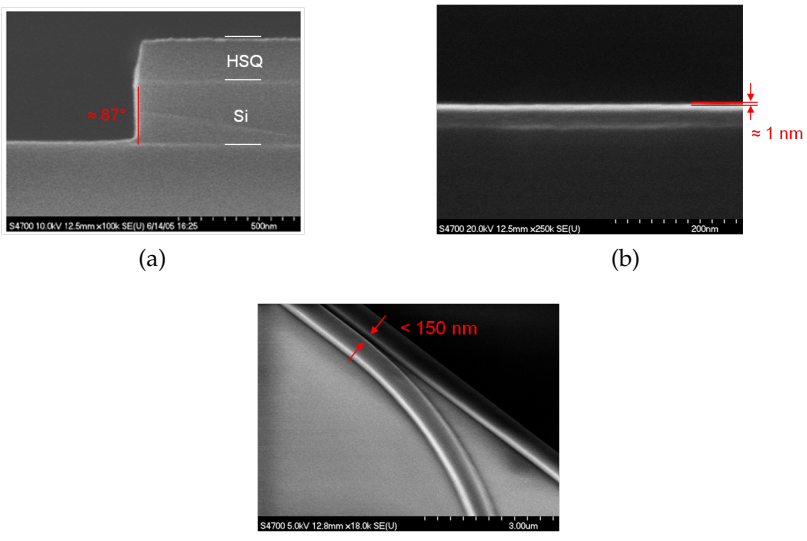

(a) (b)

(c)

Figure 1.3.: (Images taken from [49]) SEM images of fabricated SOI devices: (a) waveguide cross-section with near-vertical sidewall (87°); (b) top-view of the sidewall, showing low LER value ($<$ 1 nm); (c) directional coupler.

Fig. 1.3b shows then that low sidewall roughness is produced. The estimated value of the Line Edge Roughness (LER) from the SEM image is below 1 nm. Losses in integrated optical waveguides are proportional to the square of this value as well as on the square of the index contrast Δn [55]. In high index contrast guiding structures such as SOI, the minimization of the sidewall roughness it is then fundamental. State of the art values of about 1 dB/cm was measured for uncovered waveguides [21]. Moreover, an accuracy better than 0.5 nm is achieved in the waveguide lateral dimensions. Finally, the high etching selectivity between Si and SiO_2 (i.e. large difference in the etch rate of the materials) allows for the clearance of gaps as low as 100 nm (see Fig. 1.3c). This means that really compact directional couplers can be realized.

In characterization set-up schemes like those used during this thesis (see Sec. 1.5), Fabry-Pérot resonances, given by the chip end facets reflectivity due to the silicon-air interface, can strongly modulate the output spectra. This effect can be removed either in post-processing with numerical techniques [56, 57] or with the realization of inverse tapers [58]. The latter, employed during this thesis for all the devices, are realized by tapering down to 50 nm the width of the silicon wire end sections. These tapers are then buried in a SU-8 polymer waveguide with final cross section at the facets of the chip of 2×1.5 μm^2. Another important property of these mode adapters is the enhancement of the input/output fibre coupling efficiency. 5 dB/facet is the typical estimated coupling loss, which is approximately 4.5 dB lower than that obtained without tapers. Once the optical circuit and the modal adapters have been realized, they are buried in a buffer layer (i.e. overcladding). The realization of this layer provides protection to the devices as well as a surface to realize electrical circuits to tune their optical properties. In this way, the thermo-optic effect can be exploited to counteract fabrication tolerances as well as reconfigure the spectral characteristics of SOI devices. A sketch of the final structure cross section is illustrated in Fig. 1.4a.

The height of the buffer layer is set to 900 nm in order to provide high tuning efficiency together with negligible losses given by the overlap between the optical mode and the metal layer. The lower part of this layer, which is approximately 550 nm thick, is realized by spinning and baking HSQ in order to provide good gap filling. The upper part, approximately 350 nm thick, is then realized with SiO_2 deposited with Plasma Enhanced Chemical Vapour Deposition (PECVD). This layer have the chemical and mechanical robustness required by the metal strips fabrication process. High resistivity NiCr strips (i.e. heaters) with $50 \times 900 nm^2$ are then realized over the waveguides via deposition and lift-off. The experimental value of the resistivity found during this doctoral work is $\rho_{NiCr} = 1.14$ $\Omega\mu m$. In order to bring the electrical signal over the waveguides with negligible power and thermal dissipation, a low resistance 200 nm thick layer made of Titanium and

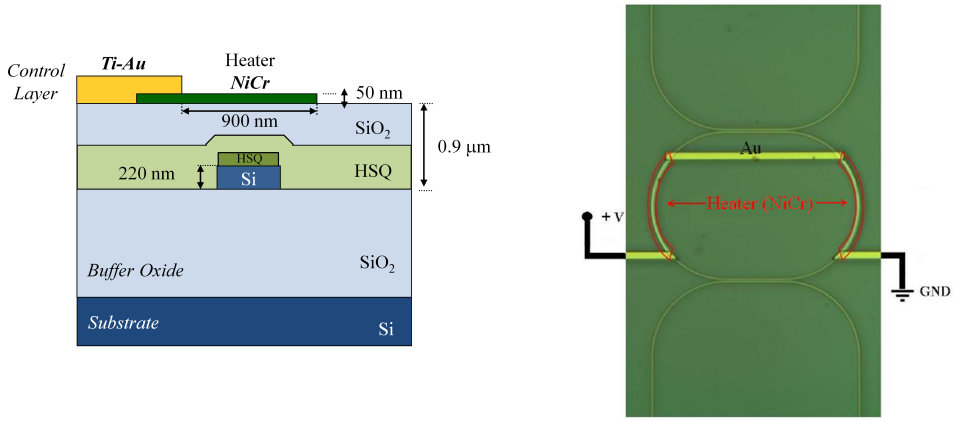

(a) (b)

Figure 1.4.: (a) Sketch of the SOI waveguide cross section with the thermo-optic control deposited over the waveguides. The dark green box on top of the silicon waveguide represents the HSQ hard mask that is not removed after the silicon etching process (see Fig. 1.3a). (b) (Image taken from [29]) Optical microscope photograph of the heaters. Red boxes highlight the NiCr high resistivity strips where the heat is generated.

Gold is then fabricated. The optical microscope photograph top view of a RR with thermo-optic controllers is illustrated in Fig. 1.4b.

With the described electrical circuit, a 2π phase shift can be obtained by dissipating an electrical power P_D of about 20 mW over a heater with length L_h between 55-60 µm. During this doctoral work it was found experimentally that, in order to avoid the fuse of the heater, the ratio P_D/L_h should be kept smaller than 0.6 mW/µm. Finally, typical response times of the described actuator are in the order of ten microsecond [29, 49].

To conclude this Section where the fabrication processes and the machines have been briefly reviewed, it is possible to underline that modal adapters and heaters constitute the first example of BB. The geometry and the performance of this devices are in fact well defined. The designer can employ them in his own circuits without performing any simulation, electromagnetic or thermal, being the optimization already performed by the technological platform.

1.5 STANDARD MEASUREMENT SETUP

In order to characterize the devices developed during this thesis, the author used the facilities of the University of Glasgow and of the Politecnico di Milano. These universities were in fact involved in the SAPPHIRE project (see Section 1.3). Both setup were already optimized to characterize SOI passive devices and were based on an 'end fire' coupling scheme. At the University of Glasgow, the frequency

domain analysis of the devices linear response was carried out. At the Politecnico di Milano, the author of this dissertation performed also nonlinear experiments and time domain characterizations, evaluating both eye diagram acquisitions and bit error rate (BER) measurements. In this Section, the description of both setup is carried out. Having similar characteristics, the setup used at the Politecnico di Milano is presented first, then the one used at the Univesity of Glasgow is briefly described focusing on the differences between the two.

Fig. 1.5a shows a sketch of the experimental setup used for frequency response and time domain characterizations in Milan.

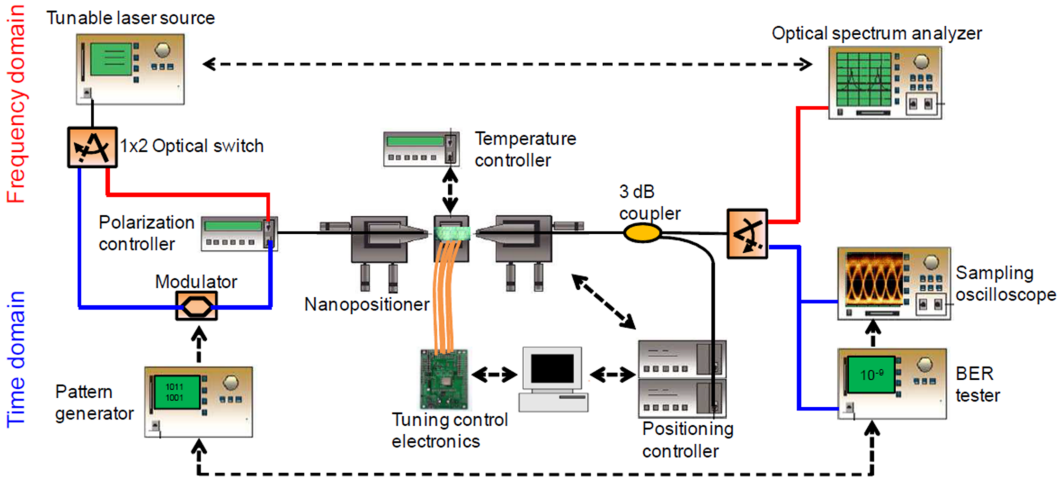

(a)

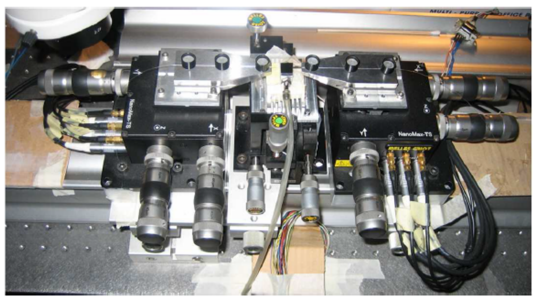

(b)

Figure 1.5.: Setup at Politecnico di Milano: (a) (Image taken from [59]) Schematic of the typical experimental setup employed for the characterization of the devices in the frequency (red links) and time (blue links) domains. Dashed lines indicate electrical control connections. (b) (Image taken from [49]) Photograph of the alignment block of the optical setup showing the two piezo-controlled three-axis nano-positioning stages with tapered lensed fibres and a SOI chip in the middle.

An optical spectrum analyser (OSA) is employed to acquire the spectral response of the devices. The OSA is synchronized to a stepped tunable laser source and controlled by a PC-based acquisition system. The OSA has large dynamic (> 50 dB) and

high sensitivity (i.e. optical signal levels smaller than 60 dBm can be detected). The minimum wavelength resolution is 1 pm and the maximum amount of points that can be acquired is 12000. Nonlinear experiments (see Section 6.5.8) are performed by inserting an Erbium Doped Fiber Amplifier (EDFA) followed by a Variable Optical Attenuator (VOA) between the polarization controller and the input nanopositioner. The output power from the EDFA is fixed to 30 dBm and the power at the input of the chip is regulated by the means of the VOA. Reflection measurements (see Section 4.2.2) are performed placing in the same position a fibre circulator. In order to perform time-domain measurements, the eye diagrams of intensity modulated data patterns are acquired with a wide-band sampling oscilloscope. A BER tester is then employed to realise bit error rate measurements. Details on the modulation format and on signal generation are given in Section 6.5.9. Light is injected and collected respectively at the input and at the output of the device under test (DUT) by butt coupling tapered lensed fibres. Typical coupling loss is of about 5 dB/facet with polymer waveguides as taper and TE polarized light. The polarization state of the input light is set before measurements with a free space polarizer and a polarization controller having an extinction ratio of 30 dB between the two orthogonal polarizations states (i.e. TE and TM). Piezo-electric controlled nano-positioning stages with active feedback loop are employed to obtain a stable setup and achieve an alignment resolution of 5 nm. A photograph of the alignment block is illustrated in Fig. 1.5b. The DUT temperature is controlled by using a Peltier thermocooler with a resolution lower than ± 0.1 °C. A multiprobe head sustained by a mechanical arm is employed to contact the printed circuit board that sends the electrical signals and the pads of the heating circuit on-chip. The device reconfiguration is achieved with a software that regulates the current feeding each heater.

As introduced at the beginning of this Section, the setup scheme employed at the University of Glasgow is similar to that just described. The schematic and the photographs of this setup are illustrated respectively in Fig. 1.6a and Fig. 1.6b. The spectral response of the devices is acquired by a digital real-time oscilloscope synchronized to a tunable laser source with continuous sweep. Conversion between the oscilloscope temporal axis and wavelengths is automatically performed by the control software. With this system, the DUT output spectrum can be sampled with a wavelength resolution below the picometer. The dynamical range is however limited to a maximum of about 20 dB. The light is injected through a tapered polarization maintaining (PM) fibre. The fibre holder can be manually rotated in order to set the desired polarization before measurements with a free space polarizer having a 30 dB extinction between orthogonal polarizations. The output light from the DUT is collected with a $20X$ lens and split by a beam splitter between a camera, employed for the alignment, and an InGaAs transimpedence amplifier photodetector with tunable gain. The detector output is then connected to the digital oscilloscope.

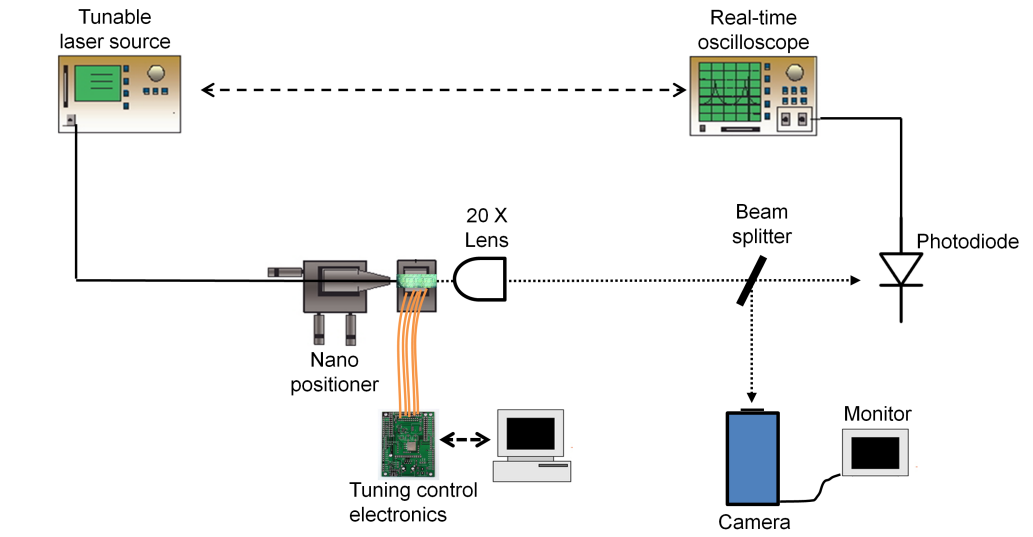

(a)

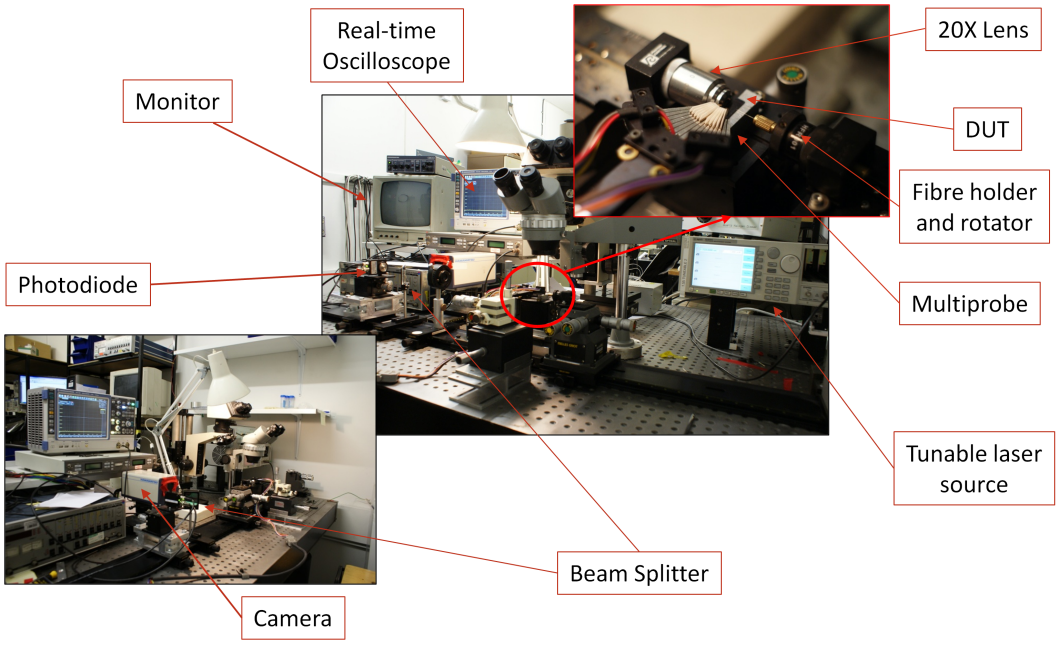

(b)

Figure 1.6.: Setup at Univeristy of Glasgow: (a) Schematic and (b) photographs of the typical experimental setup employed for the characterization of the devices. In (a) dashed lines indicate electrical control connections while dotted lines indicate free space propagation.

Positioning stages are controlled manually. A multiprobe system similar to that described previously is employed to reconfigure the devices spectral response.

1.6 SUMMARY

To summarize, the motivations for the development of reconfigurable PICs able to filter and route optical signals have been given in this Chapter. These devices can play a key role in the development of future flexible telecom systems and of high speed data interconnects. The main features of one of the most promising material to realize such devices (i.e. SOI) have been then illustrated. The generic foundry paradigm have been presented together with the BB based approach to the design of PICs. These two concepts allow to access to photonic integrated technologies at reduced costs and to focus the design on complex systems on-chip rather than on single devices. The technological platform and the characterization set up exploited to realize and characterize the devices during this doctoral work have been then presented. In the following Chapter, the first set of BBs, fundamental for the realization of optical integrated circuits, will be defined.

2

BASIC BUILDING BLOCKS

In this Chapter the functionality, the models and the characteristic parameters of the first basic set of Building Blocks necessary for the realization of optical integrated circuits will be illustrated. This set is constituted by the waveguide (straight and bent) and the Directional Coupler (DC). Despite being composed of just three elements, it already offers a wide range of possibilities for the design of an optical system. Two important classes of devices such as the ring resonator (RR) and the Mach-Zehnder Interferometer (MZI) are in fact based on these three elements. The MZI and the RR are first order filters with respectively a Finite Impulse Response (FIR) and an Infinite Impulse Response (IIR). By combining or cascading these devices, it is then possible to synthesize the desired higher order filter response [38]. They can also, but not only, be employed for the realization of modulators [25], receivers [60], WDM multi/demultiplexers [11, 61] and sensors [62]. Moreover, the complex filters designed and characterized in Chapter 5 and 6 are based on their functionality. Due to their importance and in view of the development of a consistent notation with the following parts of this work, a brief review of RRs and MZIs will be carried out in the last two Sections of this Chapter.

2.1 THE WAVEGUIDE

2.1.1 *Straight waveguide*

The design of any integrated optical circuit starts from the waveguide geometry. The propagation of guided modes through a straight waveguide of length L is associated with the complex factor $e^{-(\alpha+j\beta)L}$ where $\beta = 2\pi n_{eff}/\lambda$ is the propagation constant of the excited mode, n_{eff} the effective index, λ the free space optical wavelength and α is the attenuation constant. The effective index dispersion with λ can be then taken into account through the so called group index $n_g(\lambda) = n_{eff}(\lambda) - \lambda(\partial n_{eff}(\lambda)/\partial\lambda)$. The described parameters are all dependent on the waveguide cross section geometry as well as on the chosen technology (see Section 1.4). These degrees of freedom have then to be fixed in order to allow the designer to focus only on higher complexity devices. The first two requirements

for a straight waveguide are low losses and single mode operation at the desired wavelength.

Waveguides with 480×220 nm^2 cross section size were deeply investigated in the framework of the European Project SPLASH [29, 49] and became the standard dimensions for this basic BB in the framework of the project SAPPHIRE. An SOI waveguide with this geometry sustains just one guided TE mode and shows optical parameters at $\lambda = 1.55$ μm that are illustrated in Tab. 2.1. Note that $A_{\mathrm{dB}} = 20 \cdot \alpha / \ln(10)$ represents the value of the power propagation losses expressed in dB/cm. These values have been then taken into account for the design of the devices presented in Chapter 3 and 6 and Section 4.2. From now on, the described waveguide geometry will be addressed as standard in the following of this thesis. The standard waveguide sustains also one guided TM mode at $\lambda = 1.55$ μm. The high aspect ratio ($\approx$ 2 : 1) provides however a large difference between the propagation characteristics of TE and TM polarized modes [49]. This property allows to study the devices considering either one of the two polarization states. As stated at the end of Section 1.3, the technological platform on which this doctoral work is based is developed for TE polarized fields and, unless specified, this polarization is taken into account in the following of this dissertation. The first TE mode is more confined but has a larger overlap with the waveguide sidewalls than the first TM mode. This allows for the realization of more compact structures at the cost of larger propagation losses. Propagation loss difference was measured to be about $0.7 - 1$ dB/cm in [49].

Table 2.1.: Straight Waveguide Optical Parameters

Parameter	**Symbol**	**Typical value**	**Min**	**Max**
Effective Index	n_{eff}	2.413	2.412	2.414
Group Index	n_g	4.22	4.219	4.221
Losses	A_{dB}	2.5/3	1	6

Some of the realized devices required different waveguide widths than that previously defined as well as evaluations at different wavelengths (see Section 4.3 and Chapter 5). In order to simulate the guided modes properties in these situations, a commercial software (COMSOL Multiphysics) implementing the Finite Element Method (FEM) was employed. Some of the results obtained will be now presented in order to review some well know properties of SOI waveguides, useful in the following of this thesis. The FEM simulation window as well as its dimensions and characteristics are illustrated in Fig. 2.1a. A silicon refractive index $n_{Si} = 3.47572$ and a silica refractive index $n_{SiO_2} = 1.4456$ have been taken into account. Note that the same optical properties have been assumed for the SiO_2 BOX undercladding and the overcladding. These values have been taken accordingly to that used in [49],

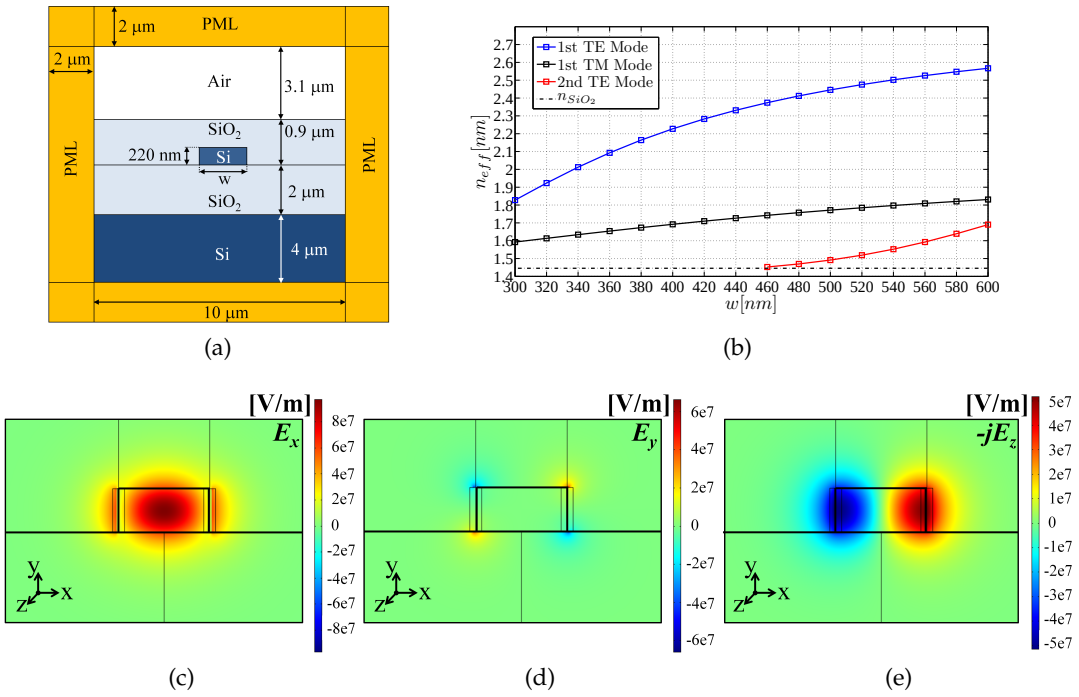

Figure 2.1.: (a) Sketch of the simulation domain. (b) TE modes and first TM mode effective index as a function of the waveguide width w. Electric field components of the first TE mode for $w = 480$ nm: (c) Principal transversal component E_x; (d) E_y; (e) longitudinal component $-jE_z$.

where a good estimation of the waveguides optical properties is demonstrated. Perfectly Matched Layers (PML) sections were introduced as boundary conditions in order to compute modes with leakage in the silicon substrate and maintain the same computational window size regardless the computed mode confinement. Higher order modes are in fact less confined than the fundamental one and can have a large overlap with the silicon substrate, leading to large values of leakage losses. The PML provided by COMSOL produced, in some of the investigated cases, reflections at the edges of the computation window, thereby influencing the simulation results. In order to overcome this problem PML have been implemented by defining an anisotropic medium in these regions [63–65]. Permittivity and permeability of the medium are second order diagonal tensors with elements that depend on the material properties, on the desired absorption profile and on the type of wave that have to be absorbed [66], being it evanescent in the lateral regions and oscillating in the bottom region of our domain. Perfect electric conductor boundary conditions have been then defined at the edges of the considered computational window.

We can now focus on the effective index dependence on w of the defined structure modes. This behaviour is illustrated in Fig. 2.1b. Note that for completeness simulations of the first TM mode have been also included in the figure (black trace in Fig. 2.1b). As introduced at the beginning of this Section, a waveguide with $w = 480$ nm is monomode. The second order TE mode effective index (red trace in Fig. 2.1b) is

close to the refractive index of silica and moreover it shows a value of 30 dB/cm of leakage loss in the substrate. It can be then considered in attenuation. Widening the waveguide width w, the waveguide starts to be multimodal, sustaining two TE modes in propagation at $w = 600$ nm. The calculated leakage loss in the substrate for the second order TE mode is in fact lower than 0.005 dB/cm. At $w = 500$ nm the waveguide can still be considered monomode being the calculated leakage loss of the higher order TE mode of about 9 dB/cm.

Another interesting consideration can be done by looking at the first TE mode electric field components for $w = 480$ nm illustrated in Fig. 2.1c, 2.1d and 2.1e. The longitudinal component E_z (Fig. 2.1e) reach maximum values that are slightly higher than half the maximum value of the mode fundamental component E_x (Fig. 2.1c). This hybridness was expected, being related to the index contrast of the material. The higher the index contrast the higher the hybridness [13]. Although in this case it would be more correct to speak of quasi-TE mode, in the following of this thesis they can be referred as TE modes to simplify the nomenclature.

Having reviewed the parameters and the models used to compute SOI straight waveguides, we can now focus on the last property we are interested in: the minimum bend radius allowing negligible bending losses. This issue will be treated in the following subsection for the standard waveguide of this work.

2.1.2 *Bends*

One of the most interesting feature of high index contrast technologies such as the SOI platform, is the possibility to realize micrometer sized bends [19, 55] that enables a high level of integration. However, in some cases like the filter presented in Chapter 6, the bend radius is not critical for the device footprint. On the other hand, the extreme miniaturization of this parameter can lead to bend losses that can limit the device performance increasing its loss figure. In this Section we will then firstly focus on the minimum bending radius that introduces negligible bend losses. In addition, the minimization of the transition losses in straight-bent waveguide connections is also highly desirable in order to decrease the overall loss figure of the designed devices. In this view considerations will be drawn in order to set a minimum curvature radius allowing to describe the bent waveguide BB with the same optical parameters as the straight waveguide BB.

An evaluation of the waveguide bend losses can be performed simulating the characteristic bend modes with a mode solver over the 2D transversal plane. In order to calculate these modes two approaches can be followed: conformal transformation to obtain an equivalent straight waveguide [67,68], or solving the wave equations directly using a cylindrical coordinate system [69,70]. The first approach can however lead to unreliable results when dealing with small bend radii [69, 71]. Moreover, in the commercial FEM mode solver used for this analysis it was more straightfor-

ward to express the wave equation in cylindrical coordinates than to implement the conformal transformation. The latter requires in fact the manual implementation in the software of the wave equation expressed through its weak formulation, while the former can be set just by enabling the 2D 'axisymmetry' option through the Graphical User Interface. In order to describe this option it is better to look at Fig. 2.2 where the optical bent waveguide, defined by the red lines, is sketched in the Cartesian (black arrows) and the cylindrical (green arrow) reference frames. The

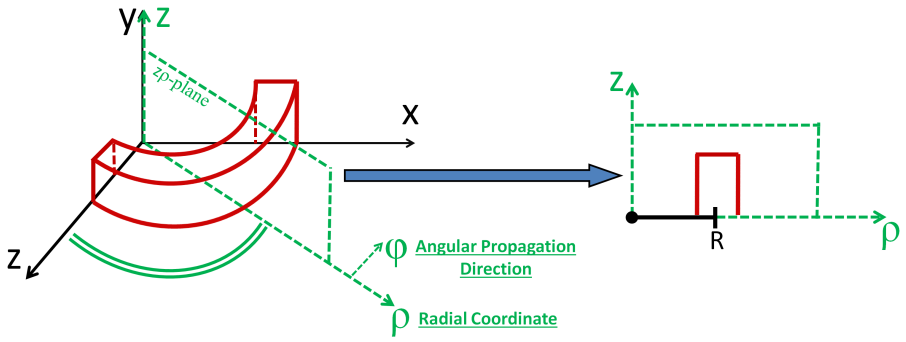

Figure 2.2.: Cartesian (black arrows) and cylindrical coordinate (green arrows) coordinate system. The red lines define the bent waveguide. The bend modes are calculate on the $z\rho$ cylindrical transversal plane where R is the curvature radius of the bent waveguide.

2D 'axisymmetry' model takes into account the cylindrical coordinate system and a rotational symmetry of the structure with respect to the z axis. The wave equation is then solved on the transverse $z\rho$ plane where the distance between the z axis and the waveguide centre along ρ is equal to the bend curvature radius R. Note that, in this case, the propagation direction coincides with the angular coordinate φ. PML can be also implemented following the same procedure described in the previous subsection. In this case, the tensors describing the absorbing anisotropic medium properties must be expressed in the cylindrical coordinate system as detailed in [66, 69, 72, 73].

By exploiting the described tool, the bend losses for different curvature radius R can be then straightforwardly calculated from the imaginary part of the mode effective index. In Fig. 2.3 the optical power losses expressed in dB for a 90° bend for the standard waveguide of this work (i.e. a waveguide with $w = 480$ nm) are illustrated as a function of the bend radius R. As expected, bend losses increases as R reduces and a negative exponential behaviour can be observed. The tighter the bend the larger part of the guided mode tends to radiate into the cladding. The bend mode leakage is clearly noticeable at $R = 1$ µm, where the real part of the mode principal component E_ρ normalized respect to its maximum is illustrated. In this figure, the white lines delimit the PML regions that, as required, absorb the leaky part

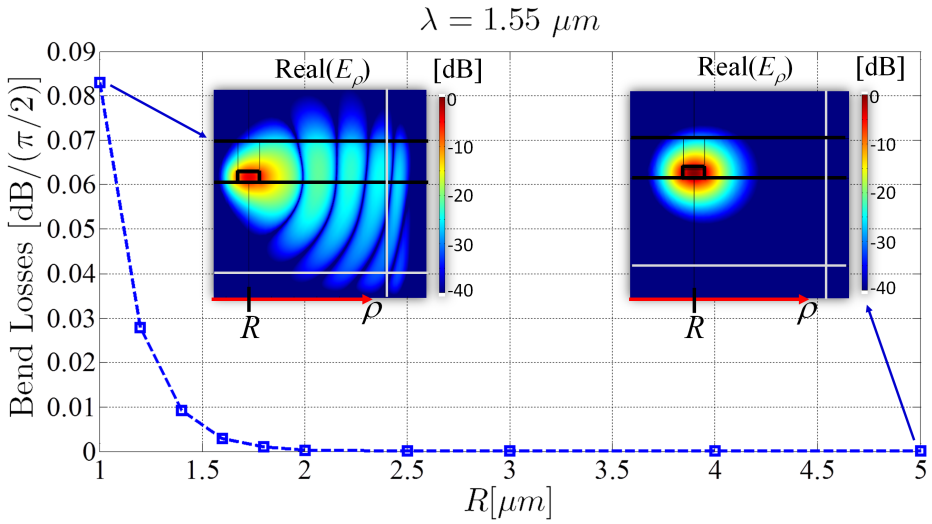

Figure 2.3.: Bend losses expressed in dB per 90° bend as a function of the bending radius R. Insets show the real part of the mode principal component E_ρ normalized to its maximum in logaritmic scale. White lines delimit the PML regions.

of the mode producing negligible reflections. The bend losses associated with this curvature are of about 0.08 dB/(π/2). Increasing the radius of one micron (i.e. considering $R = 2$ µm) reduces this value to the order of 10^{-4} dB/(π/2). Taking then into account $R = 5$ µm, the calculated losses are on the order of 10^{-12} dB/(π/2) and can be then considered negligible. Looking at the mode principal component it is in fact immediately noticeable that the leaky part is not visible anymore. A curvature radius of 5 µm can then constitute the minimum bending radius to obtain negligible bending losses. However, it is possible to notice that with the considered geometry the guided mode shows a slight asymmetry with respect to the centre of the waveguide, tending outwards in radial direction. This behaviour can bring to non negligible transition losses when the bend is connected to a straight waveguide. Moreover, the mode tends to be larger close to the waveguide right sidewall than in the straight waveguide case. This can bring to an increase of the scattering losses. In order to minimize these two undesired effects and apply with a reasonable approximation the same model of the straight waveguide to the bent waveguide BB, a minimum curvature radius $R = 10$ µm has been then set for this work. The optical parameters listed in Tab. 2.1 have been then employed. As a concluding remark, it can be highlighted that in the framework of the project SAPPHIRE, an even more conservative $R = 20$ µm minimum curvature radius have been indicated for the bent waveguide BB.

Having defined the geometry and the parameters of the straight and bent waveguide, it is now possible to pass to the description of the last device that completes the first set of basic BBs. A device enabling power splitting functionalities: the Directional Coupler.

2.2 DIRECTIONAL COUPLERS

Power splitting devices are fundamental BBs for the realization of integrated optical circuits. Together with straight and bent waveguides, they are at the basis of some of the most important first order filters such as RRs and MZIs. The spectral characteristics of these components, which will be reviewed in the following Sections, depend on the reliability of the power splitter design. Two main topologies can be employed in SOI: the Directional Coupler [74] and the Multimode Interference Coupler (MMI) [75].

At the beginning of this doctoral work, DCs had already been designed and characterized on the considered technological platform [29, 49]. For MMI couplers instead, a systematic study were never performed. For this reason we chose to focus only on DCs when devices with power splitting functionalities were needed. The characterization performed on higher complexity devices based on DCs (see Chapter 3 and 6) allowed to extract useful information improving that obtained in previous works [29,49]. The measured parameters were used in fact to realize the DC BB in the framework of the SAPPHIRE project.

In the following of this Section the DC model will be described first. After, the obtained results will be analysed and compared to the ones already available defining in the end, the DC model parameters.

2.2.1 *Model*

The DC is based on two parallel waveguides separated by a gap g. This device can be realized with either bend-straight or bend-bend input/output sections. These configurations are sketched respectively in Fig. 2.4a and Fig. 2.4b. According to

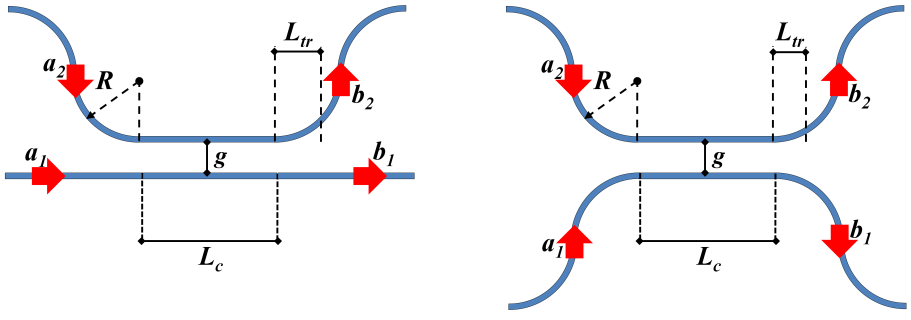

(a) (b)

Figure 2.4.: (a) Directional coupler with bend-straight input and output sections. (b) Directional coupler with bend-bend input and output sections.

the Coupled Mode Theory (CMT) and considering equation (A.41), it is possible to

express the power K coupled between the waveguides and normalized to the input power as $K = \frac{|\kappa|^2}{S^2}\sin(SL_{eff})^2$. In this equation, L_{eff} is the effective length of the coupler, $S = \sqrt{(|\kappa|^2 + \Delta\beta^2/4)}$, κ is the CMT coupling coefficient and $\Delta\beta = \beta_1 - \beta_2$ is the phase mismatch term between the two waveguides. Note that if identical waveguides are considered $\Delta\beta = 0$. The effective length takes into account not only the coupling region of length L_c but also the contribution to the coupling given by the so called transition regions. It can be defined as $L_{eff} = L_c + 2L_{tr}$ where the transition length L_{tr} is calculated considering a fixed κ equal to that of the coupling region. With this assumption and considering the field exponential decay outside the waveguide core as a function of the distance $d(z)$ between the waveguides centre, L_{tr} can be estimated as [38,76]:

$$L_{tr} = \int_0^\infty exp(-\gamma(d(z) - d_{min}))dz = \frac{1}{2}\sqrt{\frac{\pi R}{\gamma}}, \tag{2.1}$$

in the case of bend-bend transitions and as:

$$L_{tr} = \int_0^\infty exp(-\gamma(d(z) - d_{min}))dz = \sqrt{\frac{\pi R}{2\gamma}}, \tag{2.2}$$

in the case of bend-straight transitions. In both equations R is the curvature radius of the bends depicted in Fig. 2.4, γ is the exponential decay constant of the field and d_{min} is the distance between the waveguides centre in the coupling region.

The DC scattering matrix can be also calculated following the CMT of Appendix A.4 and reads as:

$$ae^{-j(\beta_1 - \frac{\Delta\beta L}{2})}e^{-\alpha L}\begin{bmatrix} \cos(SL_{eff}) - j\frac{\Delta\beta}{2S}\sin(SL_{eff}) & -j\frac{\kappa}{S}\sin(SL_{eff}) \\ -j\frac{\kappa}{S}\sin(SL_{eff}) & cos(SL_{eff}) + j\frac{\Delta\beta}{2S}\sin(SL_{eff}) \end{bmatrix}. \tag{2.3}$$

In this equation L takes into account the DC total geometrical length and a is the coupler amplitude loss factor. The common phase term $e^{-j(\beta_1 - \frac{\Delta\beta L}{2})} = e^{-j(\beta_2 + \frac{\Delta\beta L}{2})}$ shows that the asyncronism (i.e. the phase mismatch) is divided in equal parts between the waveguides with opposite sign. Finally, $e^{-\alpha L}$ takes into account the coupler propagation losses, considered equal for both waveguides.

The coupling coefficient κ depends on the waveguide geometry and on the gap g. The method of calculation of this parameter is illustrated in Appendix A.4. From this method it can be understood that the smaller the gap or the less confined the modes are, the higher the CMT coupling coefficient is (i.e. a smaller L_{eff} to reach the desired K is required). This functionality principle brings one of the drawbacks related to the use of DCs for power splitting purposes: the wavelength dependence of the power splitting ratio K. The mode confinement is in fact inversely proportional to the operational wavelength (i.e. the longer the wavelength the less

confined the mode the higher κ). The power splitting ratio depends on the product κL_{eff} and consequently the shorter the coupler the lower will be the wavelength sensitivity.

Considering now a lossless device (i.e. $\alpha = 0$ and $a = 1$) and a fixed κ, values of K ranging from 0 to 1 can be obtained employing synchronous couplers. As illustrated in fact in Appendix A.4, the maximum transferable power between the two waveguides reduces as $\Delta\beta$ increases. In order to obtain the maximum design flexibility, nominally identical waveguides with a standard cross section have been considered in this work. Under this assumption, κ can be calculated through the propagation constants of the supermodes of the structure (see Appendix A.4). In the next section, the design procedure adopted to realize DCs as well as the comparison with the obtained results will be illustrated.

2.2.2 *Characterization*

As introduced at the beginning of this Section, the comparison between the design (based on the CMT as previously discussed) and the characterization of synchronous DCs realized on the exploited SOI platform, was already performed in previous works [29, 49]. An undercoupling between simulations and experiments with a mean relative error of 25% was found measuring couplers with K always lower than 0.64. This effect can be related to a slightly lower value in the effective index of the HSQ overcladding with respect to the bulk SiO_2 undercladding which brings to a higher confinement of the modes. The HSQ effective index depends in fact on the curing temperature. Moreover, the presence of residual air in the gap of the DC, despite the optimized gap filling fabrication technique (see Section 1.4), can bring a reduced value of this effective index inside the gap. In order to design our DCs we took then into account this systematic relative error.

DCs with a fixed gap $g = 300$ nm and fixed transitions (bend-bend with $R = 20\mu$m) varying L_c to obtain the desired K were realized. This analysis has been carried out for DCs allowing to couple power between 40 and 95 % of the input power. This values were in fact required for the realization of the devices presented in Chapter 3 and 6.

In Fig. 2.5 the measured results are indicated with black crosses while the red trace is obtained by fitting the CMT equation with the measurements. The blue trace represents then the values simulated through the CMT. The relative error $((K - K_m)/K)$ between the simulated K and the coupled power fitted from the measurements K_m is then illustrated by the green trace in the inset of the figure. It can be immediately noticed that the relative error decreases as the simluated K increase. For values of K between 0.65 and 0.003 the relative error goes from 18 % to 24 %, in agreement with [29, 49]. However, it can be as low as 10 % for $K = 0.95$. This

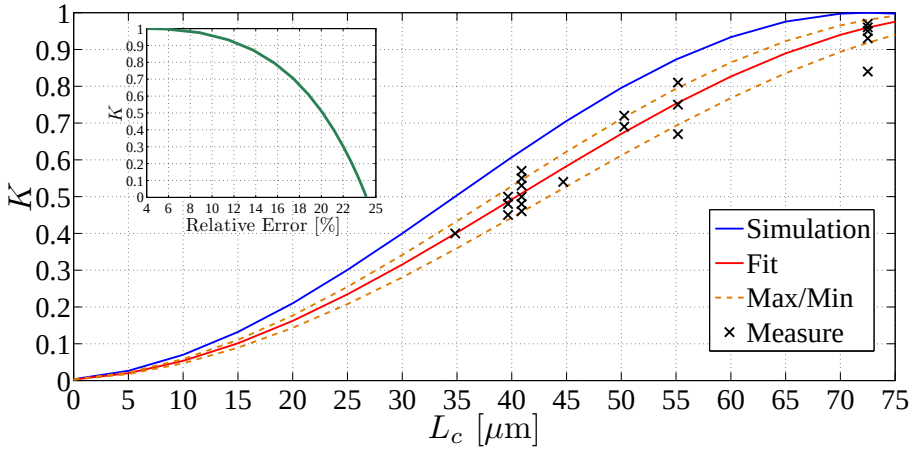

Figure 2.5.: Simulated (blue trace) and measured (black crosses) K. The red trace has been obtained by fitting the measured results with the CMT analytical equation A.41 obtaining $\kappa = 0.018$ μm^{-1}. Dashed orange traces are simulated by considering $\kappa = 0.017$ μm^{-1} and $\kappa = 0.019$ μm^{-1}. The inset shows the relative error $((K - K_m)/K)$ between the simulated K and the coupled power fitted from the measurements K_m.

relative error variation corresponds to a difference in the CMT coupling coefficient. This difference is of about 0.002 μm^{-1}, being 0.018 μm^{-1} and 0.02 μm^{-1} the fitted and the simulated κ respectively.

From Fig. 2.5 the variability of K_m between nominally identical devices can be also evaluated. The coupled power can vary more than 10 % between two devices with the same geometry. The registered value is quite high and has to be taken into account when it comes to the design of such couplers. This means that circuits and devices robust to these variations or methods for the postfabrication tuning have to be realized (see Chapter 3 and 6). However, it can be pointed out that the considered range of fabricated K is the most sensible to κ. This is shown again in Fig. 2.5 where the orange dashed traces have been calculated considering $\kappa = 0.017$ μm^{-1} and $\kappa = 0.019$ μm^{-1}. Smaller variability is then expected for lower values of the coupled power. We can then notice that the majority of the measured K lies within the region defined by the orange traces. We can then consider $\kappa = 0.019$ μm^{-1} and $\kappa = 0.017$ μm^{-1} as an upper and lower bound for DCs realized with $g = 300$ nm, $R = 20$ μm, bend-bend input/output sections.

The described characterization was then useful to define the DC BB for the SAPPHIRE project. Typical κ values of 0.018 μm^{-1} with ± 0.001 μm^{-1} of typical variations are indicated. Knowing that for $R = 20$ μm and bend-bend transitions $L_{tr} = 1.416$ μm, the designer can then choose the desired value of K by selecting the suitable L_c. Losses must be also taken into account. Propagation loss coefficient α can be assumed as that of the standard waveguide of the platform indicated in Tab. 2.1. For what concerns the coupler losses, typical experimental values were already determined as $A = -20 \cdot \log_{10}(a) = 0.06$ dB [77] (i.e. a ≈ 0.993). Finally,

the wavelength dependence of K has been also observed. DCs with K between 0.5 and 0.75 (i.e. L_c between 40 and 55 μm) at $\lambda = 1.55$ showed a variability of about ± 0.03 for wavelength variations of ± 10 nm.

This Section concludes the description of the first basic set of BBs. In the next Section, the ring resonator (RR) will be rapidly reviewed as a first example of application of the BB model. The RR has been chosen since it is a fundamental device for the realization of optical integrated circuits.

2.3 RING RESONATOR

Ring resonators constitute an important BB for the realization of integrated optical circuits [78–81]. Geometries including one or more RRs have been proposed for the realization of various functionalities for the optical signal processing such as for example filtering, modulation, mux/demux, routing, buffering and switching [5, 37, 61, 82–88]. Due to their importance they have been widely studied during the years and their properties and functionalities are well described in many papers and textbook (see for example [38, 89, 90]). However, it is useful now to perform a brief review on the RR architecture and characteristics, focusing on the ones that will be useful in the following of this thesis.

RRs are based on the coupling of a circular waveguide with one or two straight waveguides, sketched respectively in Fig. 2.6a and Fig. 2.6b. They grey boxes in both figures represent phase shifters that allow, as will be clear later, the rigid shift in wavelength of the device spectral characteristics. The first of the two configurations

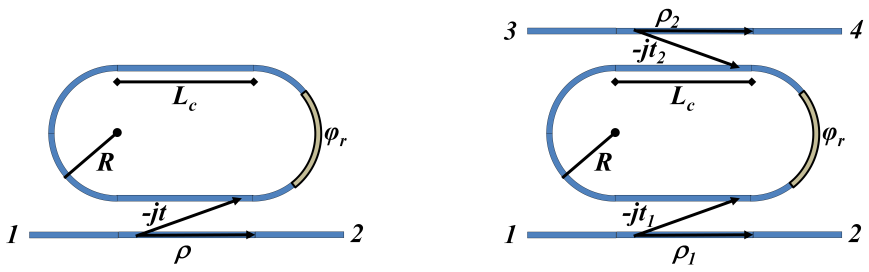

(a) (b)

Figure 2.6.: (a) All-pass and (b) add-drop ring resonator sketch.

is known as all-pass RR while the latter as add-drop RR. The reasons of this name will be clarified in the following subsections. Note that the term ring resonator refers by definition to structures with coupling section lengths $L_c = 0$. For $L_c > 0$ the correct definition is Racetrack Resonators. In this Section however as also sometimes in literature, no distinction will be made between the two, being the

working principles and functionalities equal. The same acronym (i.e. RR) will be then employed to identify both devices.

The light inside a RR is partially forced to recirculate from the output port to the input port. This functionality principle gives to the device an IIR behaviour [38]. The frequency response of a RR is periodical and at given frequencies, the so called resonant frequencies, the light interfere constructively and it is trapped inside the ring. The resonant frequencies of a RR satisfy the relation

$$\beta L_r + \varphi_r = \frac{2\pi}{\lambda} n_{eff} L_r + \varphi_r = 2m\pi, \tag{2.4}$$

where m is a positive integer λ is the free space optical wavelength and $L_r = 2L_c + 2\pi R$ is the ring cavity length. The spectral distance between two consecutive resonances is usually called Free Spectral Range (FSR) and can be calculated as [90]

$$FSR_\lambda = \frac{\lambda^2}{n_g L_r} \qquad \text{or} \qquad FSR_f = \frac{c}{n_g L_r}, \tag{2.5}$$

expressed respectively in the wavelength or the frequency domain and being c the speed of light in vacuum. The unit delay T provided by the ring loop at each roundtrip of the light is then inversely proportional to the filter periodicity being $T = 1/FSR$ [38]. It can be then shown that the filter group delay τ_g is proportional to T [38]. Around the resonant wavelengths the phase nonlinear behaviour rapidly varies and the group delay is enhanced with respect to that of a straight waveguide of length L_r [89]. This group delay enhancement is also associated with an intracavity power enhancement [89, 91].

Having summarized the main properties common to both the RR configurations illustrated in Fig. 2.6 it is now possible to separately discuss the all-pass and the add-drop resonator. In this view, the Z-transform notation and a pole-zero analysis, typical of digital filters, can be exploited to present the device complex transfer function and its dependence on the optical and geometrical parameters of the structure. [38]

2.3.1 *All–pass Filter*

As sketched in Fig. 2.6a, the All-pass RR is composed by a DC, two bent waveguides having a π angle and a straight waveguide with the same length of the coupling section L_c. To describe the DC coupler we can take into account the scattering matrix defined in the previous Section considering identical waveguides (i.e. $\Delta\beta = 0$). The RR losses can be grouped in the roundtrip loss factor $\gamma_r = a\gamma$ where $\gamma = e^{-\alpha L_r}$ include propagation and possible bend losses and a is the coupler loss factor. Referring to the notation of Fig. 2.6a we can then define the waveguide to ring amplitude coupling coefficient $t = \sin(\kappa L_{eff}) = \sqrt{K_r}$, where K_r is the power

coupling coefficient. Moreover, the ring to ring transmission amplitude coefficient $\rho = \cos(\kappa L_{eff}) = \sqrt{1 - K_r}$. It holds $|t|^2 + |\rho|^2 = 1$.

The complex transfer function of this device can be then easily calculated by summing up the infinite series composed by all the contributions to the RRs response:

$$H(z) = a\rho - at^2\gamma_r e^{-j\varphi_r} z^{-1} \sum_{i=0}^{\infty} (\rho\gamma_r e^{-j\varphi_r} z^{-1})^n = \\ = a\frac{(\rho - \gamma_r e^{-j\varphi_r} z^{-1})}{1 - \rho\gamma_r e^{-j\varphi_r} z^{-1}} \tag{2.6}$$

where $z^{-1} = e^{-j\beta L_r}$.

$H(z)$ shows one pole at $z_p = \gamma_r \rho e^{-j\varphi_r}$ and one zero at $z_z = (\gamma_r/\rho)e^{-j\varphi_r}$. The complex variable $e^{-j\varphi_r}$ rigidly rotates z_p and z_z of an angle φ_r on the complex plane z. This translates in a rigid shift of the filter spectral characteristic in wavelengths. We can then from now on consider $\varphi_r = 0$ for the analysis of the filter spectral characteristics without affect the generality of the discussion. The pole z_p lies always inside the unit circle, thus making the filter stable. The zero z_z, instead, can be placed inside, outside or on the unit circle giving different properties to the filter response:

- When $\gamma_r > \rho$ (i.e. $K_r > 1 - \gamma_r^2$), z_z lies outside the unit circle and the filter assumes a maximum phase response. An all-pass RR filter with this configuration is also usually addressed as overcoupled. A particular case is observed when $\gamma_r = 1$. The resonator transfer function is equal to that of a digital all-pass filter [92], showing one pole and one zero placed at reciprocal positions with respect to the unit circle.

- When $\gamma_r < \rho$ (i.e. $K_r < 1 - \gamma_r^2$), z_z lies inside the unit circle and the filter assumes a minimum phase response. An all-pass RR working under this condition is referred as undercoupled.

- When $\gamma_r = \rho$ (i.e. $K_r = 1 - \gamma_r^2$), z_z lies on the unit circle and the so called critical coupling condition is satisfied. The filter response is identically zero at the resonances.

To better understand the effect of the z_z position with respect to the unit circle on the filter response as well as underline the peculiarities of the different coupling conditions of the resonator, we can observe the resonator response keeping ρ fixed and varying γ_r. This behaviour is illustrated in Fig. 2.7 for an all-pass RR with $\rho = 0.8$ and FSR= 3 nm. The power transfer function $|H|^2$ is illustrated in Fig. 2.7a while the phase response of the filter is illustrated in Fig. 2.7b. Note that the phase is normalized to π and limited within the interval $[-\pi, \pi]$. We can start to analyse the case of a lossless resonator (i.e. $\gamma_r = 1$). This is represented by the blue traces

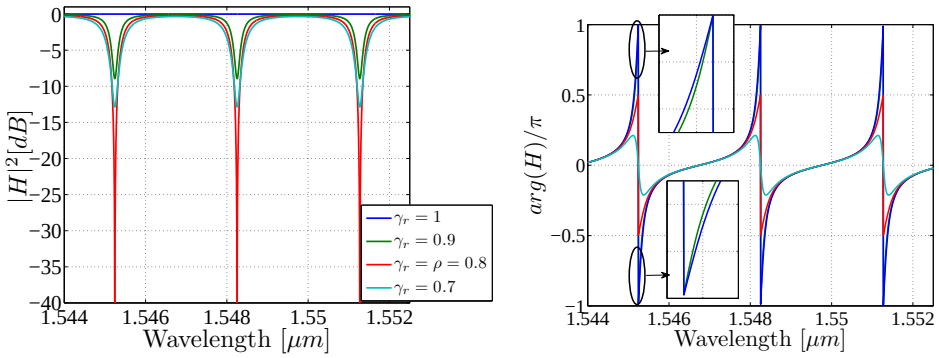

(a) (b)

Figure 2.7.: (a) Transmission ($|H|^2$) and (b) phase response of an all-pass RR with $K_r = 0.36$ ($\rho = 0.8$) and FSR=3 nm, varying γ_r.

in Fig. 2.7. $|H|^2$ (Fig. 2.7a) is equal to unity at all wavelengths and the filter phase is nonlinear and periodical (Fig. 2.7b). This is the typical behaviour of a digital all-pass filter [92]. The phase response shows rapid variations around the resonances as highlighted in the insets of Fig. 2.7b. Values of the group delay τ_g larger than that of a straight waveguide of length L_r are achieved at these wavelengths. The optical wave is in fact trapped inside the resonator and sees a larger effective length. As introduced at the beginning of this Section, an enhancement of the optical power inside the resonator with respect to the input one [89] is then achieved.

By considering roundtrip losses different from zero (i.e. $\gamma_r \neq 1$) $|H|^2$ shows minima in correspondence of the resonances (see Fig. 2.7a). Maximum transmission is instead achieved at the so called antiresonance wavelengths, where the condition $\beta L_r = (2m+1)\pi$ with m integer is satisfied. At the antiresonances the optical wave sees an effective length smaller than L_r and consequently a smaller group delay. This can be noticed by observing the slow variations of the phase around this wavelengths for all the values of γ_r in Fig. 2.7b.

At the critical coupling condition ($\gamma_r = \rho = 0.8$ red trace in Fig. 2.7a) the filter output power is identical to zero at resonances. The minima of $|H|^2$ progressively reduces in fact as the filter approaches the critical coupling from an overcoupling configuration (i.e. z_z approaches the unit circle from the outside as γ_r decrease from 1 to 0.8). This effect can be observed by looking at the green trace and the red trace of Fig. 2.7a, representing respectively an overcoupled and a critically coupled lossy resonator. The resonator values at the resonances instead progressively increase as the filter pass from the critical coupling to the undercoupling condition (i.e. z_z move from the unit circle into it as γ_r decrease from 0.8). This effect can be observed again in Fig. 2.7a by looking at the red trace and at the cyan trace, representing respectively a critically coupled and an undercoupled resonator (i.e. with $\gamma_r = 0.7 < \rho$). The realization of all-pass resonator close to critical coupling is then of interest if high extinction notch filters has to be developed.

Focusing again on the phase response, it can be noticed that reducing γ_r in the overcoupling region increases the phase slope around resonant wavelengths (as shown by the blue and the green traces in the insets of Fig. 2.7b). The group delay, and consequently the resonator power enhancement factor, increases in fact as the critical coupling condition is approached. At critical coupling (red trace in Fig. 2.7b) the filter phase shows an abrupt π variation around the resonances, leading to a singularity in the group delay. When the resonator is in undercoupling condition (cyan trace in Fig. 2.7b), the phase slope around the resonances has opposite sign with respect to that typical of overcoupled resonators (blue and green traces in Fig. 2.7b). Negative values of the group delay can be then observed. This effect does not indicate any causality violation. Considering in fact pulse propagation, strong attenuation and envelope reshaping effects can cause apparent negative velocities [93]. Considering now the power enhancement factor, it can be shown that it progressively decreases as the filter configuration pass from critical coupling to undercoupling. Close to critical coupling, the resonator shows the maximum value of the power enhancement factor. This condition is then desirable when developing devices to exploit nonlinear effects with low input optical power [94–96]. On the other hand, it can be detrimental in complex filters based on resonators when linear operations are the aim [59].

Up to know we have highlighted the all-pass RR properties under different coupling regimes. We can now move to analyse another important figure of the resonator: the quality factor Q. The quality factor can be defined as $Q = \lambda_0/\Delta\lambda_{3dB}$ where $\Delta\lambda_{3dB}$ is the 3 dB bandwidth of the resonance and λ_0 is a resonant wavelength. The analysis of this parameter will be then useful to understand how $\Delta\lambda_{3dB}$ varies with the losses and the coupling values. It is in fact clear that, by definition, the higher Q is, the smaller $\Delta\lambda_{3dB}$ becomes.

Q can be expressed with many different analytical formulations depending on the selected approximation and formalism [62, 89, 97]. In this Section we followed the approach of [89] that assumes $|H|^2 = 1$ at the antiresonance (i.e. a low loss resonator) and 3 dB bandwidth points close to λ_0 (i.e. a narrow linewidth). These assumptions are in fact widely taken into account in literature since they are verified for most applications. Moreover, the simplified equation that can be obtained result useful in developing a brief but still general discussion. For the same reason negligible coupler insertion loss (i.e. $a = 1$, $\gamma_r = \gamma$) is taken into account. Under this assumptions the quality factor can be expressed as:

$$Q = \frac{\lambda_0 \pi}{FSR_\lambda} \frac{\sqrt{\gamma\rho}}{1-\gamma\rho}. \tag{2.7}$$

Eq. (2.7) shows that Q is then inversely proportional to the FSR. $\Delta\lambda_{3dB}$ is in fact proportional to the filter periodicity. The smaller the FSR is, the smaller $\Delta\lambda$ and the larger Q are. Fixing now γ and the FSR we can notice that the larger ρ or, in

other words, the smaller the coupling between the resonator and the waveguide, the higher Q. For $\rho = 1$ the resonator is not coupled with the waveguide and $Q = Q_i$ represents the so called intrinsic quality factor that is determined just by the losses and the FSR. For the sake of completeness, when $\rho < 1$, Q is usually addressed in literature as the loaded quality factor. Reducing the losses (i.e. increasing γ) allows the wave to experience more roundtrips around the ring, increasing then its quality factor. This appears clear from equation (2.7) and translate into a narrower linewidth resonator. At critical coupling $Q = Q_i/2$. This can be verified again from equation (2.7) by noticing that under the assumption of low losses $\gamma = e^{-\alpha L_r} \approx 1 - \alpha L_r$. From this analysis we saw that the critical coupling condition not only provides maximum extinction but also a narrow linewidth (i.e. high Q). Both these properties are useful to realize a sensor [62].

The all-pass RR properties reviewed in this subsection will be then useful in view of the following part of this thesis, in particular in Chapter 3 and 6. This subsection has been also of use to introduce the Z-transform formalism for the description of integrated optical filters. Although we illustrated the spectral and phase characteristic of the all-pass RR over multiple FSRs, it is common to analyse the functionality of a periodical filter just over one FSR. In this view, the complex variable z can be expressed as $z^{-1} = e^{-j2\pi fT} = e^{-j\Omega T}$ where f is the optical frequency and Ω is the angular frequency. With this definition we have assumed $n_{eff} \approx n_g$. Although in SOI the group index almost double the effective index (see for example Tab. 2.1), this assumption can be justified by noticing that n_{eff} determines only λ_0 while n_g determines the filter spectral characteristics. Note that FSR and T and thus the bandwidth and the group delay are related to n_g. When designing an optical periodical filter we are more interested on its characteristics than on its λ_0. The resonance position will be in fact in turn different between the designed and the fabricated device due to unavoidable fabrication tolerance effects and postfabrication tuning mechanism will be required. Following this reasoning it is also common to express and analyse the filter response as a function of the normalized frequency $\nu = (f - f_0)T$ or the normalized angular frequency $\omega = 2\pi\nu$, where f_0 represent the resonance frequency or, more generally, the filter central frequency.

2.3.2 *Add–drop Filter*

The typical geometry of an add-drop RR is sketched in Fig. 2.6b. Referring to the notation of Fig. 2.6b we will assume from now on the port labelled with 1 as the input port. The output labelled with 2 is then usually addressed as the Through port while output 3 and 4 are usually called the Drop and the Add port respectively. This device can be then viewed as an all-pass RR coupled to an output waveguide that is parallel to the input one. It is composed by two DCs and two bent waveguides having a π angle. To describe the directional couplers we can take into account, as

in the former subsection, the scattering matrix defined in Section 2.2 considering identical waveguides (i.e. $\Delta\beta = 0$). We can then use the same notation employed previously and the subscripts 1 and 2 to distinguish the input and the output DC. With $i = 1, 2$, t_i is the coupler to waveguide amplitude transmission coefficient, $K_{ri} = |t_i|^2$ is the power coupling coefficient and the ring to ring amplitude transmission coefficient is then $\rho_i = \sqrt{1 - K_{ri}}$. It holds $|\rho_i|^2 + |t_i|^2 = 1$. Taking into account two sections of coupler losses in a roundtrip the loss factor is now defined as $\gamma_r = a^2 e^{-\alpha L_r}$. In order to obtain the filter transfer function we will from now on consider $L_c = 0$. This means that the DC is assumed to be a point coupler where coupling is provided just by the input/output transition regions. This assumption does not affect the generality of the discussion developed here but the interested reader can find details on the equations that takes into account $L_c \neq 0$ in [89].

With the described notation and assumptions, the complex transfer function between the input and the Through port of the filter is

$$H_{21}(z) = a \frac{\rho_1 - \gamma_r \rho_2 e^{-j\varphi_r} z^{-1}}{1 - \gamma_r \rho_1 \rho_2 e^{-j\varphi_r} z^{-1}}, \tag{2.8}$$

similar to that of the all-pass RR (see equation (2.6)). As in the previous subsection, φ_r provides only a rigid shift of the spectral characteristic of the filter and will be considered equal to zero from now on. The coupling provided by the output DC can be viewed as an additive source of roundtrip losses for the wave circulating inside the resonator. Assuming an equivalent roundtrip loss factor $\gamma_{r_E} = \rho_2 \gamma_r$, $H_{21}(z)$ is formally equal to the transfer of the all-pass RR discussed in the previous subsection. Consequently, characteristics can be highlighted. In this case, the pole of the transfer function placed inside the unit circle is at $z_p = \gamma_{r_E} \rho_1$ while the zero is at $z_z = \gamma_{r_E} / \rho_1$. The ratio γ_{r_E} / ρ_1 determines whether the zero lies inside, outside or onto the unit circle. Critical coupling (i.e. zero transmission at resonances) is then achieved when $\gamma_{r_E} = \gamma_r \rho_2 = \rho_1$.

The complex transfer function at the Drop port of the filter can be then expressed as

$$H_{31}(z) = -a \frac{t_1 t_2 \sqrt{\gamma_r z^{-1}}}{1 - \gamma_r \rho_1 \rho_2 z^{-1}}. \tag{2.9}$$

The expression of $H_{31}(z)$ has a single pole placed inside the unit circle at $z_p = \gamma_r \rho_1 \rho_2$ and a zero placed at infinity. The resulting power transfer function $|H_{31}|^2$ is illustrated in Fig. 2.8a considering, to simplify the discussion, $\rho_1 = \rho_2 = \rho$ (i.e. $K_{r1} = K_{r2} = K_r$). Fig. 2.8a shows the Drop port behaviour for three different values of ρ and two different values of γ_r in a resonator with FSR= 3 nm. The first property that can be highlighted is the filter periodical and Lorentzian shaped behaviour. Maxima occur at the resonances while minima occur at the antiresonance wavelengths. We can then pass to analyse the filter dependence on γ_r and ρ, considering first a lossless resonator (i.e. $\gamma_r = 1$). It can be noticed that increasing ρ

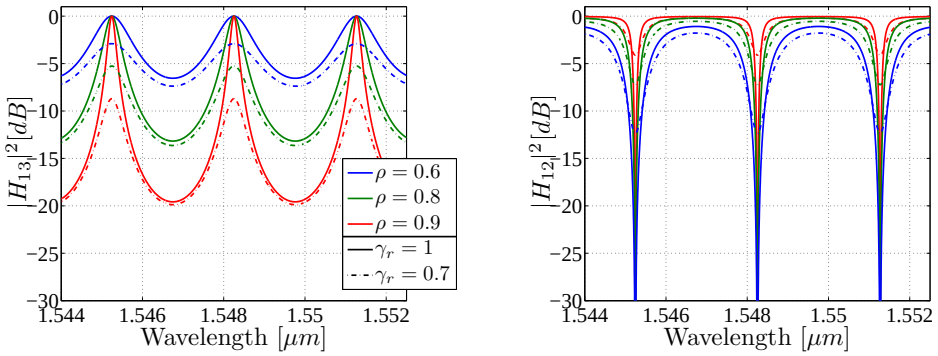

(a) (b)

Figure 2.8.: (a) Drop ($|H_{13}|^2$) and (b) Through ($|H_{12}|^2$) port transfer functions of a RR add-drop filter with FSR=3 nm, $\gamma_r = 1$ (solid traces) and $\gamma_r = 0.7$ (dash-dotted traces) varying $\rho_1 = \rho_2 = \rho$.

(i.e. decreasing the ring to waveguide power coupling coefficient K_r) the filter selectivity increases: the 3 dB bandwidth reduces and the off-band rejection, defined here as the ratio between maximum and the minimum of the filter transfer function, increases. By considering now $\gamma_r = 0.7$ it can be noticed that the losses affects more the filter performance at the resonances. The additional insertion loss is higher at the filter maxima. At resonance, the light is in fact trapped inside the resonator and experiences more round trips. The same observations can be done for the Through port characteristic that is illustrated in Fig. 2.8b for the same values of γ_r and ρ. The insertion loss at the antiresonances is lower than the off-band rejection reduction. The second effect brought by a loss increase is the enlargement of the filter 3 dB bandwidth $\Delta\lambda_{3dB}$ as highlighted in the previous subsection. The filter 3 dB bandwidth can be in fact expressed as:

$$\Delta\lambda_{3dB} = \frac{FSR_\lambda}{\pi}\frac{1-\gamma_r\rho_1\rho_2}{\sqrt{\gamma_r\rho_1\rho_2}}. \tag{2.10}$$

As for the all-pass RR this parameter depends on the FSR and reduces as γ_r and/or ρ increase (i.e. the losses increase and/or the coupling to the ring resonator K_r reduces). Finally, we can then notice that last port to be analysed, the Add port, is theoretically isolated when an input wave at port 1 is assumed.

The properties of the add-drop RR described so far make it then suitable to perform WDM routing [11, 61]. Assuming a WDM spectrum at the considered input port, the desired channel can be selected and routed (dropped) at the Drop port. In this case, maximum extinction at the Through port would be desirable. Critical coupling condition represents then a suitable choice for the design of such a filter. Moreover, an input signal at the Add port can be added to the incoming spectrum.

Having reviewed the properties of ring resonators we can now move to the description of the second important device that can be realized using the first basic set of BB defined in this Chapter: the Mach-Zehnder interferometer (MZI).

2.4 MACH-ZEHNDER INTERFEROMETER

The Mach-Zehnder interferometer is another fundamental device for the realization of optical integrated circuits able to process signals on chip. As the RR, it can be employed for modulation, switching, mux/demux and filtering [25, 38, 98–101] but also for detection schemes of differential phase encoded signals [60, 102, 103]. Moreover, the Mach-Zehnder interferometer geometry can be employed for the realization of couplers with a power coupling coefficient that can be tuned [101, 104–106] or having a constant value over a broad spectrum [107, 108].

A sketch of the typical MZI geometry is illustrated in Fig. 2.9. It is based on

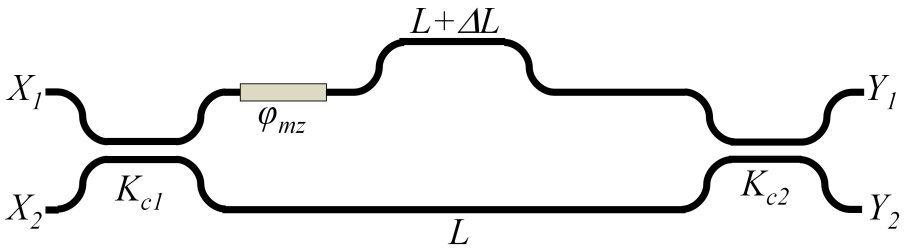

Figure 2.9.: Sketch of a Mach-Zehnder interferometer.

two power splitting devices (DCs in this case) at the input and at the output of the device with a power slitting ratio of K_{c1} and K_{c2} respectively. The two couplers are connected by two arms having an optical path length difference ΔL. The length L will be then addressed from now on as the common path length. A phase shifter can be then realized on one of the two arms in order to tune the devices spectral characteristic. Depending on ΔL the MZI can be employed as a filter or a tunable coupler. In both cases the Z-transform approach can be employed for the description of the device behaviour [38].

For values of $\Delta L \neq 0$ the MZI can be addressed as unbalanced or asymmetric. In this case an input signal at either one of the two ports (i.e. $X_1 = 1$ and $X_2 = 0$ or vice versa in Fig. 2.9) is split between the two arms of the device and then recombined at the output. In other words, the input signal is made interfere with a delayed copy of itself. This working way gives to the unbalanced MZI a Finite Impulse Response

(FIR) filter characteristic. The device transfer functions can be calculated through the transfer matrix method as follows

$$\begin{aligned}\begin{bmatrix} Y_1 \\ Y_2 \end{bmatrix} &= \begin{bmatrix} H_{11}(z) & H_{12}(z) \\ H_{21}(z) & H_{22}(z) \end{bmatrix} \begin{bmatrix} X_1 \\ X_2 \end{bmatrix} = \\ &= \gamma e^{-j\beta L} \begin{bmatrix} c_2 & -js_2 \\ -js_2 & c_2 \end{bmatrix} \begin{bmatrix} \gamma_{mz} e^{-j\varphi_{mz}} z^{-1} & 0 \\ 0 & 1 \end{bmatrix} \times \\ &\quad \times \begin{bmatrix} c_1 & -js_1 \\ -js_1 & c_1 \end{bmatrix} \begin{bmatrix} X_1 \\ X_2 \end{bmatrix} \end{aligned} \tag{2.11}$$

where $s_i = \sqrt{K_{ci}}$ and $c_i = \sqrt{1 - K_{ci}}$ with $i = 1, 2$ represent respectively the amplitude transmission and coupling coefficients of the input and output DCs, $z^{-1} = e^{-j\beta\Delta L}$ and $\gamma_{mz} = e^{-\alpha\Delta L}$ represents the amplitude loss factor related to the extra path in the longer MZI arm. γ and $e^{-j\beta L}$ are then respectively the amplitude loss factor and the phase term related to the mode propagation through the common path length L. It can be noticed that this two latter elements described adds to the transfer functions a constant insertion loss and a constant group delay. These two properties are then not of interest in the description of the MZI transfer functions properties and will be considered equal to unity from now on.

$$\begin{bmatrix} H_{11}(z) & H_{12}(z) \\ H_{21}(z) & H_{22}(z) \end{bmatrix} = \begin{bmatrix} c_1 c_2 \gamma_{mz} e^{-j\varphi_{mz}} z^{-1} - s_1 s_2 & -j(s_1 c_2 \gamma_{mz} e^{-j\varphi_{mz}} z^{-1} + c_1 s_2) \\ -j(c_1 s_2 \gamma_{mz} e^{-j\varphi_{mz}} z^{-1} + s_1 c_2) & -s_1 s_2 \gamma_{mz} e^{-j\varphi_{mz}} z^{-1} + c_1 c_2 \end{bmatrix}. \tag{2.12}$$

To simplify the discussion we will consider from now on $X_1 = 1$ and $X_2 = 0$. In this case $H_{11}(z)$ and $H_{21}(z)$ represents respectively the Through and the Cross port transfer functions. Both functions show one zero. For $H_{11}(z)$ the zero is placed at $z_{zT} = (c_1 c_2 \gamma_{mz} / s_1 s_2) e^{-j\varphi_{mz}}$ while for $H_{21}(z)$ is placed at $z_{zC} = (-s_1 c_2 \gamma_{mz} / s_1 c_2) e^{-j\varphi_{mz}}$. In order to analyse z_{zT} and z_{zC} we can for now neglect $e^{-j\varphi_{mz}}$, common to both zeroes. It in fact provides only a rigid rotation of their position. When $\varphi_{mz} = 0$, z_{zT} and z_{zC} are placed at the opposite side of the real axis of the complex plane z. Maximum transmission (i.e. constructive interference) at the Through port and consequently minimum transmission (i.e. destructive interference) at the Cross port occurs when z is real and negative. In other words, this condition is satisfied for wavelengths at which the phase difference between the two paths $\beta\Delta L = (2m + 1)\pi$ with m integer. $H_{21}(z)$ shows then minima equal to zero when z_{zC} is on the unit circle. This implies $s_1 c_2 \gamma_{mz} = s_1 c_2$ that in the lossless case (i.e. $\gamma_{mz} = 1$) can be written as $K_{c1} = K_{c2}$. Destructive and constructive interference respectively at the Through and the Cross port is instead obtained when z is real and positive. In other words, this condition is satisfied for wavelengths at which the phase difference between the two paths $\beta\Delta L = 2m\pi$ with m integer. $H_{11}(z)$ shows then minima equal to zero when z_{zT} is on the unit circle. This implies $c_1 c_2 \gamma_{mz} = s_1 s_2$ that in the lossless case (i.e.

$\gamma_{mz} = 1$) can be written as $K_{c1} = 1 - K_{c2}$. Minima equal to zero at both ports can be then obtained for $\gamma_{mz} = 1$ when $K_{c1} = K_{c2} = K_c = 0.5$ (i.e. designing input/output 3 dB couplers).

Under these assumptions and using Eq. (2.11), the power transfer functions can be written as

$$|H_{11}|^2 = \sin^2\left(\frac{\beta\Delta L + \varphi_{mz}}{2}\right), \tag{2.13}$$

$$|H_{21}|^2 = \cos^2\left(\frac{\beta\Delta L + \varphi_{mz}}{2}\right). \tag{2.14}$$

Through and Cross port transfer functions show a sinusoidal characteristic with a periodicity (FSR) that can be calculated as

$$FSR_\lambda = \frac{\lambda^2}{n_g \Delta L} \qquad \text{or} \qquad FSR_f = \frac{c}{n_g \Delta L}, \tag{2.15}$$

for the wavelength and the frequency domain. The unit delay given by the extra path length ΔL is again defined as in the RR case as $T = 1/FSR$. From equations (2.13) and (2.14) we can also notice that a variation of φ_{mz} provides a rigid translation of the device spectral characteristics.

The power transfer functions $|H_{11}|^2$ and $|H_{21}|^2$ of a lossless Mach-Zehnder interferometer with $\varphi_{mz} = 0$ and FSR= 1.5 nm are illustrated as a function of the wavelength in Fig. 2.10. The filter 3 dB bandwidth at both ports is then equal to

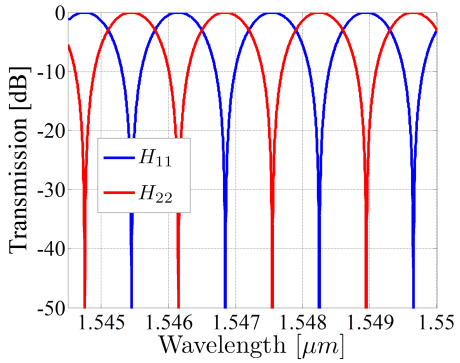

Figure 2.10.: $|H_{11}|^2$ (blue trace) and $|H_{21}|^2$ (red trace) of a lossless Mach-Zehnder interferometer with FSR= 1.5 nm.

FSR/2 in the considered situation.

In this Section we highlighted that the MZI can be viewed as a first order FIR filter. On the other hand, the RR filter presented in the previous Section is a first order IIR filter. It can have a transfer function with a single pole or with a pole and a zero. Pole and zeroes of these two first order filters can be designed by choosing suitable functional and consequently geometrical parameters. By combining these

devices is it then possible to design higher order filters with the desired response as proposed for example in [38, 99, 109–112].

Finally, it is worth to highlight that when $\Delta L = 0$ the MZI can be used as a tunable coupler. In this case the MZI can be addressed as balanced or symmetric. By considering equations (2.13) and (2.14) the power coupled by the MZI normalized with respect to the input X_1 can be expressed as $K = |H_{21}|^2/(|H_{11}|^2 + |H_{21}|^2) = \cos^2(\varphi_{mz}/2)$. A variation of φ form 0 to π makes K vary from 0 to 1. This solution, described in detail in [38], is widely used in SOI [26, 110, 111, 113–117] to obtain the required device flexibility or counteract fabrication tolerances. An alternative solution to this scheme, offering more compactness and lower losses, has been developed during this thesis and will be presented in the next Chapter.

2.5 CONCLUSIONS

In this chapter, a first set of basic BB for the SOI platform has been illustrated. It is composed by straight/bent waveguides and directional couplers.

Regarding the SOI straight waveguide BB, an already optimized and characterized geometry was available at the beginning of this doctoral work and its optical parameters have been presented. The cross sectional dimension of the silicon waveguide core is 480×220 nm^2. A minimum curvature radius allowing to describe the bent waveguide with the same model and parameters of the straight waveguide (i.e. with negligible bend and transition losses) have been set equal to $R = 10$ μm. This parameter has been found through considerations on the bend modes simulated with a commercial FEM mode solver. Some important properties of the modes sustained by SOI waveguides varying their geometry have been also reviewed. The aforementioned mode solver has been employed to design devices based on straight waveguides with geometries or operational wavelengths different form the those defined in the BB.

Regarding the DC, the model and the results of the characterization have been presented and discussed. In particular, the extracted values of the CMT coupling coefficient have been used to define the relative BB in the framework of the project SAPPHIRE. A variability of the coupled power in the order of 10% have been measured for nominally identical devices. Postfabrication tuning methods or the design of complex devices robust to these variations are then required.

This set of basic BBs will be then extended in the following of this thesis in order to allow the realization of circuits with more functionalities. In particular, a novel BB based on the DC and allowing to tune its power splitting ratio will be presented in the next Chapter. This BB is realized with an heater asymmetrically placed respect to the DC gap, allowing the control of the phase mismatch $\Delta\beta$ between the waveguides of the DC and consequently the amount of coupled power. This device is of interest not only to counteract fabrication tolerances, but also for the design of integrated

optical circuits with flexible functionalities. First order filters like RRs and MZIs, reviewed at the end of the Chapter, are in fact based on DCs and their properties depends on the power splitting ratio provided by the coupler.

3

A NOVEL BUILDING BLOCK: A TUNABLE COUPLER

3.1 INTRODUCTION

In the previous chapters the first set of basic BBs used to realize complex passive systems in SOI have been reviewed. Results of their characterization have also been described. Finally, the importance of the realization of PICs devices with post-fabrication tuning mechanisms has been highlighted. In this Chapter, attention will be given to the design and the characterization of a novel and compact coupler with tunable split ratio. This class of devices are in fact important BBs that can be employed for many different purposes, including the compensation of fabrication tolerances effects [110], the development of reconfigurable PICs [26,111,113,118,119], switching [120], optical modulation [121] and lasing [122]. In addition, they can be employed to control the critical coupling condition [123]. As reviewed in Section 2.3 this condition is of great interest in case of sensing [62], nonlinear [94, 95] and filtering [115] applications. This explains why tunable integrated power-splitting devices have been deeply investigated since the early stages of integrated optics. They can be realized through thermally or electro-optically actuated directional couplers [124], asymmetric waveguide junctions [125] and MMI couplers [126, 127]. Actuators can be also based on MEMS [128–130] and optical gradient forces [131].

In silicon photonics the most common approach to realize a tunable coupler exploits a thermally actuated balanced Mach-Zehnder interferometer [26,110,111,113–117]. As illustrated in Section 2.4, this solution combines easy design and a wide tuning range (theoretically form 100% to 0%) with a moderate electric power consumption (i.e. just a π shift of one arm phase is required). However, the MZI tunable coupler is based on a pair of 3 dB splitters. This leads to the realization of devices usually longer than 100 μm and with higher insertion loss. For example, if we consider 0.06 dB as the typical loss figure of the exploited SOI platform evanescent couplers (see subsection 2.2.2) and 0.16 dB/turn as the typical RR filter round trip loss [77], the insertion of other two 3 dB couplers almost double the round trip loss figure.

The tunable directional coupler (TDC) described in this chapter has been conceived with a new topology, which is more compact and exhibits lower losses than the previously described MZI based solution, while keeping a reasonably low power

consumption. The device is based on a single silicon photonic DC and is driven by the transverse temperature gradient induced by a laterally shifted heater. The thermally induced phase velocity mismatch between the coupled modes of the silicon waveguides allows for the device tuning. The position of the heater and the DC cross section are optimized through systematic 2D thermo-optical simulations to maximize the tunability range, while reducing both footprint and electric power consumption. The tool employed to simulate the TDC behaviour takes into account the temperature dependence of the electro-optic coefficient as well as a reduced thermal conductivity of the overcladding with respect to the bulk SiO_2 undercladding. Finally, the device behaviour is experimentally characterized showing good agreement with simulations and good performance in the optimized configuration.

3.2 THE TUNABLE COUPLER

3.2.1 *Geometry and Functionality*

The cross sectional sketch of the proposed device is shown in Fig. 3.1a. The standard SOI platform 480 × 220 nm^2 silicon core waveguide on a 2 µm buried oxide (BOX) under-cladding and a 700 µm bulk silicon substrate is employed. Two

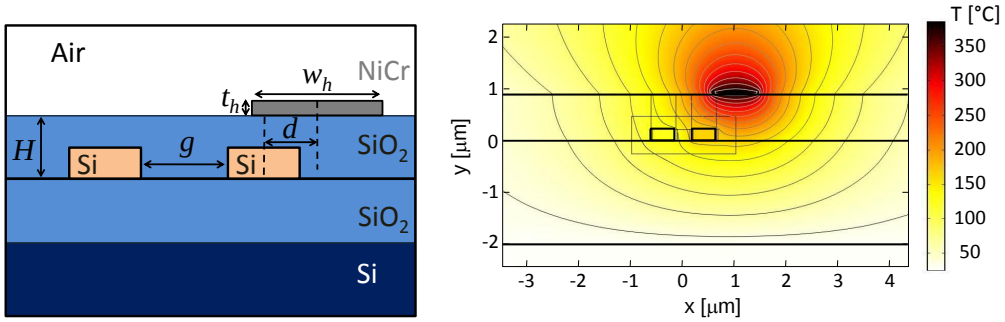

(a) (b)

Figure 3.1.: (a) Sketch of the TDC cross section.(b) 2D thermal FEM simulation of the silicon TDC cross section.

straight waveguides are spaced by a gap distance, g, and the NiCr heater is placed on top of the overcladding at a distance, d, from the centre of one of the coupled waveguides. Finally, the heater length was designed to be equal to the straight coupling section L_c.

From Eq. (A.41) it is possible to express the power K coupled between the waveguides of the TDC and normalized to the input power as $K = \frac{|\kappa|^2}{S^2}\sin(SL_{eff})^2$, where $S = \sqrt{(|\kappa|^2 + \Delta\beta^2/4)}$, κ is the coupling coefficient, $\Delta\beta = 2\pi\Delta n/\lambda$ is the phase mismatch term and λ is the free space optical wavelength. The tuning of the phase mismatch term allows then the control of the coupled power.

An example of the device behaviour is shown in Fig. 3.1b, which reports the temperature distribution in the transversal section of the device for $P_D = 34.5$ mW, $L_c = 74$ μm and $g = 300$ nm simulated with COMSOL Multiphysics. Switching on the heater induces an evident transverse temperature gradient ΔT proportional to the dissipated electric power P_D. The SiO_2 overcladding acts in fact as a thermal insulator between the two waveguides having thermal conductivity of about 100 times smaller than that of Si [27, 28]. In this example, the heater temperature $T_h = 385$ °C produces a temperature gradient $\Delta T = 38$ °C, evaluated as the difference between the average temperatures in the waveguide silicon cores (165 °C and 127 °C, respectively). This provides, due to the thermo-optic effect, an extra effective index difference Δn_{th} between the two waveguides that adds to the intrinsic one, Δn.

In order to perform this simulation and the ones that will be presented in the following, a thermal conductivity of 163, 1.38, and 1 $W/(m \cdot K)$ for Si, SiO_2 BOX, and oxide overcladding layers, respectively [27, 28] have been assumed. Room temperature (25 °C) was fixed at the boundaries of the 40 μm × 83 μm computational window. Regarding the thermo-optic coefficients, $K_{T_{SiO_2}}$ was fixed at 10^{-5} and the temperature dependence of $K_{T_{Si}}$ [132] was taken into account.

The effect of the induced thermal gradient over the device can be observed in Fig. 3.2 where the electric field principal component of the two supermodes of the structure is plotted for different values of P_D. When $P_D = 0$, the first (Fig. 3.2a) and the second (Fig. 3.2b) supermodes show respectively the typical symmetric and antisymmetric behaviour of a synchronous coupler. When P_D is increased to 25 mW, the coupler starts to be asynchronous as indicated by the mode profile of the supermodes in Fig. 3.2c and Fig. 3.2c. At $P_D = 50$ mW (Fig. 3.2e and Fig. 3.2f), the two waveguides are almost decoupled and the supermodes tend to resemble the modes of the single waveguides.

Having illustrated the geometry, the simulation tool and the main features of the novel proposed structure under analysis, it is now possible to describe the design flow followed to optimize the device tuning efficiency.

3.2.2 *Design*

The dependency of K versus P_D can be calculated applying Eq. (A.41). This equation depends on the Δn between the two modes of the single waveguides. The two modes have then to be then computed separately. This can be done with a three step simulation process. In the first step the calculation of the thermal profile in the presence of both waveguides is done (see Fig. 3.1b). In the second step, a mode solver is employed for a geometry that includes the previously calculated thermal profile and just one of the two waveguides. The third step is similar to the second one considering the other waveguide. In Eq. (A.41), the values of κ extracted during

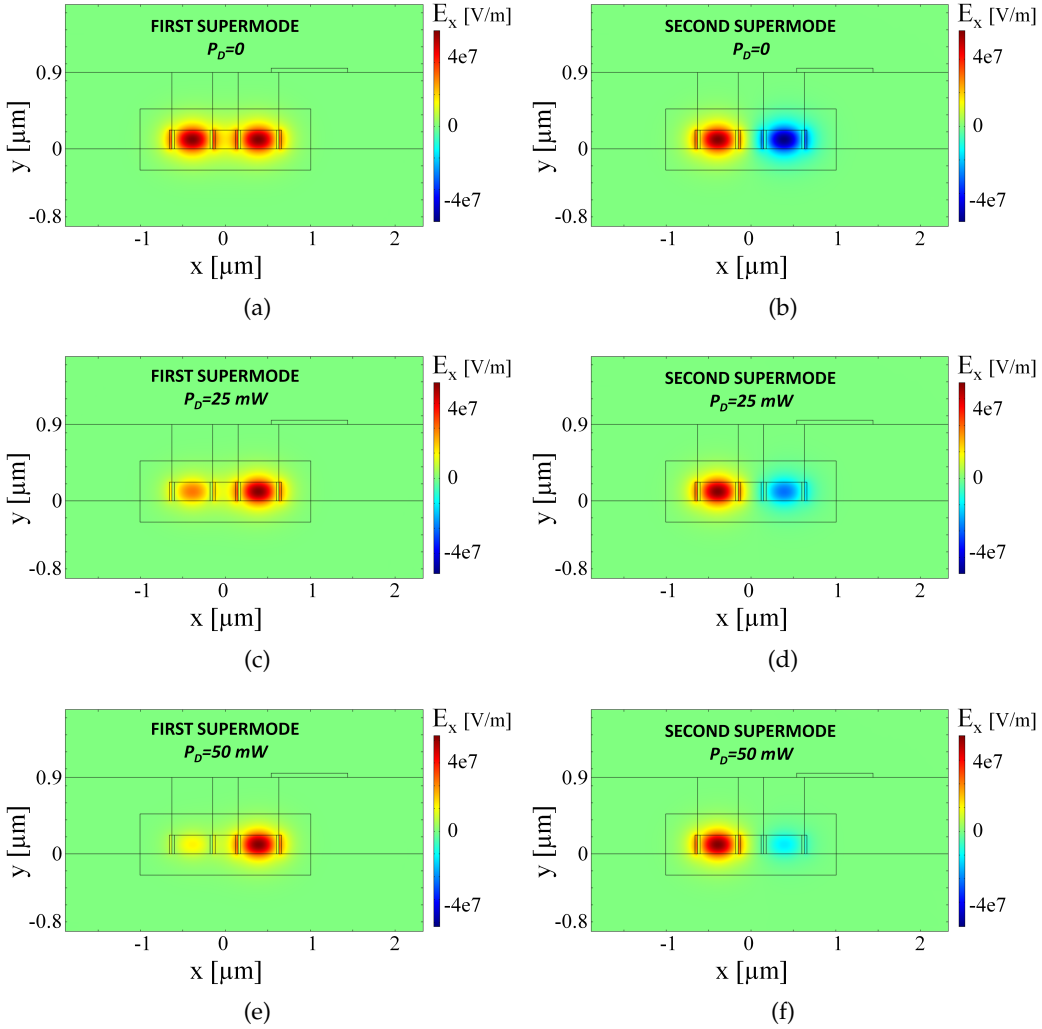

Figure 3.2.: Electric field principal component (E_x) of the: (a) First (Symmetric) and (b) Second (Antisymmetric) supermode of the coupler for $P_D = 0$; (c) First and (d) Second supermode of the coupler for $P_D = 25$mW; (e) First and (f) Second supermode of the coupler for $P_D = 50$mW;

the DC characterization part of this work (see 2.2.2) have been used. Moreover κ has been assumed independent from P_D. In other words, it has been assumed that the mode profile has negligible variations when P_D changes. Finally, as illustrated in subsection 2.2.1, the effective length $L_{eff} = L_c + 2L_{tr}$ have been considered in (A.41) instead of just L_c. Bend-bend input/output sections with $R = 20$ µm have been assumed in all simulations.

The tuning efficiency (i.e. the amount of coupled power reduction for a given P_D) depends in principle on four geometrical parameters: H, d, g, L_c and on the intrinsic phase mismatch between the two waveguides (Δn). The latter is related to the waveguide width difference (which may be designed on purpose or result from fabrication tolerance effects). The optimization of the device requires the investigation on which combination of the cited parameters gives the best performance.

The overcladding height H is however fixed by the exploited silicon platform and consequently can be considered constant (900 nm in our simulations).

The tuning efficiency dependence on the heater lateral shift d and on the coupler gap g is analysed first. This can be done by comparing the performance of TDCs having different d and g but the same intrinsic Δn and the same coupled power K when $P_D = 0$. We selected three synchronous couplers ($\Delta n = 0$) designed to couple 100% of the power ($K = 1$) when no electrical power is dissipated over the heater. The minimum gap was set to 200 nm, a value chosen considering the technological possibility to guarantee good gap filling and consequently good coupler values repeatability. The maximum gap was set to 300 nm in order to work with TDCs having compact size. As discussed in subsection 2.2.1, the larger is g the lower is κ and consequently the length of the coupling region L_c required in order to achieve a given K becomes longer. The third gap was then set to 250 nm. Performance are in this case evaluated evidencing the changes of the effective index difference Δn_{th} normalized to Δn_{th0}, the amount of effective index difference necessary to switch off the coupler (i.e. to pass from $K = 1$ to $K = 0$). With $\Delta n = 0$ and $K = 1$ (i.e. $\kappa L_{eff} = \pi/2$) it can be in fact easily derived from Eq. (A.41) that the coupled power depends on $\Delta n_{th}/\Delta n_{th0}$, with $\Delta n_{th0} = \lambda\kappa\sqrt{3}/\pi$. TDCs with larger κ (i.e. smaller g) require then larger values Δn_{th} to obtain a given coupling variation.

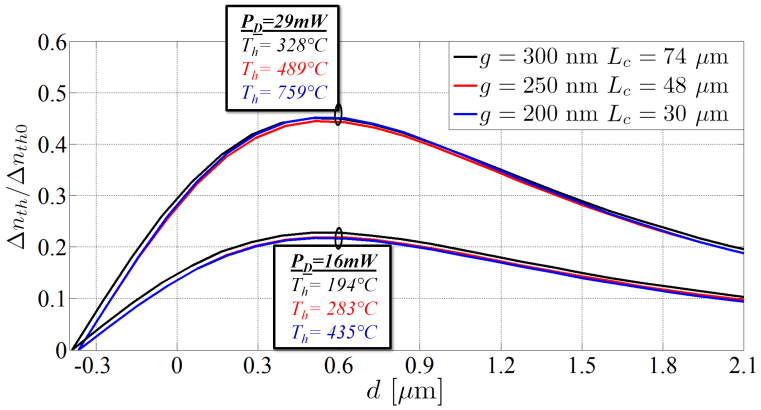

Figure 3.3.: Normalized thermally induced effective index difference versus d for three TDCs with $g = 200$ nm (blue curve), 250 nm (red curve), and 300 nm (black curve). The length of the coupling region L_c is chosen to have $K = 1$ for $P_D = 0$. Heater temperatures T_h refer to the case $d = 0.6$ μm.

Fig. 3.3 shows the simulated performance as a function of d of the three considered TDCs for two different values of P_D. Each coupler is represented by a different colour. Different traces with the same colour corresponds to different values of P_D. Results are quite interesting and look promising for setting up a simple and general design procedure. Curves in fact group in bundles depending basically only on the dissipated power. The lower bundle corresponds to the results obtained with a

dissipated power $P_D = 16$ mW. In this case maximum tuning efficiency (i.e. larger $\Delta n_{th}/\Delta n_{th0}$) is reached for d of about 0.6 μm. Moreover, it is possible to notice that the tuning efficiency is almost independent on the coupler gap. As introduced previously, smaller gaps are associated to smaller values of L_c. The same P_D dissipated over a shorter length results then in a larger heater temperature T_h. Consequently, a larger value of Δn_{th} is achieved. However, it should be noted that a lower bound exists for L_c, set by the fuse temperature of the heaters.

Increasing the dissipated power P_D to 29 mW, (upper bundle of curves in Fig. 3.3), the same conclusions can be drawn.

Though the figure reports only two examples concerning $P_D = 16$ and 29 mW, these results are general. A maximum tuning efficiency is always reached for d of about 0.6 μm, no matter on the value of the dissipated power. The maximum is rather flat, indicating that the index change is expected to change not so much for varying d. Moreover, the gap g does not significantly affect results. The ensemble of these features allows a robust design and fabrication procedure. The precision in the mask alignment during the fabrication process can in fact be as good as few nanometers (50 nm at very most) making the device almost insensible to heater positioning fabrication tolerances.

It is now possible to analyse the behaviour of the TDCs with a fixed value of the gap ($g = 300$ nm) and of the heater lateral shift ($d = 0.6$ μm) and varying L_c (i.e. varying K when $P_D = 0$). In Fig. 3.4, the simulated K of four synchronous TDCs ($\Delta n = 0$, solid lines) for several lengths of the coupling region $L_c = 41$ μm (red), 52 μm (blue), 57 μm (orange), and 74 μm (black) are compared. For all these devices

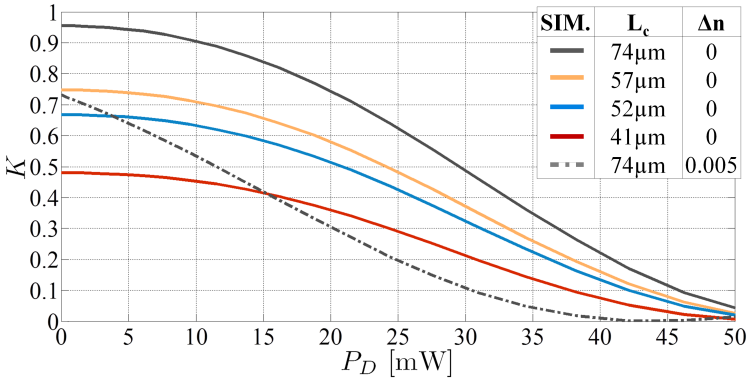

Figure 3.4.: Simulated K versus P_D of four synchronous TDCs with lengths of the coupling region $L_c = 41$ μm (red), 52 μm (blue), 57 μm (orange), and 74 μm (black). The dashed-dotted line show the performance of an asynchronous TDC ($\Delta n = 0.005$) with $L_c = 74$ μm. All the devices have $g = 300$ nm and $d = 0.6$ μm.

K can be reduced by about three times with P_D varying from 0 to 35 mW. More than 50 mW are required to make K smaller than 0.05. Note that the absolute K reduction for a given P_D reduces with the length of the coupler (i.e. with the value

of K when $P_D = 0$). The design of couplers with low values of K can then lead to highly inefficient devices. Moreover, due to the small length required to design such couplers they may reach the fuse temperature of the heater before showing any appreciable K variation. To give a practical example, the limit value of P_D/L_h, which is in this case equal to P_D/L_c, experimentally found during this work and described in Section 1.4 can be used. For a TDC with $L_c = 41$ μm the maximum safe P_D would be equal to about 24.6 mW. This would limit this coupler tuning range between $K = 0.48$ and $K = 0.3$.

The low efficiency of the described synchronous couplers ($\Delta n = 0$) is suggested by Eq. (A.41), stating that, for these devices, the derivative of K versus $\Delta\beta$ (that is, versus P_D) vanishes at a small P_D. The tuning efficiency can be increased by designing asynchronous TDCs ($\Delta n \neq 0$) in order to steepen the K–P_D characteristic. The grey dashed-dotted trace in Fig. 3.4 shows the measured and simulated performance of an asynchronous TDC with the same g, d, and L_c parameters of that indicated by the black curve. The only difference is that one of the two coupled waveguides is narrowed to $w = 477$ nm in order to have an initial $\Delta n = 0.005$. Due to this intrinsic phase mismatch, the tuning curve decreases linearly at small P_D with a K–P_D slope of 0.021 mW^{-1}. Less than 32 mW are now required to bring K from 0.7 to 0.05.

Once the device numerical optimization has been performed, a set of devices has been fabricated to analyze their performance and their agreement with simulations. The analysis of the results will be illustrated and discussed in the next Section.

3.3 FABRICATED DEVICES

3.3.1 *Characterization*

In order to test the TDC performance a set of racetrack resonators (RRs) in all-pass filter configuration, such as that shown in Fig. 3.5, has been realized. The K values

Figure 3.5.: Optical microscope top-view photograph of a silicon TDC embedded in an integrated RR all-pass filter.

were extracted from RRs with a radius of 20 μm, a round trip geometric length $L_r = 270.5$ μm and λ around 1.55 μm using the device analytical model (i.e. Eq. (2.6)).

This procedure allows for accurate extraction of the coupling coefficient with respect to a simple evanescent coupler configuration. The latter in fact relies on the equal performance of the two outputs since the power at one port is usually normalized with respect to the sum of the power at the two ports of the device. Any variation from this condition could lead to erroneous evaluation of the coupling coefficient. Fig. 3.6 shows the good matching between fitting and the measured response for two different coupling conditions of the resonator. Fitting was performed using

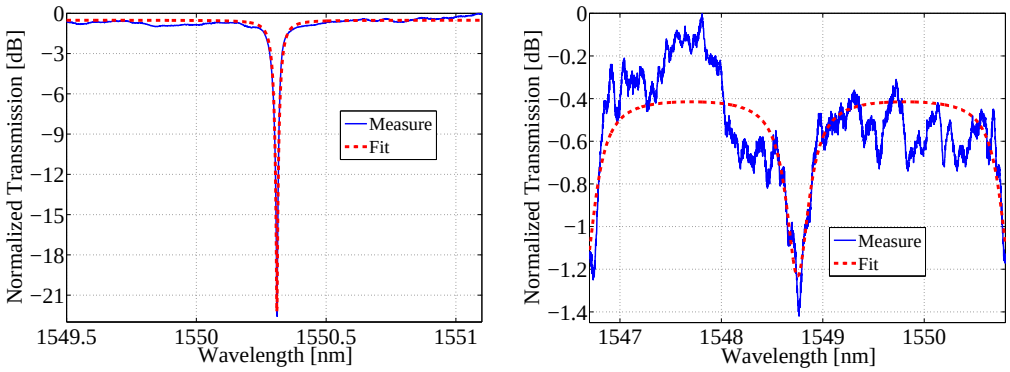

Figure 3.6.: Fitting of RRs normalized transmission characteristic with the analytical model. (a) $K = 0.07$, $\gamma \approx 0.97$. (b) $K = 0.55$, $\gamma \approx 0.98$.

the *nlinfit* function of the commercial software Matlab, leaving the power coupling coefficient of the DC K and the field roundtrip loss factor γ as free parameters. Errors between the analytical model and the measured trace are minimized in the least square sense. In Fig. 3.6a, the fitted K is equal to 0.07 and the fitted $\gamma \approx 0.97$. In Fig. 3.6b instead, the result of the fitting procedure is $K = 0.55$ and $\gamma \approx 0.98$. It can be noticed that the shallower the notch the more the RR characteristic is affected by fluctuations in the transmission spectra, leading to a slightly less accurate estimation of the coupling coefficient. Averaging over different FSRs as well as fixing γ can be used to improve the accuracy in the power coupling coefficient estimation. It is in fact reasonable to assume that on the same RR γ is independent from the coupling condition set by the TDC. The loss value can be taken from measurements where the coupling condition provides shallow notches. Up to now, nothing has been said about the uniqueness of the solution found by the described fitting procedure. It can be in fact highlighted that filters having the same poles but zeroes placed in reciprocal positions with respect to the unit circle show the same magnitude response [92]. As illustrated in subsection 2.3.1, an all-pass RR has one pole in $z_p = \gamma\rho$ and one zero in $z_z = \gamma/\rho$ with $\rho = \sqrt{1-K}$. The same measured transmission can be then fitted with the squared magnitude response of an overcoupled ($\gamma > \rho$) and of an undercoupled ($\gamma < \rho$) resonator having the same z_p. However, unreliable results of the fitting procedure can be identified evaluating the resulting roundtrip

losses. In such cases losses are considerably different with respect to the typical values given by the technology. The corresponding solution can be then discarder and the fitting performed again with different intial values for the free parameters and/or over a wavelength domain with different dimensions.

As an example of the device spectral response, the wavelength domain characteristic of one of the fabricated RRs when the K value of the TDC ($g = 300$ nm, $L_c = 74$ µm) is thermally tuned is showed in Fig. 3.7a. Moreover, Fig. 3.7b shows the relative values of K and of the Q factor. The average round-trip loss

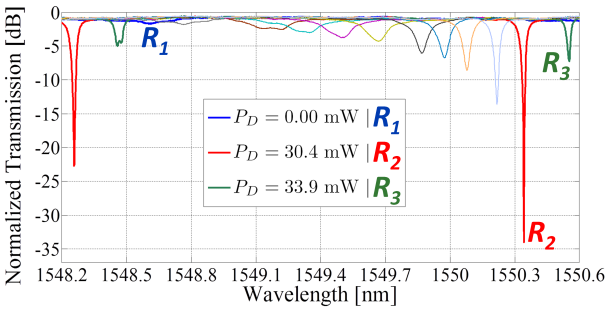

(a)

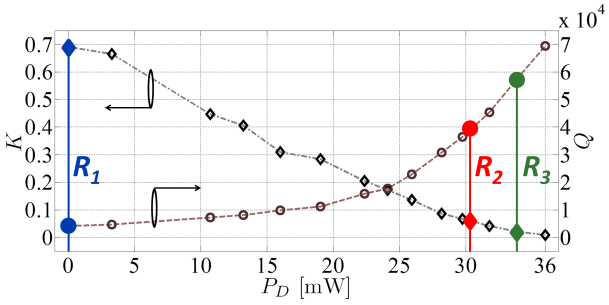

(b)

Figure 3.7.: (a) Wavelength domain response of a RR all-pass filter for increasing power P_D dissipated in the TDC and (b) relative K and Q factor values: overcoupling ($P_D = 0$, $K = 0.7$, blue curve R_1), critical coupling ($P_D = 30.4$ mW, $K = 0.06$, red curve R_2) and undercoupling condition ($P_D = 33.9$ mW, $K = 0.022$, green curve R_3).

is about 0.26 dB/turn, corresponding to a field round-trip loss factor $\gamma = 0.97$. When no power is dissipated in the heater ($P_D = 0$, blue trace R_1), $K = 0.7$ and the resonator is highly overcoupled ($K >> 1 - \gamma^2$) and the Q factor is about 4200. When the heater temperature increases, the power coupled into the RR decreases because of the thermally induced Δn_{th}. As a result, the notch depth progressively increases until the critical coupling condition is reached ($P_D = 30.4$ mW, red trace R_2). Here $K = 0.06 \approx 1 - \gamma^2$, the notch depth is maximum (≈ 33.3 dB) and the Q factor is in the order of 40000. A further increase of P_D undercouples the resonator ($P_D = 33.9$ mW, green trace R_3), so that the notch depth monotonically decreases as well as K, showing a Q factor of about 57000.

This example of the device characterization shows already the potentials of the proposed TDC. The precision in the critical coupling condition setting is demonstrated by the really small minima of the RR resonance notch. Note that this value is also limited by the receiver resolution in wavelength (1pm). Moreover the Q factor has been tuned of one order of magnitude. This feature could allow in a PIC the on and off switching of RR nonlinear effects.

3.3.2 *Heater position and Coupler gap*

The characterization method described in the previous section allowed analyzing the properties of the realized devices. The first investigated property is the tuning efficiency dependence on the heater position. This has been done via the realization of different tunable couplers with the same nominal waveguide widths $w = 480$ nm, length $L_c = 74$ µm and gap $g = 300$ nm but with different values d of the heater position. L_c was set in order to obtain complete power transfer between the two waveguides (i.e. $K = 1$). Before describing the experimental results it is important to remark that resonators that are highly overcoupled (i.e. having large K values) show shallow notches. Consequently, the larger the fluctuations in the transmission characteristic of a device, the more the fitting of large K is unreliable. The maximum experimental K that will be illustrated in the following is then limited by this issue and varies form device to device.

It is now possible to look at Fig. 3.8 where, as predicted by the simulations, the highest tuning efficiency is provided by the heater with the lateral shift $d = 0.6$ µm. In this situation, K is reduced down to 0.52 with $P_D = 29$ mW. The same

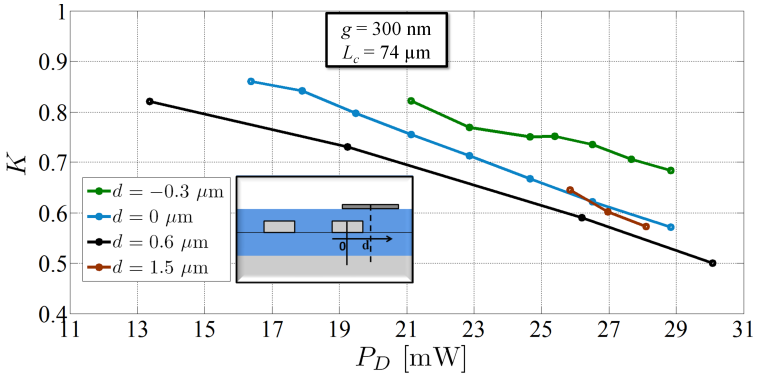

Figure 3.8.: Measured K of four synchronous TDCs with $g = 300$ nm and $L_c = 74$ µm for $d = -0.3$ µm (green circles), 0 µm (blue circles), 0.6 µm (black circles) and 1.5 µm (brown circles).

power dissipation leads to $K = 0.57$ for $d = 0$ µm and $K = 0.68$ for $d = -0.3$ µm, respectively. It is also possible to notice that the efficiency decreases faster if the heater position moves in the direction of the center of the coupler gap (placed at $d = -0.39$ µm) than in the opposite direction. Fig. 3.8 shows in fact that similar

efficiencies have been measured for $d = 0$ and 1.5 µm. To drop the efficiency at that level from the maximum efficiency point ($d = 0.6$ µm) the heater position must move by 0.6 µm in the direction of the gap and of 0.9 µm in the opposite direction as predicted by the simulations. Furthermore it can be noticed that the efficiency dependence on d is not particularly critical confirming the device robustness versus tolerances on the heater positioning.

Once the tuning efficiency dependence on the heater lateral offset has been demonstrated to be in agreement with simulations, it is now possible to verify experimentally the tuning efficiency independence on the coupler gap. To this purpose four synchronous TDCs have been then realized. Two of them have nominal $K = 1$ and $g = 200$ or 250 nm and the others with nominal $K = 0.5$ and $g = 200$ or 300 nm. The heater offset is fixed to $d = 0.6$ µm. In Fig. 3.9 one can see that TDCs with the same nominal K, but different g, have almost the same efficiency, the small difference being due to fabrication tolerances in the DC waveguide widths [133] and thus on the value of K for $P_D = 0$. It is also possible to notice the device efficiency

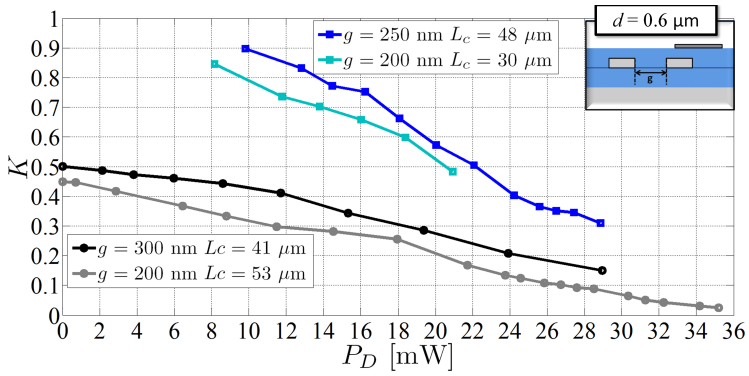

Figure 3.9.: Measured K versus P_D of four synchronous TDCs with nominal $K = 1$ (squares, $g = 200$ and 250 nm) and $K = 0.5$ (circles, $g = 200$ and 300 nm). The heater offset is $d = 0.6$ µm.

independence on the solution order of eq. (A.41). The TDCs with $K = 0.5$ were in fact designed with $SL_c = \pi/4$ (black trace) and $SL_c = 3\pi/4$ (grey trace).

Once the tuning efficiency dependence on the heater lateral shift as well as on the coupler gap have been demonstrated to be in agreement with the simulations, it is now interesting to analyze the performance of the fabricated devices in terms of the coupled power variations as a function of the dissipated power.

3.3.3 *Performance*

In this section, the experimentally measured device performance will be compared to the calculated ones shown in Fig. 3.4. Superimposing the measured points to the simulated features, one gets the results shown in Fig. 3.10. Experimental

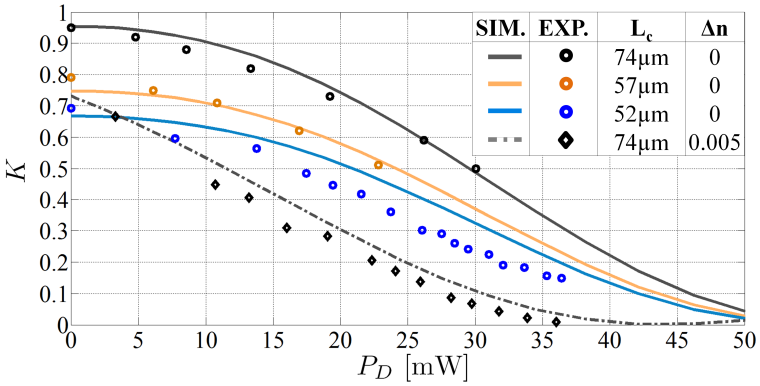

Figure 3.10.: Measured (circles) and simulated (solid curves) K versus P_D of three synchronous TDCs with lengths of the coupling region $L_c = 52$ μm (blue), 57 μm (orange), and 74 μm (black). Diamonds and the dashed-dotted line show the performance of an asynchronous TDC ($\Delta n = 0.005$) with $L_c = 74$ μm. All the devices have $g = 300$ nm and $d = 0.6$ μm.

results agree well with the model, predicting that the maximum K can be reduced by about three times with $P_D = 35$ mW. Fig. 3.10 also shows that the tuning efficiency can be increased if asynchronous TDCs are realized. By realizing one of the two waveguides of the TDC with $L_c = 74$ μm and $g = 300$ nm with a cross section width 3 nm narrower ($w = 477$ nm and $\Delta n = 0.005$) it is possible to steepen the tuning curve as illustrated in Fig. 3.10 by comparing the results represented by the black circles and the black diamonds. The optimized device shows a linear decrease also at small P_D with a $K - P_D$ slope of about 0.021 mW^{-1}. Less than 32 mW are required to bring K from 0.7 to 0.05 and 36 mW must be dissipated to reduce its value below 0.01.

Once the device optimization and characterization has been carried out at about $\lambda = 1.55$ μm (see Fig. 3.7a), it is interesting to see how the device performance varies with wavelength. In general the split ratio of standard evanescent couplers have a wavelength dependence that is related to the coupler geometry. For example longer couplers show larger wavelength dependence. Consequently, it is reasonable to expect that the TDC performance shows this dependence as well, considering, as shown in Fig. 3.10, that the TDC efficiency varies as the K values when $P_D = 0$ vary.

This aspect has been analyzed for the optimized asynchronous TDC on a wavelength span of about 16 nm. The results are shown in Fig. 3.11. In this case the device performance are almost independent on the wavelength being the variations inside the uncertainty bar in the measurements of K. The optimized device shows then good performance also considering this particular aspect. These results are good. However, one can say that they are generally valid only after a set of systematic measurements on different TDCs together with a phase shift control on the RRs to allow the precise wavelength locking of the resonance has been carried out to

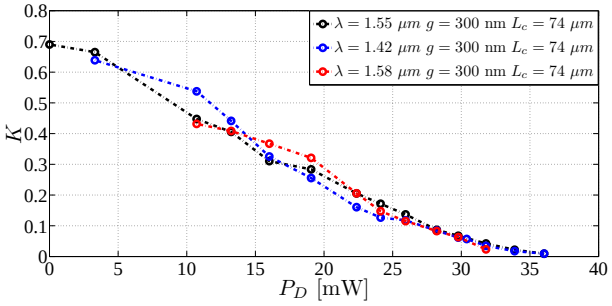

Figure 3.11.: K versus P_D of the optimized asynchronous TDC ($\Delta n = 0.005$) measured for λ around 1.55 µm (black circles), 1.42 µm (blue circles) and 1.58 µm (red circles) and with $L_c = 74$ µm, $g = 300$ nm and $d = 0.6$ µm.

extensively characterize both coupler and TDC performance variations over a wide span of wavelengths.

The last aspect worth of investigation on TDCs concerns their response time. It is known that for a single waveguide realized with the exploited SOI platform this feature is in the order of ten microseconds [49]. One may then wonder if the proposed device, being based on a laterally shifted heater and on the thermal insulation effect of the coupler gap, shows a slower response than that of a device where the heater is placed exactly on top of the waveguide (phase shifter case) or not. Response times of reconfigurable filter geometries based on both phase and coupling tuning such as, for example, that presented in [26, 111], could be then limited (or not) by the proposed TDC.

In order to obtain an estimation of this value for a TDC, the device response to a step dissipated power change was studied by transient FEM simulations based on the presented model. A synchronous device with $L_c = 74$ µm, $g = 300$ nm, $d = 0.6$ µm and $P_D = 34.5$ mW were considered. In Fig. 3.12 the temperature variation ΔT of the two TDC waveguides as a function of time t is illustrated. The temperature in the waveguide closer to the heater (ΔT_1, black circles, upmost curve in Fig. 3.12) varies slightly faster than that of the other waveguide (ΔT_2, red circles, intermediate curve in Fig. 3.12). The response time, defined as the time required to pass from 10% to 90% of the ΔT steady-state value [28], is respectively about 6.4 µs and 6.8 µs. The waveguide position with respect to that of the heater can be then considered not critical regarding the response time. It is now possible to focus attention on the temperature difference between the two waveguides' core ($\Delta T_1 - \Delta T_2$, blue circles, lowest curve in Fig. 3.12). The proposed TDC is in fact tuned by varying this difference. The $\Delta T_1 - \Delta T_2$ steady-state value is 38 °C and the calculated time response is of about 2.6 µs. The TDC activation time has then the same order of magnitude of that of the single waveguides. These simulations allow to conclude that, at least in the considered case, the proposed TDC would not limit

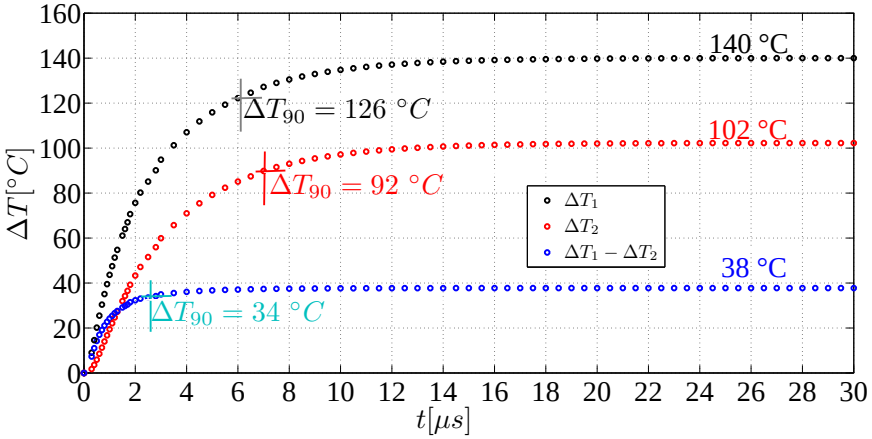

Figure 3.12.: Temperature variation ΔT as a function of time of the waveguide closer to the heater (ΔT_1, black circles) and of the waveguide farther from the heater (ΔT_2, red circles) of a TDC with: $L_c = 74$ µm, $g = 300$ nm and $d = 0.6$ µm for $P_D = 34.5$ mW. Note that $\Delta T_1 - \Delta T_2$ (blue circles) represents instead the temperature difference between the two waveguides. ΔT_{90} indicate 90% of the asymptotic (i.e. steady-state) value of the traces. At the right boundary of the figure the asymptotic value of each trace is indicated over the trace itself.

the reconfiguration time of filters based on phase and coupling tuning. It is anyway reasonable to generalize this result for different parameters of the TDC.

3.4 CONCLUSIONS

In conclusion, a novel silicon photonic TDC driven by a transverse temperature gradient induced by a laterally shifted integrated heater has been designed and characterized through a systematic numerical and experimental investigation. It has been demonstrated that the tuning efficiency is almost independent of the waveguide gap distance and the optimum heater position to minimize power consumption has been found.

Tuning efficiency can be increased by designing TDCs with an intrinsic phase mismatch. This property have been successfully demonstrated in a 74 µm long device where tunable split ratio from 0.7 to 0.01 requiring 36 mW power dissipation was achieved. Moreover, it has also been demonstrated that the presented device allows for a wide tuning of the RR Q factor (1 order of magnitude) as well as the precise setting of the critical coupling condition for RR all-pass filters. In Chapter 6 the presented device will be also successfully employed to widely tune the functionality of a novel reconfigurable filter.

Due to its small footprint, the proposed TDC is a valuable alternative to conventional MZI based schemes in PICs where extremely compact tunable couplers are required, such as in RRs with large free spectral ranges.

4

BRAGG GRATINGS AND GRATING ASSISTED COUPLERS

4.1 INTRODUCTION

The importance of the development of PICs on the SOI platform has been highlighted so far. A BB based approach to the design of the devices is fundamental for the development of circuits with increasing complexity. Some of the most important BB for the realization of passive devices able to perform signal filtering and routing have been characterized and made available for the SOI platform on which this work is based (see Chapters 1 and 2). For some others, despite being widely used and known in literature, a systematic characterization was missing.

In this Chapter, this characterization will be performed for two important BBs: the Bragg grating and the Grating Assisted Coupler (GAC). Both these devices are $1-D$ periodic structure with periodicity along the propagation axis. Due to this periodicity, such devices show a photonic bandgap around a characteristic wavelength, the so called Bragg wavelength, where the mode can not propagate. At this wavelength, coupling with the backward propagating modes is induced.

4.2 BRAGG GRATINGS

Bragg gratings constitute, due to their wavelength selectivity and phase properties [48,134,135], a basic building block for the realization of PICs. They can be employed to realize narrow-band transmission filters [136–138] and Fabry-Pérot cavities [139], for lasing [140–142], as sensors [143,144], for dispersion compensation [145,146] and in general in devices where wavelength selective reflectors are needed [112, 147]. Many of the functionalities formerly described, widely employed in fibre and early stages integrated optical technologies, have been recently demonstrated also in SOI.

The aim of the work described in this Section is the characterization of photonic wire Bragg gratings to define a BB for the SOI platform in the framework of the project SAPPHIRE. In this view, the first step is to define the periodic structure of the device and the model describing its functionality. Then, the device characterization can be carried out to provide the model parameters by fitting the model with the measured spectra. In order to perform a more accurate fitting, the so called

'cavitometric' technique [49] is employed to retrieve the device transmission and reflection characteristics. The reflection provided by the cleaved facets at both ends of the chip can in fact sensibly modulate the measured spectra, especially in reflection. Once the device spectral characteristics have been retrieved, the model parameters can be extracted with accuracy except for one: the insertion loss. This figure is in fact usually the most difficult to be determined with precision because of the low loss nature of SOI Bragg gratings. However, this parameter can be important to determine the exact value of the optical power reflected by the grating. In the following, considerations on the retrieved spectra are performed first to evaluate an upper bound for this figure. This upper bound was indicated in the framework of the project SAPPHIRE for the Bragg grating BB. After that, the analysis of the group delay of the reflected beam is proposed as a technique to estimate with more precision this figure. This Section concludes then with some comments on the design of such devices via the CMT (see Appendix A), widely employed in literature to reduce the computational weight required by numerical techniques such as 3D FDTD.

4.2.1 *Geometry and Model*

A sketch (top view) of the considered geometry is shown in Fig. 4.1, where periodicity comes from a sinusoidal modulation of the waveguide's sidewalls. The

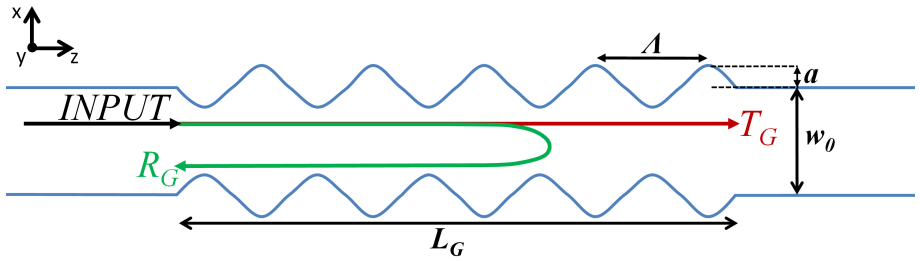

Figure 4.1.: Bragg grating top view sketch.

dependence of the device width on the propagation coordinate z can be described as $w(z) = w_0 + 2a\sin(\frac{2\pi}{\Lambda}z + \pi)$ where w_0 is the average waveguide width, a is the modulation amplitude and Λ is the modulation period. The average width equals the width of the feeding and the output waveguides and will be then fixed to the standard of the exploited SOI platform (i.e. 480 nm).

The device functionality and its reflection properties can be described through the CMT (see Appendix A.5). Due to the low loss technology used in this work, the lossless model derived from the CMT can be assumed first. In the next Section it will be shown in fact that this model well fits the experimental results. The insertion losses I_R and I_T, respectively inside and outside the device reflection band, can be then estimated after the device characterization. The CMT model allows to

design the maximum reflection, the reflection bandwidth and its central wavelength by selecting suitable values of Λ and of the grating length L_G once the coupling coefficient κ and the average waveguide effective index n_{eff} and group index n_g are known. The maximum reflection

$$R_{G_{\lambda_B}} = \tanh^2(\kappa L_G) \tag{4.1}$$

is achieved at the Bragg wavelength

$$\lambda_B = 2n_{eff}\Lambda \tag{4.2}$$

and the grating bandwidth can be calculated by the means of equation (A.60) as

$$\Delta\lambda_{00} = \frac{\lambda_B^2}{\pi n_g}\sqrt{\kappa^2 + (\pi/L_G)^2}. \tag{4.3}$$

The three parameters on which the grating characteristic depend (κ, n_{eff} and n_g) are all functions of the modulation amplitude a. Regarding the coupling coefficient, the higher is a (i.e. the perturbation of the straight waveguide in Appendix A.5) the higher will be the value of κ. A higher value of the coupling coefficient allows for the realization of more compact reflectors (see Eq. (4.1)) with larger bandwidths (see Eq. (4.3)). Considering then n_{eff} and n_g, it can be noticed that their dependence on w is nonlinear (see [49] and Fig. 2.1b). Their average value diverges then from the one of the average waveguide width increasing the value of a.

Bragg gratings can be then designed through the suitable selection of Λ and L_G once a is fixed and the characteristic parameters have been determined. To this purpose we realized different devices with the described geometry and $a = 5, 10, 15, 20$ nm. Two of these amplitude modulations were chosen to be inserted into the SAPPHIRE grating BB library: $a = 5$ nm ('Type A' grating) and $a = 20$ nm ('Type B' grating) in order to allow the designer for the selection between smaller and larger bandwidth reflectors. Note that $a = 5$ nm is close to the minimum perturbation that can be successfully realized (i.e. 3 nm). The grating period was fixed to 320 nm to obtain, in the hypothesis of a sinusoidal perturbation of the effective index, a Bragg wavelength close to 1550 nm (i.e. $\lambda_B = 1544.3$ nm).

In the following subsection the characterization technique employed to extract the necessary model parameters and the obtained results will be presented.

4.2.2 *Linear characterization*

Characterization technique

Transmission and reflection measurements of Bragg gratings can be easily performed through an end-fire set-up scheme such as that described in Section 1.5.

Typical measured spectra of a grating with $a = 5$ nm and $a = 20$ nm are illustrated respectively in Fig. 4.2a and Fig. 4.2b. The reflected (R_G, green trace) and the

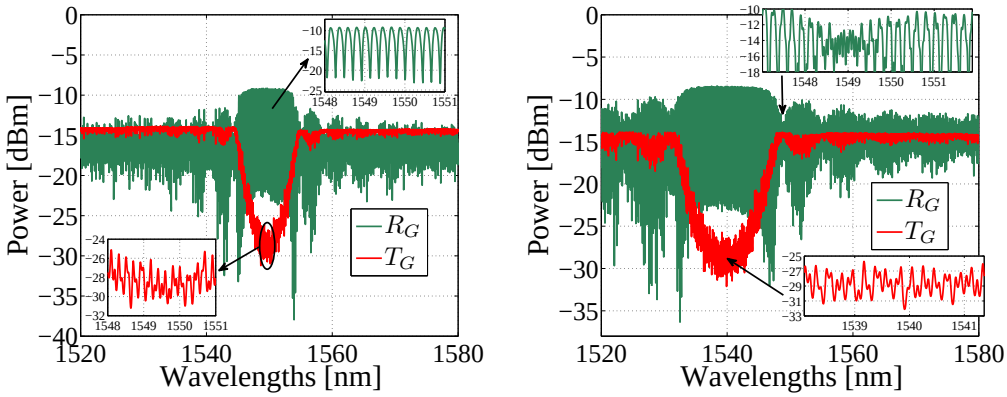

Figure 4.2.: Transmission (T_G, red trace) and reflection (R_G, greentrace) measured spectra of a Bragg grating with: (a) $a = 5$ nm, $L_G = 66.72$ µm; (b) $a = 20$ nm, $L_G = 38.56$ µm.

transmitted (T_G, red trace) spectra show a superimposed modulation (see insets in Fig. 4.2a and Fig. 4.2b) although modal adapters (inverse tapers) minimizing the reflections given by the input/output facets of the chip were realized (see Chapter 1 and [29]. The modulation depth of the R_G characteristic can be larger than 10 dB covering the grating reflection spectral features. The modulation of T_G is instead not dramatic and Bragg gratings characteristic parameters such as κ, n_g and λ_B can be easily extracted from it. However, the retrieval of R_G and T_G is necessary to obtain a more complete analysis of the device reflection properties as well as a more accurate parameters extraction.

This can be done exploiting the so called 'cavitometric' technique [49]. This technique is based on the analysis and the processing of the transmission and reflection autocorrelation functions, respectively A_T and A_R. They are obtained by Fourier antitransforming the measured transmission and reflection spectra and can be expressed as a function of the optical spatial coordinate $z_{opt} = zn_g = c\tau_g$, where z is the spatial coordinate, n_g represent the group index, c the speed of light in vacuum and τ_g the group delay. In reflection this technique is known as Coherent Optical Frequency Domain Reflectometry (C-OFDR) and is described in detail in [148].

The reflection autocorrelation function of a grating with $a = 5$ nm and $L_G = 66.72$ µm (see Fig. 4.2a for the spectral characteristic) is illustrated in Fig. 4.3. Note that in this case we have expressed A_R as a function of the normalized spatial coordinate $z' = z_{opt}/L_{cav_{opt}}$, where $L_{cav_{opt}}$ is the optical length of the chip. In this way it is easier to relate the autocorrelation function features to the paths of the light inside the chip.

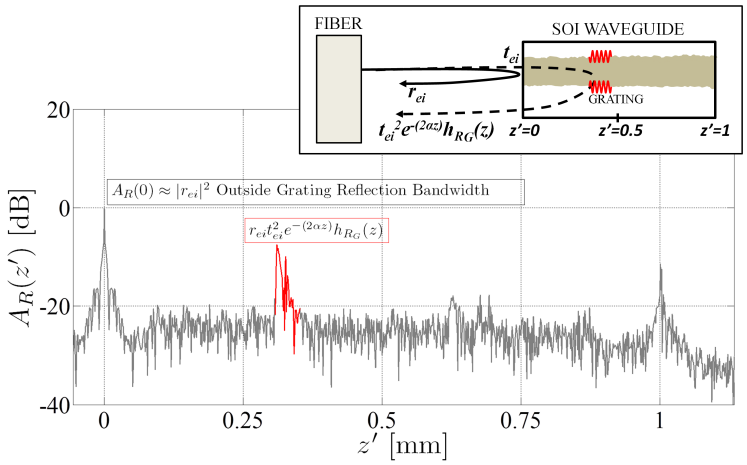

Figure 4.3.: Reflection autocorrelation function of a grating with $a = 5$ nm and $L_G = 66.72$ µm.

Around $z' = 0$, we can notice the 'DC' component of the autocorrelation function $A_R(0)$. This component contains the informations on the total reflected power coming from all the possible reflection paths. Far from the Bragg reflection bandwidth, it is reasonable to assume that the fibre to waveguide reflection dominates. Isolating this component and Fourier transforming it is then possible to retrieve the value of the input fibre to waveguide power reflection coefficient $|r_{ei}|^2$.

For $z' > 0$ different peaks exist above the bakcscattering noise floor [149]. These components of the autocorrelation function are related to the two by two products between all the possible reflection paths in the chip and occur at z values corresponding to the half of their path difference. Close to $z' = 0.25$ we can notice the term that includes the grating complex impulse response h_{R_G}, equal to $r_{ei} t_{ei}^2 e^{-(2\alpha z)} h_{R_G}$, where t_{ei} is the input fibre to waveguide amplitude transmission coefficient and $e^{-(2\alpha z)}$ accounts for the propagation losses. In Fig. 4.3 this component is highlighted in red and an IIR characteristic due to the grating reflection principles can be noticed. By filtering this component we can access to both phase and amplitude information of the grating, getting rid of the observed spurious modulations. At $z' = 1$ the component related to the optical path of a wave experiencing the reflection of the output facet and a double transmission of the grating can be observed. In the range $0.5 < z' < 0.75$ we can then find components related to optical paths characterized by roundtrips in the cavities formed by the grating and the chip facets. By proper filtering of the autocorrelation function it is then possible to verify that the strong modulation observed for R_G is present just when both the DC and the $r_{ei} t_{ei}^2 e^{-(2\alpha z)} h_{R_G}$ component are present. This indicates that the beating between the fibre to waveguide and the grating reflection are the main cause of this detrimental behaviour.

Having analysed $A_R(z')$ we can now briefly analyse the transmission autocorrelation function properties of the device. The same procedure adopted to analyse the

reflection autocorrelation function can be applied for the transmission one considering now transmission instead of reflection paths. In Fig. 4.4 $A_T(z')$ is illustrated. $A_T(0)$, evidenced in red in Fig. 4.4, contains the total transmitted power related

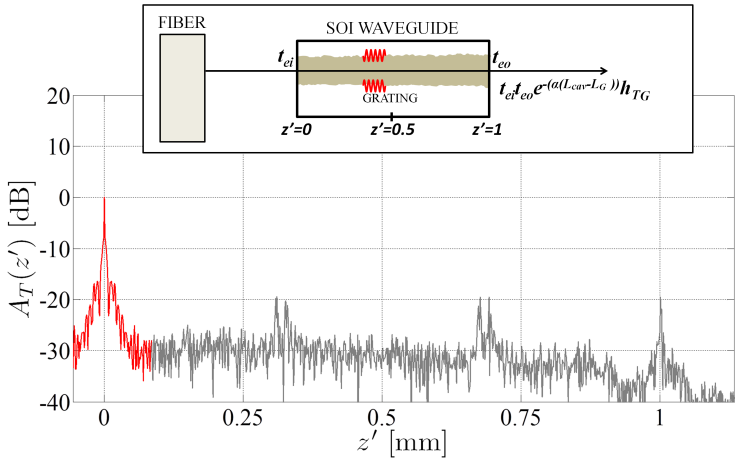

Figure 4.4.: Transmission autocorrelation function of a grating with $a = 5$ nm and $L_G = 66.72$ µm.

to all the possible optical paths. Assuming, as verified also thanks to the cavitometry, a good quality of the modal adapters (i.e. small reflection given by the chip facets) the dominant contribution in this case is given by the direct path between the source and the receiver. From this component we can then retrieve T_G getting rid of the interference pattern modulating the transmission characteristic. By Fourier transforming the filtered characteristic it is possible to obtain the following product: $t_{ei}^2 t_{eo}^2 e^{(-2\alpha(L_{cav}-L_G))} T_G$, where t_{eo} is the amplitude waveguide to fibre output transmission coefficient and L_{cav} is the geometrical length of the chip.

The observed interference pattern modulating T_G is due to the compound cavity system realized by the end facets of the chip and the grating. The presence of the grating gives rise to extra light paths in transmission with respect to the case where a simple waveguide is the DUT. We can in fact notice that the autocorrelation function shows two components above the backscattering level between $A_T(0)$ and $A_T(1)$ (component related to a light path that experience one chip cavity roundtrip before exiting the chip from the output facet). The component close to $z' = 0.25$ is related to the cavity defined by the input facet and the grating while the component close to $z' = 0.75$ is related to the cavity defined by the grating and the output facet. This brings to modulation depth of the transmission characteristic larger than that occurring in the single waveguide case where just the facets reflectivity are responsible for multiple transmission paths.

The described technique allows for the recovery of the grating power transmission characteristic as well as its amplitude and phase reflection properties. In Fig. 4.5 the recovered R_G and T_G characteristic from the gratings spectra showed in Fig. 4.2.

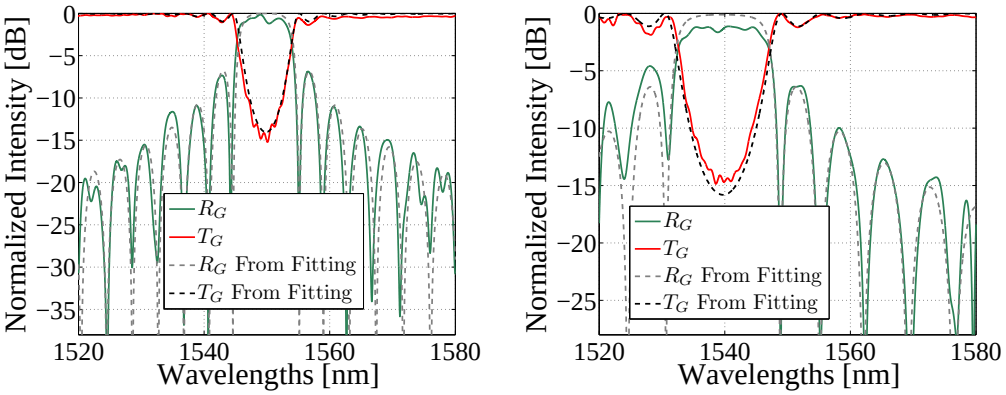

Figure 4.5.: Transmission (T_G, red trace) and reflection (R_G, green trace) spectra retrieved with the cavitometric technique of a Bragg grating with: (a) $a = 5$ nm, $L_G = 66.72$ µm; (b) $a = 20$ nm, $L_G = 38.56$ µm. Dashed lines are the results of simulations with the lossless Bragg grating model and the parameters extracted from the fitting procedure.

The grating reflection has been normalized with the retrieved value of $|r_e|^2$. Both T_G and R_G have been then normalized with respect to the maximum of T_G assuming $t_{ei} = t_{eo}$ and negligible propagation losses. The grating properties can be now easily analysed and the Bragg grating characteristic parameters can be extracted from T_G and R_G by a fitting procedure employing the CMT lossless model. Fitting was performed, as in subsection 3.3.1, using the *nlinfit* function of the commercial software Matlab. Both gratings illustrated in Fig. 4.5 show an extinction ratio in transmission at the Bragg wavelength of about 15 dB. The reflection characteristic in Fig. 4.5a shows a 3 dB bandwidth equal to 8.7 nm, $\Delta\lambda_{00} = 10.95$ nm and the higher sidelobe at about -6.5 dB from the reflection maximum. The one in Fig. 4.5b shows instead a 3 dB bandwidth equal to 15.14 nm, $\Delta\lambda_{00} = 18.23$ nm and the higher sidelobe at about -4.2 dB from the reflection maximum.

Model parameters

In order to extract the grating characteristic parameters, devices with four different L_G for each one of the considered values of the amplitude modulation were realized. In Fig. 4.5 the dashed traces are obtained using the CMT lossless model with the average values of the extracted parameters. The good agreement with the recovered traces indicates both the reliability of the model as well as the on chip performance uniformity of the gratings. The grating extracted parameters are summarized in table 4.1 together with the value of $\Delta\lambda_{00}$ calculated through equation (4.3) with $\kappa L_G = \pi$. Note that the considered κL_G brings an $R_G \approx 0.99$ in a lossless grating (see equation (4.1)).

Table 4.1.: Bragg Grating Parameters

Type	a[nm]	κ[μm^{-1}]	n_g	λ_B/Λ	σ_{λ_B}[nm]	$\Delta\lambda_{00}(\kappa L_G = \pi)$[nm]
A	5	0.035	4.181	4.843	0.14	9.11
B	20	0.065	4.294	4.811	0.3	16.12

Regarding the Bragg wavelength, it can be noticed that both type of gratings show a good on chip uniformity, being the registered standard deviation σ_{λ_B} always lower than 0.3 nm. However, as stated in Section 4.2.1, gratings with different sidewall modulations than those listed in table 4.1 were realized, measuring in some cases λ_B variation as high as 1.7 nm. This value must be taken then into account when gratings or more complex structures including gratings must be designed.

With the parameters listed in table 4.1 it would be in principle possible to design gratings with the desired λ_B, bandwidth and reflection. However, the information regarding the device insertion loss inside and outside the reflection band are still missing.

The value of the insertion loss outside the grating stopband I_T can be in principle estimated from the direct measurement of the device transmission characteristic once the input/output taper performance have been characterized. The performance of the modal adapters show however a poor repeatability on the measured chip, making its accurate and direct measure not possible. Anyway, the characterized devices are subwavelength gratings. Far from λ_B their insertion loss I_T should not differ from that of a straight waveguide of length L_G. Moreover, the selected perturbations allow the realization of really compact devices. $R_G \approx 0.99$ can be achieved with $L_G = 90$ μm and $L_G = 48$ μm if the 'Type A' or the 'Type B' grating are respectively considered. Considering typical propagation losses of about 3 dB/cm, the values of I_T can then be reasonably assumed lower than 1 dB for both types of gratings.

The insertion loss inside the grating stopband I_R is more difficult to estimate. The cavitometric technique exploited so far cannot provide the absolute value of the reflected power with precision and some assumptions are required. Moreover, as shown in Fig. 4.5, the lossless Bragg model well fits the measured spectra indicating a low value of I_R. In the following, the analysis performed in order to give an estimation of the insertion loss at the Bragg wavelength will be presented.

In Fig. 4.5 T_G and R_G have been obtained assuming negligible propagation losses and equal performance for the input and output chip to fibre coupling. In order to give a first estimation of the grating insertion loss at λ_B we can maintain the latter assumption but consider typical propagation losses (i.e. 3 dB/cm). Assuming then that the propagation losses in transmission outside the grating stopband are negligible (i.e. $I_T = 0$), the value of I_R can be calculated through the difference in R_G at λ_B between the losses CMT model simulations and the measured R_G. In this

case values of I_R always lower than 1 dB and lower than 1.7 dB have been found respectively for the 'Type A' and the 'Type B' grating.

At this point it can be natural to ask if the lossy Bragg grating model, derived again from the CMT (see Appendix A.5), can be also employed to improve the loss estimation accuracy. We can first compare the retrieved grating spectra with the simulation performed with the lossy model, increasing propagation losses and taking into account the parameters of table 4.1. Note that with this procedure we are assuming as negligible the coupling losses between the waveguide mode of the feeding waveguide and the Bloch mode of the grating. This assumption can hold in first approximation due to the relatively small values of a under inspection at least for the 'Type A' grating.

In Fig. 4.6 the retrieved normalized T_G and R_G of the grating with $a = 5$ nm and $L_G = 66.72$ µm are illustrated together with the lossy model simulations for increasing values of I_R. It is immediately noticeable that the intensity characteristic

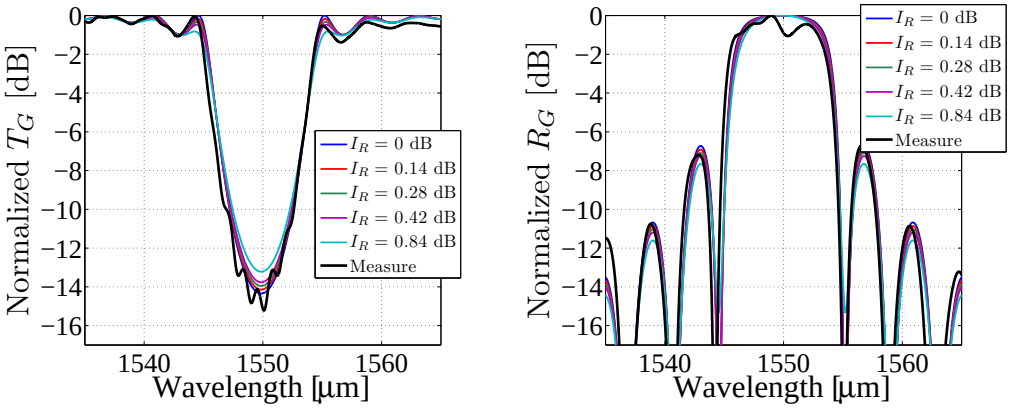

(a) (b)

Figure 4.6.: Normalized (a) T_G and (b) R_G retrieved spectra (thick black traces) and simulated characteristics (colored traces) of a grating with $a = 5$ nm and $L_G = 66.72$ µm varying I_R.

of the grating either in transmission (Fig. 4.6a) or in reflection (Fig. 4.6a) is almost insensitive to a loss increase. However, it can be noticed that for $I_R = 0.84$ dB the simulations start to loose the matching with the measurement.

Similar observations can be done for the grating with $a = 20$ nm and $L_G = 38.56$ µm (see Fig. 4.7). For this grating we can clearly notice that in transmission (Fig. 4.7a) at $I_R = 0.76$ dB the simulated characteristic shows a smoothing that is not present in the measured spectra. However in reflection (Fig. 4.7b) the grating slight asymmetry makes impossible any reasonable conclusion.

The performed simulations, although the grating characteristics are not particularly sensible to a loss increase, indicate that in both type of gratings values of I_R lower than 1 dB can be assumed. These values of I_R are in agreement with those

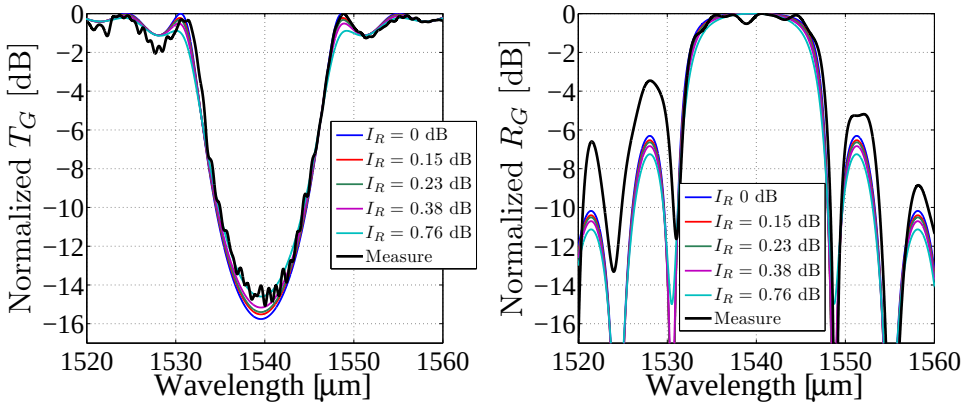

(a) (b)

Figure 4.7.: Normalized (a) T_G and (b) R_G retrieved spectra (thick black traces) and simulated characteristics (colored traces) of a grating with $a = 20$ nm and $L_G = 38.56$ µm varying I_R.

previously discussed for the grating with $a = 5$ nm. Regarding instead the grating with $a = 20$ nm, the difference with respect to the previous discussion is of about 0.7 dB. We can then conclude that I_R lower than 1 dB for the 'Type A' grating and $I_R < 1.5$ dB for the 'Type B' grating can reasonably be assumed.

Group Delay Measurements for accurate loss evaluation

In view of providing the Bragg grating BB design parameters, the information regarding I_R and I_T could conclude the device characterization part of this work. At this point it can however be underlined that the analysis performed brought to a reasonable but coarse estimation of the insertion losses. It is then now of interest to investigate if more precise values of I_R can be obtained with the tools employed in this Section. It can be shown that the Bragg grating characteristic more sensible to the losses is the group delay in reflection τ_{gGR}. Moreover, as stated previously, the cavitometric technique allows to access to the phase properties of the grating reflection and then to measure τ_{gGR}. The comparison of the measured $\tau_{g_{GR}}$ with that those obtained through the lossy Bragg grating model can constitute then a way to obtain a finer estimation of I_R. In the following part of this subsection the results of this analysis will be then illustrated. It should be mentioned before entering into the details of the results that the function $(\tau_{g_{GR}} - \tau_{g_{WG}})$ will be analysed, where $\tau_{g_{WG}}$ is the group delay of a straight waveguide having the same length of the grating. Due to the grating group delay characteristics, reviewed in Appendix A.5, values of $(\tau_{g_{GR}} - \tau_{g_{WG}})$ below 0 are expected at λ_B. For the same reasoning $(\tau_{g_{GR}} - \tau_{g_{WG}})$ maxima will be observed close to the wavelengths determining $\Delta\lambda_{00}$. Finally, far from the Bragg wavelength $(\tau_{g_{GR}} - \tau_{g_{WG}})$ will tend to 0. Moreover, in the following, when using the lossy grating model, the parameters listed in Tab. 4.1 will be employed.

In Fig. 4.8a the measured (black thick trace) reflection group delay of a grating with $a = 5$ nm and $L_G = 66.72$ nm is illustrated together with the lossy grating simulations performed for an increasing value of I_R (grey scale traces). Looking at the

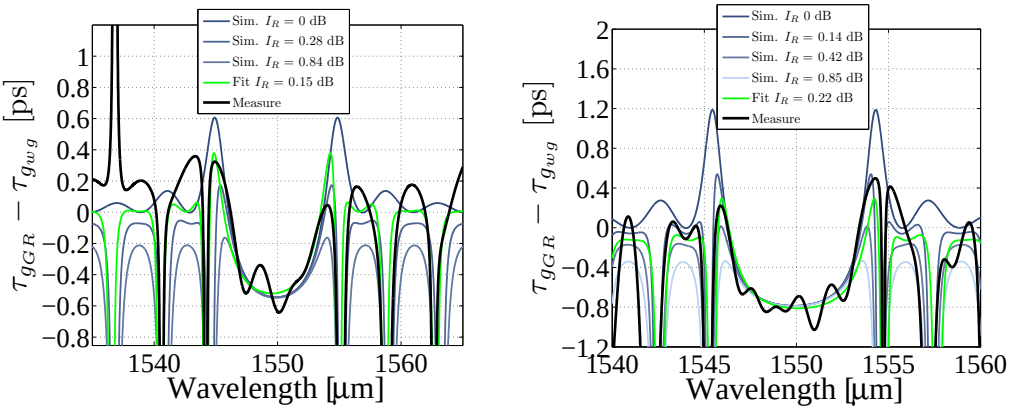

(a) (b)

Figure 4.8.: Measured (black thick trace) and fitted (light green trace) $\tau_{g_{GR}} - \tau_{g_{Wg}}$ of a grating with $a = 5$ nm and: (a) $L_G = 66.72$ μm; (b) $L_G = 84.32$ μm. Grey scale traces are obtained in both figures through simulations with the lossy Bragg grating model and increasing value of I_R.

simulations dependence on I_R it can immediately be noticed that this characteristic of the grating is more sensitive to the losses than the previously showed intensity response (see Fig. 4.6a). It is also noticeable that a good agreement between simulations and measurements can be found by choosing the right value of I_R. Fitting the measured characteristic (green trace Fig. 4.8a), I_R equal to 0.15 dB can be extracted. The measured characteristic depends however on the power reflected by the grating. Approaching the group delay characteristic maxima the grating reflection reduces. It can be then more and more dominated by that provided by waveguide backscattering. The measured group delay can be then less reliable. For wavelengths close to $\lambda = 1530$ nm, the grating has negligible reflection and the peak in the group delay is due to the random nature of the backscattering. Some features of the measured $\tau_{g_{GR}}$ such as the notch at the edges of the reflection bandwidth can be then provided by the backscattering more than by the grating, leading to unreliable results of the fitting procedure.

Due to these considerations, we have performed this analysis also on another grating with $a = 5$ nm but with $L_G = 84.32$ nm. The results are illustrated in Fig. 4.8b. Also in this case we can notice that a good agreement between simulations and measurements can be found for a certain value of I_R. $I_R = 0.22$ dB was found by fitting the measured characteristic.

The good agreement registered in both analysed cases indicates that this method can constitute a way to estimate the losses of low perturbation Bragg gratings. Moreover, the fitted results have been found within the upper bound analysed previously.

This method was also tested for a grating with $a = 20$ nm and $L_G = 38.52$ µm and the results are illustrated in Fig. 4.9. The same conclusions drawn for $a = 5$ nm

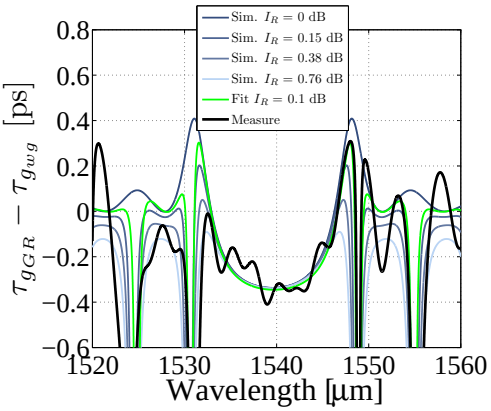

Figure 4.9.: Measured (black thick trace) and fitted (light green trace) $\tau_{g_{GR}} - \tau_{g_{Wg}}$ of a grating with $a = 20$ nm and $L_G = 38.52$ µm.

gratings hold. However, in this case, the measurement and consequently the fitting are conditioned by the asymmetry registered in the grating reflection characteristic (see Fig. 4.7b). Values of I_R below 0.38 dB can be reasonably assumed observing Fig. 4.9.

The analysis carried out in the last part of the former subsubsection showed both a way to extract the Bragg grating reflection losses at λ_B and the low loss nature of this class of devices. Despite the encouraging results shown here, this technique should be tested with more systematic measurements, accompanied also by 3D FTD simulations in order to remove the hypothesis of negligible coupling between the straight waveguide mode and the Bloch mode of the grating.

Up to now, Bragg gratings with different length and values of the sidewall modulation parameter a have been characterized. Nothing has been however said on how we selected the 'right' values of L_G to be fabricated. In order to properly characterize a grating, this length has in fact to be chosen carefully. Depending on the value of κ, too small values of L_G can lead to really low reflection with almost no sidelobes. On the other hand, too large values of L_G can lead to sidelobe values as high as the main lobe. Both cases have to be avoided since the fitting of the Bragg characteristic is critical. A reliable numerical technique have then to be employed for the device design. During this work, the value of κ has been calculated through the CMT. In the next section the comparison between the designed and the measured properties of the grating will be discussed.

4.2.3 *Considerations on the Grating design through the CMT*

The method used so far to calculate the grating coupling coefficient as a function of the sidewall modulation amplitude a is based on the CMT and the procedure applied is described in detail in Appendix A.3. With reference to the coordinate system depicted in Fig. 4.1, the coupling coefficient should be calculated as $\kappa = \kappa_x + \kappa_y - \kappa_z$ where κ_i represent the contribution of the field component along the i direction. κ_x is then related to the fundamental component of the TE mode and κ_z to the longitudinal one.

Previous results collected during this thesis showed that this calculation leads to coupling coefficient values not in agreement with the experiments. This can be related to the fact that the considered devices do not satisfy one of the CMT basic hypothesis: small perturbations. Although the sidewall modulations realized during this work can be considered geometrically small with respect to the waveguide lateral dimensions, their effect of the mode could not be considered small. Guided modes in SOI waveguides show in fact high values at the waveguide core edges (see Fig. 2.1c and 2.1e).

Before the beginning of this doctoral work we found however that by considering just the fundamental component of the field it is possible to obtain values of κ closer to the measured ones. Due to this, in order to design the L_G of the devices presented in the former subsection, we considered $\kappa = \kappa_x$. In Fig. 4.10 the measured and the calculated values of κ and κ_i for Bragg gratings with $w_0 = 480$ nm, $\Lambda = 320$ nm and different sidewall modulation amplitude a are illustrated.

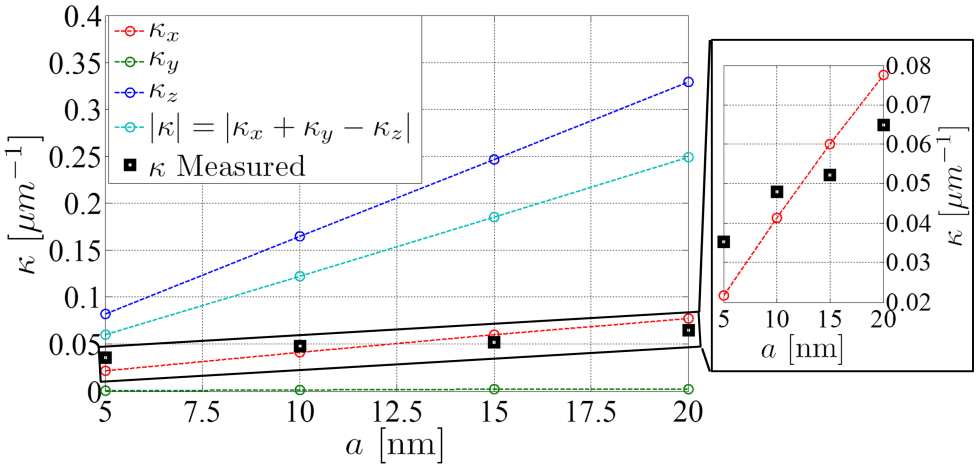

Figure 4.10.: Bragg grating coupling coefficient: measured (black squares) and calculated through the CMT.

It is clearly noticeable that the values of κ_x are those that better approximate the experimental results. The large values of κ_z with respect to κ_x is not surprising. In a high index contrast waveguide such as that considered here, the longitudinal

component of the field is in fact not negligible with respect to the fundamental one. Moreover, the component of the field along the propagation direction has its maxima and minima in correspondence with the waveguide sidewalls (see Fig. 2.1e), i.e. where the modulation to realize the grating is applied and κ is calculated (see Appendix A.3). The presented results confirm that the approximation used to calculate the coupling coefficients of SOI Bragg gratings, even though not rigorous but empirical, can offer a quick approach with a reasonable accuracy. The maximum absolute difference between the measured κ and the calculated κ_x is of about 0.015 μm^{-1} and can be observed for $a = 5$ nm and $a = 20$ nm. Respectively the 'Type A' and 'Type B' grating perturbations of the former subsection. Consequently, the maximum relative difference is registered at $a = 5$ nm.

Considering just the coupling coefficient, it is difficult to evaluate the real impact of the differences. In order to evaluate their effect on the device performance, the values of R_G and $\Delta\lambda_{00}$ as a function of L_G have been taken into account.
Assuming $I_R = 1$, R_G depends only on κ and L_G (see Eq. (4.1)). The reflection value can be then calculated through the CMT considering $\kappa = \kappa_x$ and compared to that calculated with the measured coupling coefficients.
On the other hand $\Delta\lambda_{00}$ depends also on λ_B and n_g (see Eq. (4.3)). The grating bandwidth is calculated considering $\kappa = \kappa_x$, $\lambda_B = 1550$ nm and $n_g = 4.22$ and compared to the bandwidth calculated with the measured values of Tab. 4.1.

We can start this comparison from the case with the biggest relative κ difference between simulations and measurements. The grating with $a = 5$ nm. In this case the calculated coupling coefficient is equal to 0.0216 μm^{-1} while that extracted from the measurement and listed in Tab. 4.1 is of about 0.035 μm^{-1}. Fig.4.11a shows R_G as a function of L_G calculated considering the simulated κ (κ CMT, blue trace) and calculated considering the measured coupling coefficient (κ Fitted, red trace). The difference between these two functions is illustrated in the inset of the figure. The maximum difference is of about 0.3 and occurs when $L_G \approx 35$ μm. This means that a grating designed to reflect the 40 % of the input power would reflect instead the 70 %. The R_G difference decreases as the grating reflection curve saturates. For a designed $R_G = 0.99$ (i.e. $L_G = 140$ μm) the difference is just of about 0.01.

The results concerning $\Delta\lambda_{00}$ are illustrated in Fig. 4.11b. For this figure, the values measured directly from the retrieved grating reflection spectrum has been also added. They are represented by circles. The difference between $\Delta\lambda_{00}$ calculated with the design parameters and $\Delta\lambda_{00}$ calculated with the parameters extracted from the measurements increases as L_G increases (see also the inset of 4.11b). At $L_G = 138.72$ μm, the measured $\Delta\lambda_{00}$ is 1.8 nm larger than that from the design parameters, which is of about 5.7 nm. This difference is quite large, representing almost one third of the designed bandwidth.

Considering then the grating with $a = 20$ nm, the same conclusions can be drawn. In this case the relative difference between the calculated and the measured κ was

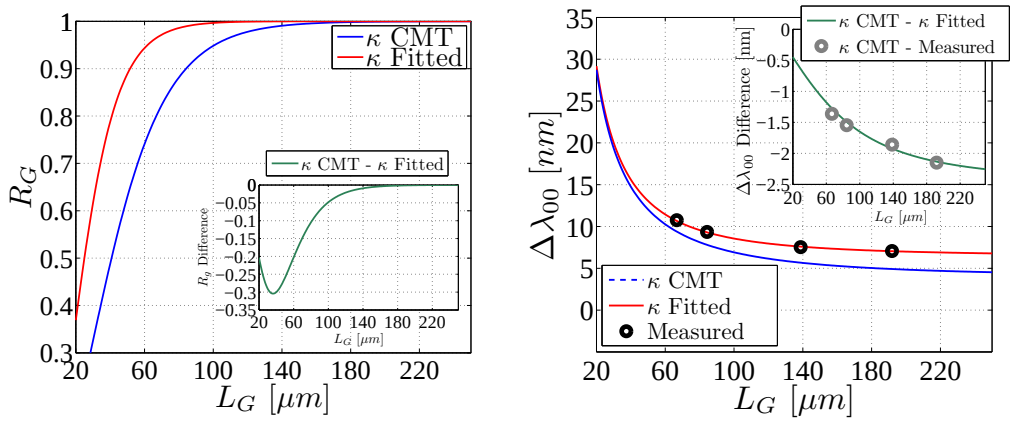

(a) (b)

Figure 4.11.: Simulated (a) R_G and (b) $\Delta\lambda_{00}$ as a function of L_G, of a grating with $a = 5$ nm. Blue traces are calculated with the design parameters while red traces are obtained with the ones extracted from the measurements. Insets of both figure show the difference between these two traces. In (b), black circles represent the measured values and grey circles represent the difference between design and measurements.

smaller and a smaller differences in R_G and $\Delta\lambda_{00}$ can be expected. The calculated coupling coefficient is equal to 0.0775 μm^{-1} while that extracted from the measurement and listed in Tab. 4.1 is of about 0.065 μm^{-1}. In Fig. 4.12a we can notice that the maximum difference is about 3 times lower than in the previous case. At

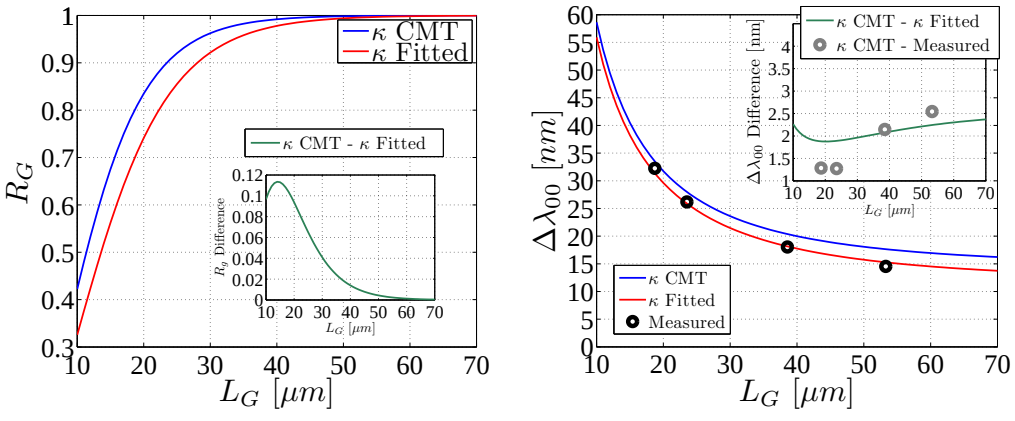

(a) (b)

Figure 4.12.: Simulated (a) R_G and (b) $\Delta\lambda_{00}$ as a function of L_G, of a grating with $a = 20$ nm. Blue traces are calculated with the design parameters while red traces are obtained with the ones extracted from the measurements. Insets of both figure show the difference between these two traces. In (b) black circles represent the measured values and grey circles represent the difference between design and measurements.

$L_G = 14$ μm the designed R_G is equal to 0.63 but it would instead reflect the 52 %

of the input power. For $L_G = 38.56$ μm, corresponding to $R_G = 0.99$ considering the design values this difference is of about 0.018. In this case the value is almost doubled with respect to the previous case but still reasonably small. Regarding instead $\Delta\lambda_{00}$, at $L_G = 38.56$ μm the measured value is 2.1 nm smaller than that calculated with the design parameters that is of about 17.7 nm. The absolute value of the difference is bigger than in the previous case but is much smaller if compared to the bandwidth. The measured $\Delta\lambda_{00}$ is just one ninth smaller than that predicted using the design values.

4.2.4 *Conclusions*

In conclusion, Bragg gratings with two different sidewall modulations have been characterized. The model describing the device features has been presented and the parameters of this model determined. On chip variability of the performance has been also discussed. The obtained results constitute the starting point of the Bragg grating BB on the considered SOI platform. Variability between different fabrication runs should be determined. Moreover, for future development of this BB, different perturbation values as well as apodized and chirped geometries could be investigated.

The insertion loss estimation issue of such devices has been also discussed. A method based on the measurements of the grating group delay in reflection has been proposed to obtain a finer estimation of the loss figure. The described method, although needs to be tested with further measurements and simulations, has shown encouraging results regarding its accuracy and applicability, confirming also the low loss nature of SOI Bragg gratings reflectors.

Finally, it has been shown that the CMT provides rather accurate results when just the fundamental component of the field is considered in the calculation of the coupling coefficient κ. The presented analysis allows to conclude that this method, although not rigorous, constitutes a good starting point for the evaluation of the grating properties. The accuracy for high values of the reflected power can be really good, but it can also be really poor if small R_G are of interest. Moreover, depending on the relative difference between the calculated and the realized κ, the values of $\Delta\lambda_{00}$ can be in good agreement between the design and the experiments and their maximum R_G difference limited. These results can be also read in view of the robustness against fabrication tolerances. Gratings with smaller values of a can be more affected to any variation of this perturbation respect to gratings realized through bigger amplitude modulations.

In the next Section, another class of devices obtained with two parallel Bragg gratings with different average waveguide widths will be presented. The properties highlighted in this Section will be used in the following to design, analyse and characterize the aforementioned devices: the Grating Assisted Couplers (GACs).

4.3 GRATING ASSISTED COUPLERS

Among the various elementary elements that can be developed as building blocks for SOI photonic circuits, an important class of devices that can perform optical routing among different waveguides while being highly wavelength selective are the Grating Assisted Couplers. GACs have been realized during the years with different technologies such as $LiNbO_3$ [150], optical fibres [151] and recently there has been an increasing interest in the development of such devices on the SOI platform [152–159]. These devices can be based either on rib [155, 156] or on ridge SOI waveguides [152–154, 157, 158]. It has been demonstrated how compact 4 channels WDM demultiplexers with low insertion loss can be based on GACs [153, 157]. Moreover, they have been employed for dispersion compensation [154] and pulse compression [159].

In this Section the results of the GAC developed characterization will be illustrated. Attention is focused on the coupling coefficients that, as for the Bragg grating presented in the former Section, can determine the bandwidth of the filter and the device length necessary to obtain the desired amount of backward power coupled. The final aim is in fact the employment of the GAC as a building block in a more complex device, i.e. as a wavelength selective coupler in a RR add-drop filter (see Chapter 5) and these coefficients are fundamental in this view. The GAC functionality and its model are presented first. Finally, the results of the characterization will be presented.

4.3.1 *Functionality and Modelling*

The GAC is a device made by two waveguides with different average widths w_1 and w_2, separated by a gap g and perturbed by gratings with the same period (Λ). A sketch of this device is shown in Fig. 4.13a, where the grating is obtained, as described in section 4.2, by a sinusoidal sidewall modulation of both waveguides with amplitudes a_1 and a_2.

The device functionality should be in principle described through the so called 4-wave model derived from the CMT. This model is briefly reviewed in Appendix A.6 when the orthogonal CMT is taken into account and developed in [160, 161] for the non-orthogonal CMT. The input wave sketched in Fig. 4.13a is: *i)* backward coupled on the same waveguide around the Bragg wavelength defined by $\beta_1 = -\beta_1 + 2\pi/\Lambda$, *ii)* backward coupled in the other waveguide around the Bragg wavelength defined by $\beta_1 = -\beta_2 + 2\pi/\Lambda$ due to the presence of the sidewall modulation, *iii)* forward coupled in the other waveguide due to the broadband codirectional coupling given by the presence of the second waveguide and the harmonic of order zero of the grating.

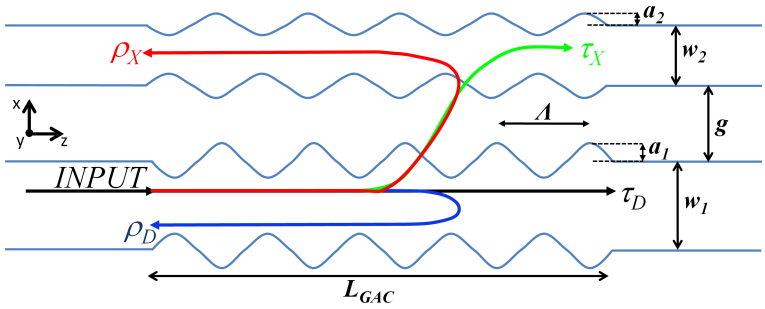

(a)

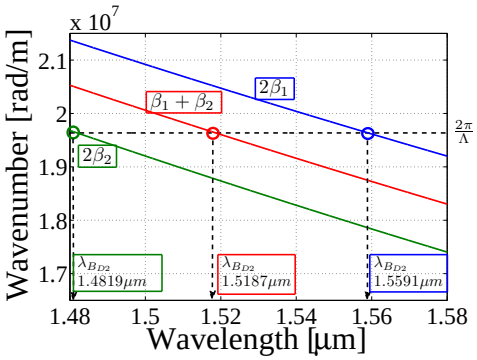

(b)

Figure 4.13.: (a) Schematic diagram of the GAC. (b) Propagation constants of a waveguide with $w_1 = 500$ nm (blue solid trace) and a waveguide with $w_2 = 400$ nm (dark green solid trace). The dash dotted black line represents the grating wavenumber.

However, when the difference between the two average waveguide widths is large enough (large asynchronism condition), the codirectional coupling can be considered negligible. Moreover, the two Bragg conditions are so well separated in wavelength that can be considered as not mutually interacting. In this case is possible to model and solve the problem neglecting the codirectional coupling and, depending on the wavelength region, consider just the contradirectional coupling between two waves as in a Bragg grating. This model is referred to as 2-wave model in [162] and can be found implemented also in [163]. Only two output ports are coupled to the input port while the fourth is considered as isolated (i.e. $\tau_X = 0$ in Fig. 4.13a).

As an example of a fabricated GAC, we can take the waveguides widths w_1 and w_2 as being respectively 500 nm and 400 nm wide, providing different propagation constant in single modal regimes and a period $\Lambda = 320$ nm. Note that this geometry and the related measurements that will be shown were obtained by our group before the beginning of this doctoral work. In this situation the GAC behaviour can be described by its two coupling regimes:

- *Direct Reflection* coupling involve counter-propagating modes (i.e. having propagation constants of equal modulus and opposite sign ($\beta_i = -\beta_j$) in each waveguide. Coupling occurs at two distinct wavelengths ($\lambda_{B_{Di}}$) according to

the phase matching condition $\beta_i = \pi/\Lambda$ depending on the waveguide that acts as the input port. This is shown in Fig. 4.13b where $\lambda_{B_{D2}} = 1.4819\ \mu m$ (the input waveguide is waveguide 2) and $\lambda_{B_{D1}} = 1.5591\ \mu m$ (the input waveguide is waveguide 1). In these conditions the input power flows out through the direct transmission port (τ_D), the output port of the coupler arm where power is injected, and through the direct reflection port (ρ_D), the same port where input power is injected (see Fig. 4.13a). Note that in the 4−wave model of Appendix A.6 these two coupling processes are represented by the coupling coefficients κ_{d1} and κ_{d2}.

- *Exchange coupling* involves counter-propagating modes of the different waveguides ($|\beta_i| = |\beta_j|$, $\operatorname{sign}\beta_i \neq \operatorname{sign}\beta_i$) and occurs at a wavelength halfway between the two direct coupling conditions ($\lambda_{B_{Ex}} = 1.5187\ \mu m$ in the considered case, Fig. 4.13b). In this condition the input power flows out of the device through the direct transmission port (τ_D) and through the exchange reflection port of the coupled waveguide ρ_X (see Fig. 4.13a). Note that in the 4−wave model of Appendix A.6 this coupling process is represented by the coupling coefficient κ_{Ex}.

In Fig. 4.14a the behaviour of a measured device with $a_1 = 10$ nm and $a_2 = 8$ nm is illustrated. The average gap between the two waveguides is $g = 200$ nm and the length of the coupling region is $L_{GAC} = 100$ μm. Exchange and direct Bragg conditions are well separated being $\lambda_{B_{D1}} \approx 1.57$ μm and $\lambda_{B_{Ex}} \approx 1.532$ μm. We can also notice that the codirectional coupling can be considered negligible for the GAC functionality. The lossless Bragg grating model exploited in the former Section and described by Eq. (A.56) and Eq. (A.57) has been then employed to fit the coupling coefficients values κ for each one of the two coupling regimes of the device. In the wavelength range $1.52 - 1.5575$ μm the coupling coefficient related to the exchange coupling $\kappa_{Ex} = \kappa = 0.0072\ \mu m^{-1}$ was found. In the wavelength range from 1.5575 μm onwards, the coupling coefficient related to the direct reflection $\kappa_{d1} = \kappa = 0.033\ \mu m^{-1}$ was extracted. By the means of another device with the same geometry but different input waveguide (i.e. waveguide 2), the value of κ_{d2} was found being of about $0.039\ \mu m^{-1}$. Fig. 4.14b shows the simulation performed through the extracted parameters and the 2−wave model. The GAC spectral characteristics are magnified in the inset around the chosen separation point between direct and exchange reflection. Note that the cross coupling characteristic $|\tau_X|^2$, which is identical to zero at every wavelength, has been offset to improve its readability. Note also that in order to match the Bragg wavelengths, the so called self-coupling coefficients (see Appendix A.5) have also been fitted and considered in the simulations.

The good agreement between simulation and measurements confirms the applicability of the 2−wave model with GAC based on the considered waveguides asyn-

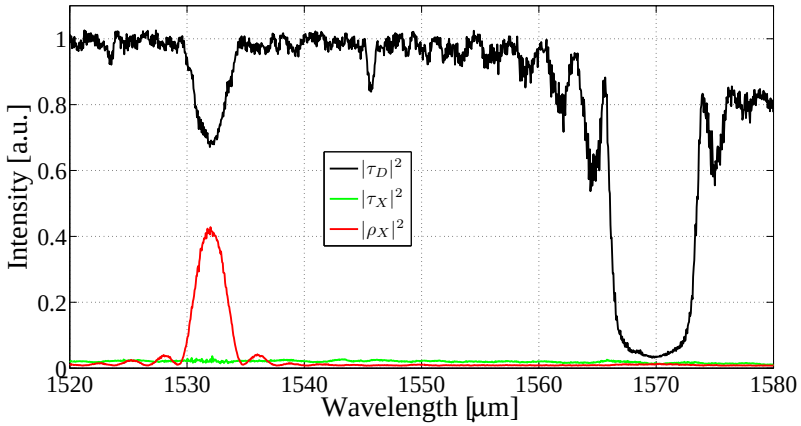

(a)

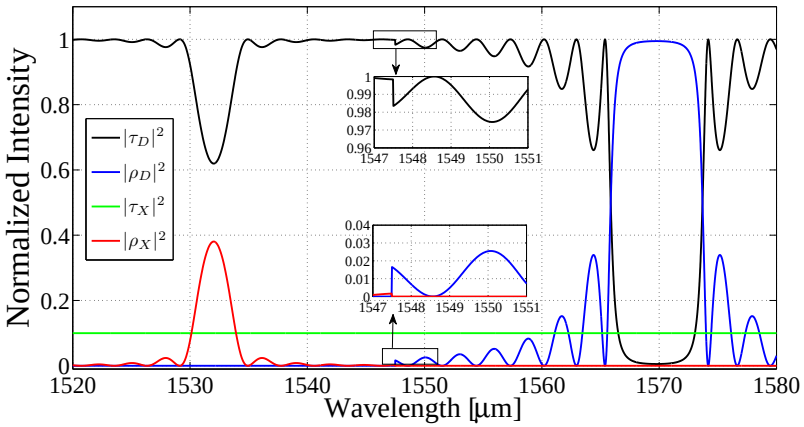

(b)

Figure 4.14.: (a) Experimental behaviour of a GAC with $w_1 = 500$ nm, $a_1 = 10$ nm and $w_2 = 400$ nm, $a_2 = 8$ nm. The average gap between the two waveguides is $g = 200$ nm and the length of the coupling region is $L_{GAC} = 100$ µm. The period is set to $\Lambda = 320$ nm. (b) GAC behaviour simulated with the coupling coefficients extracted from the measurements and the 2−wave model.

chronism. Moreover, the large distance between the direct and the exchange Bragg condition provided by this asynchronism (i.e. ≈ 38 nm) allows focusing attention only on the exchange coupling properties of the device. In fact, if applications inside the optical C-band are of interest, it is easily possible to chose a period Λ in order to have $\lambda_{B_{Ex}}$ inside the desired band and both $\lambda_{B_{Di}}$ outside of it. The applicability of the 2−wave model indicates that, once κ_{Ex} is known, properties such as the power coupled between the waveguides and the bandwidth can be calculated through the same equations used in the former Section for the Bragg grating. The GAC normalized power coupling coefficient at $\lambda_{B_{Ex}}$ can be written as

$$|\rho_X|^2 = \tanh^2(\kappa_{Ex} L_{GAC}), \tag{4.4}$$

while the GAC bandwidth can be written as

$$\Delta\lambda_{Ex_{00}} = \frac{\lambda_{B_{Ex}}^2}{\pi n_{g_{Ex}}} \sqrt{\kappa_{Ex}^2 + (\pi / L_{GAC})^2}, \tag{4.5}$$

where $n_{g_{Ex}}$ is the average between the group index relative to w_1 and the group index relative to w_2. Smaller κ_{Ex} allows the realization of a GAC with smaller bandwidth $\Delta\lambda_{00_{Ex}}$ for a given coupled power $R_{GAC_{Ex}}$. To give an example, in order to have 99 % of the power coupled within a 100 GHz bandwidth considering $\lambda_B = 1550$ nm and $n_{g_{Ex}} = 4.28$, $\kappa_{Ex} = 0.0031$ μm^{-1} and L_{GAC} longer than 900 μm are required. The desired κ_{Ex} can be obtained, in a GAC with fixed waveguide dimensions, by varying 3 geometrical parameters: a_1, a_2 and g (see Appendix A.6). In the next section the exchange coupling coefficient dependence on this three parameters will be then characterized.

4.3.2 *Characterization*

As introduced at the end of the former subsection, the determination of κ_{Ex} is fundamental to design a GAC. Having fixed the waveguide widths $w_1 = 500$ nm and $w_2 = 400$ nm, the exchange coupling coefficient depends on the modulation amplitudes a_1, a_2 and on the gap g. The values of these geometrical variables were selected based on the results obtained by our group before the beginning of this doctoral work. An example of these results has been already shown in Fig. 4.14a. The set of GACs already realized and measured had:

- Three different couples of amplitude modulations:
  - $a_1 = 15$ nm, $a_2 = 10$ nm;
  - $a_1 = 10$ nm, $a_2 = 8$ nm;
  - $a_1 = 6$ nm, $a_2 = 4$ nm.
- Three different gap:
  - $g = 200$ nm;
  - $g = 220$ nm;
  - $g = 240$ nm.

This work was focused on GACs with a relatively small value of κ_{Ex}, ideally lower than < 0.003 μm^{-1}. This interest is explained and justified in Chapter 5, where the GAC have been exploited to realize the wavelength selective coupling of an add-Drop RR. In this view, only the two smaller couples of amplitude modulations have been maintained and the gap variation rage has been expanded. Moreover, $\Lambda = 0.336$ μm was chosen in order to realize devices with a $\lambda_{B_{Ex}}$ closer to 1550 nm.

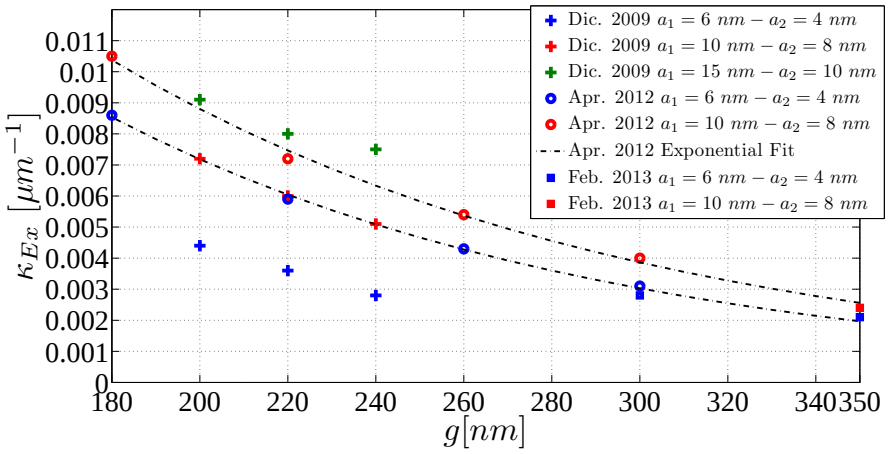

Figure 4.15.: Measured κ_{Ex} as a function of the GAC gap g for different fabrication runs (marker shape) and a_1, a_2 combinations (marker colour). All the measured GACs had $w_1 = 500$ nm, $w_2 = 400$ nm and $\Lambda = 336$ nm.

In Fig. 4.15 the exchange coupling coefficient as a function of the gap for different fabrication runs are illustrated. Results related to different fabrication runs are indicated by different markers. Different colours represent different couples of amplitude modulations. The first fabrication run of this doctoral work was performed in April 2012 (circles in Fig. 4.15) though fabrications have been done since 2009 (crosses in Fig. 4.15). A substantial difference is immediately noticeable. An overall larger value of the coupling coefficients has been obtained. The more recent results obtained for $a_1/a_2 = 6/4$ (blue colour in Fig. 4.15) equals that extracted for $a_1/a_2 = 8/10$ of the previous fabrication run (red colour in Fig. 4.15). In some cases the exchange coupling coefficient is almost doubled. Since the fabrication technique and recipe did not change, a possible reason for this result is a drift in the machines. This drift could have in turn changed the device cross section geometry such as perturbation amplitudes and waveguide widths. The last fabrication run analysed during this work (squares in Fig. 4.15), performed after a shorter period of time, is in fact in line with the expected results. For $a_1/a_2 = 6/4$ and $g = 300$ nm a minimum absolute difference of 0.0003 μm^{-1} can be observed, being the two measured coupling coefficients respectively 0.0031 μm^{-1} and 0.0028 μm^{-1}. The relative difference is approximately one tenth the coupling coefficient value indicating a not dramatic variation in the device performance (see subsection 4.2.3). Moreover, measurement performed for $g = 350$ nm referred to February 2013 are in line with the exponential fitting curve drawn from the April 2012 results. We will then refer from now on to these two fabrication runs for the analysis of the GAC performance.

Focusing on the GAC properties as a function of its geometrical parameters, Fig. 4.15 shows the behaviour expected from the CMT. Larger gaps as well as smaller perturbation amplitudes allow the realization of smaller κ_{Ex}. Moreover, in view of the complex device analysed in Chapter 5, it is important to notice that different combination of a_1, a_2 and g can be used to obtain the same κ_{Ex}. If large values of

g are needed, larger values of a_1, a_2 can be used maintaining the same exchange coupling properties.

Further considerations can be done by observing some example of the spectral behaviour of GACs realized during this work. In Fig. 4.16a the normalized output intensities of a GAC with $a_1 = 10$ nm, $a_2 = 8$ nm, $g = 180$ nm and $L_{GAC} = 235.2$ μm is illustrated. Note that in this case the input waveguide is the one with w_2 as average width. The exchange coupling coefficient is about 0.01 μm^{-1} and

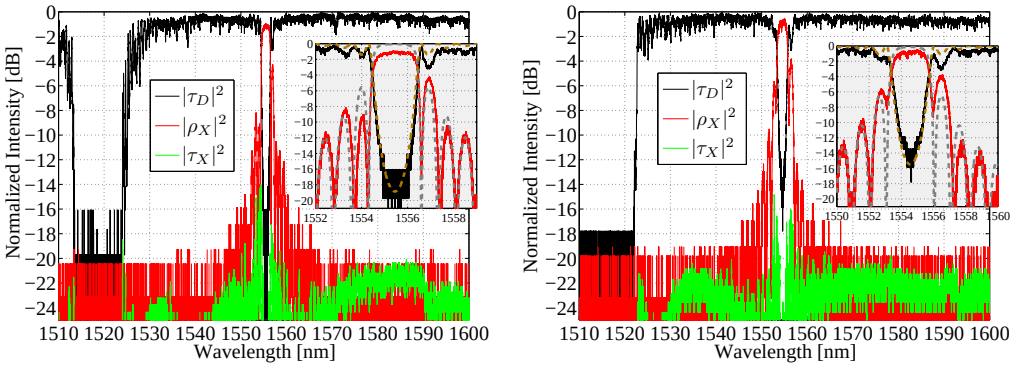

Figure 4.16.: Output characteristics of a GAC with $w_1 = 500$ nm and $w_2 = 400$ nm, $g = 180$ nm, $\Lambda = 336$ nm and: (a) $a_1 = 10$ nm, $a_2 = 8$ nm and $L_{GAC} = 235.2$ μm; (b) $a_1 = 6$ nm, $a_2 = 4$ nm, $g = 180$ nm and $L_{GAC} = 332.64$ μm.

the result of the fitting is depicted in the figure inset with dashed traces. As in the previous subsection it can be noticed that the power levels of $|\tau_X|^2$ can be considered negligible for the GAC performance. The device shows a power dropped at $\lambda_{B_{Ex}} = 1554.57$ nm that is 0.5 dB lower than the $|\tau_D|^2$ maximum, $\Delta\lambda_{00_{Ex}} \approx 2.94$ nm and a 3 dB bandwidth equal to 2.43 nm.

As indicated by the CMT, smaller bandwidths with large the value of the coupled power can be obtained reducing the value of κ_{Ex} at the cost of a device footprint increase. The coupling coefficient reduction can be obtained maintaining the same gap and reducing the sidewall modulation amplitudes as in Fig. 4.16b, where the output normalized intensities of a GAC with $a_1 = 6$ nm, $a_2 = 4$ nm, $g = 180$ nm and $L_{GAC} = 332.64$ μm are illustrated. The measured exchange coupling coefficient for this structure is of about 0.0085 μm^{-1}. The device shows a power dropped at $\lambda_{B_{Ex}} = 1555.46$ nm that is 1 dB lower than the $|\tau_D|^2$ maximum, $\Delta\lambda_{00_{Ex}} \approx 2.31$ nm and a 3 dB bandwidth equal to 2 nm.

The coupling coefficient and consequently the bandwidth reduction has been obtained by keeping $g = 180$ nm and varying the GAC modulation amplitudes of a few nanometers. By looking at Fig. 4.15 it can be however noticed that $\kappa_{Ex} = 0.0085$ μm^{-1} can be also obtained keeping the sidewall modulation amplitudes at $a_1/a_2 = 10/8$ and increasing the gap of more than 20 nm (i.e. from 180 to

203 nm). The coupling coefficient is less sensitive to g than to a_i variations. This means that if a system based of multiple GACs sections with different κ_{Ex} has to be made, fixing the value of a_i and varying g allows for a more robust design to fabrication tolerance effects.

Having characterized the exchange coupling coefficient as a function of a_1, a_2 and g, it is now possible to analyse the Bragg wavelength $\lambda_{B_{Ex}}$ and its dependence on these geometrical parameters. From the characteristics of the GACs illustrated in Fig. 4.16, we can already expect that having fixed g and Λ, the higher the sidewall modulation amplitudes the shorter the exchange Bragg wavelength. This result is in agreement with the behaviour of a simple Bragg grating (see Section 4.2). Increasing a_1 and a_2 can in fact reduce the waveguides' average effective index and consequently the $\lambda_{B_{Ex}}$ value. The dependence of $\lambda_{B_{Ex}}$ on g for $a_1/a_2 = 6/4$ and $a_1/a_2 = 10/8$ are illustrated in Fig. 4.17a. As for the coupling coefficients of Fig. 4.15 different colours correspond to different sidewall modulation pairs and different marker shapes correspond to different fabrication runs. Moreover, different results for the same g, a_1, a_2 and fabrication run refer to devices with different L_{GAC}. Looking first at the results referred to the fabrication run of April 2012, indicated by circle markers in Fig. 4.17a, for both $a_1/a_2 = 6/4$ (blue colour in Fig. 4.17a) and $a_1/a_2 = 10/8$ (red colour in Fig. 4.17a), the on chip variability of λ_{Ex} is larger than the one observed for single Bragg gratings. The maximum difference in λ_{Ex} between devices with the same geometrical parameters but different L_{GAC} can be larger than 4 nm (i.e. 4.8 nm in the worst case). However, it can be noticed that in the majority of cases, this value is below 1 nm. An example of this behaviour is illustrated in Fig. 4.17b, where the $|\rho_X|^2$ characteristics normalized with respect to their maxima of GACs with $a_1/a_2 = 10/8$, $g = 220$ nm and varying L_{GAC} are illustrated. Three traces show their $\lambda_{B_{Ex}}$ within a 0.8 nm band while the fourth one, corresponding to $L_{GAC} = 295.68$ µm, has its central wavelength 4.8 nm apart. This variability has then to be taken into account if a circuit based on different GACs has to be developed. The circuit will have to be either robust to these variations or include postfabrication tuning methods.

Regarding the $\lambda_{B_{Ex}}$ dependence on g, dashed lines in Fig. 4.17a have been drawn as guidelines. They refer to the April 2012 fabrication run and have been obtained averaging the values $\lambda_{B_{Ex}}$ that were bundled within a 1 nm band. This average value shows the same trend as g varies for both a_1/a_2 considered. It increases as g reduces and reduces with an asymptotic behaviour as g increases. This trend can be explained by recalling that one of the assumptions at the base of the CMT is that the modes of the coupler (i.e. supermodes) can be expressed as the linear combination of the single modes of the waveguides composing the structure. This hypothesis is less accurate as the gap decreases. For lower values of the gap, higher values of the supermodes effective indices can be found, leading then to an increase of $\lambda_{B_{Ex}}$.

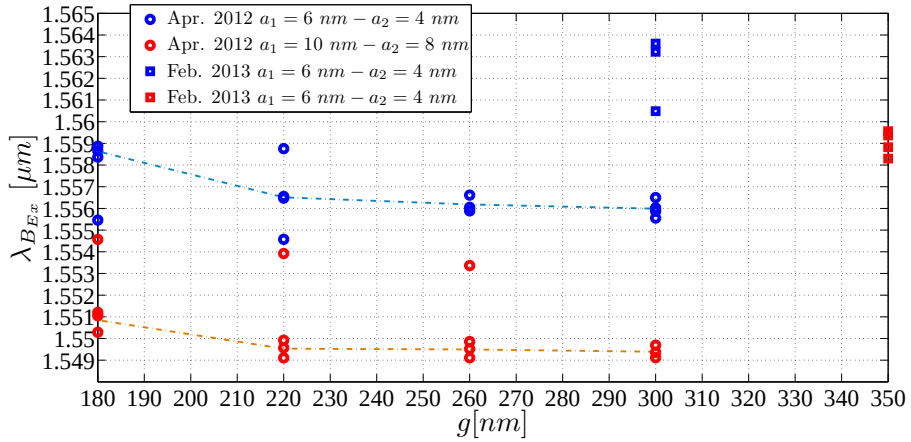

(a)

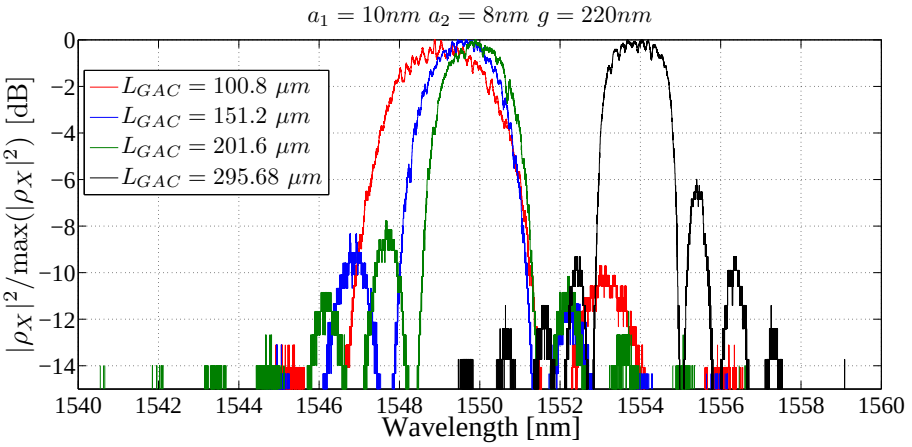

(b)

Figure 4.17.: (a) Measured $\lambda_{B_{Ex}}$ as a function of the GAC gap g for different fabrication runs (marker shape) and a_1, a_2 combinations (marker colour). Different results for the same g, a_1, a_2 and fabrication run refers to devices with different L_{GAC}. (b) $|\rho_X|^2/max(|\rho_X|^2)$ of GACs within the April 2012 fabrication run with $g = 220$ nm, $a_1 = 10$ nm, $a_2 = 8$ nm and varying L_{GAC}.

Finally, the work carried on for the GACs allowed us to monitor the $\lambda_{B_{Ex}}$ variations over different fabrication runs. Looking at the GACs with $a_1/a_2 = 6/4$ and $g = 300$ nm in Fig. 4.17a (blue squares) it is noticeable that variations as large as 9 nm can be detected. Moreover, looking at the results obtained for $a_1/a_2 = 10/8$ and $g = 350$ nm (red squares) we can notice a shift of about the same amount (i.e. 9 nm) with respect to the results that can be expected by looking at the dashed orange guideline.

4.3.3 *Conclusions*

In conclusion, in this Section it has been shown that a GAC based on two waveguides with 100 nm difference in their average width can be successfully described through the CMT based 2−wave model. A systematic characterization of κ_{Ex} dependence on the device gap and perturbation amplitudes has been performed. The GAC exchange coupling coefficient showed a good repeatability comparing the two different fabrication runs performed during this doctoral work. The values measured were however not in agreement with the results available from previous works of our group on the same technological platform. A possible drift in the machines exploited to perform the GACs fabrication during the years could have led to the observed inconsistency between the results. These observations can be used to highlight the general need of periodical controls on the performance and the quality of the fabrication runs. This is in fact at the base of a successful exploitation of the BB based approach.

Regarding the exchange Bragg wavelength, its sensitivity to fabrication tolerances has been highlighted. Variations as high as 4.8 nm have been observed for the devices with nominally identical geometrical parameters but the length. In the majority of the devices analysed, this value is however below 1 nm. Between different fabrication runs, the difference between the measure and the expected λ_{Ex} was of about 9 nm. GACs show then a greater sensibility of $\lambda_{B_{Ex}}$ to fabrication tolerances than κ_{Ex}. Postfabrication tuning methods or circuits robust to these variations have then to be designed.

4.4 CONCLUSIONS

The characterization of Bragg gratings and GACs have been carried out in this Chapter.
Regarding the Bragg grating, the CMT model parameters have been measured as well as their on chip variability. The measured reflection group delay have been also analysed in order to obtain a more accurate estimation of the reflection losses. The proposed technique have shown encouraging results regarding its accuracy and applicability. A more systematic analysis have however to be performed in order to confirm the reliability of the method.
Regarding the GAC, the coupling coefficient and the Bragg wavelength have been measured varying the device geometrical parameters. Variability between different fabrication runs have been measured, evidencing the device sensitivity to fabrication tolerances.

In the next Chapter 5 the acquired results will be taken into account for the design of a complex device that relies on two GACs in a resonant configuration.

5

RING RESONATORS WITH GRATING ASSISTED COUPLERS

5.1 INTRODUCTION

In the previous Chapters, the philosophy of the BB based approach to the design of Photonic Integrated Circuits has been illustrated as well as the main features of the classical BBs (straight waveguide, bends, Mach-Zehnder interferometer, ring resonator, Bragg gratings and Grating Assisted Couplers). In this chapter, the first multi-element PIC designed with the previously defined circuit elements is presented. A combination of two basic BB, the RR (subsection 2.3.2) and the GAC (Section 4.3) will be considered. The studied device combines them into a Grating Assisted Coupler ring resonator (GAC-RING in the following) to exploit the wavelength selectivity of the GAC to filter the comb of wavelengths selected by RRs with standard couplers.

A sequence of RRs can be in fact used to add/drop all the channels of a WDM spectrum [11, 61] but problems arise when the WDM overall spectrum is larger than the FSR of the devices. In this case more than one wavelength would be dropped/added by the same Ring. The design problem is not simple since the RR bandwidth also depends on the FSR (see Eq.(2.10)). Two approaches have been proposed to overcome this problem.

- The first one is based on the realization of a series of coupled resonators realized with different cavity lengths to exploit the Vernier effect [164–166]. This approach allows the realization of RRs with extended FSR, through the suppression of the RR resonant modes that are not integer multiple of the RRs FSR ratio. Devices with FSR larger than the C-band have been realized on a silicon platform, showing however a small value of the ratio between the selected and the suppressed modes (9 dB in [167]). Just recently this value has been optimized to 25 dB for a device with a dropped 3 dB bandwidth equal to 0.09 nm [168], showing however an insertion loss value larger than 5 dB.

- The second approach is based on the inclusion of a wavelength selective device inside the RR. This approach, to the knowledge of the author, has been so far poorly investigated. The sidewall modulation of half RR cavity length allows for the realization of a single resonance reflector with a ratio between the

selected mode and the side mode of about 7.8 dB [169]. This solution if used for WDM channel selection would however require a circulator to separate the optical channels.

Also the GAC can perform optical add/drop routing between adjacent waveguides and can be used to build devices with similar overall behaviour. However, GACs can be designed to operate over a single spectral range allowing the so called FSR-free operation [157, 158]. The drawback intrinsic to these devices comes from the fact that nanometer or subnanometer bandwidths (e.g. for applications such as WDM add-drop filters or sensors) require weak perturbations, resulting in many hundreds micrometer long devices (see Section 4.3). For Bragg gratings, solutions based on spiral waveguides instead of straight waveguides have been proposed to realize really compact devices with small reflection bandwidths [170–172] while for the GACs the compactness remain still an issue.

The GAC-RING, studied in this Chapter, combines the positive features of the composing elements. If the RR coupling region is realized using a GAC, the occurrence of possible multiple resonances passed by a single RR is hopefully eliminated by the GAC. Moreover, the RR allows narrow bandwidth filtering keeping compact the device geometry.

Devices with similar topology have been already presented in literature but with a different purpose, either to control the loss/coupling ratio in a fibre based RR add-drop filter [173] or to trap light inside an all-pass RR [174]. It must also be mentioned that, during this work, a proof of concept of the GAC-RING has also been independently proposed in [175]. However, that device was not optimized as it will be shown at the end of this Chapter that is organized as follows.

The GAC-RING behaviour is analysed first using the GAC $2-$wave model (see Section 4.3) and the scattering matrix approach [176–178]. After the device functionality has been described through not optimized parameters, extensive simulations are performed. Potentials and limits of the GAC-RING are then discussed in view of the device fabrication, indicating suitable device working points. The validity of the GAC $2-$wave model BB in a resonant configuration is then discussed and geometries of the GAC minimizing possible spurious effects are investigated. Devices are then fabricated selecting from Section 4.3 the GACs that best suit the design requirements. Finally, evaluations of the device performance as well as considerations on the BB based approach are carried out.

5.2 FUNCTIONALITY

The schematic of the GAC-RING is illustrated in Fig. 5.1a, where GACs replace the DCs of the standard RR add-Drop filter configuration.

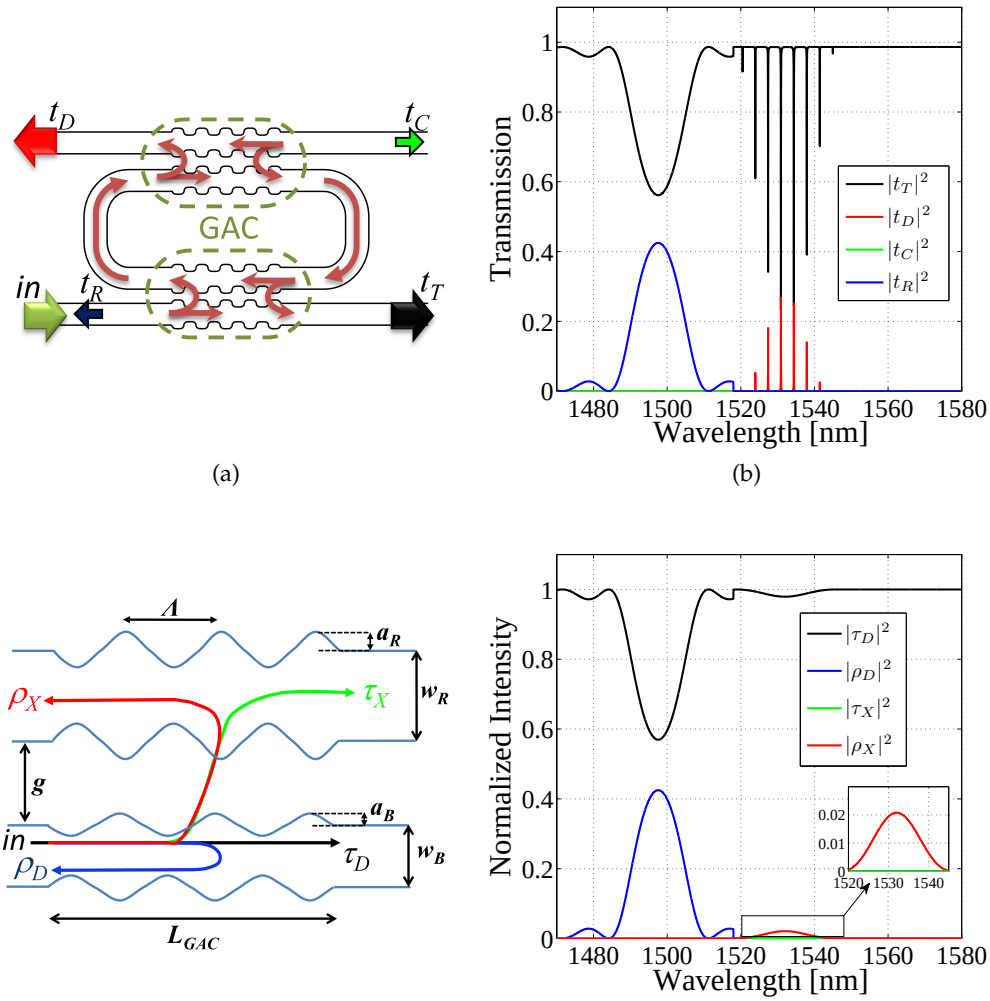

Figure 5.1.: (a) Sketch of the GAC-RING geometry. (b) Output spectra of the GAC-RING simulated using the GAC 2−wave model and the scattering matrix method. (c) Sketch of the GAC geometry. (d) Output spectra of the GAC within the GAC-RING of Fig. 5.1a and Fig. 5.1b, simulated using the GAC 2−wave model.

The description of this device can be based on the 2−wave model that has been previously exploited to successfully describe the behaviour of the GACs (see section 4.3). In this view, the dark red arrows in Fig. 5.1a represent the optical path of the circulating wave inside the resonator, t_T indicates the amplitude of the wave transmitted at the so called Through port and t_D the amplitude of the wave that is transmitted at the so called Drop port (i.e. as in a standard RR). The amplitude of the wave reflected back by the direct reflection of the GAC is indicated as t_R while the amplitude of the wave coming out from the last port (Cross port) is indicated as t_C. Before discussing the simulation of the device, it can be immediately understood

that using the 2−wave model the output at t_C will be identically zero being this port uncoupled at all the wavelengths.

In order to explain the device functionality a bending radius of the RR $R = 20$ μm and a GAC coupler length $L_{GAC} = 20.16$ μm have been set. This choices provide negligible bend losses (see subsection 2.1.2) and compact size. The device has been simulated through the scattering matrix approach [176–178] by the means of 4×4 matrices. Propagation losses of 2.5 dB/cm for the RR bent sections and an insertion loss for each GAC of 0.06 dB have been considered. These values are consistent with the used technology. The simulated GAC geometry, apart for L_{GAC}, is the same of the device presented in Fig. 4.14 from which the coupling coefficients have been extracted. The sketch of the GAC has been reported in Fig. 5.1c to ease the readability for the reader. The average waveguide width outside the resonator, named here as w_B, is 400 nm and its perturbation amplitude $a_B = 8$ nm. Inside the resonator the average waveguide width, named here as w_R, is equal to 500 nm and its perturbation amplitude $a_R = 10$ nm. The grating period is $\Lambda = 0.320$ μm. The exchange coupling coefficient $\kappa_{Ex} = 0.0072$ μm^{-1} leading to a normalized power coupled inside and outside the resonator $|\rho_X|^2 \approx 0.986 \tanh(\kappa_{Ex} L_{GAC})^2 = 0.0205$ at $\lambda_{B_{Ex}}$ (see Fig. 5.1d). The GAC-RING spectral response is illustrated in Fig. 5.1b. It can be immediately noticed that this device achieves spectral limitation to the add-drop functionality inherent to the ring resonance thanks to the GAC, that allows power coupling only over a limited spectral span.

When both GACs are in the *exchange coupling condition*, the ring is coupled to the input/output waveguides and the resonance based add-drop behaviour is enabled as shown by the frequency comb visible in the range 1512 nm–1550 nm of Fig. 5.1b. Therefore the GAC effectively limits the working wavelengths of the ring. Moreover it can be noticed that when the input GAC is in the *direct reflection coupling condition* the device behaves as a simple Bragg grating since the GAC does not couple the input power to the ring-waveguide. This occurs in the wavelength range 1460 nm–1512 nm.

The wavelength selectivity of the GAC reduces the spectral region over which the ring can resonate and the resonance effect enhances the wavelength selectivity of the GAC despite its short length. The next step is the optimization of the circuit parameters to achieve a single mode resonator providing low insertion loss at the Drop port. This task, as well as the definition of the device figures of merit, is carried out in the next Section.

5.3 NARROW-LINEWIDTH SINGLE MODE RESONATOR

Before entering into the details of the numerical approach used to design the GAC-RING, it is useful to define first the single resonance GAC-RING figures of merit that will be taken into account in the optimization process. In principle, the

presented device should completely suppress all the RR resonances but one. At a given wavelength, the Drop port characteristic should exhibit a single peak while the Through port characteristic should have a single notch. In the following, the mode at this wavelength will be called as the Central Mode and will be always assumed or simulated at the same wavelength of the Bragg exchange condition. Note that the Through port spectral behaviour will also show the characteristic photonic bandgap of the GAC input waveguide (see Fig. 5.1b). In practice, as it will be shown later, a complete suppression of the undesired resonator modes (denoted in the following as the Side Modes) is not achievable. Due to the GAC spectral characteristic the Side Modes will be progressively more suppressed as moving away from the Central Mode. The ratio between the peak power carried by the Central Mode and the peak power carried by the neighbouring Side Modes represents one of the most important figure of our device and will be called Side Modes Suppression Ratio (SMSR). Another important figure of merit that will be taken into account in the design procedure is the maximum notch depth of the Side Modes (Side Modes Notch Depth) at the Through port characteristic. The last three figures refer just to the Central Mode and they are the same of a standard RR: the insertion loss (IL Central Mode) and the 3 dB bandwidth at the Drop port, the notch depth at the Through port (Central Mode Notch Depth).

In the next subsections, in order to optimize the described figures, three parameters will be varied: the GAC exchange coupling coefficient κ_{Ex}, that will be simply indicated as κ to simplify the notation, the GAC length L_{GAC} and the resonator bending radius R. It will also be assumed that the larger waveguide of the GAC will constitute the ring and consequently that the smaller waveguide will constitute the bus. This choice ensures lower losses inside the resonator. As in the previous Section, the average waveguide widths will be respectively named w_R and w_B and consequently their perturbation amplitude will be named a_R and a_B. w_B will be considered fixed at 400 nm while two values of w_R will be taken into account. The standard $w_R = 500$ nm that ensures a suitable distance between direct and exchange reflection in the GAC and $w_R = 600$ nm, for reasons which will be clarified later in this Chapter. The RR radius will be assumed always larger than 10 μm, to ensure negligible bending losses. Finally, when $w_R = 500$ nm, the GAC period Λ will be set equal to 336 nm to bring the exchange Bragg wavelength closer to $\lambda = 1550$ nm with respect to the previously discussed GAC-RING simulation (Fig. 5.1b). For the same reason, when $w_R = 600$ nm, the GAC period Λ will be set equal to 328 nm.

To get a first idea on how this parameters can influence the device figures one can notice that a given κ, L_{GAC} sets the fraction of power coupled into the ring. Such power will determine, as in the standard RRs add-drop filter shown in Section 2.3.2), the selected mode insertion loss and 3 dB bandwidth. The ring FSR (see Section 2.3) is defined by the aforementioned length together with R and the width of the waveguide inside the resonator w_R that determines the waveguide group

index. The relationship between the resonator FSR and the GAC Bandwidth ($\Delta\lambda_{00_{Ex}}$ in Section 4.3) will then impact on the SMSR of the single mode resonant device.

A device with so many parameters and figures of merit is expected to show many different suitable working points depending on the required specifications. In order to make the analysis clearer, some more specifications will be fixed still allowing a broad overview on the device performance.

The numerical approach to the device design will be based on extensive simulations varying the aforementioned parameters. Simulations will be performed using the GAC 2−wave model and the scattering matrix method as in Section 5.2. Although this approach is based on simple and low computational weight calculus, the amount of parameters and figures of merit can greatly increase the computational time. In this view, the development of a simplified model based only on analytical equations could help to have a quick overview on the device functionality as well as highlighting the device parameter values range worth to simulate. In the next section this model will be called the RR model and will be investigated also to assess its validity limits. The numerical approach to the GAC-RING design will be then defined as a mix between the RR model and the one based on the 2−wave model.

5.3.1 *Numerical approach to the GAC-RING design*

When it comes to RR add-drop filters the first and simplest approach to their description is that described in Section 2.3. In this model, in the following referred to as the RR model, a point coupler with an insertion loss represented through the parameter a is assumed. The resonator length L_r as well as the propagation losses are determined by the bending radius R and by the real evanescent coupler length L_c (i.e. $L_r = 2\pi R + 2L_c$). Though a GAC and not a standard evanescent coupler is present in the coupling section, it will be initially assumed that this model can be still applied. The GAC behaviour in the exchange band can be calculated first for different values of L_{GAC} fixing κ. The resonator FSR can be then determined by means of Eq. (2.5) and the group index of the waveguide inside the resonator. The selected mode insertion loss and 3 dB bandwidth can be then calculated by means of Eq. (2.9) and Eq. (2.10) assuming that the amount of power coupled inside the RR is that provided by the GAC at the Bragg wavelength (i.e. maximum coupled power by the GAC). This calculation can be repeated with the amount of power coupled by the GAC at a wavelength that is one FSR far from the exchange Bragg wavelength (i.e. at a wavelength at which a Side Mode exists). In this way, again by the means of Eq. (2.9), it is possible to calculate the amount of power carried by the Side Mode at the Drop port.

This model suggest that one would need a wavelength selective device with a bandwidth lower than twice the FSR of the RR (i.e. Side Modes occurring outside

the GAC exchange bandwidth $\Delta\lambda_{00_{Ex}}$) in order to select a single resonance of the RR typical output comb. This situation can never be achieved in practice considering $w_R = 500$ nm and $w_B = 400$ nm or $w_R = 600$ nm and $w_B = 400$ nm. This appear clear by looking respectively at Fig. 5.2a and at Fig. 5.2b, where $\Delta\lambda_{00_{Ex}}$ for different values of the coupling coefficient κ and twice the FSR of the RR (2FSR) are illustrated as a function of the GAC length L_{GAC}. Note that a resonator radius $R = 10$ µm is considered. As indicated by Eq. (4.5) and (2.5) both $\Delta\lambda_{00_{Ex}}$ and the ring FSR reduce

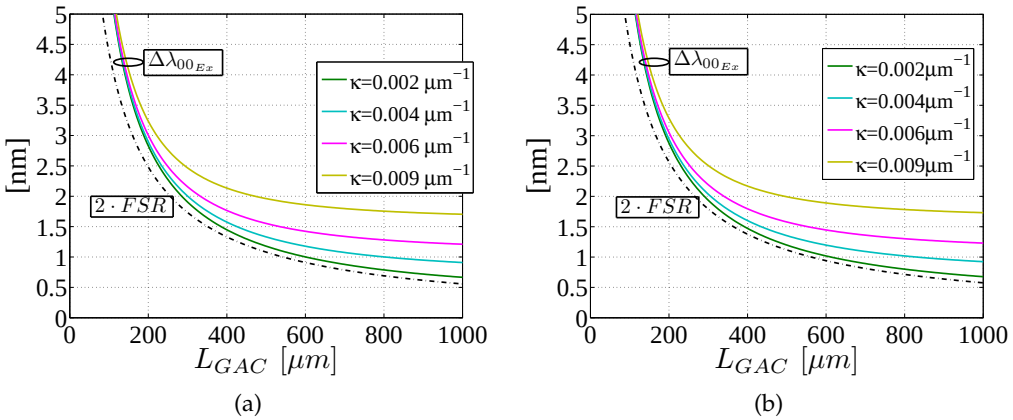

Figure 5.2.: $\Delta\lambda_{00_{Ex}}$ and $2 \cdot$FSR of a RR with $R = 10$ µm and: (a) $w_R = 500$ nm, $w_B = 400$ nm; (b) $w_R = 600$ nm and $w_B = 400$ nm.

as L_{GAC} increases. The $\Delta\lambda_{00_{Ex}}$ never becomes lower than 2FSR. It can be however noticed that, for a given κ, the difference between these two variables reaches a minimum for a certain L_{GAC}. This value of L_{GAC} increases as κ reduces. These working points may then indicate a suitable design point of our devices in order to maximize the SMSR.

The RR model used so far offers an easy and quick way to describe the device behaviour as κ and L_{GAC} vary. It however assumes that the wave coupled by the GAC inside the resonator experiences the same group delay of a wave propagating in a straight waveguide. As shown in Appendix A.5 this can be considered true just for small κL. In order to verify the validity limit of the RR model we can also calculate the SMSR exploiting the 2−wave model discussed in Section 5.2. Simulations have been performed for both models for a coupler with typical insertion loss values (i.e. 0.06 dB) and 2.5 dB/cm propagation losses. Note that, to match the two models, the GAC in the 2−wave approach will be considered here and in the following Sections without propagation losses that have been instead added to the bent waveguides. Moreover, the wavelength matching between the Central Mode and the exchange Bragg wavelength for this model has been obtained in every simulation by the numerical tuning of the RR bend waveguides effective index. The results of these simulations are illustrated in Fig. 5.3. The RR model behaves as

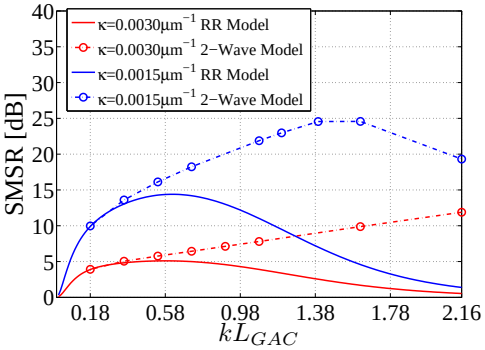

Figure 5.3.: SMSR calculated with the RR model (solid traces) and the 2−wave model (circles) for GAC-RINGs with $\kappa = 0.03$ (red) and $\kappa = 0.0015$ (blue), $R = 20$ μm and increasing L_{GAC}

expected. It is in agreement with the 2−wave model just for small κL_{GAC}, and the highest predicted SMSR is reached when a minimum between $2 \cdot \text{FSR}$ and $\Delta\lambda_{00_{Ex}}$ is achieved. Increasing L_{GAC}, the two models starts to diverge and the 2−wave model shows larger reachable SMSR than the RR model.

To understand the SMSR results given by the 2−wave model we can observe in Fig. 5.4 the device characteristics for $R = 20$ μm, $\kappa = 0.0015$ μm^{-1} and three significant values of κL_{GAC} (i.e. 0.36, 1.395 and 2.16). When $kL_{GAC} = 0.36$ (Fig.

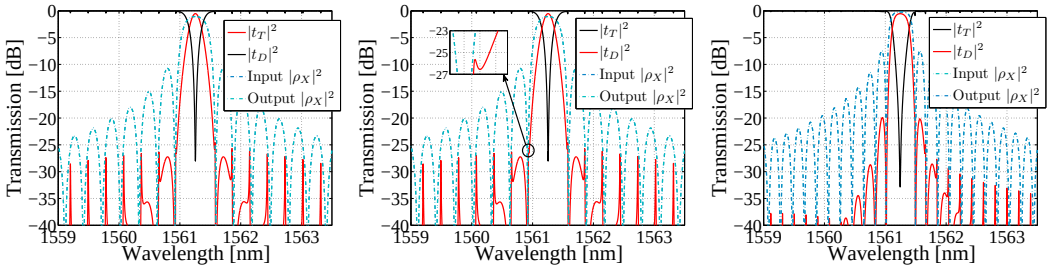

(a) (b) (c)

Figure 5.4.: GAC-RING spectral characteristics simulated with the 2−wave model, for $R = 20$ μm, $\kappa = 0.0015$ μm^{-1} and (a) $kL_{GAC} = 0.36$, (b) $kL_{GAC} = 1.395$ and (c) $kL_{GAC} = 2.16$. Dash-dotted lines represent the input (dark blue trace) and output (light blue trace) GAC spectral behaviour.

5.4a), the amount of normalized power coupled inside and outside the RR ($|\rho_X|^2$) at the Bragg wavelength is 0.12. Note that the Input and Output GAC exchange spectral characteristics overlap having the same perturbation period $\Lambda = 0.336$. The SMSR is 13.6 dB and the 3 dB bandwidth at the Drop port is 6.14 GHz. For this value of kL_{GAC}, the RR model and the 2−wave model agree quite well (see Fig. 5.3). The FSR calculated between the Central Mode and the neighboring Side Modes of Fig. 5.4a is in fact about 119 GHz, just one GHz larger than the value calculated with the RR model. Increasing kL_{GAC} to 1.395 (Fig. 5.4b), the amount of normalized coupled

power inside and outside the RR become 0.78 at the Bragg wavelength and the 3 dB bandwidth increases to 26.2 GHz. With this amount of coupled power the GAC-RING shows almost completely suppressed Side Modes. The largest simulated SMSR value is achieved and is equal to 24.5 dB. The difference in the FSR between the two models is maximum and it is equal to 3.5 GHz. Increasing further the value kL_{GAC}, one can observe from Fig. 5.4c that the device behaviour resembles that of a grating. The amount of coupled power for $kL_{GAC} = 2.16$ is about 95% and the GAC-RING acts almost as a delay line. In this case there are almost no more resonances and the FSR looses its meaning. The SMSR is now evaluated with the maximum of the first sidelobes of the Drop port characteristic and, as in a uniform grating, they increase as L_{GAC} increases.

A mix between these two models will then be used in order to design the single mode GAC-RING. The RR model can be employed for $\kappa L_{GAC} < 0.18$ while for larger values of this parameter the $2-$wave model can be used. The RR model, being based on analytical equations, requires reduced computational times and is then preferred inside its $\kappa L_{GAC} < 0.18$ validity region over the $2-$wave model. Moreover, the exploitation of the RR model allowed to limit the range of values of the device parameters. In the following Section $R < 20$ μm and $0.0015\mu m^{-1} < \kappa < 0.009\ \mu m^{-1}$ will be considered.

5.3.2 *Single Resonance Design*

The first parameter that will be analysed in this section is the resonator bending radius R. Fig. 5.5 shows the SMSR dependence on L_{GAC} of GAC-RINGs with different κ and two different R. $R = 20$ μm (Fig. 5.5a) and $R = 10$ μm (Fig. 5.5b).

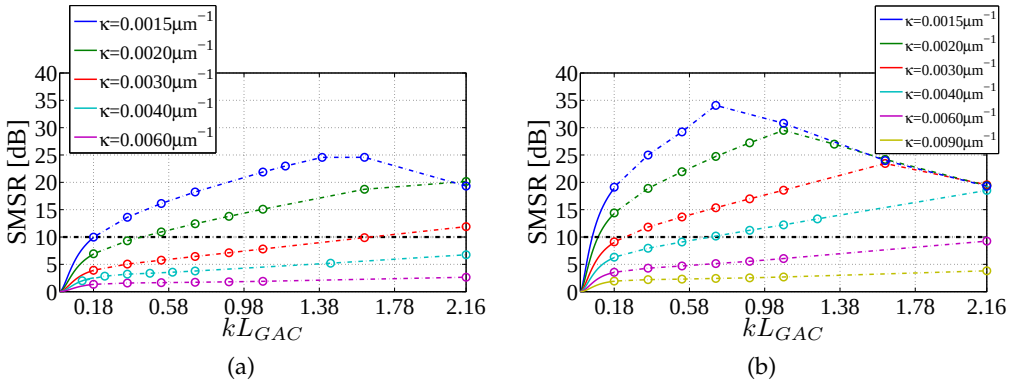

Figure 5.5.: SMSR of GAC-RINGs with (a) $R = 20$ μm and (b) $R = 10$ μm. In both cases $w_R = 500$ nm and $w_B = 400$ nm.

It can be immediately noticed, comparing these two figures, that the device performance increases as R reduces. For a given value of κL_{GAC}, larger values of the SMSR can be achieved. In other words, the same or better performance can be

achieved with devices having larger κ or smaller L_{GAC}. With $R = 10$ μm, SMSR larger than 10 dB are achievable with a large amount of possible κ–L_{GAC} combinations and can then represent a good value for the GAC-RING design. In general, even better performance can be expected with smaller values of R. However the choice of curvature radius smaller than 10 μm can lead to round trip loss increase due to bending and transition losses as well as reflections at the bent-straight section (see subsection 2.1.2). For these reasons and in order to be able to describe the bent waveguide section as a straight waveguide in our BB based approach, $R \geq 10$ μm has always been considered in our simulations.

Having fixed R, it is now possible to inspect the device suitable κ and L_{GAC} working points. The starting point will be, as before, the SMSR now calculated as a function of the GAC length in order to better evaluate the device dimensions. Also the Notch Depth of the two neighboring Side Modes will be evaluated.

As anticipated before, the performance of a GAC with $w_R = 600$ nm will be also taken into account. A waveguide with this width supports two modes above cutoff (see subsection 2.1.1). However, the two modes have quite different effective indexes and the GAC period is optimized to couple the first guided mode. Moreover, the large bend radius should provide negligible excitation of the higher order guided mode.

The results of the simulations done considering the just given geometrical parameters are illustrated in Fig 5.6.

Fig. 5.6a and Fig. 5.6c show respectively the SMSR and the Notch Depth of the neighbouring Side Modes of GAC-RINGs with $w_R = 500$ nm and $w_B = 400$ nm. The simulations have been limited to $L_{GAC} < 400$ μm to keep compact the device size and have been stopped at $\kappa L_{GAC} = 2.16$ (i.e. 0.95 of coupled power).

SMSR larger than 10 dB with the Notch Depth smaller than 2.5 dB can be obtained using $\kappa < 0.006$ μm^{-1}. The lower is κ, the lower is the minimum value of L_{GAC} which satisfies these two minimum specifications. For example, if $\kappa = 0.003$ μm^{-1}, $L_{GAC} > 80$ μm is required. If, instead, $\kappa = 0.004$ μm^{-1}, one needs $L_{GAC} > 270$ μm. Looking now at Fig. 5.6b and Fig. 5.6d, which show respectively the SMSR and the Notch Depth of the neighboring Side Modes of GAC-RINGs with $w_R = 600$ nm and $w_B = 400$ nm, a performance increase can be noticed. The SMSR values have a larger slope dependence on L_{GAC} and the Side Modes Notch Depth reduces faster with L_{GAC} after its maximum point. SMSR larger than 10 dB keeping the notch depth lower than 2.5 dB can now be obtained with shorter GAC lengths for a given κ. For example, if $\kappa = 0.003$, one requires $L_{GAC} > 65$ μm (i.e. a GAC 20 μm shorter than before).

The selection of the suitable κ, L_{GAC} pair can be now completed analysing the figures which involve just the Central Mode and depend mostly just on the coupled power (i.e. the value of κL_{GAC}). Because of that, it is not necessary to distinguish among devices with different w_R since minimum differences in these figures will

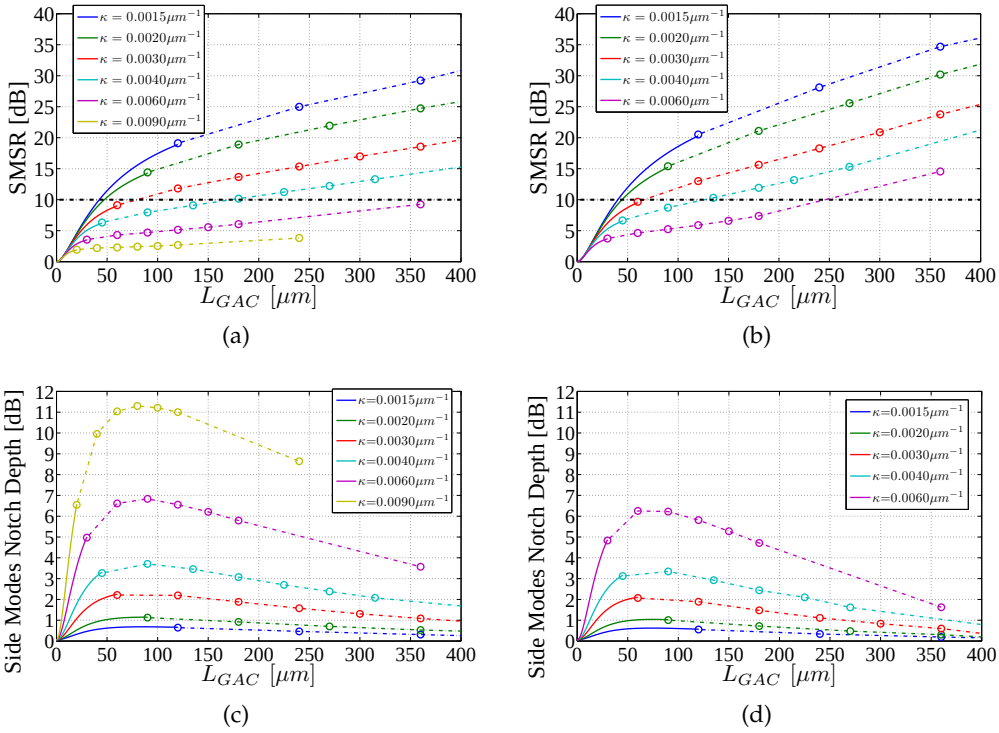

Figure 5.6.: (a) SMSR and (c) Side Modes Notch Depth as a function of L_{GAC} for GAC-RINGs with $w_R = 500$ nm, $w_B = 400$ nm and $R = 10$ µm. (b) SMSR and (d) Side Modes Notch Depth as a function of L_{GAC} for GAC-RINGs with $w_R = 600$ nm and $w_B = 400$ nm and $R = 10$ µm.

be detected. In Fig. 5.7 the insertion loss (Fig. 5.7a), the Notch Depth (Fig. 5.7b) and the 3 dB bandwidth (Fig. 5.7c) are plotted as a function of L_{GAC} just for a GAC-RINGs with $w_R = 500$ nm and $w_B = 400$ nm and $R = 10$ µm.

Looking together at Fig. 5.7a and Fig. 5.7b one can see that for $\kappa = 0.0015$ µm^{-1}, L_{GAC} equal to about 300 µm are needed to obtain respectively 1.5 dB of insertion loss and 16 dB of Notch Depth. In order to obtain a compact device, larger values of κ are necessary.

Focusing now attention on devices that can provide dropped channels with 3 dB bandwidths between 10 and 20 GHz, devices with $\kappa < 0.004$ µm^{-1} must be selected. From Fig. 5.7c one can in fact see that this coupling coefficient requires GACs shorter than 150 µm. These lengths would bring the device to work under the minimum SMSR and over the maximum Side Modes Notch Depth previously fixed (see Fig. 5.6) both for GAC-RINGs with $w_R = 500$ nm and $w_R = 600$ nm. These specifications can be maintained if $\kappa = 0.003$ and L_{GAC} between 100 and 200 µm are designed. If, on the contrary, devices with a 3 dB bandwidth just around 10 GHz are desired, $\kappa = 0.002$ µm^{-1} and L_{GAC} between 150 and 250 µm can be assumed in the design with even better SMSR and Side Modes Notch Depth performance (see Fig. 5.7c and Fig. 5.6).

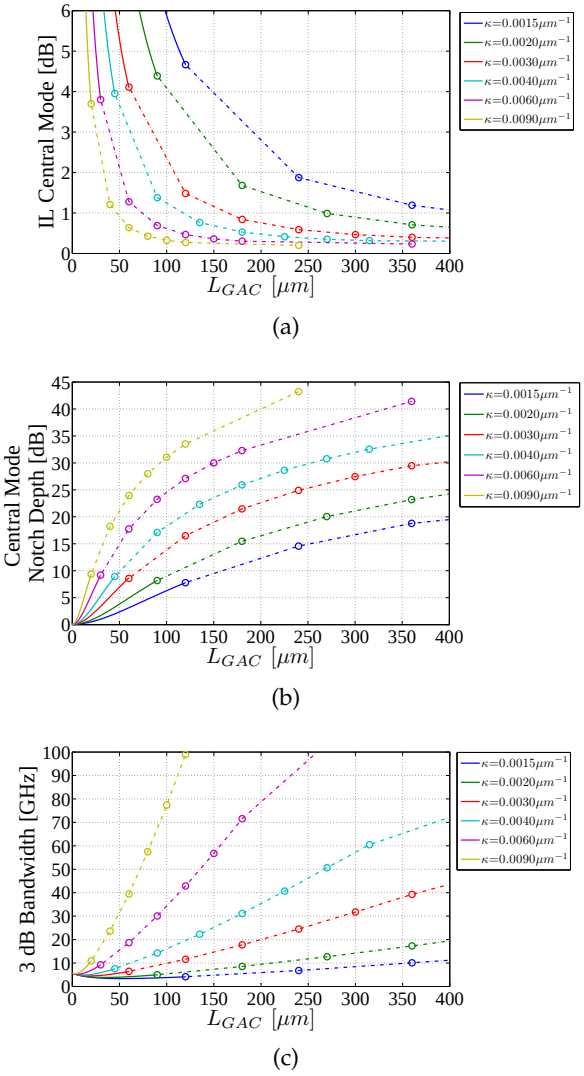

Figure 5.7.: Central Mode (a) Drop port insertion loss, (b) Through port Notch Depth and (c) Drop port 3 dB bandwidth. All the simulated GAC-RINGs have $w_R = 500$ nm and $w_B = 400$ nm and $R = 10$ µm.

In conclusion, the presented device could show practical limitations if a device with increasing value of the 3 dB bandwidth and compact size must be realized. Large bandwidths are achieved with large power coupled inside the ring. This requires high κ values for which, as shown in Fig. 5.6, it could be difficult to achieve high performance. Anyhow, different specifications should be evaluated case by case taking into account the possibility to further enlarge w_R, at the cost of increasing the possible issues given by a multimodal waveguide, or reducing the size of w_B at the cost of a possible increase of the GAC losses. Moreover, looking together at Fig. 5.6 and Fig. 5.7 it is possible to notice how a variation of 0.001 µm^{-1} in κ with respect to the design value can significantly vary the device performance. In view of the design of such a device it is consequently of primary importance the knowledge of the κ dependence on the GAC geometrical parameters. κ variations in

the order of 0.001 μm^{-1} can in fact cause sensible changes in the device performance and consequently in the required value of L_{GAC}.

Up to now, identical GAC at the input and at the output section of the GAC-RING have been considered. However, in Section 4.3 it has been shown that identical GACs could differ in the exchange Bragg condition wavelength of an amount smaller than 1 nm in most of the cases. This value can also be in some cases larger than 4 nm. The effect of this misalignment, that will be addressed from now on as $\Delta\lambda_{B_{Ex}}$, are illustrated in Fig. 5.8.

Fig. 5.8a shows the ideal situation (i.e. input and output GACs are aligned, $\Delta\lambda_{B_{Ex}} = 0$) for a GAC-RING with $R = 10$ μm, $w_R = 500$ nm, $w_B = 400$ nm, $\kappa = 0.003$ μm^{-1} and $L_{GAC} = 120$ μm. Here the SMSR is 11.8 dB and the Side Modes Notch Depth is 2.13 dB. The Central Mode shows an insertion loss of 1.5 dB at the Drop port, a Notch Depth of 16.5 dB at the Through port and a 3 dB bandwidth of 11.6 GHz. If the output GAC spectral behaviour (Output $|\rho_X|^2$) is shifted by 1.2 nm and the resonator resonance is tuned in order to have a symmetric $|t_D|^2$ (Fig. 5.8b) the SMSR increases to 16.7 dB. However, the notch depth of the left Side Mode becomes larger than that of the Central Mode. The performance can be partially recovered by tuning the Central Mode resonance at the input GAC $\lambda_{B_{Ex}}$ (Fig. 5.8c). The Central Mode Notch Depth is increased by 2.5 dB and the SMSR is decreased by about 2 dB with respect to the ideal situation. The 3 dB bandwidth is 3 GHz lower, the insertion loss and the maximum Side Mode notch depth (left one) are respectively increased by 1.2 dB and 1.5 dB. We can then conclude that this working point is robust against misalignment between the input and output $\lambda_{B_{Ex}}$ below 1.2 nm. Note that this value represents about 1/4 of the GACs $\Delta\lambda_{00_{Ex}}$.

Increasing the misalignment to 2.5 nm (about half $\Delta\lambda_{00_{Ex}}$) and tuning again the Central Mode resonance at the intersection between the input and output GAC $|\rho_X|^2$ (Fig. 5.8d) in order to obtain a symmetric Drop port characteristic, a performance reduction with respect to the ideal case is evident. In this situation no performance recovery is possible. The input $\lambda_{B_{Ex}}$ corresponds in fact to a minimum of the Output $|\rho_X|^2$ spectrum. An even larger shift (i.e. 4.2 nm in Fig. 5.8e), corresponding to about $\Delta\lambda_{00_{Ex}}$, would lead to a completely distorted Drop port output no matter of the resonance tuning.

If no control is available for the GACs wavelength tuning, GAC with large $\Delta\lambda_{00_{Ex}}$ are then desirable to be robust against input and output $\lambda_{B_{Ex}}$ misalignments. In other words, the smaller L_{GAC} and the larger κ are, the more robust the GAC-RING will be against this fabrication tolerance effect.

At this point it would be in principle possible to select the desired κ and design the GAC geometry according to Section 4.3 or other approaches such as the CMT or FDTD. However, nothing have been said on the applicability of the GAC $2-$wave model in a resonant configuration. In subsection 4.3.1 it has been shown that the GAC $|\tau_X|^2$ broadband coupling as well as the direct reflection given by the grating

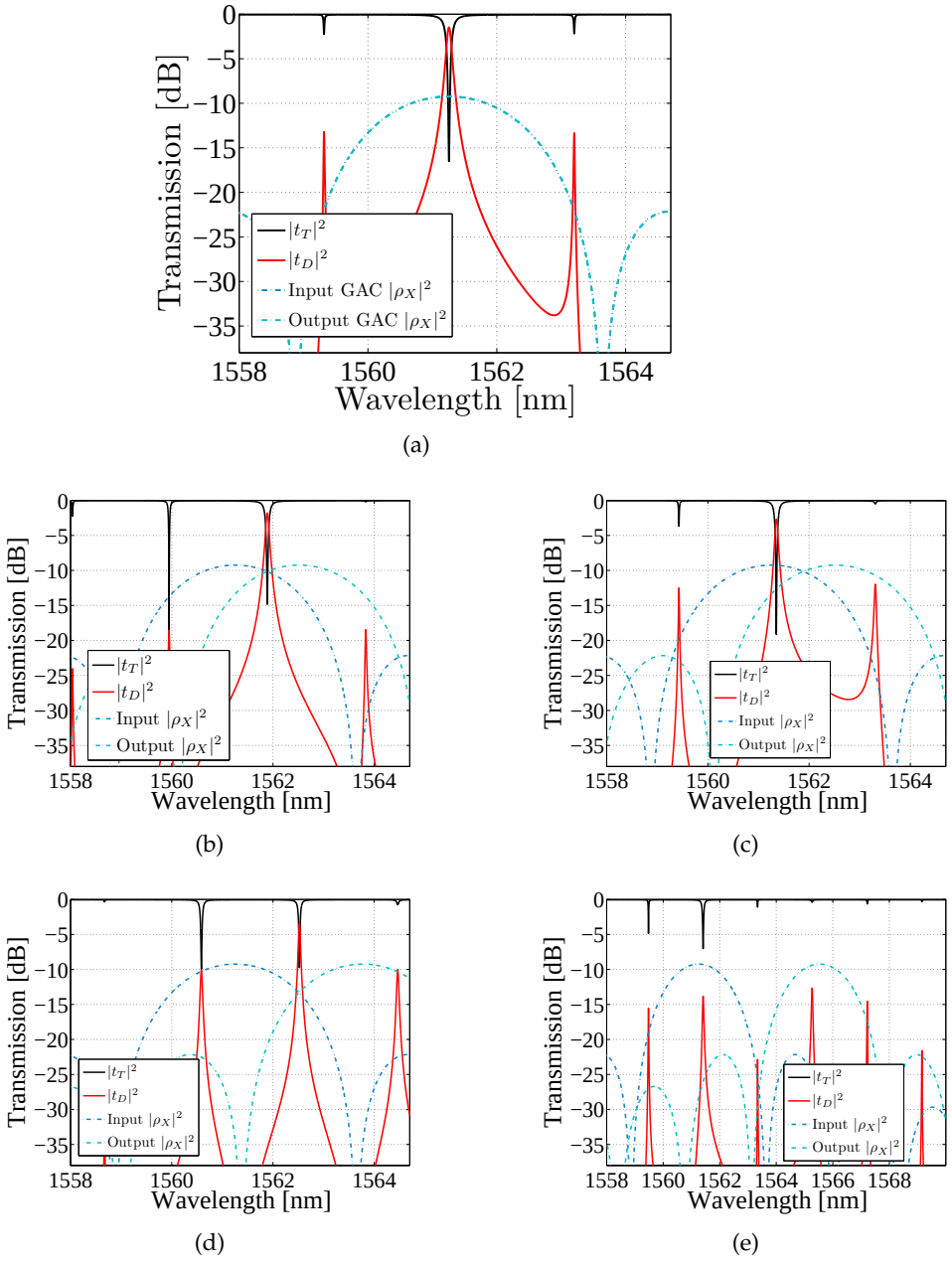

Figure 5.8.: GAC-RING spectral characteristics simulated with the 2−wave model, for $R = 10$ µm, $\kappa = 0.003$ µm^{-1}, $w_R = 500$ nm, $w_B = 400$ nm, $w_R = 500$ nm, $w_B = 400$ nm, $L_{GAC} = 120$ µm and: (a) $\Delta\lambda_{B_{Ex}} = 0$; (b) $\Delta\lambda_{B_{Ex}} = 1.2$ nm, Central Mode resonance tuned at the intersection between the input and output GAC $|\rho_X|^2$; (c) $\Delta\lambda_{B_{Ex}} = 1.2$ nm, Central Mode resonance tuned at the maximum of the input GAC $|\rho_X|^2$; (d) $\Delta\lambda_{B_{Ex}} = 2.5$ nm; (e) $\Delta\lambda_{B_{Ex}} = 2.5$ nm. Dash-dotted lines represent the input (dark blue trace) and output (light blue trace) GAC spectral behaviour.

inside the exchange stopband can be considered negligible. In the ring loop these contributions, although small, can lead to detrimental effects to the GAC-Ring spectral behaviour. In the next subsection the GAC 4−wave model will be employed to

describe these aspect of the GAC-Ring. After that it will be demonstrated how it is possible to minimize these undesired spurious effects.

5.3.3 *Spurious effects minimization*

In order to describe the GAC functionality when all the ports are coupled the CMT 4−wave model can be employed (see Appendix A.6). The GAC geometry and parameters can be again taken as the same used in Section 5.2. Note that, in the 4−wave model informations about the coupling coefficient representing the codirectional coupling between the two waveguides constituting the GAC are also required. Unfortunately, though direct and exchange reflection coupling coefficients can be easily extracted form GAC measurements, this is not true for the codirectional coupling. The intensity of the transmission coefficient t_X can be at noise level making impossible any reliable fitting. With reference to Appendix A.6 notation a test value $\kappa_{12} = \kappa_{21} = 0.0137\ \mu m^{-1}$ was then considered in order to perform these simulations.

After the determination of the coupling coefficients, the CMT partial differential equation system of the GAC can be numerically solved. Then, the GAC spectral behaviour can be evaluated. As a first step, a comparison between the GAC 2−wave and 4−wave model spectra can be performed. Figure 5.9 shows the results of this simulation for a GAC with $w_B = 400$ nm, $w_R = 500$ nm, $a_B = 8$ nm, $a_R = 10$ nm, $\Lambda = 320$ nm and $L_{GAC} = 20.16$ µm when the larger waveguide is excited. Note that this is then the spectral response seen by a wave propagating inside the resonator. The curves of the 2−wave model (Fig. 5.9a) are compared with those of the 4−wave

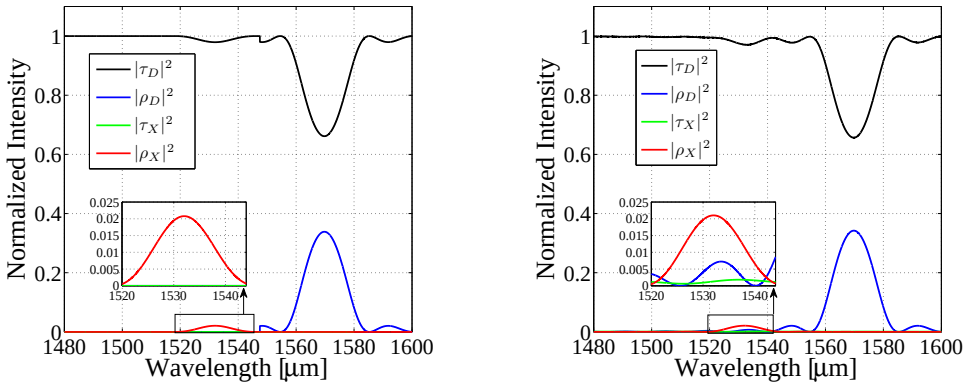

Figure 5.9.: GAC spectral behaviour simulated with: (a) the 2−wave model; (b) the 4−wave model.

model (Fig. 5.9b). Despite the large qualitative similarity, there are two important differences. The first is the residual coupling of the ports that are not involved in the

main coupling. As shown in the inset, the side-lobes of the direct reflection curve extend up to the exchange stop-band region. The second concerns the codirectional coupling which remains under 0.2% over the entire spectrum. Although the four wave model shows a small change in behaviour of the GAC, such small changes can have a detrimental impact on the GAC-RING device due to its resonant behaviour.

Once the GAC scattering matrix have been retrieved, the GAC-RING spectra is simulated through the scattering matrix approach considering an insertion loss of 0.06 dB for the GAC and 2.5 dB/cm as propagation losses for the bent waveguide sections. The bend curvature radius has been set equal to 20 µm. The result of this simulation is illustrated in Fig. 5.10b. The spurious behaviour can be immediately

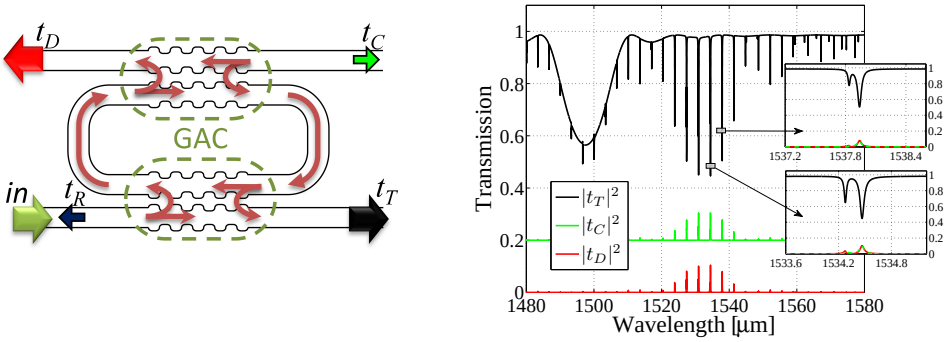

(a) (b)

Figure 5.10.: (a) Sketch of the GAC-RING geometry. (b) Spectal behaviour of the GAC-RING simulated with the GAC 4−wave model and the scattering matrix method.

noticeable: the power at the Cross port $|t_C|^2$ is similar to that at the Drop port $|t_D|^2$, the resonance peaks show splitting and there are undesired resonance features all over the spectrum. The residual broadband codirectional coupling is responsible for the presence of resonance notches not only in the bandwidth range where the exchange coupling takes place. Due to the losses there are no resonances at the Drop port away from the exchange stop band even if dips on the through characteristic are noticed over all spectrum.

The behaviour in the exchange stopband is more complex. In this range the input power is also coupled forward by residual codirectional coupling. Moreover, the GAC reflects a small fraction of the power coming from each side of the ring. This causes the presence of some signal that propagates in both directions of the ring with similar intensity and couples back to both exchange ports. Since the ring supports two counter-propagating waves coupled by the GAC, a coupled-cavity is generated and this results in the split-peak spectral features [97, 179].

This brief analysis showed that in order to make the device work with the desired performance, a GAC minimizing these effects has to be designed. Taking into account the codirectional coupling it can be noticed that this parameter in inversely proportional to the gap g. The minimum gap that guarantees the codirectional coupling minimization has then to be found. A numerical approach can show to this purpose practical limitations. The small values of this broadband coupling can be easily covered by numerical errors leading to erroneus estimations. Due to this reasoning we chose an experimental approach. The evaluation of the codirectional coupling effects can be done by observing the GAC-RING resonant behaviour outside the exchange bandwidth, fixing all the GAC parameters but g. The experimental results for GAC-RINGs with $R = 10$ µm, $w_R = 500$ nm, $a_R = 6$ nm, $w_B = 400$ nm, $a_B = 4$ nm, $\Lambda = 0.336$ µm, $L_{GAC} = 100.8$ µm and different g are show in Fig. 5.11. Fig. 5.11a shows that $g = 180$ nm leads the device to resonate at almost all

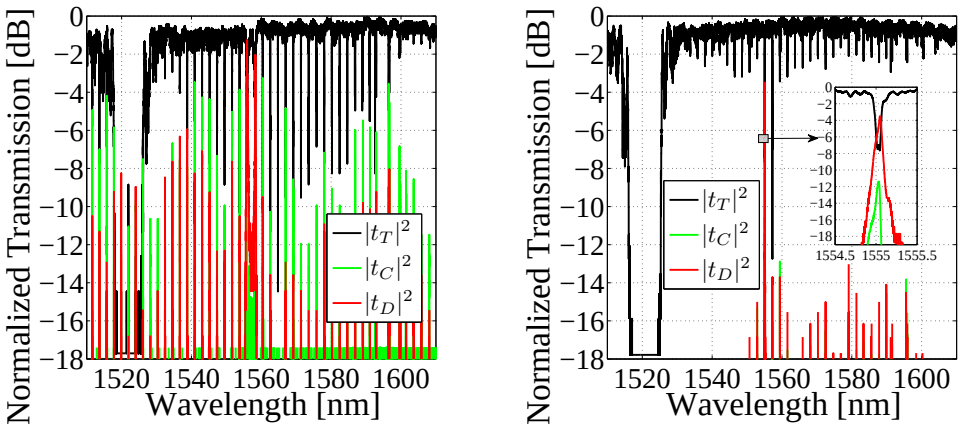

Figure 5.11.: Spectral behaviour of a GAC-RING with $R = 10$ µm, $w_R = 500$ nm, $w_B = 400$ nm, $\Lambda = 0.336$, $L_{GAC} = 100.8$ and: (a) $g = 180$ nm; (b) $g = 300$ nm.

the wavelengths. It can in fact be difficult to recognize the range of wavelengths where the GAC exchange coupling takes place. Increasing the gap to 300 nm (see Fig. 5.11b) greatly reduces the codirectional coupling. The GAC exchange coupling takes place at wavelengths around $1550 - 1560$ nm. Over this wavelength range it is also possible to notice that the deeper notch of $|t_T|^2$ and the smaller insertion loss of $|t_D|^2$ do not occur at the same resonance. As illustrated in subsection 5.3.2 and Fig. 5.8, this is the typical effect given by different input/output GAC $\lambda_{B_{Ex}}$. Only the tuning of the resonance position can indicate whether the GAC-RING performance are robust to these misalignments. This aspect will be investigated in the next subsection. Looking far from the GAC exchange coupling condition (i.e. around $1580 - 1590$ nm), the notch depths of $|t_T|^2$ are smaller than 2.5 dB and the resonance at $|t_D|^2$ and $|t_C|^2$ are always lower than 9.5 dB with respect to the largest peak at the

centre of the Bragg condition. Note that this performance is in agreement with the minimum target specifications given in the previous subsection. $g = 300$ nm can be then considered as the minimum gap for the fabrication of the devices.

Moreover, to reduce the interaction between exchange and direct reflection bandwidth, GAC with waveguide widths difference larger than 100 nm can be realized. Considering GACs with $w_R = 600$ nm and $w_B = 400$ nm can also lead to improved performance of the device in terms of SMSR as shown in the previous Section.

5.3.4 *Fabricated devices performance*

Once the device theoretical investigation have been carried out and a minimum GAC gap allowing the description of the GAC-RING behaviour with the $2-$wave model has been found, it is now possible to design the GAC-RING according to well defined specifications having fixed $R = 10$ μm from the previous analysis.

Before entering into the details of the realized devices it is important to highlight that NiCr heaters were realized on top of the resonator bent sections in order to exploit the thermo-optic effect to tune the resonance position. Low resistivity Ti-Au strips were also realized in order to bring the electrical signal over the device waveguides as described in 1.4. The NiCr heaters cross section is set to 920×50 nm^2 and heater lengths $L_h = 32.44$ μm are chosen. An example of the fabricated GAC-RINGs is illustrated in the optical microscope photograph of Fig. 5.12. It can be immedi-

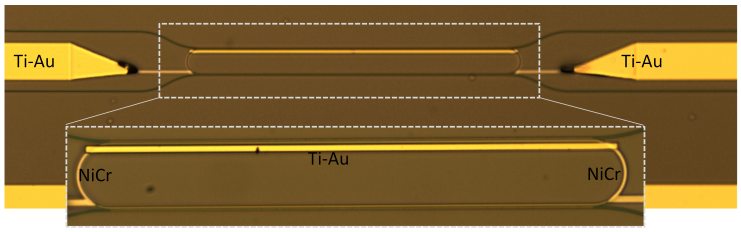

Figure 5.12.: Example of a fabricated GACR-RING with heater control over the ring resonator phase.

ately noticed that NiCr strips are present not only over the device waveguides. On this chip some Ti-Au parts overlapping the NiCr strips were in fact lifted due to fabrication problems. The only drawback arising from this condition is the inefficient tuning. Resistances are higher than those expected form the exploited SOI platform. Consequently, higher voltages are required to tune the RR resonance in the desired position. The following procedure has been applied in order to retrieve realistic values of the necessary power dissipated to set the resonance at the wavelength that gives the maximum GAC-RING performance. The electrical current I_h was monitored during the tuning process. The heater resistance R_h was calculated through the heater geometrical parameters and taking into account the average NiCr resis-

tivity (see Section 1.4). The value of the electrical power dissipated $P_D = R_h {I_h}^2$ has been obtained and will be reported in the following.

The analysis developed in the previous Section has shown that GAC with $\kappa \leq 0.003$ μm^{-1}, $g \geq 300$ nm should be selected in order to realize a compact device with SMSR larger than 10 dB and a filter 3 dB bandwidth between 10 and 20 GHz. At the time of this fabrication run only one already characterized GAC with this characteristics was available (see Section 4.3.2). To obtain $\kappa \approx 0.003$ μm^{-1}, $w_R = 500$ nm, $a_R = 6$ nm, $w_B = 400$ nm, $a_B = 4$ nm and $g = 300$ nm were then selected. As previously shown in subsection 5.3.2, the larger is the GAC bandwidth the more robust is the GAC-RING to GACs exchange wavelength misalignments (i.e. $\Delta\lambda_{B_{Ex}} \neq 0$). $L_{GAC} = 100.8$ μm was chosen providing a $\Delta\lambda_{00_{Ex}} \approx 5.68$ nm. The described geometrical parameters are collected in the first row of Tab. 5.1 together with the simulated performance of the GAC and of the GAC-RING (D_1 row, Tab. 5.1). A dropped 3 dB bandwidth (BW) of 9.8 GHz with 2 dB of insertion loss (IL) and a SMRS = 11.1 dB is then expected from the design. Moreover, the selected working point provides a Central Mode Notch Depth (CM ND) equal to 14.3 dB and a Side Modes Notch Depth (SM ND) equal to 2.2 dB.

In Fig. 5.13 the measured output spectra of this device are illustrated. Fig. 5.13a shows the measured GAC-RING spectral characteristic when no electrical power is dissipated on the heater. It is possible to notice that for lower wavelengths $|t_D|^2$ shows larger bandwidth resonance peaks. This behaviour is due to the presence of a TM component of the field. The presence of this component can be addressed to a polarization conversion effect of the mode adapters [29] or to a reduced extinction at the chip input more than to the GAC-RING itself. A GAC-RING with identical parameters was in fact fabricated in a former run and its spectral behaviour, shown in Fig. 5.11b, does not show these extra features. For this reasoning, from now on the GAC-RING spectra obtained through a TE polarizer at the output of the chip will be illustrated. This does not cause loss of any important information, as it can be noticed comparing the GAC-RING spectra without (Fig. 5.13a) and with (Fig. 5.13b) the output TE polarizer in the set up.

The desired device performance can be obtained dissipating a P_D of about 9 mW over the resonator. The measured output optical normalized power at the three ports of the GAC-RING under this electrical condition are illustrated in Fig. 5.13c. By looking at the Drop port characteristic ($|t_D|^2$, red trace), a 3 dB bandwidth of the Central Mode of about 8.4 GHz and a SMSR of 11 dB can be observed. The SMSR is also maintained over the whole spectrum as shown by the dashed horizontal line. Looking at the Through port characteristic ($|t_T|^2$, black trace) we can notice that the Central Mode Notch Depth is larger than 13 dB and the notch depth of the Side Modes is smaller than 2.7 dB in the whole measured wavelength interval. By comparing the described performance, collected in row M_{1a} of Tab. 5.1, with that

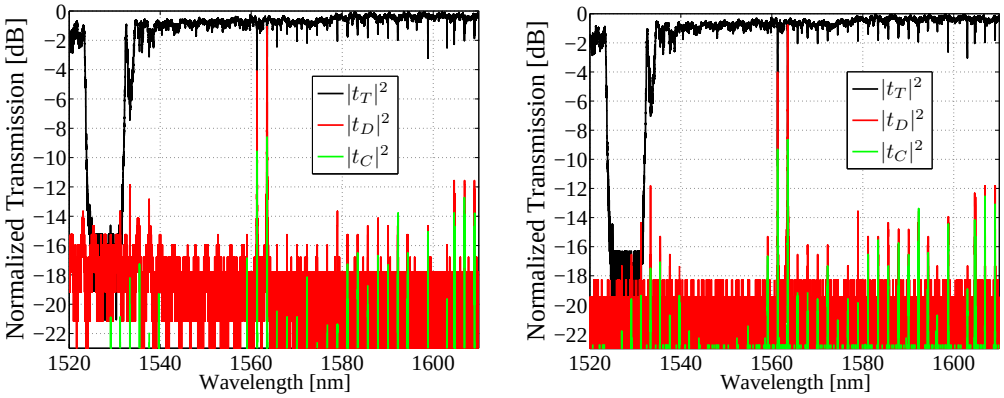

(a) (b)

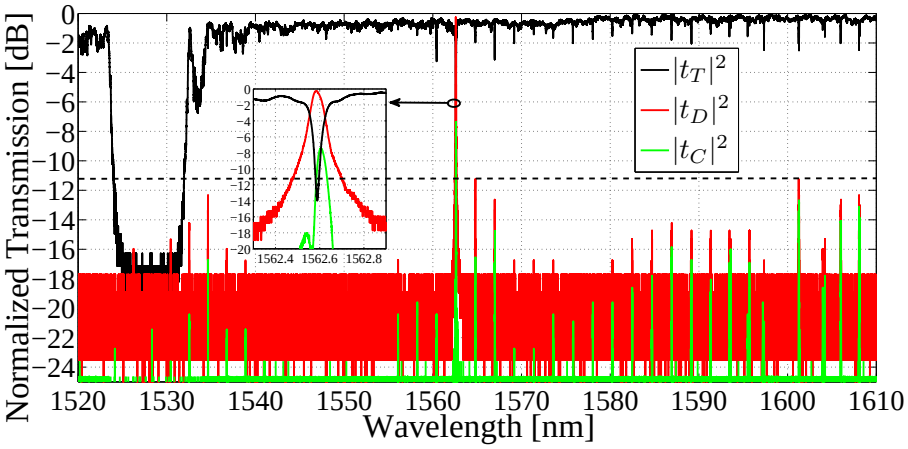

(c)

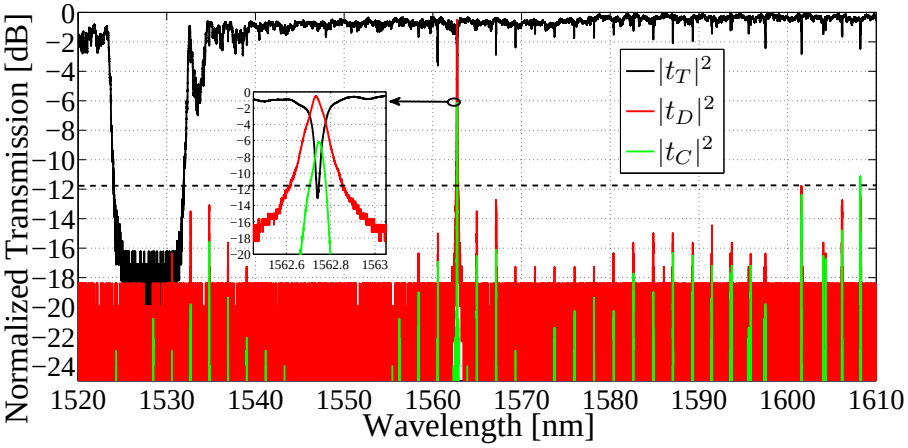

(d)

Figure 5.13.: Spectral behaviour of a GAC-RING with $R = 10$ µm, $w_R = 500$ nm, $a_R = 6$ nm, $w_B = 400$ nm, $a_B = 4$ nm, $\Lambda = 0.336$, $L_{GAC} = 100.8$ µm, $g = 300$ nm and: (a) $P_D = 0$; (b) $P_D = 0$ and the TM component of the field filtered at the output of the chip; (c) $P_D = 9$ mW and the TM component of the field filtered at the output of the chip; (d) $P_D = 10$ mW and the TM component of the field filtered at the output of the chip.

Table 5.1.: Designed and Measured Parameters of the Realized GAC-RINGs

GEOMETRY									**PERFORMANCE**									
									GAC			**GAC-RING**						
w_R [nm]	w_B [nm]	a_R [nm]	a_B [nm]	g [nm]	L_{GAC} [μm]	Λ [nm]	R [μm]		κ [μm^{-1}]	$\lvert\rho_X\rvert^2$ @ $\lambda_{B_{Ex}}$	$\Delta\lambda_{00_{Ex}}$ [nm]	**SMSR** [dB]	**BW** [GHz]	**IL** [dB]	**CM ND** [dB]	**SM ND** [dB]	P_D [mW]
500	400	6	4	300	100.8	336	10	D_1	0.003	0.085	5.676	11.1	9.8	2	14.3	2.2	n.a.
								M_{1a}	0.0028	0.075	5.673	11	8.4	n.a.	13.5	2.7	9
								M_{1b}	0.0028	0.075	5.673	11.3	9.4	n.a.	12	3	10
500	400	10	8	350	100.8	336	10	D_2	0.0026	0.065	5.67	12.59	7.8	2.5	12.4	1.7	n.a.
								M_2	0.0024	0.055	5.667	9	5.8	n.a.	11	1.7	6
600	400	6	4	300	150.88	328	10	D_3	0.0015	0.046	3.8	22.8	4.9	3.5	9.8	0.4	n.a.
								M_{3a}	0.0015	0.046	3.8	12.36	9.6	n.a.	8	0	0
								M_{3b}	0.0015	0.046	3.8	11.96	6.9	n.a.	5	3.5	5.5

D: Design.
M: Measurements; M_{1a} → Fig. 5.13c, M_{1b} → Fig. 5.13d, M_2 → Fig. 5.14, M_{3a} → Fig. 5.15a, M_{3b} → Fig. 5.15b.
n.a.: Not calculated or not available.

designed (row D_1, Tab. 5.1) the good agreement is immediately noticeable. Note that, for the sake of completeness, in Tab. 5.1 the value of κ and $\Delta\lambda_{00_{Ex}}$ measured from GAC test devices on the same chip are also reported. Moreover, the GAC $|\rho_X|^2$ at $\lambda_{B_{Ex}}$ calculated using Eq. (4.4) and assuming 0.06 dB of GAC insertion loss is also reported. The detected variability of the input/output mode adapters performance (i.e. larger than 5 dB) did not allow in fact for a reliable measurement of this parameter.

Due to this variability it was also not possible to have a reliable estimation of two important parameters of the GAC-RING: the Central Mode insertion loss at the Drop port (IL in Tab. 5.1) and at the Cross port. The first figure is required to be small to obtain efficient channel selection, while the latter is required to be large if the Cross port is used to add a channel into the system like in a standard add-drop RR. Regarding the Central Mode insertion loss at the Drop port, the accordance between simulated and measured spectral features indicates a good estimation of the device losses in the design stage. An insertion loss close to the simulated value (i.e. 2 dB) can be then expected from the considered device. Regarding instead the Central Mode insertion loss at the Cross port, in the following it will be highlighted whether the variation of the tuning can increase or reduce this parameter.

The Central Mode 3 dB bandwidth can be in fact finely tuned without dramatically affect the other figures of merit of the device. By increasing P_D of 1 mW it is possible to increase this figure of 1 GHz, reducing then the difference between designed and measured bandwidth from about 1.4 GHz to about 0.4 GHz. This condition is illustrated in Fig. 5.13d and the measured performance are collected in row M_{1b} of Tab. 5.1. The SMSR is practically unchanged, being in fact increased by only 0.3 dB. Looking at Fig. 5.13d it is possible to notice that this figure is now limited by the Side Modes outside the GAC exchange bandwidth and not by the Side Modes close to the Central Mode. The insertion loss of the Central Mode increases of about 0.3 dB at the Drop port while decreases of about 1 dB at the Cross port.

In comparison with the proof of concept device proposed in [175], a SMSR larger of about 3 dB has been then achieved in a single mode resonator with a 1.5 GHz larger bandwidth. In [175], the resonance tuning was not performed and moreover $R = 20$ μm was set. As shown in subsection 5.3.2, this design choice reduces the ranges of κ and L_{GAC} over which a SMSR larger than 10 dB can be achieved.

As it has been shown in the previous Section, the device performance can be further improved by selecting different values of the GAC κ and L_{GAC} than that just described. The improvement of the SMSR in the neighbourhood of the GAC exchange bandwidth wavelength is however pointless if not realized together with a further suppression of the resonances outside the cited bandwidth. The same reasoning applies for the Side Modes Notch Depth. In order to overcome this problem, two design strategies can be taken: the increase of the GAC gap, which can in turn reduce the codirectional coupling value, and the widening of w_B, which can in

turn reduce the codirectional coupling value and the reflections given by the grating inside the resonator. Both of these solutions have been tested.

The first of these two solutions is tested through the realization of a GAC-RING with $R = 10$ µm, $w_R = 500$ nm, $a_R = 10$ nm, $w_B = 400$ nm, $a_B = 8$ nm, $L_{GAC} = 100.8$ and $g = 350$ nm (see second row of Tab. 5.1). Note that in this device the gap and the perturbations of the two waveguides have been increased with respect to the device geometry presented so far. The exponential fitting curve shown in Fig. 4.15 have been employed in order design a GAC keeping the value of the coupling coefficient higher than 0.002 µm (i.e. ≈ 0.0026 µm^{-1} for this device). This choice allows to obtain performance similar to that of the previously presented GAC-RING since κL_{GAC} is not sensibly reduced. Note that also the same robustness to GACs $\lambda_{B_{Ex}}$ misalignments is expected since the GAC $\Delta\lambda_{00_{Ex}}$ is reduced by just 6 pm. The designed GAC and GAC-RING performance are illustrated in row D_2 of Tab. 5.1.

Fig. 5.14 shows the spectral characteristic of the described device with $P_D = 6.3$ mW.

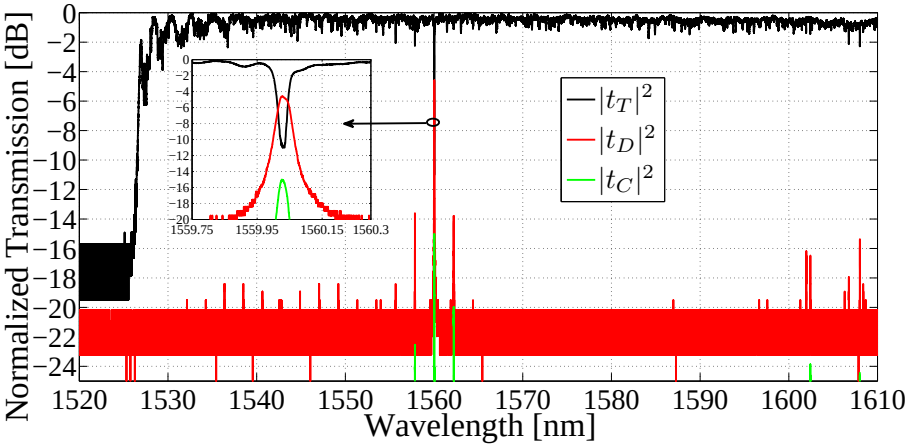

Figure 5.14.: Spectral behaviour of a GAC-RING with $R = 10$ µm, $w_R = 500$ nm, $a_R = 6$ nm, $w_B = 400$ nm, $a_B = 4$ nm, $\Lambda = 0.336$, $L_{GAC} = 100.8$, $g = 300$ nm, $P_D = 6.3$ mW and and the TM component of the field filtered at the output of the chip.

This GAC-RING presents a 'cleaner' spectrum with respect to the previously characterized one, which confirms the reduction in the broadband coupling obtained. At the Through port (black trace, Fig. 5.14) the notches outside the GAC bandwidth have in fact a maximum depth of 1.5 dB. More than 1 dB smaller than in the previous case. However, looking at the Drop port characteristic (red trace, Fig. 5.14) it can be noticed that the resonance occurring at wavelengths around 1610 nm is 11 dB lower than the Central Mode: the same value detected in the previously presented device. This behaviour can be related to an increase in the insertion loss of the Central Mode. In fact, as illustrated in Section 5.3.2, a larger input/output GAC $\lambda_{B_{Ex}}$ ($\Delta\lambda_{B_{Ex}}$) can increase this figure. In such case, a larger deviation from the designed

performance is also expected. The comparison between the target and the measured performance for this device, illustrated respectively in row D_2 and M_2 of Tab. 5.1, shows in fact larger differences than those previously detected. For example, the dropped 3 dB bandwidth (5.8 GHz) and the SMSR (9 dB) are of about 2 GHz and 3.6 dB smaller than their relative target values.

It is now possible to highlight that, although the discussed differences are larger than in the previous case, they are not dramatic. They can be due in fact not only to a larger $\Delta\lambda_{B_{Ex}}$ but also to higher losses and/or different κ between the input and the output GACs. These effects can be easily taken into account for future design of this class of devices through the $2-$wave model. Moreover, it can be noticed form row M_2 of Tab. 5.1 that the present GAC-RING has input/output GACs that nominally couples 5.5% of the input power at $\lambda_{B_{Ex}}$. This value is about 2% less than in the previously analysed case (see rows M_{1a} and M_{1b} of Tab. 5.1). With these levels of coupled power, even though the two GAC waveguides are 350 nm apart, the GAC-RING performance can be more sensitive to the codirectional coupling. In such case it is possible to set a lower κL_{GAC} limit for the applicability of the $2-$wave model other than the minimum GAC gap. Also the grating direct reflection inside the ring can be responsible for the observed performance deviation from the target values. This reflection can be in fact also increased with respect to the previous case due to the increased ring waveguide perturbation (a_R in Tab. 5.1). Geometries minimizing the interaction between the GAC direct reflection inside the ring and the GAC exchange reflection can be then preferred in the design stage.

Finally, to demonstrate the latter solution to reduce codirectional coupling, a GAC with 100 nm larger w_R with respect to the first GAC-RING analysed in this section was realized. The perturbation period Λ has been reduced from 336 nm to 328 nm in order to maintain the GACs $\lambda_{B_{Ex}}$ in the same wavelength region. All the other geometrical parameters have been kept unchanged except L_{GAC}, which has been increased to 150.88 μm (see the third row of Tab. 5.1). The coupling coefficient of a GAC with these parameters was calculated with the CMT (see Appendix A) involving just the principal component of the electric fields as in subsection 4.2.3. The calculated κ is about 0.0015 μm^{-1}. From this κ and L_{GAC} combination it would be possible to expect a 3 dB bandwidth of 4.9 GHz and a SMSR larger than 20 dB (see row D_3 of Tab. 5.1). However, the lower value of κ as well as the larger value of L_{GAC} brings a $\Delta\lambda_{00_{Ex}}$ of about 1.8 nm lower than that of the first GAC-RING analysed in this section. A bigger sensitivity to $\Delta\lambda_{B_{Ex}} \neq 0$ and consequently a sensible reduction of the ideal performance are then expected. Fig. 5.15a shows the spectral characteristic of the described device with $P_D = 0$. The measured performance are collected in row M_{3a} of Tab. 5.1.

With the described geometrical parameters it is possible to achieve a transmission spectrum (black trace of Fig. 5.15a) with practically only one notch. The Drop port characteristic ($|t_D|^2$, red trace) shows that the maximum value of the resonance

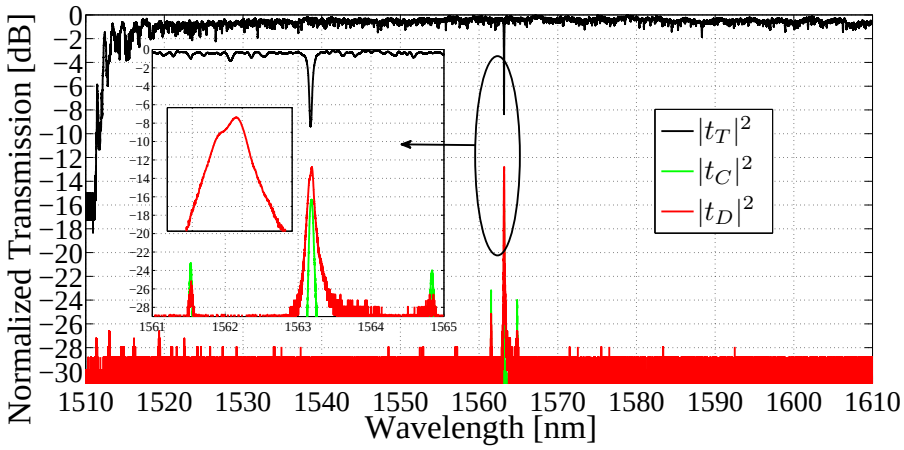

(a)

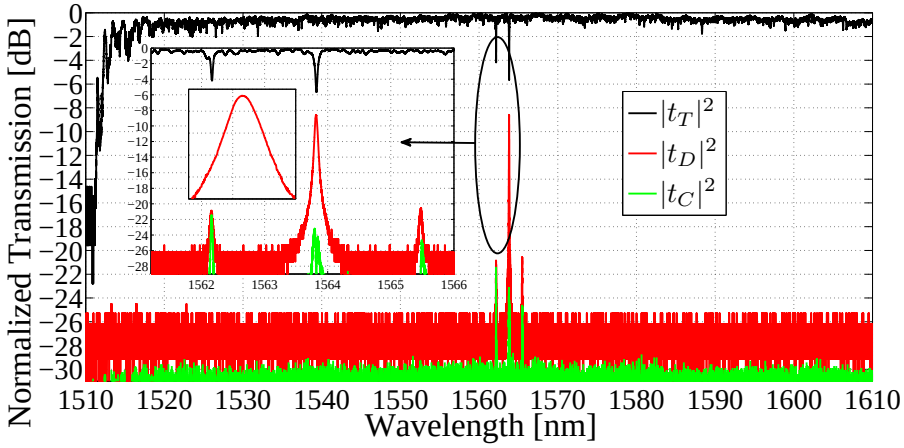

(b)

Figure 5.15.: Spectral behaviour of a GAC-RING with $R = 10$ µm, $w_R = 600$ nm, $a_R = 6$ nm, $w_B = 400$ nm, $a_B = 4$ nm, $\Lambda = 0.336$, $L_{GAC} = 100.8$ µm, $g = 300$ nm and: (a) $P_D = 0$ mW; (b) $P_D = 6.3$ mW. In both experiments the TM component of the field has been filtered at the output of the chip.

peaks outside the GAC exchange bandwidth is now about 14 dB lower than the Central Mode maximum power level.

By increasing P_D to 5.5 mW it is possible to achieve a better condition for the Drop port (red trace of Fig 5.15b). The SMSR, reported in row M_{3b} of Tab. 5.1, is in fact maintained almost unchanged at about 12 dB but now the Central Mode is almost perfectly symmetrical with respect to its central wavelength. The difference between the simulated 3 dB bandwidth and the measured one have been reduced from 4.7 GHz to about 2 GHz. The insertion loss at the Drop port is reduced by 4.2 dB and the insertion loss at the Cross port is increased by 8 dB with respect to the previous tuning condition.

However, at the Through port, the Notch Depth of the Central Mode is reduced by 3 dB and two notches can now be appreciated. As illustrated in subsection 5.3.2

and Fig. 5.8, this effect is given by $\Delta\lambda_{B_{Ex}} \neq 0$ and can be easily tackled down by realizing heaters controlling the input/output GAC $\lambda_{B_{Ex}}$. A performance improvement bringing the SMSR closer to the design value is also expected by implementing this solution.

5.4 CONCLUSIONS

In conclusion, the design tool based on the GAC 2−wave model BB allowed an estimation of the device behaviour that was proven by the reported experimental results. This demonstrates the applicability of the approach based on BBs and of the developed model to the design of a complex device like the GAC-RING.

Moreover, the in depth experimental and numerical analysis of the GAC-RING carried out has evidenced its limits and potentials. In general, a trade-off between performance, bandwidth and device footprint is required when designing the proposed narrow linewidth single mode resonator. However, smaller bandwidths within a more compact device with respect to simple GACs solutions can be achieved.

In particular, a GAC-RING with dropped 3 dB bandwidth of about 9 GHz and SMSR of 11 dB was designed and characterized. It has been shown that the SMSR is actually limited more by the spurious resonances outside the GAC exchange bandwidth than by the neighbouring modes of the selected resonance. A reduction of this undesired effect is possible by changing the geometry of the GAC: increasing the GAC gap or the waveguide widths difference. Both these solutions have been successfully demonstrated. In general, by considering also the simulated results, an increase in the GAC waveguides asynchronism can be preferred in the design stage. Increasing the gap can bring in turn just to a lower value of the broadband codirectional coupling while widening the ring waveguide can also reduce the interaction between the direct and the exchange stopband. The latter solution can also offer higher SMRS maintaining the same footprint size or more compact devices maintaining the same SMSR.

The extensive simulations carried out showed that higher performance than that demonstrated can be obtained by choosing smaller κ and larger L_{GAC}. For example, ratios larger than 20 dB between the power carried by the selected mode and the side modes are achievable. In this situation, the realization of actuators controlling of the GACs exchange Bragg wavelength is however mandatory due to the increased sensitivity of the GAC-RING to fabrication tolerances. The wavelength selective couplers tuning would also allow to reconfigure the filter central wavelength. This feature is highly desirable to give a degree of flexibility to the device. The price to pay for increasing performance and flexibility is then an increasing complexity in the device control. Three actuators are then required instead of one to obtain the same reconfigurability of a simple RR.

The presented device showed also some practical limits. The larger the required bandwidth the more it can be difficult to maintain large performance. Moreover, the GAC-RING performance is sensitive to the highlighted spurious effects.

6

TUNABLE BANDWIDTH FILTER

6.1 INTRODUCTION

The second multi-element PIC designed through the BB based approach concerns a reconfigurable filter, an integrated circuit able to reconfigure and adapt its characteristics to the system requirements. As stressed in Section 1.1, these circuits are becoming increasingly important in many applications including on-chip networking [113, 180], optical communication systems [9] and also microwave photonics [26, 117, 181], playing a key role in the development of highly functional modules to meet the required system flexibility.

Photonic integrated filters design has been deeply investigated and many different techniques have been proposed for the synthesis of the desired filter response [37, 39, 109, 112]. The development of these techniques together with the high fabrication quality standards of SOI photonic devices reached by many foundries all over the world led to the realization of multi-element chip-scale filters with high complexity and high performance [100, 110, 182–184]. However, the capability to tune both the filter bandwidth and the filter central wavelength maintaining high performance for all the filter configuration is not straightforward and represents still an open issue. For example, single resonators with tuning of their coupling sections [115, 185] offer limited bandwidth tunability range or poor Off-band Rejection. By embedding ring resonators in an unbalanced Mach-Zehnder Interferometer it is possible to improve the filter performance [111, 186]. The use of RRs in add drop configuration [186] can bring to a limited bandwidth tuning range due to in-band ripples and insertion loss despite high Off-band Rejection values. Better design flexibility, bandwidth tunability, high Off-band Rejection and simple control can be obtained using several all pass RRs [111]. All pass RRs combined with a MZI have also been used as unit cells of cascaded filters with two [114] or more stages [26] to allow a wide tunability of the filter characteristics. To achieve the described performance a large number of actuators to control the phases and the coupling coefficients of the RRs and of the MZI are however required. Moreover, as previously shown in this work, devices robust to fabrication tolerances effects have to be developed.

In this chapter a simpler geometry, where only one arm of the MZI loaded with two RRs in all-pass configuration is deeply investigated. This device requires only tuning of the RRs and of the MZI unloaded arm phases. It provides wider bandwidth tunability range, easier management with reduced power consumption and central wavelength tunability over the full Free Spectral Range at the price of a modest Off-band Rejection reduction.

The device is theoretically investigated through the transfer matrix and the Z-transform formalism by the means of the exploited SOI platform BBs. This approach allows the definition of the design rules to maximize the filter performance taking into account losses and fabrication tolerances effects. The comparison between the design and the realized devices is then carried out to demonstrate the feasibility of the described design procedure. Moreover, improved flexibility can be also achieved by realizing two tunable coupling sections for the all pass RRs through the BB developed in Chapter 3.

Finally, in order to test the devices suitability for channel subset selection in WDM systems, reconfigurable filters for gridless networking and adaptive filtering of signals, the simultaneous and correct tuning of many passbands and the filter robustness against nonlinear effects is investigated as well as bit error rate (BER) measurements.

6.2 FILTER FUNCTIONALITY

The filter architecture is shown in Fig. 6.1. It is based on an asymmetric MZI with input and output couplers power coupling coefficients K_{c1} and K_{c2}. Two RRs in all pass configuration with the same geometric length L_r and power coupling coefficient K_r load one of the MZI arms. The length of the unloaded arm is set to have an optical path difference equal to L_r so that the FSR of the RRs matches that of the MZI (see Sections 2.3 and 2.4).

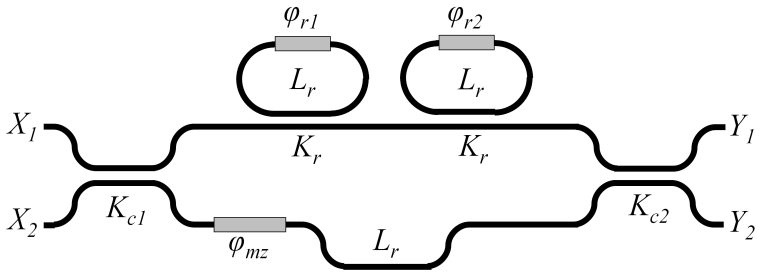

Figure 6.1.: Schematic diagram of the tunable filter architecture.

Bandwith tunability is achieved by controlling the three phase shifters represented by the grey boxes in Fig. 6.1. The tuning of the RRs phase difference $\Delta\varphi = \varphi_{r2} - \varphi_{r1}$ allows the control of the filter 3 dB bandwidth while the condition

$\varphi_{mz} = m\pi + (\varphi_{r1} + \varphi_{r2})/2$ with m integer allows a filter transfer function always symmetric with respect to the filter central frequency f_0.

Following the notation introduced in Section 2.3, the spectral response of the device can be described through the Z-transform approach [187] and the transfer matrix method as

$$\begin{bmatrix} Y_1 \\ Y_2 \end{bmatrix} = \begin{bmatrix} H_{11}(z) & H_{12}(z) \\ H_{21}(z) & H_{22}(z) \end{bmatrix} \begin{bmatrix} X_1 \\ X_2 \end{bmatrix} = \tag{6.1}$$

$$= \begin{bmatrix} c_2 & -js_2 \\ -js_2 & c_2 \end{bmatrix} \begin{bmatrix} H_R(z) & 0 \\ 0 & \gamma e^{-j\varphi_{mz}} z^{-1} \end{bmatrix} \times \tag{6.2}$$

$$\times \begin{bmatrix} c_1 & -js_1 \\ -js_1 & c_1 \end{bmatrix} \begin{bmatrix} X_1 \\ X_2 \end{bmatrix}, \tag{6.3}$$

where X_i and Y_i represent respectively the complex amplitudes of the optical fields at the input and at the output of the system. In the following $X_1 = 1$ and $X_2 = 0$ will be assumed. It holds that $z^{-1} = e^{-j2\pi fT}$, where f represents the optical frequency and T is the unit delay. This delay is given by $T = (n_g L_r/c) = (1/\mathrm{FSR})$, with n_g the waveguide group index and c the speed of light in vacuum. Note that as justified at the end of subsection 2.3.1, an effective index $n_{eff} \approx n_g$ is assumed by using the presented notation. $H_R(z)$ represent the all-pass RRs cascade transfer function and can be expressed as (see Eq. (2.6))

$$H_R(z) = \prod_{i=1}^{2} \frac{a e^{-j\varphi_{ri}} (\rho e^{j\varphi_{ri}} - a\gamma z^{-1})}{(1 - \rho a \gamma e^{-j\varphi_{ri}} z^{-1})}, \tag{6.4}$$

where, as in Section 2.3, $\rho = \sqrt{1 - K_r}$ is the coupler field transmission coefficient and a is the coupler loss factor. Moreover, γ is the field propagation loss factor associated to a propagation length L_r. The ring resonator round trip loss factor is then defined by the product $a\gamma = \gamma_r$. The input and the output MZI couplers are represented by the first and the last matrix at the right side of Eq. (6.3) being, as in Section 2.4, $c_i = \sqrt{1 - K_{ci}}$ and $s_i = \sqrt{K_{ci}}$ with $i = 1, 2$.

Using Eq. (6.3) and (6.4) the Through and the Cross port transfer functions ($H_{11}(z)$ and $H_{21}(z)$) can be expressed as the ratio between two third order polynomials $N(z)$ and $D(z)$ as (see in Appendix B, Eq. (B.7) and Eq. (B.12)):

$$H_{11}(z) = \frac{N_{11}(z)}{D_{11}(z)}, \tag{6.5}$$

$$H_{21}(z) = -j\frac{N_{21}(z)}{D_{21}(z)}. \tag{6.6}$$

These two equations account for the behaviour of a general filter. Its key parameters (3 dB bandwidth, Off-band Rejection and Shape Factor), besides $\Delta\varphi$, depend also

on the coupling coefficient ρ (or K_r) and the loss factors a and γ. To highlight how $\Delta\varphi$ influences the system poles and zeros location and consequently the filter performance, a lossless device will be considered first (i.e. $a = \gamma = 1$) with a given value of K_r. Moreover, 3 dB couplers will be considered at the input and at the output of the MZI (i.e. $K_{c1} = K_{c2} = 0.5$). This choice, as in a standard unbalanced MZI (see Section 2.4) ensures equal performance at the two ports as illustrated in Appendix B. Using Eq. (6.3) and Eq. (6.4) one gets:

$$\begin{aligned} N_{11}(z) =& \rho^2 + [1 - 2\rho\cos(\Delta\varphi/2)]\, z^{-1} \\ &+ [1 - 2\rho\cos(\Delta\varphi/2)]\, z^{-2} \\ &+ \rho^2 z^{-3}, \end{aligned} \tag{6.7}$$

$$\begin{aligned} N_{21}(z) =& \rho^2 - [1 + 2\rho\cos(\Delta\varphi/2)]\, z^{-1} \\ &+ [1 + 2\rho\cos(\Delta\varphi/2)]\, z^{-2} \\ &- \rho^2 z^{-3} \end{aligned} \tag{6.8}$$

and

$$D_{11}(z) = D_{21}(z) = 2 \cdot (1 - 2\rho\cos(\Delta\varphi/2) z^{-1} + \rho^2 z^{-2}). \tag{6.9}$$

where $\varphi_{r2} = -\varphi_{r1} = \varphi_r$ and $\varphi_{mz} = \pi$ has been considered to simplify the notation without lack of generality. In fact adding a phase φ_0 to the three phases produce just a rigid shift of the filter characteristic while a π variation of φ_{mz} produce a swap between the Through and Cross port transfer functions.

Assuming for example $K_r = 2/3$ (i.e. $\rho = 1/\sqrt{3}$), the filter Through port transfer functions for different $\Delta\varphi$ and the corresponding pole-zero diagrams are illustrated in Fig. 6.2 using the normalized frequency $\nu = (f - f_0)/FSR$ and $z^{-1} = e^{-j2\pi\nu}$. The upper left diagram of Fig. 6.2b shows that when $\Delta\varphi = \pi$ the filter has three zeros in $z = -1$ and two purely imaginary complex conjugated poles. The filter transfer function (green trace in Fig. 6.2a) shows then two nulls at $\nu = \pm 0.5$ and a spectral behaviour similar to the symmetric interleaver presented in [188]. The 3 dB bandwidth is equal to FSR/2 and a flat passband is obtained [38]. Varying $\Delta\varphi$ from π to 0 induces a rotation of two zeros towards $z = 1$ onto the unitary circle and of two poles towards the positive real axis on a circle of radius equal to ρ (see the upper part of Fig. 6.2b). This changes the filter transfer function reducing the 3 dB bandwidth from FSR/2 to its minimum (see Fig. 6.2a).

Looking at the corresponding pole zero diagram in Fig. 6.2b, one can notice that the filter has three zeros in $z = -1$ and two purely imaginary complex conjugated poles. The amplitude of the filter transfer function is thus that of a 3^{rd} order Butterworth filter with a cut off at the normalized frequency $\nu_c = 1/4$ [38]. Varing $\Delta\varphi$ from π to 0 changes the filter 3 dB bandwidth from FSR/2 to its minimum (see Fig.

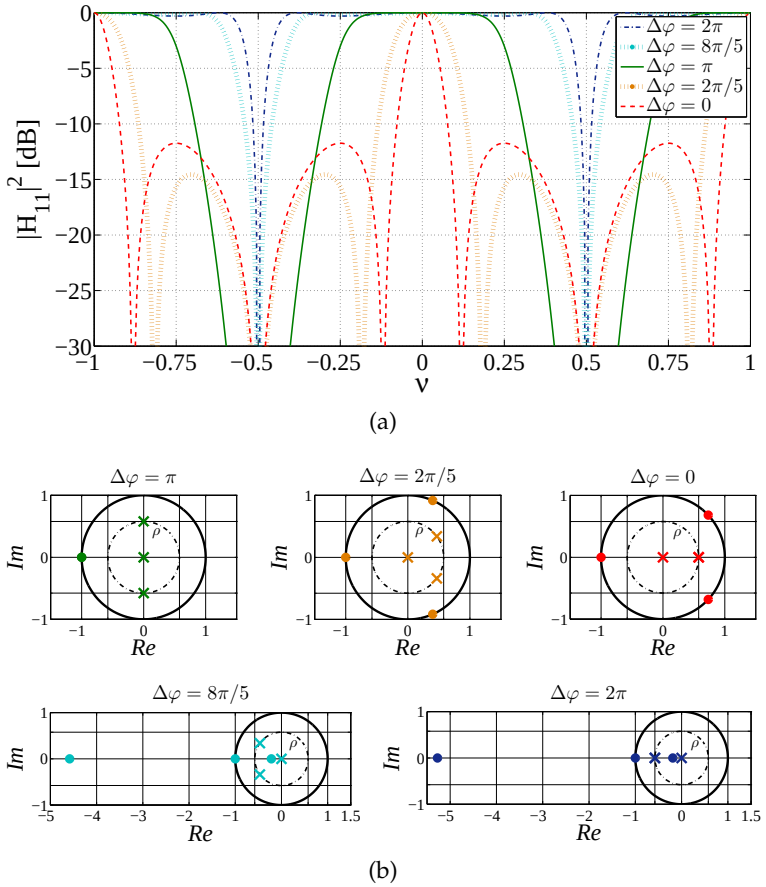

Figure 6.2.: (a) Filter Through port intensity transmission for $K_r = 2/3$ (i.e. $\rho = 1/\sqrt{3}$) and different $\Delta\varphi$ as a function of the normalized frequency $\nu = (f - f_0)/\mathrm{FSR}$. (b) Relative pole-zero diagrams where poles and zeroes are represented respectively by crosses and dots.

6.2a). This corresponds to a rotation of two zeros towards $z = 1$ on the unitary circle and of two poles towards the positive real axis on a circle of radius equal to ρ (see the upper part of Fig. 6.2b).

Instead, by varying $\Delta\varphi$ from π to 2π it is possible to increase the filter 3 dB bandwidth from FSR/2 to its maximum (see Fig. 6.2a). In this case two zeros move apart from $z = -1$ along the real axis in reciprocal positions with respect to the unit circle, while two poles are rotated toward the negative real axis always on the circle of radius ρ (see the lower part of Fig. 6.2b). As it will be shown in subsection 6.3.2, for any K_r, a perfectly flat passband response can be obtained only for one value of $\Delta\varphi$. For different values some in-band ripples appear but they are always below 0.3 dB, which is not too detrimental.

The Through port has been considered so far. The behaviour of the Cross port is complementary. The maximum (minimum) bandwidths are obtained for $\Delta\varphi = 0$ ($\Delta\varphi = 2\pi$) respectively. Inspection of Eq. (6.7), (6.8) and (6.9) also shows that for

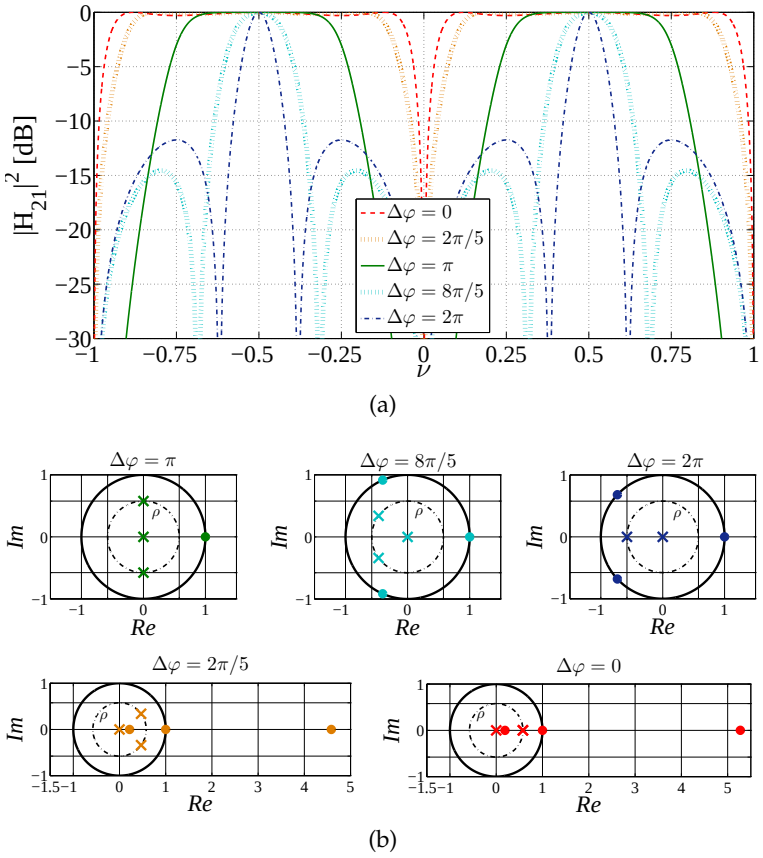

Figure 6.3.: (a) Filter Cross port intensity transmission for $K_r = 2/3$ (i.e. $\rho = 1/\sqrt{3}$) and different $\Delta\varphi$ as a function of the normalized frequency $\nu = (f - f_0)/\mathrm{FSR}$. (b) Relative pole-zero diagrams where poles and zeroes are represented respectively by crosses and dots.

given spectral characteristics, the pole zero plot is that of the Through port rotated by π. This complementary behaviour is shown in Fig. 6.3.

Once the main characteristics of the filter behaviour have been introduced, in the next section its design process will be illustrated evidencing the role of the parameters that have been kept constant in this analysis.

6.3 FILTER DESIGN

In this section the effect of the RRs coupling coefficient K_r as well as that of the losses (a and γ) and of the input/output MZI couplers will be discussed in view of the filter design. The effect of K_r will be studied first, with fixed losses. This study has been performed doing extensive numerical simulations varying K_r from 0.6 to 1 (the reason of this choice will be discussed later) and $\Delta\varphi$ from 0 to 2π (corresponding to minimum and maximum 3 dB filter bandwidth) and calculating the corresponding values of 3 dB bandwidth, Off-band Rejection and Shape Factor with coupler insertion loss $A = -20\log_{10}(a) = 0.06$ dB and ring resonator round

trip loss $\Gamma_r = -20\log_{10}(\gamma_r) = 0.2$ dB/turn. Losses have been set in accordance with typical SOI platform figures (see Chapter 2 and [77]). Then, once the desired value of K_r has been found, the impact of the losses on the overall performance is studied. Variations from the 3 dB input/output MZI coupler condition will be then analysed and finally, a brief discussion on the possibility to obtain filter responses with a maximally flat passband characteristic will be done.

Before illustrating the results it should also be noticed that the Off-band Rejection must be defined differently depending on the presence or not of sidelobes (see Fig. 6.2). In particular the Off-band Rejection is calculated with respect to the maximum of the filter sidelobes, if they exist, or, if they are not present, with respect to the filter absolute minimum. Moreover, the Shape Factor is defined as the ratio between the 1 dB and the 10 dB filter bandwidth.

6.3.1 *RRs Coupling Coeffcient*

The filter 3 dB bandwidth as a function of K_r and $\Delta\varphi$ are illustrated in the map of Fig. 6.4, where level curves are drawn to help reading the different values of the colormap.

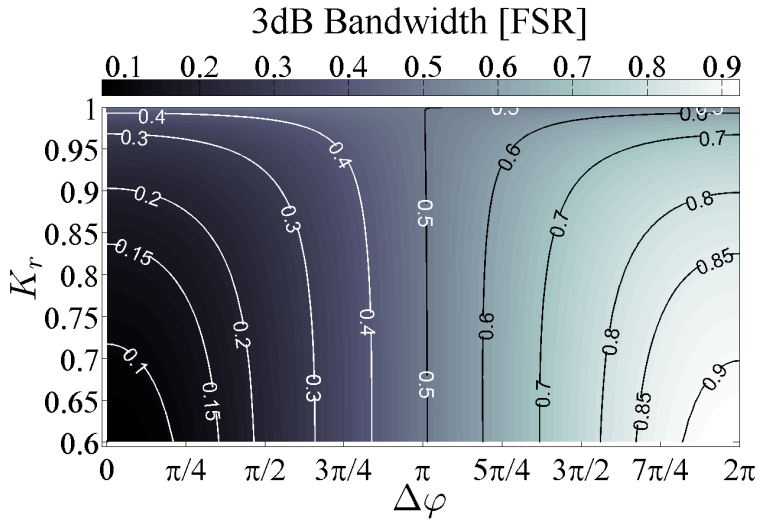

Figure 6.4.: Map of the filter Through port 3 dB bandwidth normalized to the FSR as a function of $\Delta\varphi$ (x axes) and K_r (y axes).

The figure shows that for $\Delta\varphi = \pi$ the 3 dB bandwidth is always of about 50 % of the FSR, no matter of the value of K_r. Suitable combinations of $\Delta\varphi$ and K_r allow all the possible values of the 3 dB bandwidth, with minimum and maximum values obtained for $\Delta\varphi$ close to 0 and 2π respectively. Large values of K_r reduce the bandwidth tunability as well as its sensitivity to $\Delta\varphi$ variations. The limit case is represented by $K_r = 1$, where the two RRs act as pure delay lines and the filter transfer function is that of an unbalanced MZI with a bandwidth of 0.499 FSR in-

dependently on $\Delta\varphi$. One can conclude that small values of K_r are then desirable to maximize the filter bandwidth tunability.

However, this figure is not the only one that has to be taken into account in the design of the filter. The effects of K_r on the Off-band Rejection as well as on the Shape Factor have to be considered too. The dependence of these figures of merit on K_r is illustrated in Fig. 6.5. The Off-band Rejection (Fig. 6.5a) and the Shape Factor

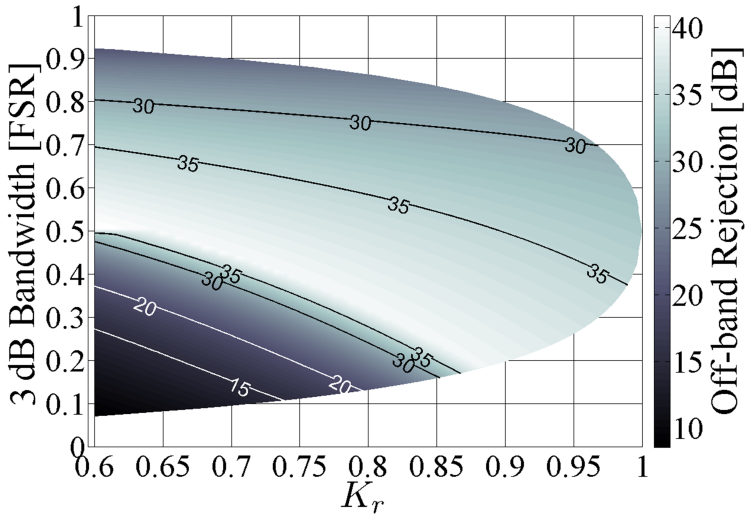

(a)

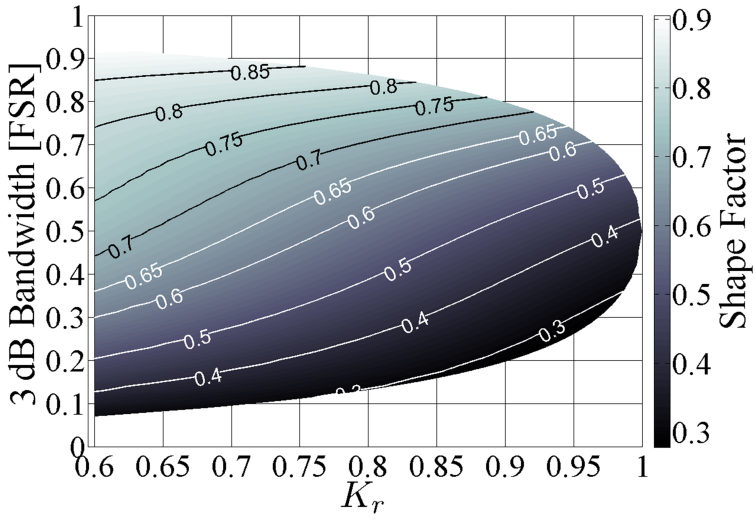

(b)

Figure 6.5.: Map of the (a) filter Off-band Rejection and (b) Shape Factor (color bar and contour lines) for the 3 dB bandwidths obtained for $0 < \Delta\varphi < 2\pi$ (y axes) as a function of K_r (x axes).

(Fig. 6.5b) are shown as a function of K_r and of the 3 dB bandwidth normalized to the filter FSR. Level curves are drawn to help reading the different values of the colormap.

Considering the Off-band Rejection first, Fig. 6.5a shows that an overall increase of this figure of merit can be obtained increasing K_r. A trade-off is thus needed to obtain both wide bandwidth tunability and a reasonable Off-band Rejection for all the filter configurations. In this trade-off the filter shape has also to be taken into account. Considering the map of Fig. 6.5b one can also see that, increasing K_r also smoothens the shape of the filter thus reducing the Shape Factor. An upper limit for K_r can be thus also given by this figure depending on the required performance.

These maps allow the designer to choose the value of K_r corresponding to the desired performance, providing at the same time a general view of the mutual effect of the parameters. A good compromise can be obtained for K_r within 0.7 and 0.8. With $K_r = 0.7$ a large bandwidth tunability, from 90% to 10% of the FSR, can be obtained with an Off-band Rejection always larger than 12.7 dB. With $K_r = 0.8$ an Off-band Rejection larger than 20 dB is achieved for all the filter configurations but the bandwidth tunability is reduced by about 7% (i.e. $0.86 - 0.13$ FSR). With $K_r = 0.75$ an Off-band Rejection always larger than 20 dB can be obtained for bandwidths larger than FSR/5 maintaining an overall larger value of the Shape Factor.

This is why we limited the lower value of K_r to 0.6 although K_r can decrease down to 0, value which corresponds to an unbalanced MZI transfer function, independently on the choice of $\Delta\varphi$. RRs coupling coefficients $K_r < 0.6$ can lead in fact to small values of the Off-band Rejection for bandwidths smaller than FSR/2 and high values of the in-band ripples for bandwidths larger than FSR/2. This effect can be observed looking at Fig. 6.6a and Fig. 6.6b where the filter 3 dB bandwidth and Off-band Rejection for $\Delta\varphi = 0$ (red dashed trace) and $\Delta\varphi = 2\pi$ (blue dash-dotted trace) are shown for K_r between 0.6 and 0.3. As K_r decreases the filter Off-band Rejection decreases too, reaching a value near to 0 for the minimum bandwidth condition ($\Delta\varphi = 0$) at $K_r = 0.3$. The maximum bandwidth condition ($\Delta\varphi = 2\pi$) shows instead Off-band Rejection values always larger than 10 dB. However in-band ripples of about 3 dB can be observed at $K_r = 0.3$ (see Fig. 6.6c).

In conclusion, small values of K_r provide large bandwidth tunability as well as large Shape Factor. However, to obtain good Off-band Rejection, large values of K_r are required. A good trade-off between these figures can be obtained by choosing K_r between 0.7 and 0.8. Once a suitable value of K_r have been chosen between this range, it is now interesting to analyse whether and how a variation between the designed and the fabricated working point can affect the devices spectral behaviour. This aspect will be investigated in the following subsection.

6.3.2 *Robustness against fabrication tolerance effects*

The analysis of the maps of Fig. 6.5, besides providing the optimal range of the design parameters, can also be useful to evaluate the filter robustness against

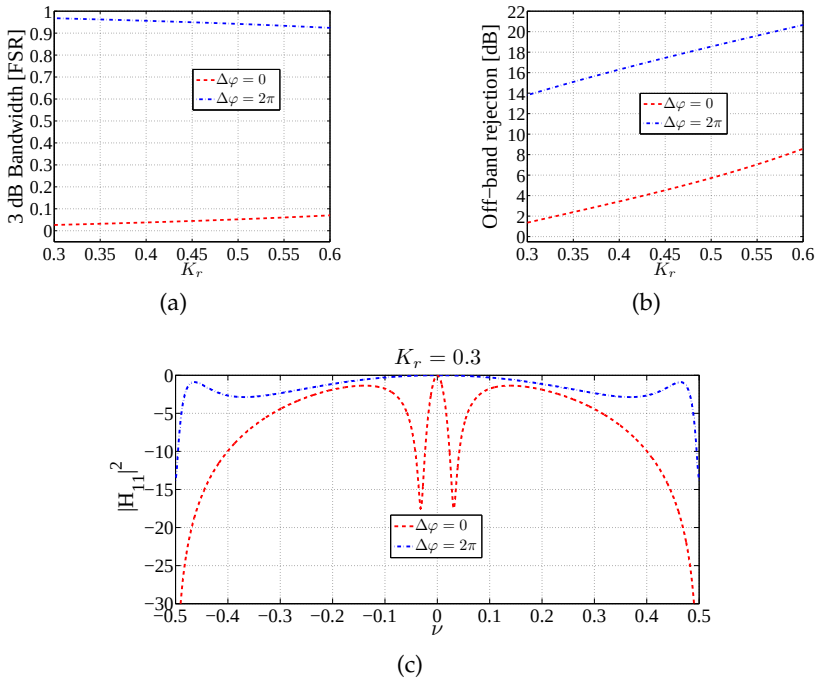

Figure 6.6.: (a) 3 dB bandwidth and (b) Off-band Rejection for $\Delta\varphi = 0$ and $\Delta\varphi = 2\pi$ as a function of K_r (varied between 0.3 and 0.6). (c) Filter Through port normalized intensity transmission for $\Delta\varphi = 0$, $\Delta\varphi = 2\pi$ and $K_r = 0.3$ as a function of ν.

fabrication tolerances. This property strongly depends on the filter working point as well as on the considered figure of merit. This issue will be thus discussed focusing in particular on the regions of the maps within $K_r = 0.7$ and $K_r = 0.8$.

Considering first bandwidth tunability, the device shows a good robustness to fabrication tolerances. For K_r between 0.7 and 0.8, bandwidth tunability varies in fact by about 0.7% for every 1% of K_r. However, its sensitivity to a K_r variation increases as K_r increases. High values of the RRs coupling coefficient are then not recommended if a device with low sensitivity to fabrication tolerances is desired.

With regards to the Off-band Rejection, Fig. 6.5a shows that larger bandwidths (> 0.5 FSR) have lower sensitivity to coupler values variation than the smaller ones (< 0.5 FSR). If, for example, $K_r = 0.75$ and a 3 dB bandwidth equal to 0.2 FSR is considered, a $\pm 5\%$ change of K_r causes a variation of $+5.5/-3.5$ dB in the Off-band Rejection from its design value (i.e. 20 dB). If this figure of merit is expected to be critical for the considered application it is then convenient to use coupling coefficients with larger values or, as it will be shown in subsection 6.5.6 by the means of the thermally driven tunable coupler developed during this thesis (see Chapter 3), add a control on the RR couplers to set K_r precisely.

Finally, regarding the Shape Factor, it can be observed from the map of Fig. 6.5b that in general this figure of merit varies slowly with K_r (especially for small 3 dB

bandwidths) and can be thus considered less critical: the slope of the isolevel curves is in fact low almost everywhere in the map.

One can then conclude that the filter performance are not very sensitive to fabrication tolerance effects when K_r is in the range $0.7 - 0.8$. Having deeply investigated the filter performance dependence on K_r it is now time to focus on other parameters, such as K_{c1}, K_{c2} and the losses, that can affect the filter spectral behaviour. In the next subsection, the effect of the input/output MZI couplers will be investigated to see if the choice of 3 dB couplers assumed so far is the best one.

6.3.3 *MZI Input/Output Couplers*

In the analysis carried out until now, a pair of 3 dB couplers have been considered. It has been in fact previously shown (and also proven with the extended demonstration reported in Appendix B) that this condition provides identical performance at the two ports of the device. Similar performance, or better, equal performance at the two ports, is generally desirable. If just one output port of the device is to be used, this condition ensures that, maximizing the Off-band Rejection at one port, the amount of power lost at the unused port is minimized. If, on the contrary, both the outputs are to be used (e.g. interleaver applications), the 3 dB couplers guarantee the same filtering properties at the two output ports.

In this section, it will be analysed whether this condition maximizes the filter performance and if the presented filter is robust against variations of the coupling coefficients of the two couplers, K_{c1} and K_{c2}, from the designed value. To this purpose K_r is fixed to 0.8, a value chosen in order to analyse a filter showing Off-band Rejections larger than 20 dB in any configuration.

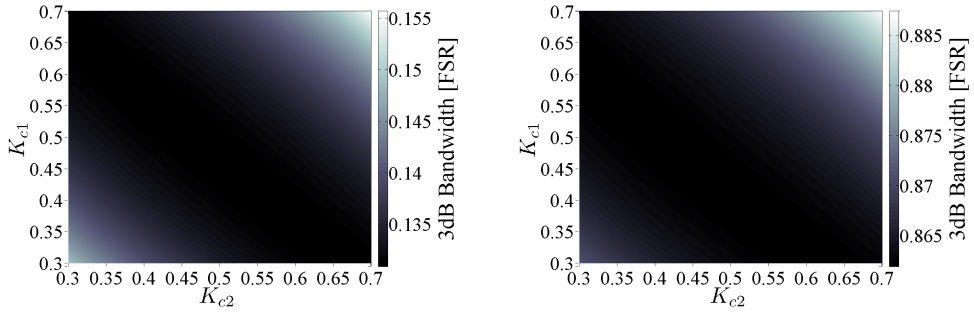

(a) (b)

Figure 6.7.: Map of the Through port 3 dB bandwidth for (a) $\Delta\varphi = 0$ and for (b) $\Delta\varphi = 2\pi$ as a function of K_{c1} and K_{c2}. Note the different scales of the figures.

The analysis can start focusing on the device bandwidth tunability. In the maps of Fig. 6.7 the Through port minimum 3 dB bandwidth ($\Delta\varphi = 0$, Fig. 6.7a) and

maximum 3 dB bandwidth ($\Delta\varphi = 2\pi$, Fig. 6.7b) are plotted as a function of K_{c1} and K_{c2}.

One can notice that a combination of K_{c1} and K_{c2} that, at the same time, maximizes the maximum bandwidth and minimizes the minimum bandwidth cannot be achieved. Both maps of Fig. 6.7 show minimum values on the antidiagonal region and maximum values at the upper right and lower left corners. Despite that, bandwidth tunability poorly varies with the MZI input/output couplers choice. Both bandwidth conditions show a 2% maximum variation for a 20% variation of K_{c1} and K_{c2} form the 3 dB condition.

The same conclusions can be drawn for the Cross port. The maps of Fig. 6.8 show in fact that both minimum ($\Delta\varphi = 2\pi$, Fig. 6.8a) and maximum ($\Delta\varphi = 0$, Fig. 6.8b) 3dB bandwidth of the filter Cross port are just slightly affected by K_{c1} and K_{c2} variations. The only difference is that now the minimum values of both bandwidth

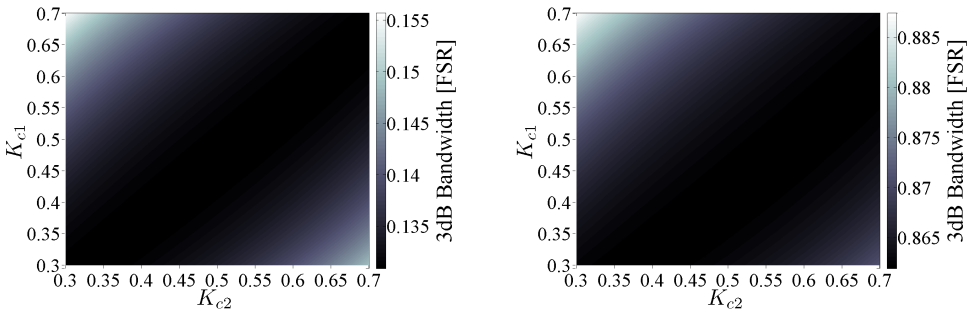

(a) (b)

Figure 6.8.: Map of the Cross port 3dB bandwidth for (a) $\Delta\varphi = 2\pi$ and for (b) $\Delta\varphi = 0$ as a function of K_{c1} and K_{c2}. Note the different scales of the figures.

conditions are found around the diagonal region of the maps and the maximum values can be found instead at the bottom right and at the upper left corners.

We can then conclude that regarding bandwidth tunability, $K_{c1} = K_{c2} = 0.5$ represents a good design choice and that this figure is almost insensitive to K_{c1} and K_{c2} variations due to fabrication tolerance effects.

We can now move to the analysis of the Off-band Rejection. In this case, to give a better overview, also at the $\Delta\varphi = \pi$ condition behaviour will be considered. The Through port performance is shown in Fig. 6.9. In the minimum bandwidth condition ($\Delta\varphi = 0$, Fig. 6.9a) the Off-band Rejection is less sensitive to changes of K_{c1} and K_{c2} with respect to the maximum ($\Delta\varphi = 2\pi$, Fig. 6.9b) and the $\Delta\varphi = \pi$ condition (Fig. 6.9c). This comes from the Off-band Rejection definition given at the beginning of this Section. A K_{c1}, K_{c2} variation affects more the filter minima than the filter sidelobes. When $\Delta\varphi = 0$, the filter shows a good robustness against fabrication tolerances on the value of K_{c1} and K_{c2}. Moreover, input/output MZI 3 dB couplers

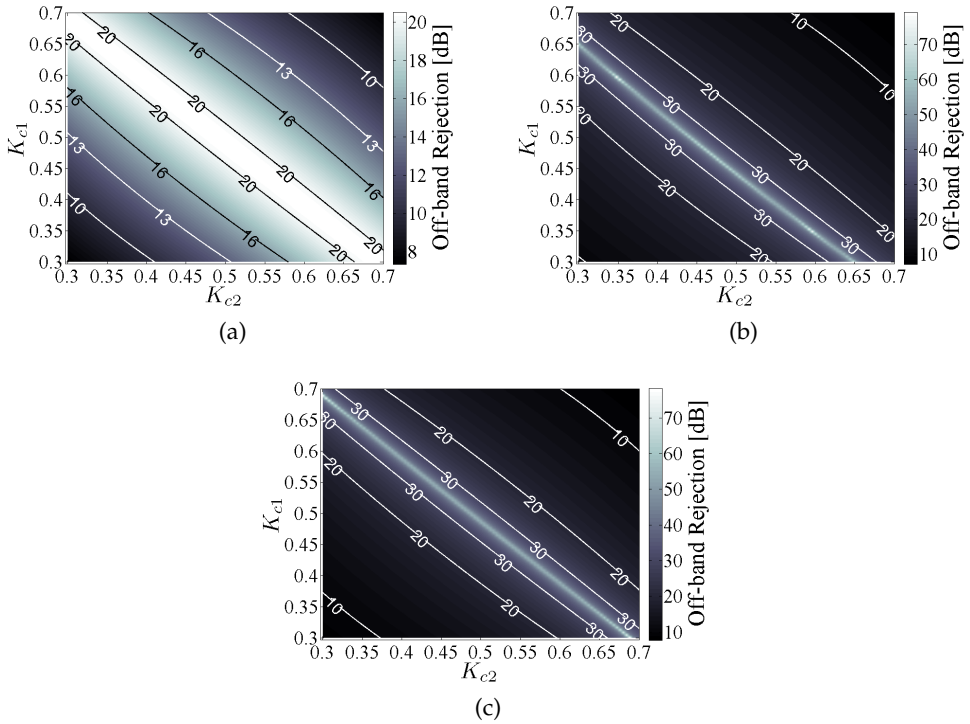

Figure 6.9.: Map of the Through port Off-band Rejection for (a) $\Delta\varphi = 0$, (b) $\Delta\varphi = 2\pi$ and (c) $\Delta\varphi = \pi$ as a function of K_{c1} and K_{c2}. Note the different scales of the figures.

provide best performance, corresponding to an Off-band Rejection of 20.5 dB. A $\pm 5\%$ variation of either K_{c1} or K_{c2} brings a maximum reduction of this value of about 1.5 dB. However, it can be noticed that the Off-band Rejection experiences the maximum reduction when K_{c1} and K_{c2} undergo the same variation. A $+5\%$ variation of both K_{c1} and K_{c2} reduces in fact the Off-band Rejection to 16.6 dB. On the other hand, the Off-band Rejection does not vary if K_{c1} is increased (decreased) and K_{c2} is decreased (increased) by the same amount.

Although input/output MZI 3 dB couplers ensure maximum performance and robustness against fabrication tolerances for the minimum bandwidth condition, this is not true for all the filter configurations. This appears clear observing Fig. 6.9b and Fig. 6.9c. $K_{c1} = K_{c2} = 0.5$ provides however, as also discussed in subsection 6.3.1, high performance. An Off-band Rejection of 37 dB for the $\Delta\varphi = \pi$ configuration (Fig. 6.9c) and of 25 dB for the maximum bandwidth configuration ($\Delta\varphi = 2\pi$, Fig. 6.9c) can be in fact observed. Moreover, the larger sensitivity to K_{c1},K_{c2} variations is partially mitigated by an overall larger value of the Off-band Rejection. A $\pm 5\%$ variation of either K_{c1} or K_{c2} can lead, in the worst case, to an Off-band Rejection of 23.8 dB and of 19.6 dB respectively for the $\Delta\varphi = \pi$ (Fig. 6.9c) and for the maximum bandwidth configuration ($\Delta\varphi = 2\pi$, Fig. 6.9b). In both cases this value results larger than that observed for $\Delta\varphi = 0$ (i.e. 19 dB). Similar conclusions can be drawn considering $K_{c1} = K_{c2} = 0.55$. In this case an Off-band Rejection of 18.9 dB

and of 16.4 dB can be observed respectively for the $\Delta\varphi = \pi$ (Fig. 6.9c) and for the maximum bandwidth configuration ($\Delta\varphi = 2\pi$, Fig. 6.9b). When $\Delta\varphi = 0$ the same input/output MZI values brings to an Off-band Rejection of 16.6 dB.

As in the bandwidth tunability analysis, the same considerations that have been drawn for the Through port can be drawn for the Cross port. The only difference is the maximum performance orientation in the K_{c1}–K_{c2} coordinate system. In Fig. 6.10 the Cross port Off-band Rejection as a function of K_{c1},K_{c2} is in fact illustrated for the minimum ($\Delta\varphi = 2\pi$, Fig. 6.10a), the maximum ($\Delta\varphi = 0$, Fig. 6.10b) and the $\Delta\varphi = \pi$ (Fig. 6.10c) condition. Note that the maximum performance orientation

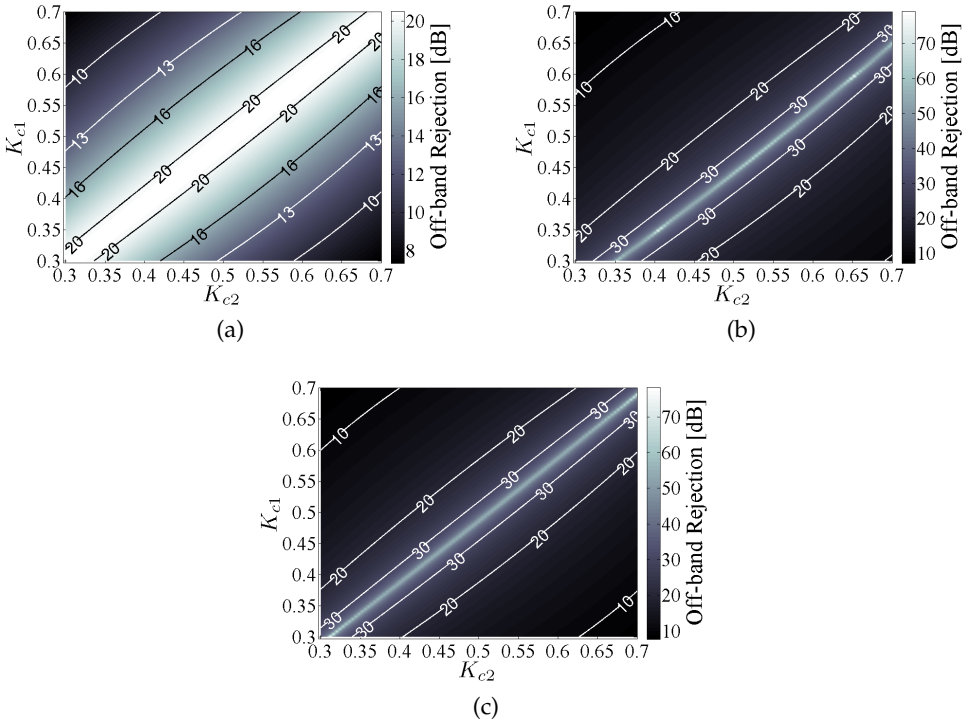

Figure 6.10.: Map of the Cross port Off-band Rejection for ((a)) $\Delta\varphi = 0$, (b) $\Delta\varphi = 2\pi$ and (c) $\Delta\varphi = \pi$ as a function of K_{c1} and K_{c2}. Note the different scales of the figures.

was expected considering that, for a lossless MZI, minima equal to zero at the Cross port are obtained for $K_{c1} = K_{c2}$ and minima equal to zero at the Through port are obtained for $K_{c1} = 1 - K_{c2}$ (see Section 2.4).

It is then possible to conclude that $K_{c1} = K_{c2} = 0.5$ represents a high performance working point for every filter configuration at both outputs. Moreover, bandwidth tunability is highly robust against fabrication tolerances on the K_{c1},K_{c2} values. The filter Off-band Rejection can be instead highly sensitive to K_{c1}, K_{c2} variations from the selected working point, depending on the filter configuration. However, the more sensitive configurations can show larger values of the Off-band Rejection than those of the less sensitive for a given $K_{c1} - K_{c2}$ combination.

These properties makes the working point defined by K_{c1} and K_{c2} less critical than that defined by the RR coupling coefficient. However, a careful evaluation must be performed after the selection of K_r. Variations of K_{c1} and K_{c2} from the 3 dB condition may in fact lead the Off-band Rejection below the minimum value required by the selected application. In such case, the analysis of different working points have to be performed and the possibility to realize tunable couplers at the input/output of the MZI can be also evaluated.

6.3.4 *Loss Effects*

A fixed value of the losses ($\Gamma_r = 0.2$ dB/turn and $A = 0.06$ dB) has been considered so far. It is now interesting to see how the losses influence the filter behaviour. The test case considers $K_r = 0.8$, as in the previous subsection, and varying γ and thus γ_r. As expected, losses have a detrimental impact on the three considered filter figures of merit and on the device insertion loss. The effect on these figures depends on $\Delta\varphi$ as shown in Fig. 6.11, where three values of $\Delta\varphi$ (i.e. $0, \pi, 2\pi$) are plotted as a function of the ring round trip losses Γ_r.

Fig. 6.11a shows that the insertion loss increases more for the minimum bandwidth condition ($\Delta\varphi = 0$) than for the maximum one ($\Delta\varphi = 2\pi$). This can be explained noting that while f_0 matches the RRs antiresonance frequency when $\Delta\varphi = 2\pi$, it matches the RRs resonance frequency when $\Delta\varphi = 0$. In the minimum bandwidth condition the wave will then experience more round trips into the RRs and consequently a larger insertion loss as well as a larger sensitivity to Γ_r variations (larger insertion loss vs. Γ_r slope). The difference between the insertion losses of these two bandwidth conditions reaches 3 dB for values of Γ_r around 1.7 dB/turn.

Fig. 6.11b shows the dependence of the Off-band Rejection on the losses. In this case, the increase in the loss factor affects more the maximum bandwidth condition ($\Delta\varphi = 2\pi$) than the minimum one ($\Delta\varphi = 0$). As it occurred in the MZI input/output couplers analysis, this comes from the definition of Off-band Rejection. This figure is in fact calculated respect to the filter sidelobes or, if no sidelobes are present in the spectral characteristic (i.e. maximum bandwidth condition), respect to the filter minima. Increasing the losses brings the zeros of the filter away from the unit circle affecting more the filter nulls than the filter sidelobes and consequently more the Off-band Rejection of the maximum bandwidth configuration than the one of the minimum bandwidth. Increasing Γ_r from 0.06 to 1.8 dB/turn the minimum bandwidth condition Off-band Rejection reduces from more than 20 dB to around 16 dB while the maximum bandwidth condition reduces of more than 20 dB. Off-band Rejection values larger than 20 dB for every filter configuration can be obtained for Γ_r lower than 0.4 dB/turn.

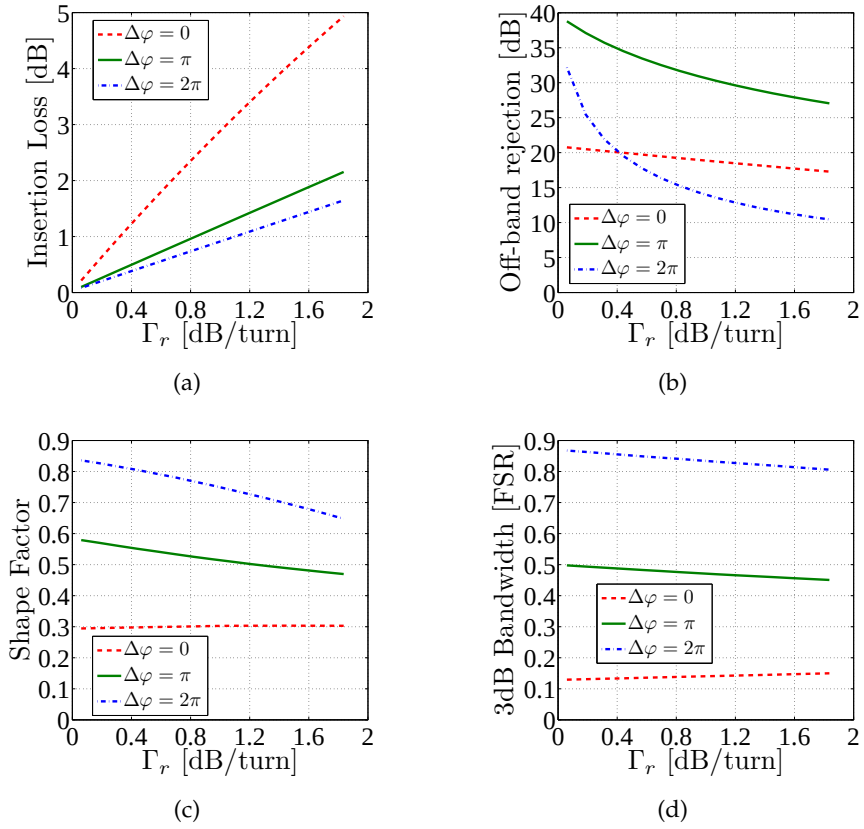

Figure 6.11.: (a) Insertion loss, (b) Off-band Rejection, (c) Shape Factor and (d) 3 dB bandwidth as a function of Γ_r for $\Delta\varphi = 0$ (minimum bandwidth), $\Delta\varphi = \pi$ and $\Delta\varphi = 2\pi$ (maximum bandwidth).

To increase the filter performance when large round trip loss occur, it is possible to design filters with a larger value of K_r at the cost of bandwidth tunability and Shape Factor reduction. It should be noticed that this reduction would add to that already caused by the losses. Fig. 6.11c and 6.11d show that the larger the round trip loss the smaller the filter Shape Factor (mostly for the maximum bandwidth condition) as well as the bandwidth tunability. This figures of merit show however a low sensitivity to loss variation and can be then considered less critical than the Off-band Rejection.

It can be now pointed out that the value of Γ_r can be interpreted in two ways. A large value of Γ_r may correspond either to larger values of the ring losses with a constant L_r or a longer L_r for a given loss figure. The balance between these two constraints affects the achievable values of FSR.

6.3.5 *Flat Passband*

After the extensive description on how the several parameters of the analysed filter influence its performance, one may wonder whether and how the filter can

be designed to obtain maximally flat passband behaviour at a certain desired $\Delta\varphi$. Moreover, if RRs tunable coupling sections are available, if this condition can be achieved for any desired bandwidth. To give a general idea on how this condition can be calculated as a function of $\Delta\varphi$ and to simplify the calculations, a lossless device will be considered. The lossy case will lead in fact to straightforward but cumbersome equations without changing the conclusions. This equations could be useful just in the case that precise values of K_r would be required. In addition $K_{c1} = K_{c2} = 0.5$ and $\varphi_{mz} = \pi$ will be considered.

The maximally flat passband condition can be derived expressing Eq. (6.3) in the frequency domain rather than in the Z-transform domain. In this case the Through and the Cross port squared magnitude transfer functions read as:

$$|H_{11}(z)|^2 = \sin^2\left(\frac{\Delta\Phi(\Omega)}{2}\right), \tag{6.10}$$

$$|H_{21}(z)|^2 = \cos^2\left(\frac{\Delta\Phi(\Omega)}{2}\right). \tag{6.11}$$

Where $\Omega = 2\pi f$ and $\Delta\Phi(\Omega) = \Phi_r(\Omega) - (\Omega T + \varphi_{mz})$ represent the difference between the phases acquired by the wave in the two arms of the MZI. $\Phi_r(\Omega)$ is the RRs cascade phase and $(\Omega T + \varphi_{mz})$ represents the phase of the MZI unloaded arm. The passband and the stopband centre frequencies occur when the phase difference is a integer multiple of π. To flatten the pass band response, a constant phase difference around the passband centre frequency $f_c = \Omega_c/(2\pi)$ is then required. This can be done by setting the derivative of $\Delta\Phi(\Omega)$ calculated with respect to Ω equal to zero [38] or, in other words, setting the RRs cascade group delay τ_{gRR} equal to the unit delay T:

$$\tau_{gRR}(\Omega_c) = -\frac{d\Phi(\Omega)}{d\Omega}\bigg|_{\Omega=\Omega_c} = \frac{d(\Omega T + \varphi_{mz})}{d\Omega}\bigg|_{\Omega=\Omega_c} = T, \tag{6.12}$$

where τ_{gRR} can be expressed as the sum of the group delay of the two RRs τ_{gr1} and τ_{gr2} as it follows:

$$\begin{aligned}\tau_{gRR}(\Omega) &= \tau_{gr1}(\Omega) + \tau_{gr2}(\Omega) \\ &= \frac{1-\rho^2}{1+\rho^2-2\rho\cos(\Omega T - \frac{\Delta\varphi}{2})}T \\ &+ \frac{1-\rho^2}{1+\rho^2-2\rho\cos(\Omega T + \frac{\Delta\varphi}{2})}T.\end{aligned} \tag{6.13}$$

Combining Eq. (6.13) with Eq. (6.12) and considering $\varphi_{mz} = \pi$ it is possible to derive a second order algebraic equation in ρ that can be easily solved either around the filter central frequency at the Through port ($\Omega T = 2m\pi$, with m integer)

or around the filter central frequency at the Cross port ($\Omega T = (2m+1)\pi$, with m integer). Once the values of ρ for every $\Delta\varphi$ have been found it is straightforward to calculate the corresponding K_r.

The values of K_r necessary to obtain a maximally flat passband filter for a given $\Delta\varphi$ are illustrated in Fig. 6.12a for the Through port (blue trace) and the Cross port (red trace). For $\varphi = \pi/2$ the Through port filter pass band is flat if $K_r = 0.26$ is

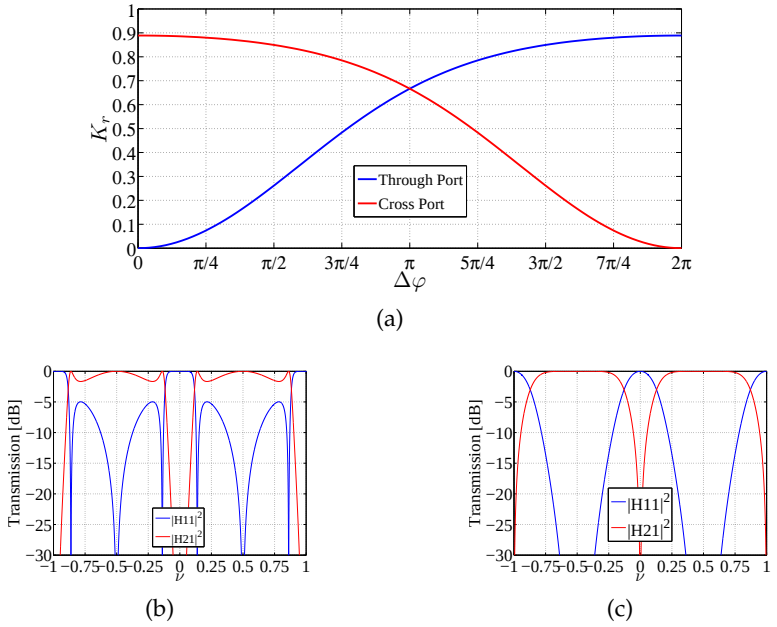

Figure 6.12.: (a) K_r necessary to obtain the maximally flat passband condition for varying $\Delta\varphi$ at the Through port (blue trace) and at the Cross port (red trace). (b) Filter response for $\Delta\varphi = \pi/2$ and $K_r = 0.26$ (maximally flat passband condition at the Through port). (c) Filter response for $\Delta\varphi = \pi/2$ and $K_r = 0.85$ (maximally flat passband condition at the Cross port).

set. This RRs coupling coefficient value should be avoided due to low Off-band Rejection values (see Section 6.3). Looking in fact at Fig. 6.12b, the Through port filter response (0.235 FSR 3dB bandwidth) shows a maximally flat passband but poor Off-band Rejection values (about 5 dB). Moreover, the Cross port shows inband ripples of about 3 dB. Setting instead $K_r = 0.84$ it is possible to flatten the Cross port bandwidth (as shown in Fig. 6.12c). The Through port bandwidth is now equal to 0.255 FSR and shows the maximum value for the Off-band Rejection. It is now possible to understand that the large Off-band Rejection line (white line) in Fig. 6.5a represent the K_r values for which maximally flat passband is obtained at the Cross port.

In conclusion maximally flat passband can be obtained for any value of $\Delta\varphi$ but, due to reduced Off-band Rejection performance, it is practically achievable only for filter configurations with 3dB bandwidths larger than FSR/2.

6.4 GROUP DELAY AND DISPERSION

Before discussing the results obtained on the fabricated devices, it is convenient to discuss also some other important characteristics of the filter, evidencing the effect of $\Delta\varphi$ in terms of group delay and dispersion.

The group delay of the proposed filter varies with the amplitude of the filter transfer function. Fig. 6.13 shows an example of the normalized group delay τ_n and the normalized dispersion D_n of a filter varying the losses for different values of $\Delta\varphi$ and $K_r = 0.8$. The curves are thicker in the frequency range within the filter 3 dB bandwidth. The normalized group delay τ_n is related to the absolute group delay τ_g through the unit delay T by the equation $\tau_g = \tau_n T$, while the normalized dispersion D_n is related to the absolute dispersion τ_g by the equation $D = -c(T/\lambda)^2 D_n$ [38].

Considering first a lossless filter (Fig. 6.13a and Fig. 6.13b), in the minimum bandwidth condition, at f_0, the light passes through both the resonances of the ring resonators experiencing thus the maximum group delay and high values of the dispersion at the edges of the 3 dB bandwidth.

Increasing the phase shift between the RRs, the filter group delay and dispersion decrease and a minimum dispersion in the 3 dB bandwidth (for $\Delta\varphi \in [0.4\pi, 0.5\pi]$) is found. A further increase of $\Delta\varphi$ reduces then the group delay at f_0 increasing the dispersion. For $\Delta\varphi = \pi$ the group delay is minimum at f_0 and maximum at about the 3 dB bandwidth edges. In the maximum bandwidth condition ($\Delta\varphi = 2\pi$), the filter exhibits an almost constant delay in the center of the 3 dB bandwidth and a maximum dispersion close to the edges larger than that occurring for $\Delta\varphi = \pi$.

The working points close to the filter maximum and minimum bandwidth conditions can be critical for signal degradation. This problem can be reduced increasing the FSR which is inversely proportional to τ_g and D.

For different values of the losses, the described group delay evolution between minimum and maximum bandwidth conditions still hold. In the following, the variations respect to this case for different values of the losses will be analysed. Assuming a lossy filter with $A = 0$ dB and $\Gamma_r = 0.2$ dB (Fig. 6.13c and Fig. 6.13d) an overall τ_n and D_n decrease occurs. The larger is the bandwidth the larger is this reduction. Adding coupler losses ($A = 0.06$ dB and $\Gamma_r = 0.2$ dB/ in Fig. 6.13e and Fig. 6.13f), the appearance of two peaks at the edges of the FSR window for τ_n can be noticed for filter configurations with $\Delta\varphi < \pi$. This behaviour does not affect however the filter functionality because of its spectral position. Finally, increasing Γ_r to 1.84 dB and keeping $A = 0.06$ dB, values of τ_n and D_n at the edges of the 3 dB bandwidth when $\Delta\varphi = 2\pi$ are almost equal to those assumed if $\Delta\varphi = \pi$. Loss increase can be then considered beneficial if dispersion and group delay are under inspection.

In this analysis, the value of K_r has been kept fixed to 0.8. To make this analysis complete it can be shown how variations of this parameter influence the de-

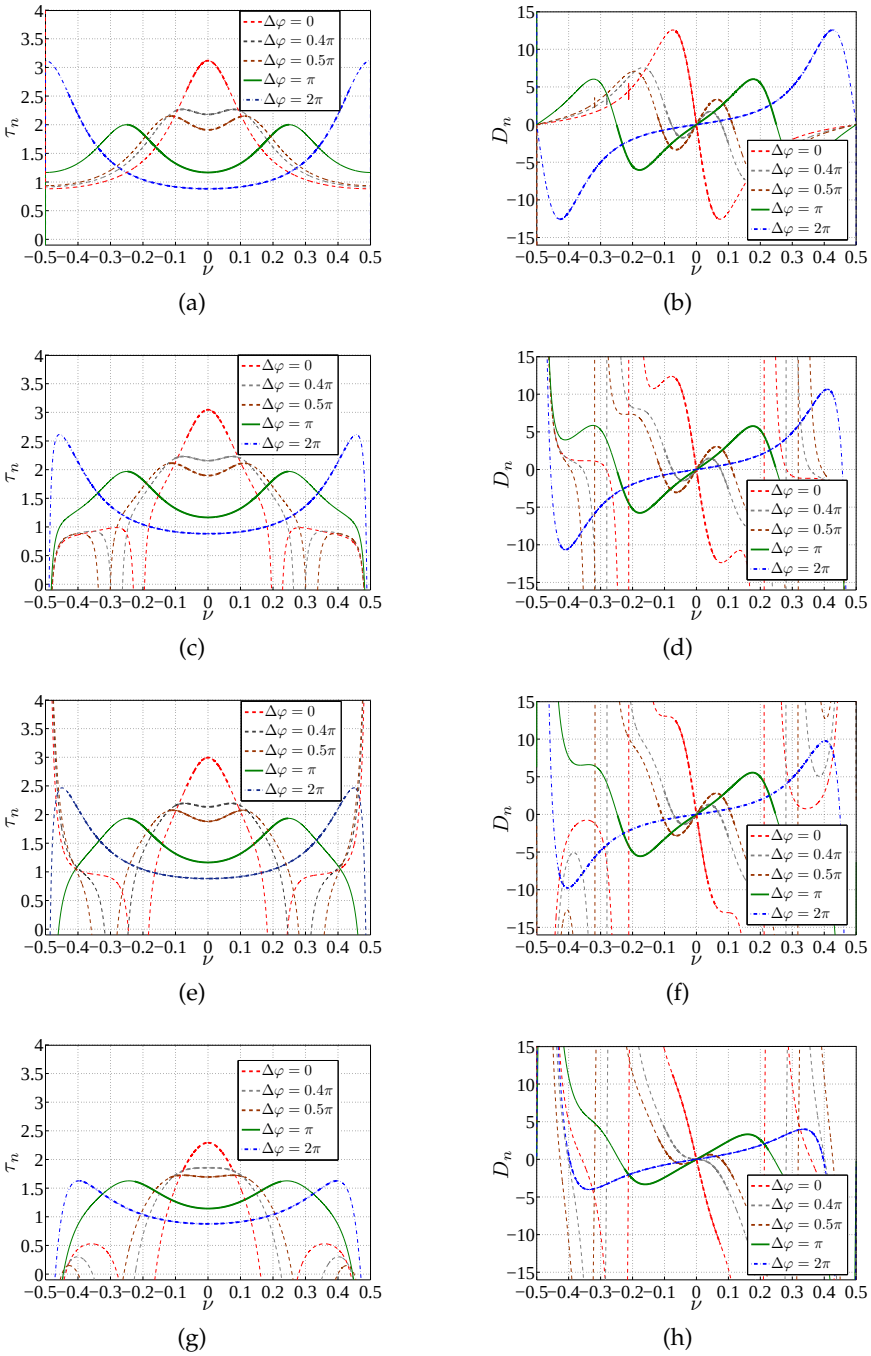

Figure 6.13.: Filter Through port (a),(c),(e),(g) τ_n and (b),(d),(f),(h) D_n for: (a),(d) a lossless device; (c),(d) $A = 0$ dB and $\Gamma_r = 0.2$ dB/turn; (e),(f) $A = 0.06$ dB and $\Gamma_r = 0.2$ dB/turn; (g) (h) $A = 0.06$ dB and $\Gamma_r = 1.84$ dB/turn. For all the considered loss conditions, τ_n and D_n simulations where performed for $\Delta\varphi = 0, 0.4\pi, 0.5\pi, \pi, 2\pi$, $K_r = 0.8$,

vice phase response properties for a fixed value of the losses ($A = 0.06$ dB, $\Gamma_r = 0.2$ dB/turn). In Fig. 6.14 the normalized group delay (Fig. 6.14a) and the normalized dispersion (Fig. 6.14b) of a filter with $K_r = 0.7$ and varying $\Delta\varphi$ is illustrated.

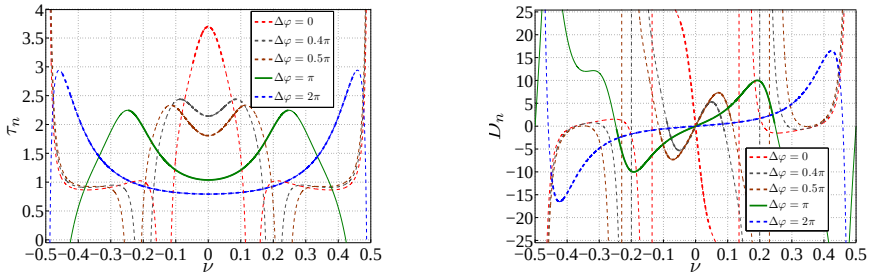

(a) (b)

Figure 6.14.: Filter Through port (a) normalized group delay τ_n and (b) normalized dispersion D_n for $\Delta\varphi = 0, 0.4\pi, 0.5\pi, \pi, 2\pi$, $K_r = 0.7$, $A = 0.06$ dB and $\Gamma_r = 0.2$ dB/turn.

Comparing these results with those obtained for $K_r = 0.8$ and the same value of the losses (Fig. 6.13e and Fig. 6.13f) one can immediately notice an increase in the dispersion and the group delay. Moreover, the general conclusions on the $\Delta\varphi$ variations still hold. It is then reasonable to expect that an increase of K_r will induce the opposite effect, reducing the filter dispersion and group delay values. This choice can be used if the calculated dispersion is expected to be particularly critical at the price of a bandwidth tunability reduction (see Section 6.3).

After describing the general features of the filter and discussing its design issues, in the next section fabrication and measurements of some devices will be presented and discussed.

6.5 FABRICATED DEVICES

The filter architecture illustrated so far has been exploited to realize devices with 200, 100 and 25 GHz FSR on the silicon platform at the base of this work. The

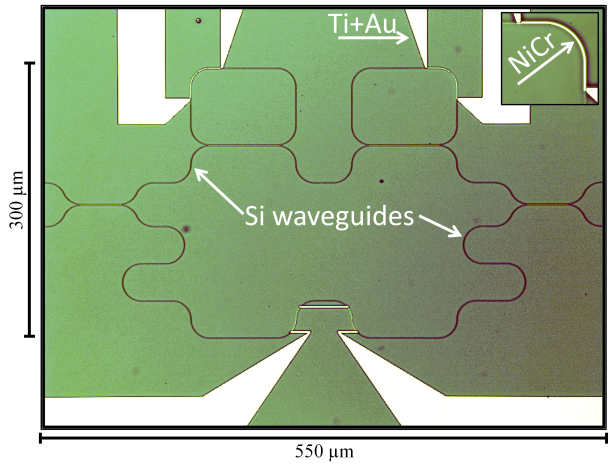

Figure 6.15.: Optical microscope photograph of a fabricated filter.

width of the realized waveguides is the standard $w = 480$ nm that provides single mode operations. The mask was designed using constant bend radii ($= 20$ μm) and constant coupler gaps in the directional couplers of the MZI and of the RRs ($= 300$ nm) both investigated in Chapter 2. In order to test the filter performance, filters with $K_r = 0.7$ were designed (i.e. with a coupler length $L_c = 55.2$ μm). An example of the fabricated structure is shown in Fig. 6.15. The design choices ensures not only negligible bending losses and good couplers gap filling but also a compact footprint size (< 0.2 mm^2 for the device in Fig. 6.15).

6.5.1 *Thermal Tuning and Fitting*

An example of the realized filters thermal tuning is shown in Fig. 6.16a for a 25 GHz FSR filter. As described in the previous analysis, the minimum bandwidth

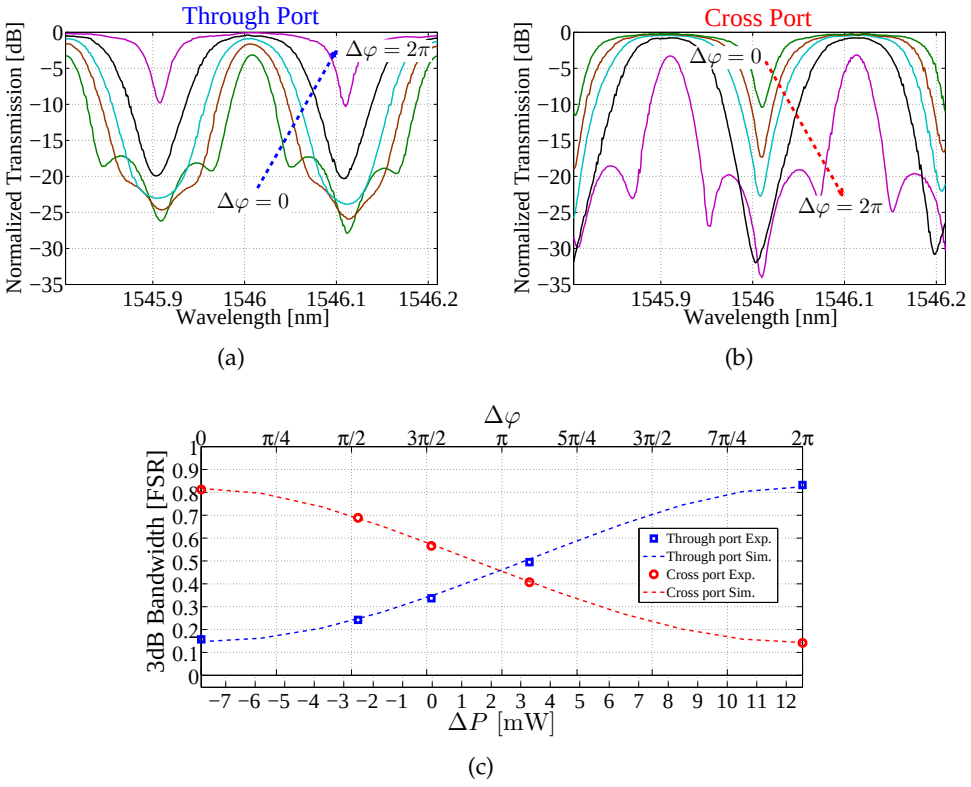

Figure 6.16.: (a) Through and (b) Cross port spectral characteristic tuning from the minimum ($\Delta\varphi = 0$) to the maximum ($\Delta\varphi = 2\pi$) bandwidth condition for a 25 GHz FSR filter with $K_r = 0.79$. At both ports, measured spectra are normalized with respect to the maximum of the filter maximum bandwidth configuration. (c) Measured and simulated 3 dB bandwidth values normalized to the FSR as a function of $\Delta\varphi$ (upper x axis) and of the required RRs power dissipated difference ΔP (lower x axis).

condition at the Through port of the filter is reached when the two RRs resonate at

the same frequencies ($\Delta\varphi = 0$) and there is a relative difference of π between the phase of the RRs and that of the MZI unloaded arm. To make the ring resonate at the same frequencies, different values of electrical power have to be dissipated over the two nominally identical RRs because of fabrication tolerances [133]. In Fig. 6.16c $\Delta\varphi = \varphi_{r2} - \varphi_{r1} = 0$ is in fact obtained for a power dissipated difference $\Delta P = P_{r2} - P_{r1} = -7.8$ mW, being respectively $P_{r2} = 8$ mW and $P_{r1} = 15.8$ mW the power dissipated over the two RRs. A power of 0.2 mW is dissipated over the MZI to obtain the minimum bandwidth at the Through port, resulting in a total power dissipated of around 24 mW. Bandwidth tuning has been then obtained cooling down one of the RRs (i.e. decreasing P_{r1}) and heating up the other (i.e. increasing P_{r2}) in a push-pull configuration to increase the value $\Delta\varphi$ up to 2π and keep constant the total power dissipated. The simulation results were obtained from fitted parameters where a RRs coupling coefficient $K_r = 0.79$, a ring loss of 1.77 dB/turn and an input/output MZI couplers value of 0.53 has been found. Note that $A = 0.06$ has been assumed in the fitting procedure. In a device with so many parameters, fitting has to be done carefully. The analysis developed in Section 6.3 is useful to distinguish between the different effects. Larger K_r brings larger bandwidth tunability together and smaller Off-band Rejections, while higher losses bring a reduction of both this figures. Values K_{c1} and K_{c2} different from 0.5 bring instead an asymmetry between the two ports characteristics that poorly affects the device bandwidth tunability. However, the same filter 3 dB bandwidth can be obtained for different $\Delta\varphi$–K_r combinations. $\Delta\varphi$ has to be then fixed in order to extract the RRs coupling coefficient and the losses with accuracy. This can be done by fitting first the filter maximum and minimum bandwidth configuration, where $\Delta\varphi$ can be assumed respectively 0 and 2π. In Fig 6.17a the $\Delta\varphi = 0$ configuration fitting is shown to be good agreement both for the Through and the Cross port.

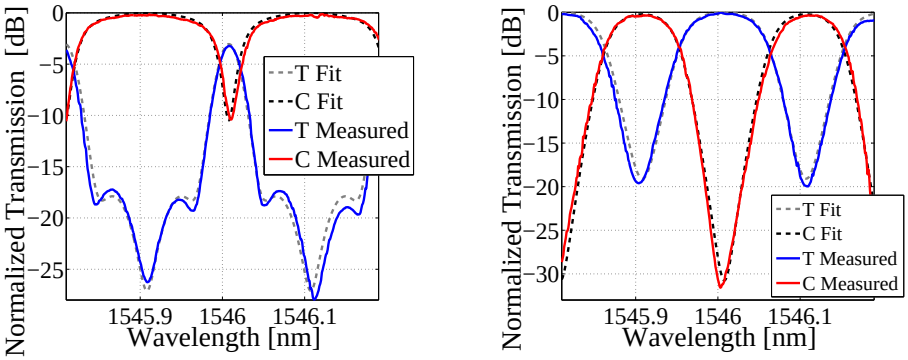

Figure 6.17.: Through port and Cross port experiment (solid curves) and fitting (dashed curves) for the 25 GHz FSR filter for (a) $\Delta\varphi = 0$ and for (b) $\Delta\varphi = \pi + \pi/25$.

Fitted K_r, γ, K_{c1} and K_{c2} can be then used varying $\Delta\varphi$ to simulate the device at different bandwidths. By comparing simulations with measurements it is finally possible to extract $\Delta\varphi$ from filter configurations different from the maximum and minimum bandwidth ones. In Fig 6.17b the measurements at the Through and the Cross port for a filter configuration close to FSR/2 are compared with a simulation preformed with the fitted parameters and $\Delta\varphi = \pi + \pi/25$. The good agreement confirms the reliability of the fitting procedure.

6.5.2 *Performance*

The previously illustrated filter through (T) and Cross port (C) performance are illustrated in the first row of Tab. 6.1, where different realized devices are compared.

To simplify the notation, the minimum bandwidth condition ($\Delta\varphi = 0$) is indicated with the letter L while the maximum bandwidth condition ($\Delta\varphi = 2\pi$) is indicated with the letter U. To obtain a 25 GHz FSR device, $L_r \approx 2.9$ mm must be designed. This implies a high value of Γ_r and, as previously described, reduced performance. However, at the Through port, the filter shows an Off-band Rejection always larger than 10 dB and an Off-band Rejection of 15 dB for the minimum bandwidth condition. The maximum bandwidth condition shows the minimum insertion loss (IL) value that is of about 2.2 dB. This value increases as the bandwidth reduces. An increase in the insertion loss (IL EXCESS) of about 3.1 dB is observed when the filter is tuned from the maximum to the minimum bandwidth condition. Bandwidth tunability is still wide, allowing to tune the device bandwidth from 21 to 4 GHz (i.e. from 83% to 16% of the FSR). For applications of this filter that require smaller 3 dB bandwidths (i.e. longer RRs cavity lengths) such as, for example, in the microwave photonics field, the losses can be easily reduced designing RRs with larger waveguides [26, 117] paying a price in term of an increased device footprint size. In this case an improvement in the performance is expected as previously discussed and illustrated in Fig. 6.11. As anticipated, similar performance can be found at the Through port. It is also noticeable that the deviation from the nominal 3 dB MZI input/output couplers condition gives rise just to small asymmetries between the Through and the Cross port performance.

The best results are obtained, as expected, for the 200 GHz filter (third row of Tab. 6.1, Fig. 6.18) because of the reduced size of L_r. The filter 3 dB bandwidth at the Through port can be tuned from 173 to 23 GHz (i.e. from 87.5% to 11.5% of the FSR) showing a low insertion loss value for all the bandwidths (maximum 1.35 for the minimum bandwidth condition). The largest improvement in terms of Off-band Rejection and Shape Factor with respect to the 25 GHz FSR filter has been obtained, in agreement with the theory, for the maximum bandwidth condition. The only consistent difference between the Through and the Cross port behaviour due

Table 6.1.: Designed and Measured Parameters of the Realized Tunable Bandwidth Filters

DESIGN			**FITTING**		**PERFORMANCE**									
FSR [GHz]	L_r [μm]	**Foot-print** [mm^2]	K_r	Γ_r [$\frac{dB}{turn}$]	**FSR [GHz]**	**PORT**	**3dB Bandwidth [% FSR]**		**IL [dB]**		**Off-band Rejection [dB]**		**Shape Factor**		P_{tot} [mW]
									IL	**EXCESS**					
							U	**L**	**U**	**L**	**U**	**L**	**U**	**L**	
25	2841.6	< 0.6	0.79	1.77	25.1	**T**	83	16	2.2	3.1	10	15	0.68	0.31	24
						C	81	14	2.2	3	10	15	0.67	0.32	
100	710.4	< 0.2	0.67	0.49	99.5	**T**	89	9	0.96	1.7	20	9.5	0.83	0.3	29.5
						C	89	8	0.98	1.6	20	9.5	0.83	0.3	
200	355.2	< 0.2	0.75	0.26	199.1	**T**	87.5	11.5	0.75	0.6	19.6	15	0.81	0.31	27.5
						C	86	10	0.75	0.9	40	14	0.81	0.29	

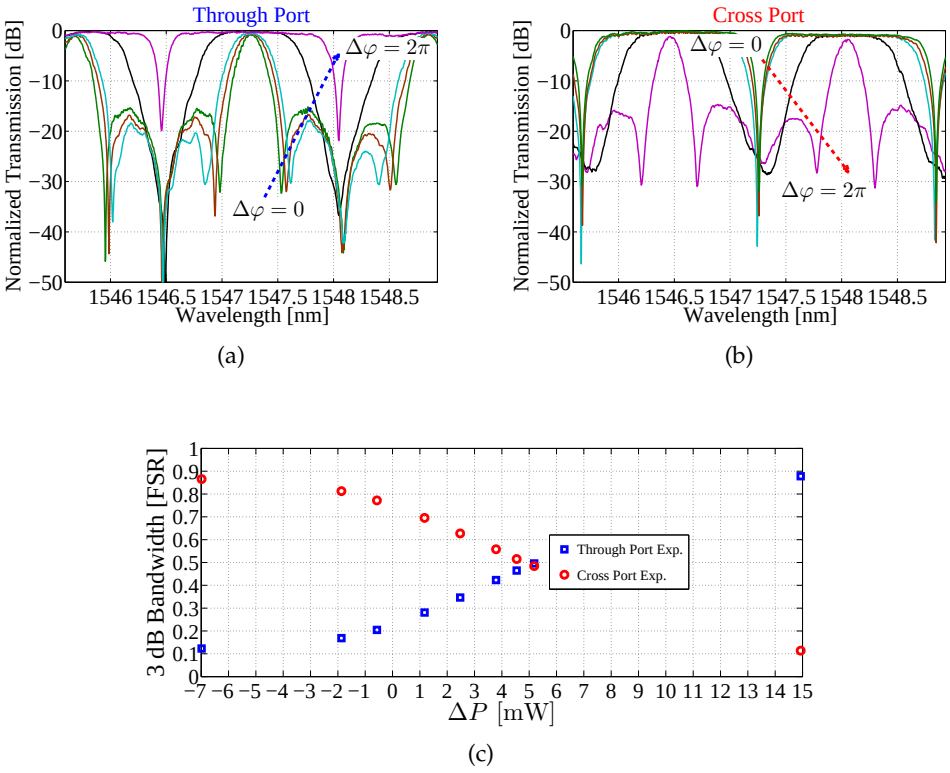

Figure 6.18.: (a) Through and (b) Cross port spectral characteristic tuning from the minimum ($\Delta\varphi = 0$) to the maximum ($\Delta\varphi = 2\pi$) bandwidth condition for a 200 GHz FSR filter with $K_r = 0.75$. (c) Measured and simulated 3 dB bandwidth values normalized to the FSR as a function of $\Delta\varphi$ (upper x axis) and of the required RRs power dissipated difference ΔP (lower x axis).

to $K_{c1} = 0.52$ and $K_{c2} = 0.49$ concerns the maximum bandwidth condition Off-band Rejection. This figure is however evaluated with respect to the filter minima and thus does not represent a major performance variation as it is clear in Fig. 6.18. Note that, in this case, the mapping between $\Delta\varphi$ and ΔP was not possible (Fig. 6.18c) as in the 25 GHz case (Fig. 6.16c). Bandwidth tunability become less sensitive to $\Delta\varphi$ (i.e. ΔP) variations as the minimum and the maximum bandwidth conditions are approached. ΔP variations in the order of 1 mW induce negligible changes in the 3 dB bandwidth but make impossible to directly map $\Delta\varphi$ over ΔP with accuracy. For this filter, also the cross talk levels averaged over the 1 dB Through port bandwidth have been calculated. Maximum values can be found approaching the minimum bandwidth condition (i.e. -11.1 dB in this particular case). Increasing the bandwidth this value decreases too, being equal to -16.3 dB when the Through port 3 dB bandwidth is about FSR/2 (black trace, Fig. 6.18a) and equal to -17.4 dB in the maximum bandwidth condition.

Finally, we can notice from the 100 GHz FSR filter (second row of Tab 6.1) that wider bandwidth tunability (from 89% to 9% of the FSR) can be obtained with a

smaller value of K_r (i.e. 0.67). However, in this case, the Off-band Rejection at the minimum bandwidth condition becomes lower than 10 dB. Finally it can be noticed that the reduced number of actuators required by the proposed geometry allows a low electrical power consumption (i.e. the total dissipated power P_{tot} is always lower than 30 mW).

The filter central wavelength $\lambda_0 = c/f_0$ can be also tuned. Adding the same positive (negative) phase φ_0 to the three phase shifters it is possible to obtain a red (blue) shift of λ_0 and thus span the whole FSR. This can be done increasing (reducing) by the same amount the power dissipated over the three phase shifters of the device. In Fig. 6.19 the tuning over the whole FSR has been measured for the device with 200 GHz FSR keeping the 3 dB bandwidth always around 44 GHz (i.e $\Delta\varphi$ between $\pi/2$ and $2\pi/5$). As shown in Fig. 6.19b, 60 mW are required to cover

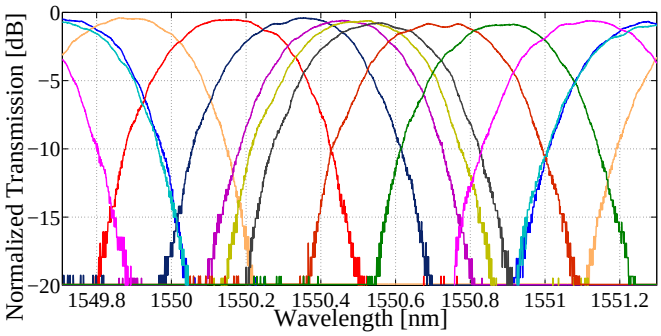

(a)

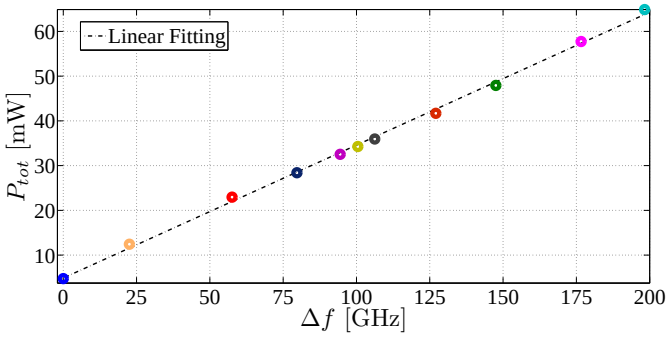

(b)

Figure 6.19.: (a) Central wavelength tuning of a 44 GHz 3 dB bandwidth filter with 200 GHz FSR and (b) corresponding total power dissipated (P_{tot}) versus the frequency shift (Δf).

the whole FSR (i.e. 3.3 GHz/mW or 0.017 FSR/mW). An average of 20 mW is in fact required by the fabricated actuators to add a 2π shift to each phase shifter.

6.5.3 *Design versus Experiments*

During the overview of the realized devices performance, some variability has been shown to occur in the coupling coefficient values of nominally identical devices while, in Section 6.3, it had been highlighted through simulations that the presented device should be robust against coupling coefficients and losses variations. In this Section this property will be verified taking into account the 25 GHz and the 200 GHz FSR filters.

All the presented devices were designed with $K_r = 0.7$ and $K_{c1} = K_{c2} = 0.5$ considering typical propagation losses 3 dB/cm and typical coupler losses $A = 0.06$ dB/cm (i.e. $\Gamma_r = 0.17$ dB/turn for a 200 GHz FSR filter and $\Gamma_r = 0.91$ dB/turn for a 25 GHz FSR filter).

The realized devices show propagation losses of about 6 dB/cm, twice as large as the design value taken into account. In a more compact device like the 200 GHz FSR filter this brings just a 0.09 dB/turn increase of Γ_r with respect to the design. From the analysis carried out in subsection 6.3.4 it is then reasonable to expect a small detrimental impact on the realized filter performance respect to the design. The 25 GHz FSR filter shows instead about 0.9 dB/turn increase with respect to the design. Such an increase in the round trip losses may bring large differences between the target and the measured spectra (see subsection 6.3.4).

Taking first into account the 200 GHz FSR filter, we measured a $K_r = 0.75$ (see third row of Table 6.1). This increased value together with the larger value of propagation losses cause a reduced bandwidth tunability of 5% FSR with respect to the design. It is now interesting to see how this parameter variation affects the filter behaviour for bandwidth conditions different from the minimum and the maximum one. Fig. 6.20 shows the comparison between measurements and design for the 40 GHz (Fig. 6.20a) and the 100 GHz (Fig. 6.20b) filter configuration. For both

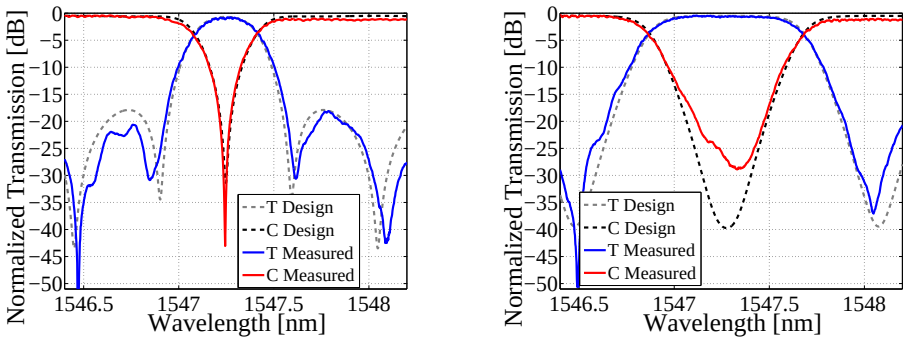

Figure 6.20.: Desing versus experiment for the 200 GHz FSR filter for (a) 40GHz 3dB bandwidth configuration and for (b) 100GHz 3dB bandwidth configuration.

examples the difference between experiment and design are negligible and the filter robustness is thus confirmed.

Considering the 25 GHz FSR filter, we measured $K_r = 0.79$ (see first row of Table 6.1). The differences between design and experiments for the round trip losses are larger than in the 200 GHz FSR case. Less agreement between expected and measured characteristics can be foreseen. Bandwidth tunability is in fact now reduced by about 10% FSR. Considering then the 6 GHz configuration (Fig. 6.21a) one can notice as expected that the filter shape is substantially different from the design. The performance is however still in agreement with that of the design. Increasing

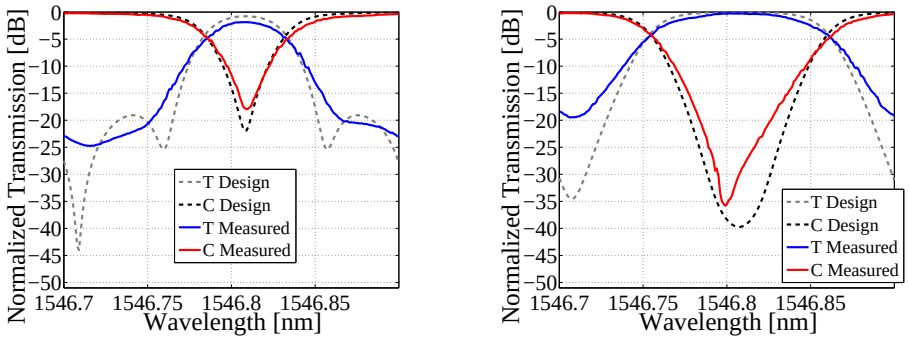

Figure 6.21.: Desing versus experiment for the 25 GHz FSR filter for (a) a 6 GHz 3 dB bandwidth configuration and for (b) a 6 GHz 3 dB bandwidth configuration.

the filter bandwidth to 12.5 GHz (Fig. 6.21b) we can notice that the major difference does not concern the Shape Factor but the filter Through port Off-band Rejection that is limited by the realized input/output MZI coupler values. The value of this figure is still however at about 20 dB. This confirms again that the presented filter is robust against variations between designed and realized coupling coefficients and loss values.

6.5.4 *RRs Coupling Coefficient Disorder Effects*

Until now, almost all the filter parameter effects on the studied filter itself have been analysed. The RR coupling coefficient K_r has however always been considered identical for the two rings to make the design not too heavy. In this subsection the disorder of this parameter value will be discussed through realized devices examples and a low sensitivity of the proposed device to this effect will be shown.

The difference in the two RRs K_r induces an asymmetry in the filter transfer function with respect to f_0 if φ_{mz} is kept equal to π. This effect cannot be observed at the minimum and the maximum bandwidths since the RRs resonate at the same wavelengths. For this configuration, the transfer function is that of a filter with a K_r

that is the average between the two RRs K_r. Fig. 6.22 shows the tuning of a 100 GHz FSR filter where the two K_r differs of about 7% (i.e. $K_{r1} = 0.74$ and $K_{r2} = 0.67$) that represents one of the largest variations registered for nominally identical couplers placed side by side on the chip during this work.

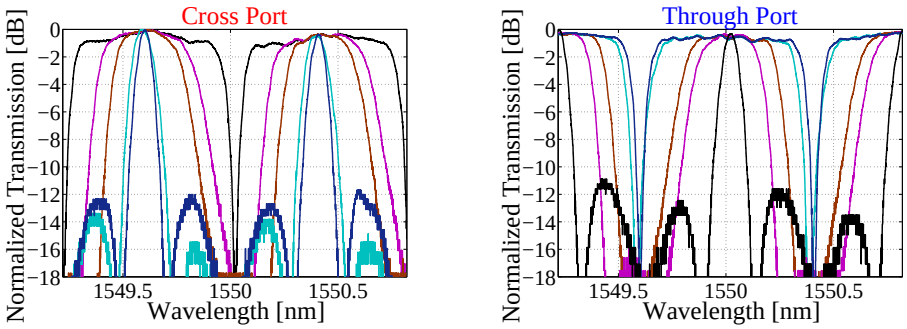

Figure 6.22.: (a) Cross port and (b) Through port 3 dB bandwidth tuning (i.e. $\Delta\varphi$ from 0 to 2π) of a 100 GHz FSR filter with $K_{r1} = 0.74$ and $K_{r2} = 0.67$.

The filter tuning has been performed, as previously described, varying $\Delta\varphi$ from 0 to 2π and keeping the MZI phase aligned with the resonances of the RRs (i.e. $\varphi_{mz} = \pi$). The only difference is that now every trace is normalized with respect to its own maximum. At the minimum and maximum bandwidth, a symmetric behaviour with respect to λ_0 of the filter characteristics can be observed. In this case, the fitted value of K_r is equal to 0.705. This value is in turn the average between the two different K_r. Increasing the value of $\Delta\varphi$, the asymmetry with respect to λ_0 becomes noticeable but it is not dramatic. Moreover, the MZI phase, if required, can be set in order to make symmetric one of the characteristics at one port and more asymmetric the other one. It is then possible to conclude that this kind of filter is also robust to the disorder in the RRs coupling coefficient values.

6.5.5 *Comparison with the state of the art*

So far the filter performance have been investigated through the characterization of the fabricated filters (see Tab. (6.1)). Large bandwidth tunability, together with good Off-band Rejection values have been obtained for all the devices with just three actuators. It is now interesting to compare the presented results with that reported in literature. Tab. (6.2) shows the most recent multi-element SOI tunable filters together with the 200 GHz and the 25 GHz FSR filter presented in this work, respectively the best and the worst performing filter characterized so far. This table lists the figures of merit analysed during this work: bandwidth tunability, Off-band Rejection, Shape Factor and Insertion Loss. Moreover, the number of actuators

Table 6.2.: Recent Multi-element Silicon Tunable Filters

	PERFORMANCE						
	Filter Order	3dB **Bandwidth** [GHz]	**FSR** [GHz]	**IL** [dB]	**Off-band Rejection** [dB]	**Shape Factor**	**Number of Actuators**
Rasras et al. (2007) [111]	4	$0.8 - 2.4$	16.5	< 6 dB	> 25 dB	$0.35^{\dagger}$	10
Ibrahim et al. (2010) [26]	1	$0.4 - 2$	10	14 (EXCESS)	> 30	n.a.	8
Alipour et al. (2011) [114]	4	$0.9 - 5$	650	$2.5 - 7.5$	> 38	n.a.	18
Ding et al. (2011) [186]	2 Add Drop RR + MZI	$58 - 110$	1000	15	30	$0.32 - 0.47$	4
This Work ($2012 - 2013$)	3	$23 - 173$	200	$0.75 - 1.35$	$15 - 20$	$0.31 - 0.81$	3
This Work ($2012 - 2013$)	3	$4 - 21$	25	$2.2 - 5.3$	$10 - 15$	$0.31 - 0.68$	3
Ong et al. (2013) [184]	10	$11.6 - 125$	900	2.8	100	n.a.	10

†: Referred to the filter configuration with a 3 dB bandwidth of 1 GHz and calculated from the ratio between the 3 dB and the 25 dB bandwidth.
n.a.: Not available.

necessary to exploit the filter tunability is considered instead of the total electrical power dissipated. This figure allows in fact a more general comparison between different devices, being the amount of power dissipated strictly dependent on the actuator technology. The reduced complexity in the control of the characterized filters (fifth and sixth row of Tab. (6.2)) with respect to the other proposed solutions is immediately noticeable.

Regarding the other device figures of merit, the 200 GHz FSR filter (fifth row of Tab. (6.2)) shows the largest bandwidth tunability together with the smallest Insertion Loss and Shape Factor values in line with the other devices. These performance together with simple control of the device comes however at a price of the lowest, although still good, values of the Off-band Rejection. It can be in fact noticed that the tunable bandwidth filter presented in this work is the lowest order filter.

Focusing on bandwidth tunability, the first three rows of Tab. (6.2) report the performance of three filters designed to operate with variable bandwidths between hundreds of MHz and few GHz. The geometry presented in this work can be easily scaled down to operate in this bandwidth range as previously discussed in subsection 6.5.2 by increasing L_r and the RRs waveguide width. This allows to keep the losses low as implemented in [111] and [26] (i.e. first and second row of Tab. (6.2)) at the cost of the device footprint increase. In this case, performance similar to the solution already presented in literature are then expected.

Having demonstrated the valuable performance of the studied device compared to the most recent multi-element tunable SOI filter, it can be know pointed out that by adding a control on the RRs coupling coefficients could further improve the filter functionality at the price of a small increase in the device control complexity. The realization of this solution is illustrated in the next section.

6.5.6 *Full Control via Tunable Couplers*

The proposed tunable bandwidth filter has shown a good performance that can be tailored through the suitable selection of the RRs coupling coefficient during the design process. The active control of K_r would allow the full control over the filter functionality shown in the maps of Fig. 6.5 as well as to correction of the unavoidable fabrication tolerance effects, adding another degree of freedom to the device reconfigurability. This allows better adapting the characteristics of the filter to a variation in the system requirements.

To demonstrate both the possibility of obtaining this desirable feature and the functionality of the tunable couplers presented in Chapter 3, a filter with $K_r = 0.95$ (i.e. $L_c = 72.5$) and 25 GHz FSR without changing the geometry illustrated so far has been realized with the cited coupling control. A schematic of the proposed filter with tunable couplers is shown in Fig. 6.23a, where K_r is shown as a function of P_{TC}. The value of K_r can be reduced detuning the directional coupler by increasing the

electrical power dissipated over the heater P_{TC}. When the two tunable couplers are switched off, the filter shows bandwidth tunability from about 70% to 28% of the FSR, Shape Factor values between about 0.53 and 0.28 and the Off-band Rejection is larger than 16 dB for every filter configuration.

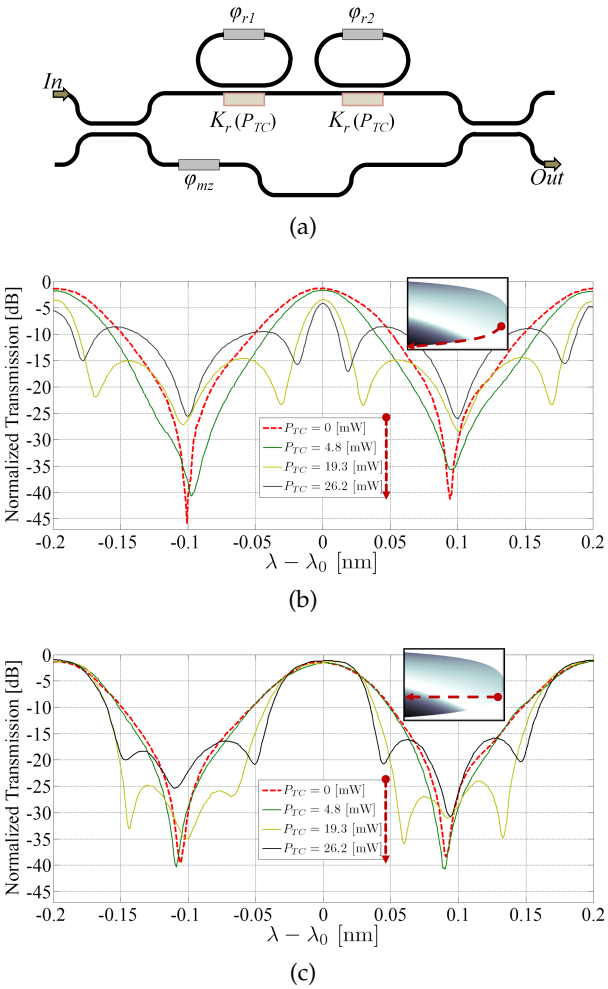

Figure 6.23.: (a) Schematic diagram of the tunable filter with tunable coupling sections. The RRs coupling coefficient K_r is illustrated as a function of the dissipated power on the tunable coupler P_{TC}. (b) Filter Cross port characteristic variation due to RRs couplers detuning (i.e. increasing values of P_{TC}) maintaining $\Delta\varphi = 2\pi$ (minimum bandwidth condition). (c) 7 GHz 3 dB bandwidth filter for different values of P_{TC} (and thus K_r) obtained slightly adjusting the value of $\Delta\varphi$ for each case. Insets in (b) and (c) show the Off-band Rejection map of Fig. 6.5a with the red dashed lines to evidence qualitatively the locus of the filter working points.

The filter Cross port minimum bandwidth condition ($\Delta\varphi = 2\pi$) for $P_{TC} = 0$ is illustrated by the dashed line in Fig. 6.23b. Keeping $\Delta\varphi = 2\pi$ fixed and increasing P_{TC}, it is possible to reduce the minimum bandwidth from 7 to 1.8 GHz. This corresponds to a $\sim 35\%$ reduction of K_r obtained with a maximum $P_{TC} = 26.2$ mW.

Referring to the maps of Fig. 6.5, this moves the filter working point along the minimum bandwidth edge (the lower one). This variation is qualitatively depicted by the red dashed line in the inset of Fig. 6.23b over the Off-band Rejection map of Fig. 6.5a.

Full control over the maps of Fig. 6.5 can be then demonstrated maintaining the same 3 dB bandwidth of the filter and changing its spectral characteristics. For example in Fig. 6.23c the same bandwidth has been maintained around 7 GHz (e.g. 0.28 FSR) for each configuration of the tunable couplers, adjusting the value of $\Delta\varphi$. The Shape Factor increases from 0.28 to 0.49 while the Off-band Rejection decreases from 38 to 15 dB. Referring to the maps of Fig. 6.5 this moves the filter working point over the horizontal line defined by the value of the 3 dB bandwidth equal to 0.28 FSR. This variation is again qualitatively depicted in the inset of Fig. 6.23c over the Off-band Rejection map of Fig. 6.5a. The price to pay to obtain the full control over the device is an increase in the overall power consumption. This value can be reduced if lower K_r tunability is required (e.g. to counteract fabrication tolerance effects) and asynchronous couplers are designed (see Chapter 3).

Up until now the filter behaviour has been discussed considering the spectral response around the central frequency. It may be questioned if the filter can be used also in cases, such as WDM, where multiple carriers are present at the same time. The next subsection will discuss this situation showing that the filter can be successfully applied in this case too, allowing different operations.

6.5.7 *Multiple Bandwidths Simultaneous Tuning*

In WDM systems one can face different needs: for example, depending on the chosen FSR, that of filtering periodically spaced subset of carriers (interleaver function) or that of selecting a single subset of carriers. This two functionality are schematically depicted respectively in Fig. 6.24a and Fig. 6.24b for a WDM system with 12 channels and a fixed grid spaced of Δf_{ch}. T and C stand for the Through and the Cross port respectively and the filter responses have been drawn with an ideal box-like shape.

Considering the first case, the use of the 200 GHz FSR filter with 3 dB bandwidth tunable from 23 to 173 GHz, would enable the periodic selection from 1 to 7 channels from a 25 GHz spacing Dense WDM optical system. In this case the device should select the same number of channels in the same way, no matter of the central frequency.

This is in effect possible as shown by Fig. 6.25a where the spectral response of the 200 GHz FSR filter over 20 nm wavelength span is plotted for three bandwidth conditions ($\Delta\varphi = 0, \pi, 2\pi$). The filter bandwidth is correctly tuned for all the passbands once the required filter configuration is selected for one wave-

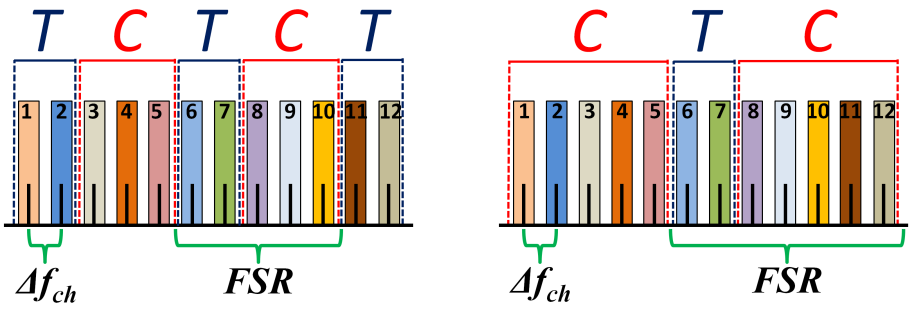

(a) (b)

Figure 6.24.: Sketch of a WDM system with 12 channels and a fixed grid spaced of Δf_{ch}: (a) Periodically spaced subset of carriers filtered (interleaver function). (b) Single subset of carriers filtered. *T* and *C* represents the Through and the Cross port respectively and the filter responses are depicted with a box-like shape.

length ($\lambda_0 = 1547.26$ nm in the considered case). This is shown more clearly in Fig. 6.25b where the 3 dB bandwidth at the minimum and at the maximum condition are plotted showing small variations across the considered 20 nm wavelength span. The minimum bandwidth varies from 21.4 GHz at $\lambda_0 = 1540.95$ nm to 27.7GHz at $\lambda_0 = 1560$ nm. The maximum deviation with respect to the value at $\lambda_0 = 1547.26$ nm is then of 4.7 GHz, that corresponds to 2.4% of the FSR. The maximum bandwidth varies instead from 175.8 GHz at $\lambda_0 = 1540.95$ nm to 170.4 GHz at $\lambda_0 = 1558.42$ nm. The maximum deviation with respect to the value at $\lambda_0 = 1547.26$ nm is then of 2.8 GHz, corresponding to 1.4% of the FSR. This change occurs because of the directional couplers' wavelength dependence ($\sim 6\%$ of absolute variation over the considered span). This impacts also on the Off-band rejection values as shown in Fig. 6.25c where the value of the minimum Off-band rejection varies for both bandwidths. This value is however maintained to be always larger than 15.7 dB for the maximum bandwidth ($\Delta\varphi = 2\pi$, blue dashed dotted curve of Fig. 6.25a) and 11 dB for the minimum one ($\Delta\varphi = 0$, red dashed curve of Fig. 6.25a). For the minimum bandwidth the optimum value is at the design wavelength and degrades far from it by about the same amount mainly because of the phase tuning which has been optimized for the central wavelength. The larger the bandwidth the less it is affected by this effect. The maximum bandwidth off-band rejection in fact varies monotonically, mainly because of the wavelength dependence of the filter couplers.

In the other previously mentioned case, where a single passband is to be used to select the desired WDM channels, a much larger FSR than the one presented in this work would be required. Silicon ring resonators with a few microns bending radius and FSR with more than 2 THz [19] can be exploited for the realization of

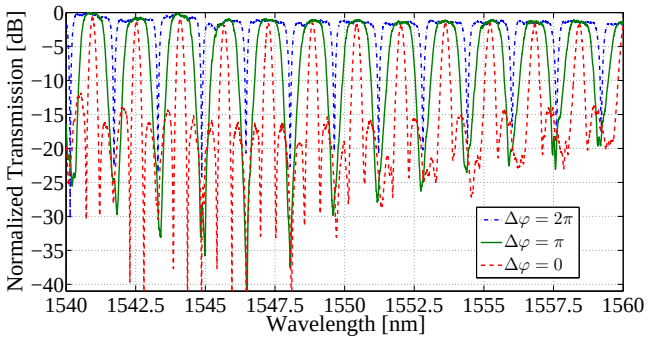

(a)

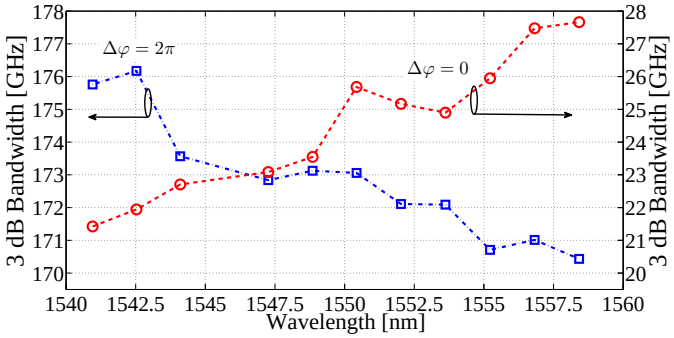

(b)

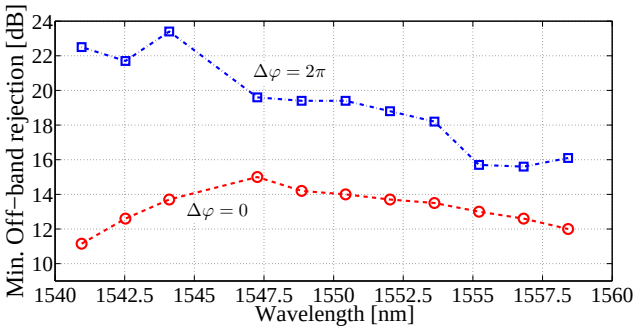

(c)

Figure 6.25.: (a) 200 GHz filter Through port spectra over 20 nm wavelength span. (b) 3 dB bandwidth and (c) Off-band Rejection variation over the analysed wavelength span for the minimum ($\Delta\varphi = 0$) and the maximum ($\Delta\varphi = 2\pi$) bandwidth condition.

the proposed architecture. With this design choice tunability from 200 GHz to 1.8 THz is expected.

The simultaneous presence of many channels may lead to high values of aggregate optical power. In this case, nonlinear effects with a negative impact on device behaviour can arise. The next subsection will address this issue.

6.5.8 *Impairments due to nonlinear effects*

The dominant non linear phenomena in silicon devices are two-photon absorption (TPA) and free-carrier absorption (FCA) [189] which cause an intensity-dependent extra-loss and refractive index change. Free carrier recombination generated by TPA [190] induces a local heating of the waveguide that depends on the local optical power. This thermal effect produces an increase of the refractive index and can alter the behaviour of RRs based optical filters. The local power inside the resonators is in fact enhanced with respect to the device waveguides (see Section 2.3). Different red shifts are then induced, causing a distortion of the filter characteristic which is not simply a rigid shift [59]. In the following it will be shown that the proposed device, being based on resonators with a small value of the enhancement factor (i.e. strongly overcoupled resonators), is robust against TPA induced distortions.

Fig. 6.26 shows the spectral characteristics at the two ports of the 200 GHz FSR filter of Tab. 6.1 for $\Delta\varphi = 0$, obtained through single source measurements for increasing values of the optical power on chip P_{in} (see Section 1.5 for more details about the measurement setup). Measuring both the Through port (Fig. 6.26a) and

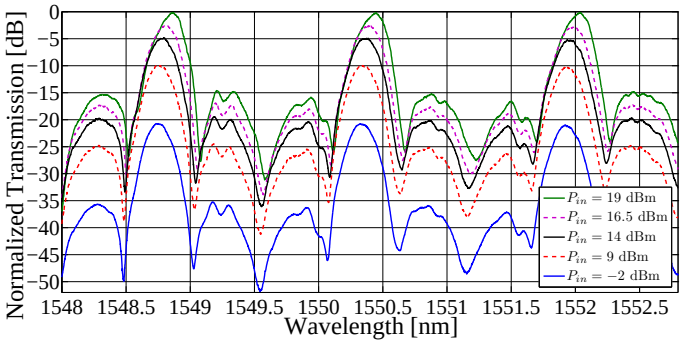

(a)

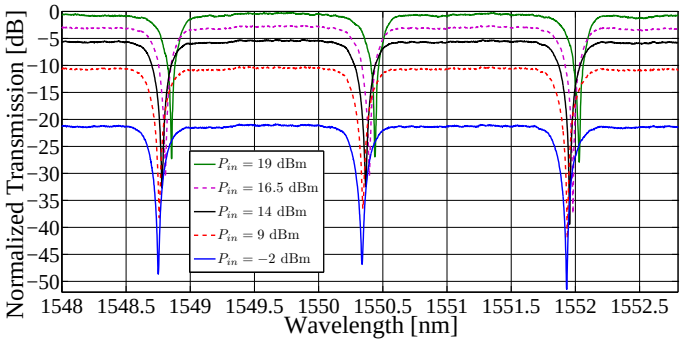

(b)

Figure 6.26.: 200 GHz FSR filter (a) Through port characteristic and (b) Cross port characteristic for $\Delta\varphi = 0$ and increasing values of the optical power P_{in} on the chip.

the Cross port characteristics (Fig. 6.26b) one can evaluate the minimum and the

maximum bandwidth filter configuration with the same exact value of P_{in}. The filter RRs power enhancement factor is about 3 (i.e. the local power inside the RRs is ~ 4.8 dB higher than P_{in}).

TPA effects start to be appreciated for $P_{in} > 9$ dBm. The difference between the filter characteristics for $P_{in} = -2$ dBm (blue solid traces in Fig. 6.26) and for $P_{in} = 9$ dBm (red dashed traces in Fig. 6.26) are in fact negligible. For $P_{in} = 14$ dBm (black solid traces in Fig. 6.26), an almost rigid shift of around 30 pm occurs. This value is less than 1/5 of the minimum filter 3 dB bandwidth and can be then considered negligible as it appears also from Fig. 6.26, looking at the difference between the black solid line and the blue solid line. For $P_{in} = 19$ dBm the different shifts between the RRs resonances and the MZI waveguides slightly distort the filter response at the Through port (green solid line in Fig. 6.26a). The Cross port characteristic, due to the larger value of the bandwidth, is instead more robust and shows an almost rigid shift of around 110 pm. Moreover a maximum of just 0.22 dB of extra-losses due to the TPA has been detected.

We can then conclude that the characterized filter is just slightly affected by impairments due to TPA/FCA for values of the aggregate optical power in a WDM system up to 19 dBm. Moreover, we showed that the bigger is the bandwidth the less the filter is sensitive to nonlinear effects. It is thus reasonable to expect from devices with the same geometry but bigger FSR to be even more robust. Note also that the TPA/FCA induced effect is thermal and can be easily compensated as shown in [191] if more channels and consequently higher aggregate power enters the filter.

To test the TPA/FCA effect on filters that operates on smaller bandwidths we have performed the same experiments for the 25 GHz FSR filter of Tab. 6.1. Results are illustrated in Fig. 6.27 where, as before, the Through port (Fig. 6.27a) and the Cross port (Fig. 6.27b) characteristics are reported when $\Delta\varphi = 0$ is set. The power enhancement factor of the filter RRs is around 2 (i.e. the local power inside the RRs is ~ 3 dB higher than P_{in}).

TPA effects starts to be visible as before for $P_{in} > 9$ dBm. At $P_{in} = 14$ dBm (black solid traces in Fig. 6.27) the characteristics of the filter are almost rigidly shifted of around 17 pm. The value of this shift is more than a half of the minimum 3 dB bandwidth and consequently cannot be considered negligible. The filter starts to be slightly distorted in the minimum bandwidth condition at $P_{in} = 16.5$ dBm (violet dashed trace in Fig. 6.27b) while the distortion is clearly visible for both filter configuration at $P_{in} = 19$ dBm (green solid traces in Fig. 6.27). With this optical power on chip a shift of about 54 pm is registered for the Cross port characteristic nulls and the Through port characteristic absolute maximum. The same maximum induced extra-loss as in the 200 GHz FSR device has been observed. Comparing the described results with the ones obtained for the 200 GHz FSR filter it is clear that TPA/FCA induced detrimental effects affects more filters that works with smaller bandwidths. The same induced shift become in fact more important as the band-

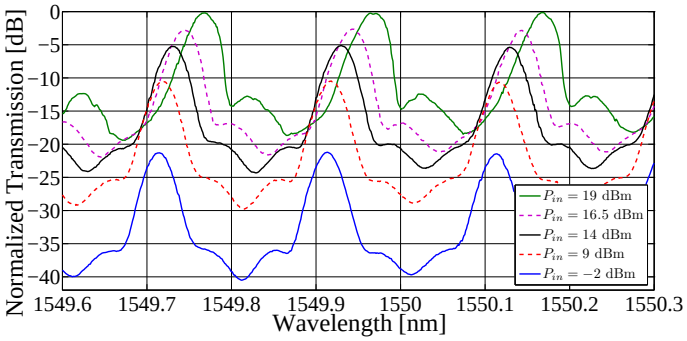

(a)

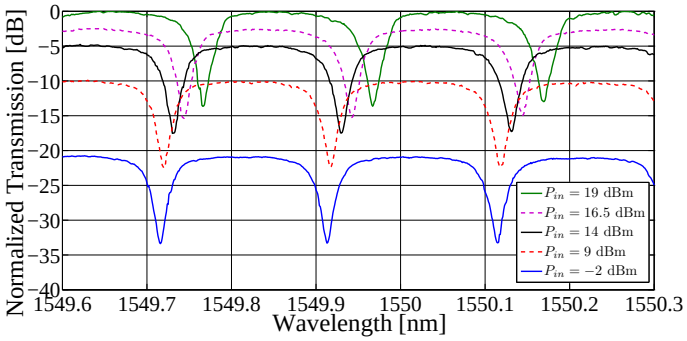

(b)

Figure 6.27.: 25 GHz FSR filter (a) Through port characteristic and (b) Cross port characteristic for $\Delta\varphi = 0$ and increasing values of the power on chip P_{in}.

width and the FSR decreases. The impairment is however still not dramatic for the considered case, confirming the filter robustness. Moreover, as it has been previously discussed, it can be easily compensated.

The intensity behaviour of our filter has been deeply investigated so far while the phase behaviour has been only illustrated in the design section of this chapter. To complete the analysis of the proposed device BER measurements of a nonreturn-to-zero (NRZ) on-off keying (OOK) modulated signal transmission through our filter have been performed and will be discussed in the next Section.

6.5.9 *BER measurements*

In order to perform BER measurements, the set-up presented in Section 1.5 has been exploited. The optical signal-to-noise ratio (OSNR) was controlled and evaluated over 0.2 nm at the chip input, by cascading a Variable Optical Attenuator (VOA), an Erbium Doped Fiber Amplifier (EDFA) and a 0.2 nm 3 dB bandwidth filter centred at the signal central frequency. The receiver is a 10 GHz bandwidth avalanche photodiode.

To evaluate the impact of the proposed device on the transmission of an optical signal, we measured the BER of a 10 Gbit/s NRZ OOK data stream ($2^7 - 1$ pseu-

dorandom bit sequence) after transmission through the Cross port the tunable filter with a 25 GHz FSR (first row of Tab. 6.1). Fig. 6.28a shows the measured BER versus the received power P_r for decreasing bandwidth of the filter, when the OSNR is 23 dB. Eye diagrams of Fig. 6.28b show that the bandwidth of the filter can be

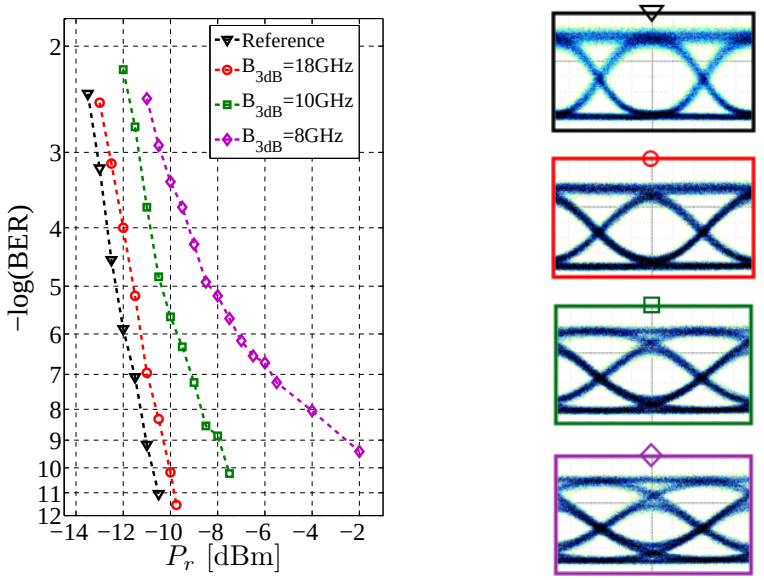

Figure 6.28.: (a) BER measurements (marks) of a 10 Gbit/s NRZ OOK signal filtered by a 25 GHz FSR device with three different 3 dB bandwidths: 18 GHz (red circles) 10 GHz (green squares) 8 GHz (magenta diamonds). Black triangles show the BER measured after propagation through a 5-mm long silicon waveguide. (b) Eye diagrams for the different conditions.

reduced down to 10 GHz (squares) without significantly deteriorating the signal quality. In this condition, the power penalty with respect to the 18 GHz bandwidth condition (circles) is about 2 dB at a BER of 10^{-9}. Above 18 GHz bandwidth, no appreciable power penalty is observed compared to the reference waveguide.

In order to test whether the signal degradation in the narrower band conditions is due to sideband filtering rather than to phase distortion, numerical simulations with the fitted filter parameters have been performed. Two types of simulations have been done: the first with the complete filter characteristic, the second just with the filter amplitude characteristic. The latter will be addressed as NO PHASE. In Fig. 6.29 the measured (left column) and the simulated (central and right column) eye diagrams of the filtered 10 Gbit/s OOK NRZ signal for different filter 3 dB bandwidths are shown. There is a good agreement between the measured eye diagrams and the simulated ones of the complete filter characteristic (amplitude and phase). This confirms the reliability of the fitting procedure also with reference to the phase

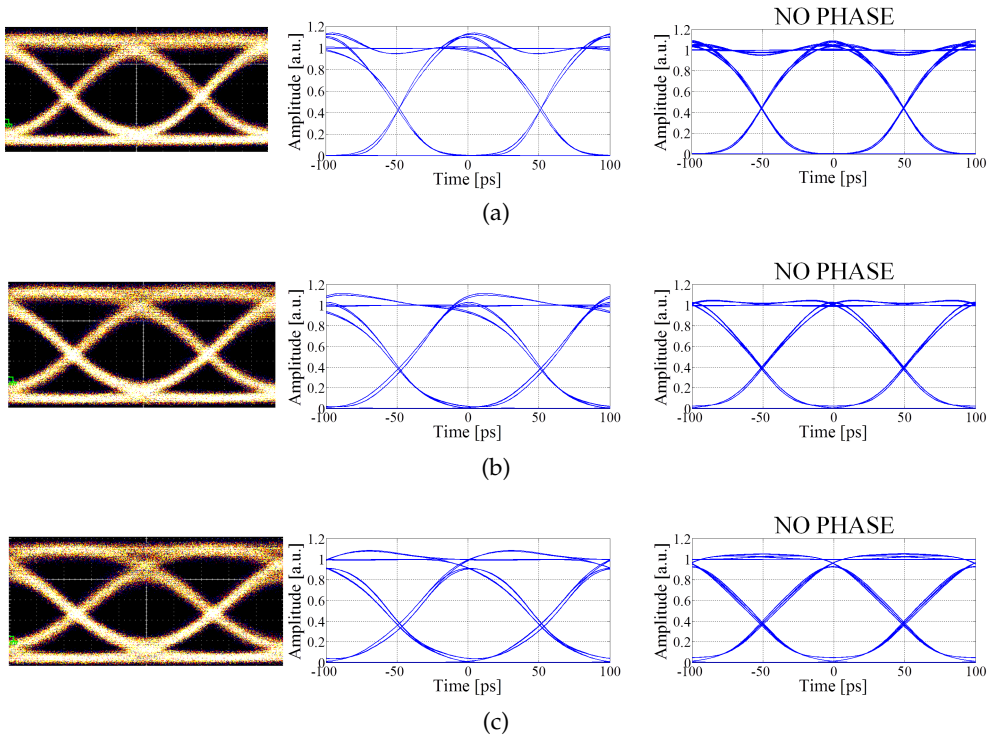

Figure 6.29.: Measured (left column) and simulated (central and right column) eye diagrams of a 10 Gbit/s NRZ OOK signal filtered with the 25 GHz filter Cross port haveing 3 dB bandwidth: (a) 18 GHz, (b) 12 GHz and (c) 10 GHz.

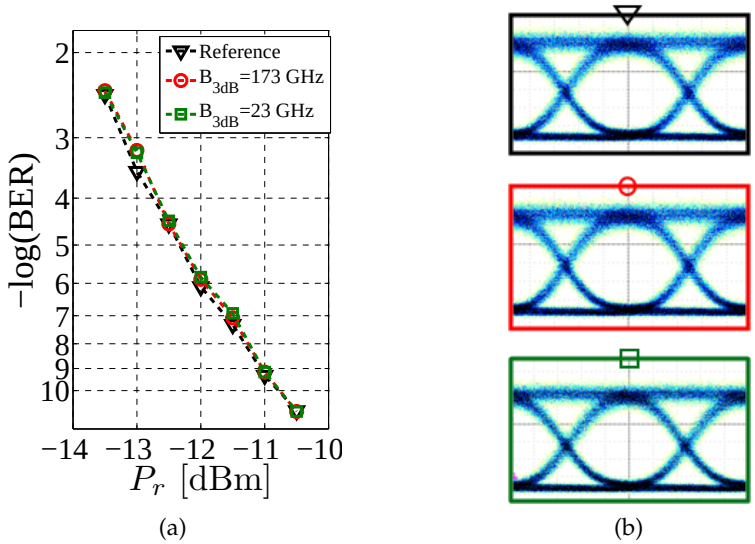

Figure 6.30.: (a) BER measurements (marks) of a 10 Gbit/s NRZ OOK signal filtered by the 200 GHz FSR device with two different 3 dB bandwidths: 173 GHz (red circles) and 23 GHz (green squares). Black triangles show the BER measured after propagation through a $5-$ mm long silicon waveguide. (b) Eye diagrams for the different conditions.

of the filter. Moreover, due the slight difference between the simulations performed with the entire filter characteristic and the NO PHASE ones, it is reasonable to expect that sideband filtering is the main responsible for signal distortion.

The performance of the 200 GHz FSR filter (third row of Tab. 6.1) at the Through port was also checked on the same signal. Results in Fig. 6.30 show the BER of the received signal when the filter is tuned to the maximum (173 GHz, red circles) and the minimum bandwidths (23 GHz, green squares) conditions. As in Fig 6.28 black triangles show the reference BER measured after propagation through a 5 mm long silicon waveguide. Since the bandwidth of the filter is much larger than the signal bandwidth, no power penalty is detected in any bandwidth condition as expected.

6.6 CONCLUSIONS

In conclusion, an extensive analysis of a compact silicon photonic passband filter with widely tunable bandwidth has been carried out in this Chapter. The circuit approach allowed to provide design rules that takes also into account fabrication tolerances as well as propagation losses variability. The measured results have shown to be in agreement with the expected performance, demonstrating the feasibility of the design procedure.

It has been shown theoretically and experimentally that wide bandwidth tunability (from about 90% to 10% of the device FSR) can be obtained maintaining the Off-band Rejection always larger than 15 dB for devices with a footprint size always smaller than 0.6 mm^2. Simple control and consequently low power consumption are allowed by only three actuators. This performance has been shown to be valuable also in comparison with the most recent silicon reconfigurable filters proposed in literature. The filter central wavelength can be also easily tuned over the whole FSR by adding a maximum of 60 mW of dissipated power. The filter robustness against fabrication tolerance effects as well as against the losses, makes it suitable for the SOI platform.

Since the filter principal figures of merit depend on the resonator coupling coefficient and a trade-off is generally needed, filters with the tunable coupler BB developed in Chapter 3 have also been realized maintaining the geometry unchanged. In this way, the full control over the device characteristics at the cost of a reasonable increase in the power dissipated has been demonstrated. The filter can be simultaneously tuned over 20 nm of the C-band and relying on strongly coupled resonator it has been shown to be robust against TPA/FCA effects. BER performance of a 10 Gbit/s OOK NRZ signal was also checked after propagation through the 200 GHz and the 25 GHz FSR tunable filer, showing that when signal degradation is detected, this is mainly due to sideband filtering rather than dispersion.

The presented characteristics make this filter suitable for flexible WDM system to select channel subsets or to adapt its characteristics to the channel requirements.

CONCLUSIONS AND FUTURE WORKS

This thesis has dealt with the design and the characterization of novel reconfigurable SOI devices able to filter and route optical signals on-chip. The chosen approach for the design was based on basic circuit elements (Building Blocks, BBs). This approach, well assessed in electronics and only recently introduced in optics, uses a functional description of the behaviour of simple (basic) optical elements (i.e. the scattering matrix, for example) and combines them to obtain higher complexity multi-element Photonic Integrated Circuits (PICs).

Models and performance of the basic BBs employed during this work have been described and characterized in the first part of this thesis. Extensive circuit simulations have been then carried out in order to evidence potentials and limits of the proposed devices taking into account fabrication tolerance effects. Two novel multi-element PICs have been investigated: a narrow linewidth single mode resonator and a passband filter with a widely tunable bandwidth.

The narrow linewidth single mode resonator (i.e. the GAC-RING), based on two Grating Assisted Couplers (GACs) in a ring resonator (RR) configuration, has been presented in Chapter 5. A suppression ratio between the selected and the suppressed modes of the resonator larger than 10 dB has been successfully demonstrated. Larger values of this figure have been shown to be achievable increasing the device control complexity. Geometries allowing larger performance are in fact more sensitive to fabrication tolerance effects. Reconfigurable add-drop multiplexers, not limited by the Free Spectral Range as that based on RRs and more compact than that based on GACs, could be realized by exploiting the proposed geometry. The device showed however sensitivity to spurious effects. Moreover, the larger the required bandwidth the more difficult is to achieve large performance. An interesting geometry that could be investigated in future works could be based on two directly coupled GAC-RINGs with different cavity lengths, exploiting then the Vernier effect. This solution could in turn increase the device performance while reducing the sensitivity to fabrication tolerance effects.

The passband filter with widely tunable bandwidth, based on an unbalanced Mach-Zehnder interferometer loaded with a pair of RRs, has been then presented in Chapter 6. Valuable performance with a reduced control complexity with respect to the solutions proposed in literature has been successfully demonstrated. In view of the realization of complex systems, where many devices and functionalities are integrated on the same chip, a reduced number of actuators per device is of key importance. This allows for power dissipation reduction as well as an easier management of the circuit. The device spectral characteristic flexibility has been also im-

proved through the employment of tunable couplers of novel concept. This tunable power splitting BB has been developed and optimized during this doctoral work (see Chapter 3). The robustness of the tunable bandwidth filter against nonlinear effects and fabrication tolerances has been also proven. These properties, together with bit error rate measurements, have confirmed that the presented device can be suitable for gridless networking and adaptive filtering applications. An interesting future development is the use of the proposed filter as functional element for the realization of a flexible wavelength selective switch. Such a device, of key importance for the development of future flexible networks, could be realized by cascading in a tree architecture the studied filter.

In conclusion, the future of PICs design relies on the ease with which complex circuits can be simulated and evaluated. Moreover, the effects of fabrication tolerances on the circuit elements performance must be well established and standardised. The work presented in this thesis performed such a validation function, demonstrating complex PICs and their operating regimes as a function of their component parts.

A

COUPLED MODE THEORY

In this appendix the Coupled Mode Theory (CMT) is briefly summarized to derive the set of coupled equations used during during this work to model and design evanescent couplers, Bragg gratings and GACs.

This theory is in fact widely used in integrated optics to analyze and/or design systems where coupling between different modes is generated by perturbations: parallel waveguides at a distance g (directional coupler) or a periodic variation of the waveguide width (photonic wire Bragg grating).

The CMT can be derived from a variational approach [192] or from the Lorentz's reciprocity theorem [193]. In this appendix, the second approach will be followed and after a brief remind on the Lorentz reciprocity theorem, the coupled mode equations will be obtained. The general form of the coupled mode equations will be then used to study the particular cases of interest for this thesis (directional couplers, Bragg grating and grating assisted couplers).

A.1 LORENTZ'S RECIPROCITY THEOREM

Let $\overline{\mathbf{E}}_1, \overline{\mathbf{H}}_1$ and $\overline{\mathbf{E}}_2, \overline{\mathbf{H}}_2$ be the solutions of Maxwell's equations in two media, with the same $\mu = \mu_0$, and with different dielectric constants, ε_1 and ε_2 respectively occupying the same volume V. Introducing two polarization vectors, defined as $\overline{\mathbf{P}}_i = (\varepsilon_i - \varepsilon)\overline{\mathbf{E}}_i$, it is possible to rewrite Maxwell's equations considering in both cases the same reference material with dielectric constant ε assumed real, so that differences, including losses, are taken into account by the polarization vector $\overline{\mathbf{P}}$. Recasting these equations is then possible as in [194] to obtain the integral formulation of the Lorentz's reciprocity theorem:

$$\int_S (\overline{\mathbf{E}}_1 \times \overline{\mathbf{H}}_2^* + \overline{\mathbf{E}}_2^* \times \overline{\mathbf{H}}_1) \cdot \hat{n}\, dS = \begin{cases} -j\omega \int_V (\varepsilon_1 - \varepsilon_2^*)\, \overline{\mathbf{E}}_1 \cdot \overline{\mathbf{E}}_2^*\, dV \\ -j\omega \int_V (\overline{\mathbf{P}}_1 \cdot \overline{\mathbf{E}}_2^* - \overline{\mathbf{E}}_1 \cdot \overline{\mathbf{P}}_2^*)\, dV. \end{cases} \tag{A.1}$$

If, in particular, $\varepsilon_1 = \varepsilon_2^*$, (A.1) reduces to:

$$\int_S (\overline{\mathbf{E}}_1 \times \overline{\mathbf{H}}_2^* + \overline{\mathbf{E}}_2^* \times \overline{\mathbf{H}}_1) \cdot \hat{n}\, dS = 0.$$

The Lorentz's theorem formulation greatly simplifies if volume V reduces to a cylindrical structure (i.e. a structure invariant along the propagation direction). The integral conjugated formulation of the Lorentz theorem for cylindrical structures is then:

$$\int_{S_\infty} \frac{\partial}{\partial z}(\overline{\mathbf{E}}_1 \times \overline{\mathbf{H}}_2^* + \overline{\mathbf{E}}_2^* \times \overline{\mathbf{H}}_1) \cdot \hat{z}\, dS = \begin{cases} -j\omega \int_{S_\infty} (\varepsilon_1 - \varepsilon_2^*)\, \overline{\mathbf{E}}_1 \cdot \overline{\mathbf{E}}_2^*\, dS \\ -j\omega \int_{S_\infty} (\overline{\mathbf{P}}_1 \cdot \overline{\mathbf{E}}_2^* - \overline{\mathbf{P}}_2^* \cdot \overline{\mathbf{E}}_1)\, dS. \end{cases} \tag{A.2}$$

which reduces to:

$$\int_{S_\infty} \frac{\partial}{\partial z}(\overline{\mathbf{E}}_1 \times \overline{\mathbf{H}}_2^* + \overline{\mathbf{E}}_2^* \times \overline{\mathbf{H}}_1) \cdot \hat{z}\, dS = 0$$

if $\varepsilon_1 = \varepsilon_2^*$ everywhere.

A.2 COUPLED MODE EQUATIONS

To derive the set of coupled mode equations used during this work three assumptions must be made. It is assumed first that radiating modes give a negligible contribution to the field of the structure. Coupling to the radiating modes is in fact undesirable for proper device working and so all the efforts are done to reduce their presence, which justifies the hypothesis.

To derive the coupled mode equations is thus necessary to define two fields. The first field, identified by subscript 1, is the combination of all the local forward and backward guided modes inside the structure. Its transverse components can therefore be written as:

$$\begin{aligned} \overline{\mathbf{E}}_{1t}(z) &= \sum_\nu (a_\nu(z) + b_\nu(z))\, \overline{\mathbf{E}}_{t\nu}(z) \\ \overline{\mathbf{H}}_{1t}(z) &= \sum_\nu (a_\nu(z) - b_\nu(z))\, \overline{\mathbf{H}}_{t\nu}(z) \end{aligned}$$

in which the dependence of the amplitudes on the longitudinal coordinate z of the magnitudes is evidenced and $a_\nu(z) = A_\nu(z)\, e^{-j\beta_\nu(z)z}$ and $b_\nu(z) = B_\nu(z)\, e^{j\beta_\nu(z)z}$ are the complex amplitude coefficients of the modes propagating in the positive and negative directions respectively.

Under the hypothesis of small perturbations it is possible also to assume (second simplifying assumption) that the field shapes in the transversal planes, $\overline{\mathbf{E}}_{t\nu}(z)$ and $\overline{\mathbf{H}}_{t\nu}(z)$ do not vary along z as well as the mode propagation constants $\beta_\nu(z)$. As a result, only the amplitude coefficients a_ν and b_ν will depend on z. The equations describing field 1 are then:

$$\overline{\mathbf{E}}_{1t}(z) = \sum_{\nu}(a_\nu(z) + b_\nu(z))\,\overline{\mathbf{E}}_{t\nu} \tag{A.3}$$

$$\overline{\mathbf{H}}_{1t}(z) = \sum_{\nu}(a_\nu(z) - b_\nu(z))\,\overline{\mathbf{H}}_{t\nu} \tag{A.4}$$

with

$$a_\nu(z) = A_\nu(z)\,e^{-j\beta_\nu z} \tag{A.5}$$

$$b_\nu(z) = B_\nu(z)\,e^{j\beta_\nu z}. \tag{A.6}$$

The second field (denoted by suffix 2) to be considered to apply the reciprocity theorem is any mode of the structure. Its transversal components can be thus written as:

$$\overline{\mathbf{E}}_{2t}(z) = \overline{\mathbf{E}}_{t\mu}\,e^{-j\beta_\mu z} \tag{A.7}$$

$$\overline{\mathbf{H}}_{2t}(z) = \overline{\mathbf{H}}_{t\mu}\,e^{-j\beta_\mu z}. \tag{A.8}$$

From now on, for formal simplicity, the explicit mention of z dependence of the variables will be omitted, though it continues to exist.

Substituting (A.3)-(A.4) and (A.7)-(A.8) into the equation of the reciprocity theorem (A.2) written for lossless cylindrical structures ($\varepsilon^* = \varepsilon$), the left hand side integral turns out to be:

$$\int_{S_\infty} \frac{\partial}{\partial z}\left[\sum_{\nu}(a_\nu + b_\nu)\,\overline{\mathbf{E}}_{t\nu} \times \overline{\mathbf{H}}^*_{t\mu}\,e^{j\beta_\mu z} + \overline{\mathbf{E}}^*_{t\mu}\,e^{j\beta_\mu z} \times \sum_{\nu}(a_\nu - b_\nu)\,\overline{\mathbf{H}}_{t\nu}\right] \cdot \hat{\mathbf{z}}\; dS. \tag{A.9}$$

The guided modes will be considered orthogonal. The coupled mode theory can be also easily extended to the case where the modes are not mutually orthogonal as in [160] but being outside the sake of this thesis this extension will not be developed in this appendix. The orthogonality between the modes allows writing:

$$\int_{S_\infty} \overline{\mathbf{E}}_{t\nu} \times \overline{\mathbf{H}}^*_{t\mu} \cdot \hat{\mathbf{z}}\; dS = 2P\delta_{\nu\mu}$$

which allows to rewrite (A.9) as:

$$4P\left(\frac{\partial a_\mu}{\partial z} + j\beta_\mu a_\mu\right)e^{j\beta_\mu z} = \tag{A.10}$$

$$= 4P\frac{\partial A_\mu}{\partial z}. \tag{A.11}$$

Considering propagation in the negative verse of the z axis[1], one should have written the following equations instead

$$\begin{aligned}\overline{\mathbf{E}}_{2t} &= \overline{\mathbf{E}}_{t,-\mu}\, e^{j\beta_\mu z} = \overline{\mathbf{E}}_{t\mu}\, e^{j\beta_\mu z} \\ \overline{\mathbf{H}}_{2t} &= \overline{\mathbf{H}}_{t,-\mu}\, e^{j\beta_\mu z} = -\overline{\mathbf{H}}_{t\mu}\, e^{j\beta_\mu z}.\end{aligned}$$

With similar algebra one also finds that integral (A.9) holds

$$-4P\left(\frac{\partial b_\mu}{\partial z} - j\beta_\mu b_\mu\right) e^{-j\beta_\mu z} = \tag{A.12}$$

$$= -4P\frac{\partial B_\mu}{\partial z}. \tag{A.13}$$

It is now time to move to the evaluation of the right member of (A.2). It holds:

$$= \begin{cases} -j\omega \int_{S_\infty} (\varepsilon_1 - \varepsilon_2)\overline{\mathbf{E}}_1 \cdot \overline{\mathbf{E}}_2^*\, dS \\ -j\omega \int_{S_\infty} (\overline{\mathbf{P}}_1 \cdot \overline{\mathbf{E}}_2^* - \overline{\mathbf{P}}_2^* \cdot \overline{\mathbf{E}}_1)\, dS. \end{cases} \tag{A.14}$$

Note that all the three components of the fields must be considered.

Before the calculation of these integrals, the third approximation which allows to get the final form of the coupled mode equations must be introduced. In particular, supposing weak coupling between the guides, one can express the fields supported by the overall structure as a linear combination of fields supported by each single guide forming the complex structure. This is obviously not true if the two guides are placed close each other but is anyway an acceptable approximation if the two waveguides are far enough not to perturb each other significantly.

Note also that this third hypothesis is not necessary for any structure. For example, in a corrugated waveguide, the second hypothesis makes the modes of the corrugated (deformed) waveguide equal to those of the not deformed structure.

To calculate the integrals appearing in (A.14), one must first define what is the deformation of the structure. In the case of two parallel waveguides separated by a gap distance g (see Fig A.1), the presence of Waveguide 2 can be seen as the deformation of the single waveguide represented Waveguide 1 and viceversa. In the case of a corrugated guide shown in figure A.2 the concept of deformation appears clearly.

In conclusion, making reference to figure A.2, for a periodically perturbed waveguide, ε is that of the unperturbed cylindrical waveguide while $\Delta\varepsilon$ accounts for the changes from that waveguide. When two parallel waveguides are considered, the distribution of relative dielectric constant to one of them is taken as ε of the structure, while $\Delta\varepsilon$ is the change from ε related to the presence of the second guide.

1 Note that one can get the same result applying the reciprocity theorem in the non conjugate form.

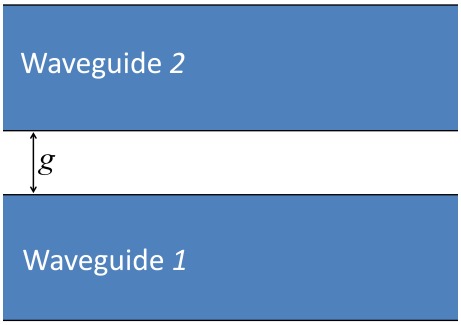

Figure A.1.: Parallel waveguides schematic, top view.

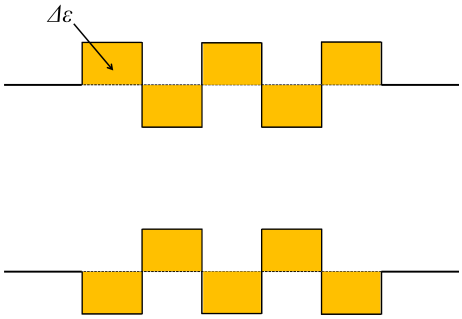

Figure A.2.: Corrugated waveguide schematic top view. The waveguide perturbation regions are evidenced in yellow.

In other words, $\Delta\varepsilon$ does not vanish only where changes occur with respect to the undeformed structure.

If suffix 1 refers to the unperturbed structure and suffix 2 is associated to the perturbation, one can then write (A.14) letting $\overline{\mathbf{P}}_2 = 0$ and $\overline{\mathbf{P}}_1 = \Delta\varepsilon\,\overline{\mathbf{E}}_1$. This leads to write the right term of the Lorentz's theorem equation (A.14) as:

$$\begin{cases} -j\omega \int_{S_\infty} \Delta\varepsilon\ \overline{\mathbf{E}}_1 \cdot \overline{\mathbf{E}}_2^*\ dS \\ -j\omega \int_{S_\infty} \overline{\mathbf{P}}_1 \cdot \overline{\mathbf{E}}_2^*\ dS. \end{cases} \tag{A.15}$$

Note that all the field components appear in these integral. The longitudinal ones can be written:

$$\begin{aligned} E_{1z} &= \tfrac{1}{j\omega\varepsilon}\ \left(\nabla_t \times \overline{\mathbf{H}}_{1t}\right) \cdot \hat{\mathbf{z}} \\ H_{1z} &= -\tfrac{1}{j\omega\mu}\ \left(\nabla_t \times \overline{\mathbf{E}}_{1t}\right) \cdot \hat{\mathbf{z}} \end{aligned} \tag{A.16}$$

and then

$$\overline{\mathbf{P}}_t = \Delta\varepsilon\,\overline{\mathbf{E}}_{1t} = \Delta\varepsilon \sum_\nu (a_\nu + b_\nu)\,\overline{\mathbf{E}}_{t\nu} \tag{A.17}$$

$$P_z = \frac{\varepsilon\,\Delta\varepsilon}{(\varepsilon + \Delta\varepsilon)} \sum_\nu (a_\nu - b_\nu)\ E_{z\nu}. \tag{A.18}$$

Considering propagation in the positive direction along z, ($\overline{\mathbf{E}}_2 = \overline{\mathbf{E}}_\mu e^{-j\beta_\mu z}$) and propagation in the negative direction of the z axis ($\overline{\mathbf{E}}_2 = \overline{\mathbf{E}}_\mu\, e^{j\beta_\mu z}$ with $E_{t,-\mu} = E_{t\mu}$ e $E_{z,-\mu} = -E_{z\mu}$) the Lorentz theorem allows to write:

$$\begin{aligned} 4P\frac{\partial A_\mu}{\partial z}\, e^{-j\beta_\mu z} &= -j\omega \int_{S_\infty} \sum_\nu \Big[(a_\nu + b_\nu)\, \Delta\varepsilon\, \overline{\mathbf{E}}_{t\nu} \cdot \overline{\mathbf{E}}^*_{t\mu} + \\ &\quad + (a_\nu - b_\nu)\, \frac{\varepsilon\, \Delta\varepsilon}{(\varepsilon + \Delta\varepsilon)}\, E_{z\nu} E^*_{z\mu} \Big]\, dS \end{aligned} \tag{A.19}$$

$$\begin{aligned} 4P\frac{\partial B_\mu}{\partial z}\, e^{j\beta_\mu z} &= j\omega \int_{S_\infty} \sum_\nu \Big[(a_\nu + b_\nu)\, \Delta\varepsilon\, \overline{\mathbf{E}}_{t\nu} \cdot \overline{\mathbf{E}}^*_{t\mu} + \\ &\quad - (a_\nu - b_\nu)\, \frac{\varepsilon\, \Delta\varepsilon}{(\varepsilon + \Delta\varepsilon)}\, E_{z\nu}\, E^*_{z\mu} \Big]\, dS. \end{aligned} \tag{A.20}$$

It is now possible to define the *transverse* and *longitudinal coupling coefficients* as:

$$\kappa^t_{\nu\mu} = \frac{\omega}{4} \int_{S_\infty} \Delta\varepsilon\, \overline{\mathbf{E}}_{t\nu} \cdot \overline{\mathbf{E}}^*_{t\mu}\, dS \tag{A.21}$$

$$\kappa^z_{\nu\mu} = \frac{\omega}{4} \int_{S_\infty} \frac{\varepsilon\, \Delta\varepsilon}{(\varepsilon + \Delta\varepsilon)}\, E_{z\nu}\, E^*_{z\mu}\, dS. \tag{A.22}$$

Considering powers normalized to 1 (e.g. $P = 1$) and using (A.5)-(A.6) to evidence the expressions of the coefficients A and B one gets:

$$\begin{aligned} \frac{\partial A_\mu}{\partial z} &= -j \sum_\nu \Big[A_\nu \left(\kappa^t_{\nu\mu} + \kappa^z_{\nu\mu} \right) e^{-j(\beta_\nu - \beta_\mu)z} + \\ &\quad + B_\nu \left(\kappa^t_{\nu\mu} - \kappa^z_{\nu\mu} \right) e^{j(\beta_\nu + \beta_\mu)z} \Big] \end{aligned} \tag{A.23}$$

$$\begin{aligned} \frac{\partial B_\mu}{\partial z} &= j \sum_\nu \Big[A_\nu \left(\kappa^t_{\nu\mu} - \kappa^z_{\nu\mu} \right) e^{-j(\beta_\nu + \beta_\mu)z} + \\ &\quad + B_\nu \left(\kappa^t_{\nu\mu} + \kappa^z_{\nu\mu} \right) e^{j(\beta_\nu - \beta_\mu)z} \Big]. \end{aligned} \tag{A.24}$$

These equations are the so-called Coupled Mode Equations. They express the dependence on the propagation direction z of the mode amplitude coefficients. Codirectional coupling occurs when the power transfer is between A_μ and A_ν while contradirectional coupling occurs when power transfer is between A_μ and B_ν. The exponential functions $e^{\pm j(\beta_\nu \pm \beta_\mu)}$ takes into account the phase missmatch between the coupled modes. The smaller $(\beta_\nu \pm \beta_\mu)$ the larger the coupling. When $(\beta_\nu \pm \beta_\mu) = 0$ the so called phase matching condition is achieved and the coupling is maximized as it will be shown in Section A.4.

Before entering into the details of the coupled mode equation solutions for specific structures, it is now useful to develop some algebra on the Fourier series to

understand the contribution of a periodic perturbation to the coupling of the modes. This analysis will be performed in the next Section.

A.3 FOURIER ANALYSIS OF PERIODIC PERTURBATIONS

Let us then consider for simplicity a planar waveguide with a surface grating such as that shown in figure A.2. Note that the same analysis can be developed for every structure that has a periodic perturbation. The perturbation $\Delta\varepsilon(z)$ can be mathematically described by a periodic function which can be expressed in terms of a Fourier series:

$$\Delta\varepsilon(z) = \sum_{n=-\infty}^{\infty} \Delta\varepsilon_n \, e^{j\frac{2\pi}{\Lambda}nz} \tag{A.25}$$

where Λ is the grating period. Since the equations accounting for the phenomenon are linear, the effect of each harmonic can be studied independently. At the end, results can be added to obtain the problem solution. For example if only a *TE* mode can propagate assuming for simplicity that $\kappa^z_{\nu\mu} = 0$, one must evaluate:

$$\kappa^t_{\nu\mu} = \frac{\omega}{4} \int_{S_\infty} \Delta\varepsilon \, E_{t\nu} \, E^*_{t\mu} \, dS, \tag{A.26}$$

also keeping in mind that the integral to evaluate $\kappa^t_{\nu,\mu}$ does not vanish only in the region where the perturbation occurs. Inserting (A.25) into it, one gets:

$$\begin{aligned} \kappa^t_{\nu\mu} &= \frac{\omega}{4} \int_{S_\infty} \sum_{n=-\infty}^{\infty} \Delta\varepsilon_n \, e^{j\frac{2\pi}{\Lambda}\,n\,z} \, E_{t\nu} \, E^*_{t\mu} \, dS = \\ &= \sum_{n=-\infty}^{\infty} \kappa_{n,\nu\mu} \, e^{j\frac{2\pi}{\Lambda}\,n\,z} \end{aligned} \tag{A.27}$$

being κ_n real positive given by

$$\kappa_{n,\nu\mu} = \frac{\omega}{4} \int_{S_\infty} \Delta\varepsilon_n \, E_{t\nu} \, E^*_{t\mu} \, dS.$$

The coupled mode equations A.23 and A.24 can be then rewritten as:

$$\begin{aligned} \frac{\partial A_\mu}{\partial z} &= -j \sum_{n=-\infty}^{\infty} \sum_{\nu} \Big[A_\nu \left(\kappa^t_{\nu\mu} + \kappa^z_{\nu\mu} \right) e^{-j(\beta_\nu - \beta_\mu)z} + \\ &\quad + B_\nu \left(\kappa^t_{\nu\mu} - \kappa^z_{\nu\mu} \right) e^{j(\beta_\nu + \beta_\mu)z} \Big] e^{j\frac{2\pi}{\Lambda}nz} \end{aligned} \tag{A.28}$$

$$\begin{aligned} \frac{\partial B_\mu}{\partial z} &= j \sum_{n=-\infty}^{\infty} \sum_{\nu} \Big[A_\nu \left(\kappa^t_{\nu\mu} - \kappa^z_{\nu\mu} \right) e^{-j(\beta_\nu + \beta_\mu)z} + \\ &\quad + B_\nu \left(\kappa^t_{\nu\mu} + \kappa^z_{\nu\mu} \right) e^{j(\beta_\nu - \beta_\mu)z} \Big] e^{j\frac{2\pi}{\Lambda}nz}. \end{aligned} \tag{A.29}$$

The arguments of the exponential functions are now $(\beta_\nu \pm \beta_\mu) \pm 2n\pi/\Lambda$. The presence of the periodic spatial structure deformation allows phase matching between modes propagating in the same or in opposite directions.

A useful case to analyse can be that of a square wave with period equal to Λ, duty cycle equal to δ and amplitude $\Delta\varepsilon$. The solution of this example can be in fact applied in order to calculate the contribution of periodic perturbations of any shape as it will be shown later for a sinusoidal one. The grating shape is described by $\Delta\varepsilon(z)$, which can be written as a Fourier series as

$$\Delta\varepsilon(z) = \sum_{n=-\infty}^{\infty} \Delta\varepsilon_n \, e^{j2\pi nz/\Lambda} \qquad \text{with } \Delta\varepsilon_n = \Delta\varepsilon\,\delta\,\operatorname{sinc}(n\delta).$$

The amplitude of the harmonics decreases as $1/n$, causing a decrease of the value of the coupling coefficient κ and then of the reflection efficiency, for a given grating length. The grating contribution can be then easily calculated also for the longitudinal component of the field, remembering Eq. (A.22), as:

$$\frac{\Delta\varepsilon(z)}{\varepsilon + \Delta\varepsilon(z)} = \sum_{n=-\infty}^{\infty} \frac{\Delta\varepsilon}{\varepsilon + \Delta\varepsilon}\,\delta\,\operatorname{sinc}(n\delta)\, e^{j2\pi nz/\Lambda}.$$

Once the square wave perturbation contribution to the coupling of the modes has been described through the Fourier analysis, it is now easily possible to describe how to calculate this contribution in the case of a sinusoidal perturbation [140]. This is in fact the perturbation geometry chosen to allow contradirectional coupling during this work (see Chapter 4 and 5). Periods that allow phase matching at the desired wavelength for $n = \pm 1$ or, in other words, first order gratings have been realized. Due to that, in the following, $n = 0, \pm 1$ will be considered. As in the former part of this analysis, the perturbation that contribute to the transversal coupling coefficient will be analysed first. In order to explain the calculation, the dependence of the longitudinal component on the transversal coordinates has to be explicit. From now on we will then indicate $\Delta\varepsilon(z) = \Delta\varepsilon(x, y, z)$.

The sketch of a sidewall sinusoidally perturbed waveguide is illustrated in Fig. A.3a. It is possible to consider first the $x - z$ plane that intersect the y axis in y_0. The grating sketch on this plane is represented in Fig. A.3b where the blue dashed line that intersects the x axis in x_0 represents the average waveguide width. We can now focus on one of the two sidewalls. The zoomed view of the left sidewall is sketched in the upper part of Fig. A.3c where two particular x axis points are highlighted, x_1 (red dashed line) and x_{-1} (blue dashed line). For each of these two points the perturbation can be modelled as a square wave perturbation, as shown in the lower part of the figure, and the Fourier series coefficients $\Delta\varepsilon_n$ can be easily calculated as previously illustrated. Considering $n = 1$, the coefficients of the two series reads as:

$$\Delta\varepsilon_1(x_1, y_0) = \Delta\varepsilon\ \delta\ \operatorname{sinc}(n\delta),$$

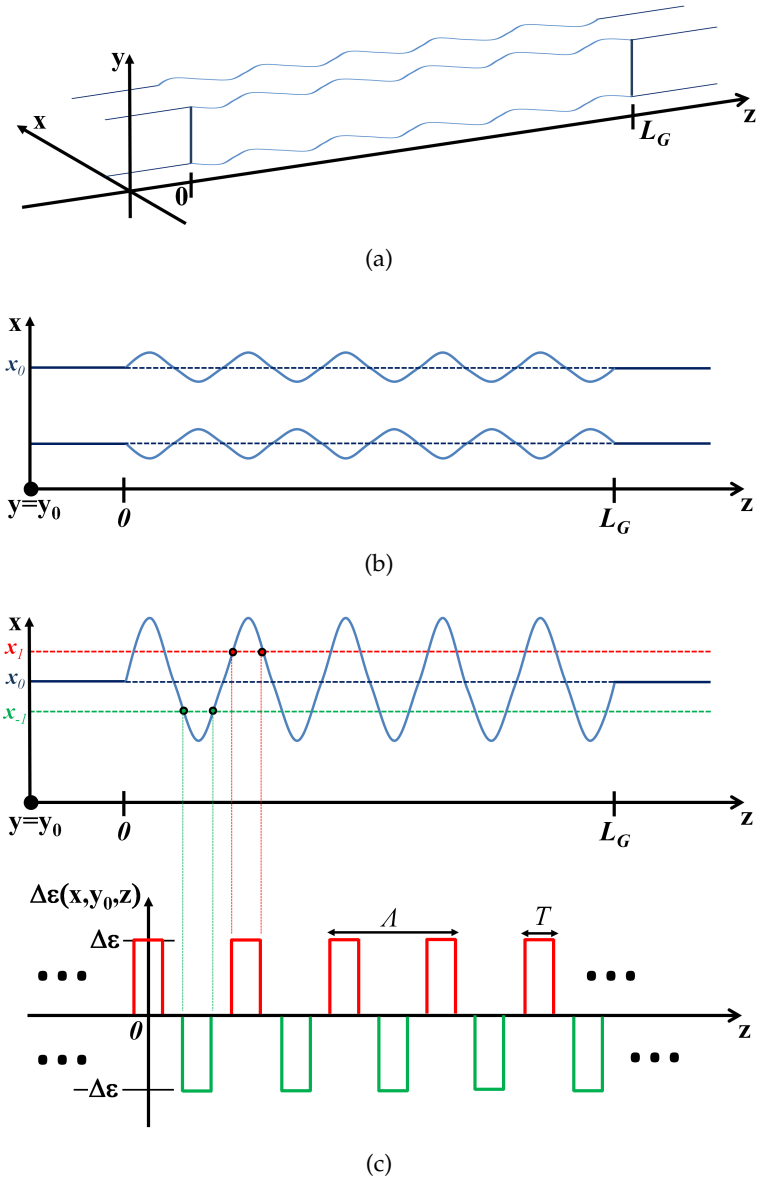

Figure A.3.: (a) Sinusoidally perturbed waveguide (b) Sinusoidally perturbed waveguide top view. Dashed lines represents the average waveguide width. (c) Upper sketch: Sinusoidally perturbed waveguide left sidewall top view. Red and green dashed lines indicate two different positions on the x axis, respectively x_1 and x_{-1}. Lower sketch: $\Delta\varepsilon(x_1, y_0, z)$, red trace and $\Delta\varepsilon(x_{-1}, y_0, z)$, green trace.

$$\Delta\varepsilon_1(x_{-1}, y_0) = -\Delta\varepsilon\ \delta\ \mathrm{sinc}(n\delta)\, e^{-j\pi}.$$

Considering instead $n = 0$, we can write the coefficients as:

$$\Delta\varepsilon_0(x_1, y_0) = \Delta\varepsilon\ \delta,$$

$$\Delta\varepsilon_0(x_{-1}, y_0) = -\Delta\varepsilon\ \delta.$$

Regarding then the coupling of the longitudinal component of the field, the Fourier series coefficient can be easily calculated through the former equations with the substitutions: $\Delta\varepsilon \leftarrow \varepsilon\Delta\varepsilon/(\varepsilon+\Delta\varepsilon)$ and $-\Delta\varepsilon \leftarrow -\varepsilon\Delta\varepsilon/(\varepsilon-\Delta\varepsilon)$.

Having described the effect on the coupling of the modes of a periodic perturbation, it is now possible to develop the coupled mode equations for the structures of interest for this dissertation.

A.4 CODIRECTIONAL COUPLING BETWEEN SINGLE MODE WAVEGUIDES: DIRECTIONAL COUPLER

The case of two single mode waveguides separated by a distance g (see Fig. A.1) is considered first. If coupling is codirectional one can neglect coupling between (A.23) and (A.24). This case is useful to model or study the behaviour of directional couplers. The equations that has to be solved reduce then to:

$$\frac{\partial A_\mu}{\partial z} = -j\sum_\nu A_\nu\,(\kappa^t_{\nu\mu}+\kappa^z_{\nu\mu})\,e^{-j(\beta_\nu-\beta_\mu)z} \tag{A.30}$$

$$\frac{\partial B_\mu}{\partial z} = j\sum_\nu B_\nu\,(\kappa^t_{\nu\mu}+\kappa^z_{\nu\mu})\,e^{j(\beta_\nu-\beta_\mu)z}. \tag{A.31}$$

Forward and backward propagating modes are then mutually independent. To simplify the notation $\kappa_{s\nu\mu} = \kappa^t_{\nu\mu}+\kappa^z_{\nu\mu}$ will be considered for this case. The coupling between the modes propagating in the positive z direction is described by Eq. A.30 while the coupling between the modes propagating in the negative z direction is described by Eq. A.31. Possible values for both ν and μ are 1 and 2. Suffix 1 refers to the mode of the first waveguide, while suffix 2 refers to the second one. Considering propagation along the positive direction of z, only (A.30) must be solved. Introducing the explicit values of ν and μ one gets:

$$\begin{aligned}\frac{\partial A_1}{\partial z} &= -jA_1\,\kappa_{s11}\,e^{-j(\beta_1-\beta_1)z} - jA_2\,\kappa_{s21}\,e^{-j(\beta_2-\beta_1)z}\\ \frac{\partial A_2}{\partial z} &= -jA_1\,\kappa_{s12}\,e^{-j(\beta_1-\beta_2)z} - jA_2\,\kappa_{s22}\,e^{-j(\beta_2-\beta_2)z}.\end{aligned}$$

As said before, it is necessary to determine which is the "guide" and which is the relevant "perturbation". Waveguide 1 is considered first as the "guide", while waveguide 2 is the "perturbation". In this case:

$$\kappa_{s11} = \frac{\omega}{4}\int_{S_2}\Delta\varepsilon\;\overline{\mathbf{E}}_{t1}\cdot\overline{\mathbf{E}}^*_{t1} + \frac{\varepsilon\,\Delta\varepsilon}{(\varepsilon+\Delta\varepsilon)}\;E_{z1}\,E^*_{z1}\;dS \tag{A.32}$$

$$\kappa_{s21} = \frac{\omega}{4}\int_{S_2}\Delta\varepsilon\;\overline{\mathbf{E}}_{t2}\cdot\overline{\mathbf{E}}^*_{t1} + \frac{\varepsilon\,\Delta\varepsilon}{(\varepsilon+\Delta\varepsilon)}\;E_{z2}\,E^*_{z1}\;dS \tag{A.33}$$

where the integral does not vanish only in the region where the core of waveguide 2 is present. At the same time, conjugation is applied to the mode that excites the structure. The first consequence is that the first integral is an infinitesimal of higher order with respect to the second one. This occurs since the first integral is calculated integrating the product of two field distributions which both have negligible values in the integration area while, in the second one, one of the two functions is not negligible. It is then reasonable to consider $\kappa_{s11} \simeq 0$. The equation to be solved is then:

$$\frac{\partial A_1}{\partial z} = -jA_2\,\kappa_{s21}\,e^{-j(\beta_2-\beta_1)z}. \tag{A.34}$$

Exchanging the roles of "guide" and "perturbation" it is then straightforward to obtain κ_{12} and κ_{22}. Since $\kappa_{22} \simeq 0$ for the same reasoning developed before for κ_{11}, one gets the second equation to be solved:

$$\frac{\partial A_2}{\partial z} = -jA_1\kappa_{s12}e^{-j(\beta_1-\beta_2)z}. \tag{A.35}$$

One can now determine the relationship existing between κ_{12} and κ_{21}. It can be demonstrated that power conservation in the system requires

$$\kappa_{s12}^{*} = \kappa_{s21} = \kappa. \tag{A.36}$$

Letting

$$\Delta\beta = \beta_1 - \beta_2 \tag{A.37}$$

Eq. (A.34) and (A.35) can also be written as

$$\begin{aligned}
\frac{\partial A_1}{\partial z} &= -jA_2\,\kappa_{s21}\,e^{-j(\beta_2-\beta_1)z} = -jA_2\,\kappa_s\,e^{j\Delta\beta z} \\
\frac{\partial A_2}{\partial z} &= -jA_1\,\kappa_{s12}\,e^{-j(\beta_1-\beta_2)z} = -jA_1\,{\kappa_s}^{*}\,e^{-j\Delta\beta z}.
\end{aligned}$$

The system formed by the two former defined equations can be solved analytically by setting the boundary conditions for A_1 and A_2. Taking into account $A_1(0) = A_0$ and $A_2(0) = 0$ the system solutions read as

$$A_1(z) = A_0\,e^{j\frac{\Delta\beta}{2}z}\left(\cos(Sz) - j\frac{\Delta\beta}{2S}\,\sin(Sz)\right) \tag{A.38}$$

$$A_2(z) = -jA_0\,e^{-j\frac{\Delta\beta}{2}z}\,\frac{\kappa}{S}\,\sin(Sz). \tag{A.39}$$

The powers carried by the two waveguides considering an input optical power normalized to 1 (i.e. $P_0 = |A_1 = (0)|^2 = 1$) read as:

$$P_1(z) = |A_1(z)|^2 = \left[\left(\frac{\Delta\beta}{2S}\right)^2 \sin^2(Sz) + \cos^2(Sz)\right] \tag{A.40}$$

$$P_2(z) = |A_2(z)|^2 = \frac{|\kappa|^2}{S^2} \sin^2(Sz). \tag{A.41}$$

where $S = \sqrt{\left(\frac{\Delta\beta}{2}\right)^2 + |\kappa|^2}$. These expressions strongly depend on $\Delta\beta$. $\Delta\beta = 0$ represents the so called phase matching or *synchronous* condition of the modes. It occurs when $\beta_1 = \beta_2$. This condition implies that the two considered waveguides have the same cross section dimensions. In fact, during this work a fixed height of the core and fixed index contrast between the core and the cladding of the waveguides were considered. $\Delta\beta \neq 0$ (i.e. $\beta_1 \neq \beta_2$) corresponds instead to the *non synchronous* or *not phase matched* case (i.e. the two considered waveguides have different cross section dimensions). Observing Eq. (A.41) it can be noticed that the power transfer between the two waveguides is periodical in z and that maximum coupling is achieved when $Sz = (2m+1)\pi/2$ with m a non negative integer. For $m = 0$, $z = L_\pi = \pi/2S$ is known as the *coupling length*. Complete power transfer between the two waveguides is achievable only in the synchronous case (i.e. $S = \kappa$). In this case the coupling length can be written as

$$L_\pi = \frac{\pi}{2S} = \frac{\pi}{2|\kappa|}. \tag{A.42}$$

Fig. A.4 shows the coupled power dependence from the longitudinal coordinate z for four different phase conditions. Increasing the asynchronism between the waveg-

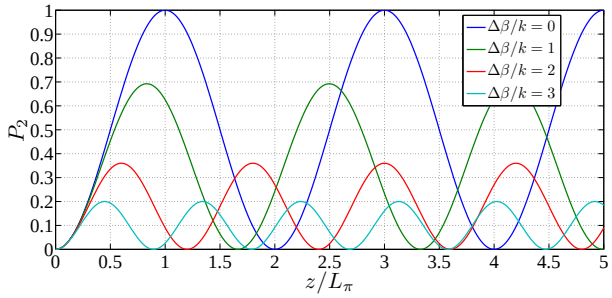

Figure A.4.: Coupled power calculated for four different values of $\Delta\beta/\kappa$ as a function of the longitudinal coordinate z normalized to L_π. Note that L_π is calculated considering the synchronous case (i.e. $\Delta\beta = 0$).

uides, the maximum achievable coupled power decreases as well as the periodicity of P_2 with z.

In the synchronous case L_π and thus κ can be related to the propagation constants of the modes sustained by the overall structure (i.e. the supermodes). In this way it is possible to ease the calculation of the coupling coefficient and consequently

the design of the coupler. A single mode coupler shows two supermodes, with symmetric and antisymmetric shapes respect to the coupler gap [195]. The power transfer, described in the coupled mode theory as the coupling between the modes of the two waveguides, is the consequence of the interference between these two supermodes. Complete power transfer occurs at a distance L_π where the supermodes interference destructively:

$$(\beta_s - \beta_a)L_\pi = \pi. \tag{A.43}$$

By inserting this equation in Eq. (A.42) it is then easy to calculate that

$$\kappa = \frac{(\beta_s - \beta_a)}{2}. \tag{A.44}$$

A.5 CONTRADIRECTIONAL COUPLING IN A MONOMODE WAVEGUIDE: BRAGG GRATING

We now consider the case of a monomode waveguide with a periodic perturbation which induce the coupling between the mode propagating in the forward ($z > 0$) direction and that propagating in the opposite one. This structures are the so called, as in Section 4.2 of this work, Bragg gratings. In this case, Eq. (A.28) and (A.29) developed in Section A.3 can be written as:

$$\frac{\partial A_1}{\partial z} = -jA_1\,\kappa_{s11} - jB_{-1}\,\kappa_{d(-1)1}\,e^{j(\beta_1+\beta_{(-1)})z}\,e^{-j\frac{2\pi}{\Lambda}z} \tag{A.45}$$

$$\frac{\partial B_{(-1)}}{\partial z} = jB_{(-1)}\,\kappa_{s(-1)(-1)} + jA_1\,\kappa_{d1(-1)}\,e^{-j(\beta_1+\beta_{(-1)})z}\,e^{j\frac{2\pi}{\Lambda}z}. \tag{A.46}$$

where A_1 is the amplitude coefficient of the mode which propagates in the positive direction of the z axis, and $B_{(-1)}$ is the amplitude of the mode which propagates in the opposite direction. Note that the subscript -1 instead of 1 has been chosen for the amplitude coefficient B in order to distinguish the coupling coefficients κ in the two differential equations. As before to simplify the notation $\kappa_{s\nu\mu} = \kappa_{\nu\mu} + \kappa_{\nu\mu}$ and $\kappa_{d\nu\mu} = \kappa_{\nu\mu} - \kappa_{\nu\mu}$ will be considered. Eq. (A.45) and (A.46) can be easily recast as:

$$\frac{\partial A_1}{\partial z} = -jB_{(-1)}\,\kappa_{d(-1)1}\,e^{j((\beta_1+\kappa_{s11})+(\beta_{(-1)}+\kappa_{s(-1)(-1)}))z}\,e^{-j\frac{2\pi}{\Lambda}z} \tag{A.47}$$

$$\frac{\partial B_{(-1)}}{\partial z} = jA_1\,\kappa_{d1(-1)}\,e^{-j((\beta_1+\kappa_{s11})+(\beta_{(-1)}+\kappa_{s(-1)(-1)}))z}\,e^{j\frac{2\pi}{\Lambda}z}, \tag{A.48}$$

showing that κ_{s11} and $\kappa_{s(-1)(-1)}$ induce just a variation of the mode propagation constant that is usually small. We can thus now neglect its contribution without lack of generality considering $\kappa_{s11} = \kappa_{s(-1)(-1)} = 0$. After the analytical solution to the system will be derived, the impact of these coefficients will be discussed.

It can be demonstrated then that, always because of power conservation, it must hold:

$$\kappa_{d(-1)1} = \kappa^*_{d1(-1)} = \kappa. \tag{A.49}$$

Keeping this into account, Eq. (A.47) and (A.48) can be written as:

$$\frac{\partial A_1}{\partial z} = -j\kappa\, B_{(-1)}\, e^{j(\beta_1+\beta_{(-1)})z}\, e^{-j\frac{2\pi}{\Lambda}z} \tag{A.50}$$

$$\frac{\partial B_{(-1)}}{\partial z} = j\kappa^*\, A_1\, e^{-j(\beta_1+\beta_{(-1)})z}\, e^{j\frac{2\pi}{\Lambda}z}. \tag{A.51}$$

It is now possible to introduce the analytical solution of the derived coupled mode equations for the contradirectional coupling between a forward and a backward wave in a single mode waveguide with a periodical perturbation. From now on, in order to simplify the notation the perturbation wavenumber $2\pi/\Lambda$ will be named as K_G. Evidencing $B_{(-1)}$ in Eq. (A.50) and inserting it into Eq. (A.51) and one gets:

$$\frac{\partial^2 A_1}{\partial z^2} - j(\beta_1 + \beta_{-1} - K_G)\frac{\partial A_1}{\partial z} - |\kappa|^2 A_1 = 0.$$

Its solutions are the linear combination of two exponential functions with arguments given by

$$j\frac{\beta_1+\beta_{-1}-K_G}{2} \pm \sqrt{|\kappa|^2 - \left(\frac{\beta_1+\beta_{-1}-K_G}{2}\right)^2} = j\frac{\Delta\beta}{2} \pm S$$

being

$$\Delta\beta = \beta_1 + \beta_{-1} - K_G \tag{A.52}$$

$$S = \sqrt{|\kappa|^2 - \left(\frac{\Delta\beta}{2}\right)^2}. \tag{A.53}$$

The solution finally is:

$$A_1(z) = A'\, e^{j\frac{\Delta\beta}{2}z + Sz} + A''\, e^{j\frac{\Delta\beta}{2}z - Sz}. \tag{A.54}$$

From this one gets

$$\begin{aligned} B_{-1}(z) &= \frac{j}{\kappa}e^{-j\Delta\beta z}\frac{\partial A_1}{\partial z} = \\ &= \frac{j}{\kappa}A'\left(j\frac{\Delta\beta}{2}+S\right)e^{-j\frac{\Delta\beta}{2}z+Sz} + \frac{j}{\kappa}A''\left(j\frac{\Delta\beta}{2}-S\right)e^{-j\frac{\Delta\beta}{2}z-Sz}. \end{aligned} \tag{A.55}$$

In this case, the synchronous or phase matching condition can still be defined by $\Delta\beta = 0$ which means that $\beta_1 + \beta_{-1} = K_G$. In the case of a mono mode waveguide the propagation constants of the propagating and the counterpropagating modes

have the same moduli ($\beta_1 + \beta_{-1} = 2\beta_1$) phase match and consequently maximum reflection, as will be shown later, is achieved at the so called Bragg wavelength $\lambda_B = 2n_{eff}\Lambda$, where n_{eff} is the average effective index of the perturbed waveguide. In the following of this Appendix β_1 and β_{-1} will be still both explicitly written in order to keep equations as general as possible. The equations that will be derived in the following of this Appendix will be in fact useful in Chapter 4 and Chapter 5 of this thesis not only to model the behaviour of the Bragg gratings, but also that of the Grating Assisted Couplers.

It is important to notice now that S, given by Eq. (A.53), is not necessarily real, as it always was in the codirectional coupling case. S, in fact, can be real only if the argument of the square root is positive, i.e. if $|\kappa|^2 > (\Delta\beta/2)^2$ or $-2\kappa < \Delta\beta < 2\kappa$. This range represents the so called photonic band-gap where the field is attenuated along the positive verse of z. Outside this range instead the field propagates in that direction.

A' and A'' appearing in (A.54) and (A.55) must be now determined in order to highlight the grating intensity and phase behaviour as a function of κ, L_G and $\Delta\beta$. To this purpose one can impose the problem general initial conditions:

$$\begin{aligned} A_1(z=0) &\neq 0 \\ B_{-1}(z=L_G) &= 0. \end{aligned}$$

After some cumbersome but straightforward algebra the coupled mode equations solutions can be written as:

$$A_1(z) = e^{j(\Delta\beta/2)z}\frac{S\cosh(S(z-L_G)) - j\frac{\Delta\beta}{2}\sinh(S(z-L_G))}{S\cosh(SL_G) + j\frac{\Delta\beta}{2}\sinh(SL_G)}A_1(0) \tag{A.56}$$

and

$$B_{-1}(z) = e^{-j(\Delta\beta/2)z}\frac{j\kappa\sinh(S(z-L_G))}{S\cosh(SL_G) + j\frac{\Delta\beta}{2}\sinh(SL_G)}A_1(0) \tag{A.57}$$

The ratio $B(z=0)/A(z=0)$ is the reflection coefficient of the field in the structure:

$$\frac{B_{-1}(0)}{A_1(0)} = \frac{-j\kappa\sinh(SL_G)}{S\cosh(SL_G) + j\frac{\Delta\beta}{2}\sinh(SL_G)} \tag{A.58}$$

while, the intensity reflection coefficient is:

$$R_G = \left|\frac{B_{-1}(0)}{A_1(0)}\right|^2 = \frac{|\kappa|^2\sinh^2(SL_G)}{S^2\cosh^2(SL_G) + \frac{\Delta\beta^2}{4}\sinh^2(SL_G)}. \tag{A.59}$$

Figure A.5 shows the intensity reflection coefficient R_G for three values of κL_G as a function of $\Delta\beta/2\kappa$. The grating spectrum consists of a main lobe placed around

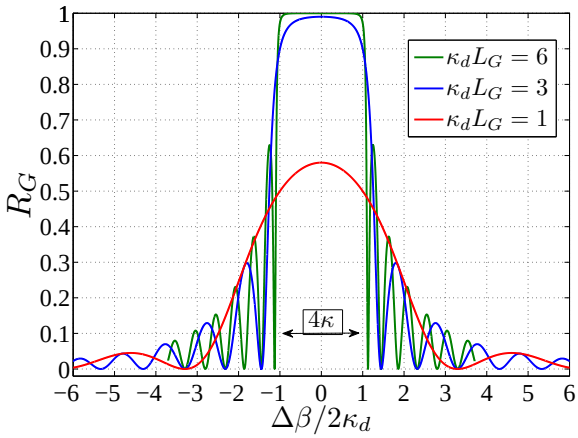

Figure A.5.: Bragg grating R_G as a function of $\Delta\beta/2\kappa$.

$\Delta\beta = 0$ and a series of sidelobes, the intensity of which decrease as $|\Delta\beta|$ increases. Outside the photonic bandgap (indicated as 4κ in Fig. A.5) the waves propagate in the periodic medium experiencing reflections at both of its ends. Interference between these reflected waves give rise to this Fabry-Pérot like behaviour [196]. As we go farer from the photonic bandgap region, the effect of the periodic medium decreases and the grating approaches the behaviour of a straight waveguide (i.e. zero reflection). When the phase matching condition is satisfied ($\Delta\beta = 0$) R_G reduces to $\tanh^2(\kappa L_G)$ and it is maximized. Increasing κL_G makes R_G tend to 1 and increase the sidelobes. Considering a finite κ, a grating with infinite length would be then required to obtain complete power transfer between the forward and backward mode (i.e. $R_G = 1$).

Nulls in the R_G coefficients occur for $SL_G = jm\pi$ ($j = \sqrt{-1}$, m integer) and consequently for:

$$\Delta\beta = \pm 2\sqrt{|\kappa|^2 + (m\pi/L_G)^2}. \tag{A.60}$$

The distance between the first two nulls (calculated with $m = 1$ in Eq. (A.60)) represents the main lobe bandwidth. It increases as κ increases and decreases as L_G increases. For increasing values of κL_G it approaches the photonic bandgap width 4κ as illustrated in Fig. A.5.

The transmission intensity coefficient $T_G = |A(L_G)/A(0)|^2$ can be then easily calculated from Eq. (A.56). In a lossless grating $T_G = 1 - R_G$, adding no further interesting information on the grating behaviour.

It is now useful to inspect the grating group delay. This results are in fact used in Chapter 4 and 5 of this thesis. By differentiating the phase of (A.58) respect to the angular frequency Ω, the group delay can be easily calculated [197]. In a lossless grating, identical functions can be obtained by differentiating the transmission characteristic. The grating can be seen in fact as cavity with the group delay representing the cavity lifetime [198] (i.e. the amount of time that the light spend inside the periodic structure). Fig. A.6 shows the grating group delay τ_g normalized respect to

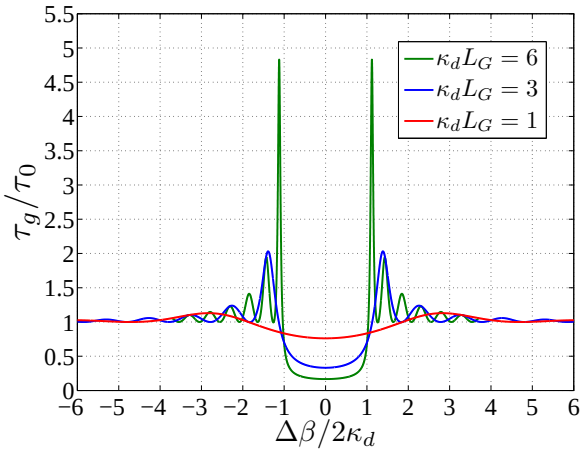

Figure A.6.: Grating group delay τ_g normalized to the group delay of a straight waveguide τ_0 as a function of $\Delta\beta/2\kappa$.

τ_0, the group delay of an unperturbed waveguide with a length equal to L_G, for different values of κL_G. When $\Delta\beta = 0$ the input light is coupled with the reflected wave reducing the cavity lifetime. This makes τ_g lower than that of a straight waveguide. Increasing the value of κL_G increases the grating reflection further reducing the group delay, which is inversely proportional to this product [197, 198]. Outside the photonic bandgap, as discussed before, the light can be transmitted or reflected after many reflections inside the cavity. This makes the group delay oscillating and reaching in some cases values higher than the one of a straight waveguide. The group delay peaks appears for $\Delta\beta$ values in close proximity with the R_G nulls (i.e. T_G maxima). At the edges of the R_G main lobe, τ_g is proportional to $\kappa^2 L_G^2$ [197, 198] leading to really high values as κL_G increase (see Fig. A.6).

Up to now the intensity and group delay characteristics of a lossless grating with the light coming just from one input port have been derived and discussed. In order to derive the scattering matrix of the Bragg grating, useful in Chapter 4 and 5 of this thesis, it is necessary to calculate its transfer functions also when the other port is excited and express them for the complex amplitude coefficients $a(z)$ and $b(z)$. This can be easily done by solving Eq. (A.54) and (A.55) with the following boundary conditions:

$$\begin{aligned} A_1(z=0) &= 0 \\ B_{-1}(z=L_G) &\neq 0. \end{aligned}$$

Then, Eq. (A.5) and (A.6) can be applied in order to obtain:

$$a_1(z) = \left(e^{-j\beta_1 z} \frac{S\cosh(S(z-L_G)) - j\frac{\Delta\beta}{2}\sinh(S(z-L_G))}{S\cosh(SL_G) + j\frac{\Delta\beta}{2}\sinh(SL_G)} e^{j(\Delta\beta/2)z} \right) a_1(0) + \left(e^{-j\beta_1 z}\, e^{-j\beta_{-1}L_G} \frac{-j\kappa\sinh(Sz)}{S\cosh(SL_G) + j\frac{\Delta\beta}{2}\sinh(SL_G)} e^{j(\Delta\beta/2)(z+L_G)} \right) b_{-1}(L_G) \tag{A.61}$$

and

$$b_{-1}(z) = \left(e^{j\beta_{-1}z} \frac{j\kappa\sinh(S(z-L_G))}{S\cosh(SL) + j\frac{\Delta\beta}{2}\sinh(SL)} e^{-j(\Delta\beta/2)z} \right) a_1(0) + \left(e^{j\beta_{-1}(z-L_G)} \frac{S\cosh(Sz) + j\frac{\Delta\beta}{2}\sinh(Sz)}{S\cosh(SL) + j\frac{\Delta\beta}{2}\sinh(SL)} e^{-j(\Delta\beta/2)(z-L_G)} \right) b_{-1}(L_G). \tag{A.62}$$

The scattering matrix $\boldsymbol{S}$ of the grating defined as

$$\begin{bmatrix} b_{-1}(0) \\ a_1(L_G) \end{bmatrix} = \begin{bmatrix} \boldsymbol{S} \end{bmatrix} \begin{bmatrix} a_1(0) \\ b_{-1}(L_G) \end{bmatrix} = \begin{bmatrix} S_{11}(z) & S_{12}(z) \\ S_{21}(z) & S_{22}(z) \end{bmatrix} \begin{bmatrix} a_1(0) \\ b_{-1}(L_G) \end{bmatrix},$$

can be immediately evaluated by calculating $a_1(L_G)$ and $b_{-1}(0)$ respectively from Eq. (A.61) and (A.62).

Finally, in some cases as in Chapter 4, it might be useful to consider a lossy grating. This can be taken into account by following the same approach developed in [199] for a grating with gain. Following this approach Eq. (A.61) and (A.62) can be rewritten as:

$$a_1(z) = \left(e^{-j\beta_1 z} \frac{S'\cosh(S'(z-L_G)) - j\frac{\Delta\beta'}{2}\sinh(S'(z-L_G))}{S'\cosh(S'L_G) + j\frac{\Delta\beta'}{2}\sinh(S'L_G)} e^{j(\Delta\beta/2)z} \right) a_1(0) + \left(e^{-j\beta_1 z}\, e^{-j\beta_{-1}L_G} \frac{-j\kappa\sinh(S'z)}{S'\cosh(S'L_G) + j\frac{\Delta\beta'}{2}\sinh(S'L_G)} e^{j(\Delta\beta/2)(z+L_G)} \right) b_{-1}(L_G) \tag{A.63}$$

and

$$b_{-1}(z) = \left(e^{j\beta_{-1}z} \frac{j\kappa\sinh(S'(z-L_G))}{S'\cosh(S'L) + j\frac{\Delta\beta'}{2}\sinh(S'L)} e^{-j(\Delta\beta/2)z} \right) a_1(0) + \left(e^{j\beta_{-1}(z-L_G)} \frac{S'\cosh(S'z) + j\frac{\Delta\beta'}{2}\sinh(S'z)}{S'\cosh(S'L) + j\frac{\Delta\beta'}{2}\sinh(S'L)} e^{-j(\Delta\beta/2)(z-L_G)} \right) b_{-1}(L_G). \tag{A.64}$$

where $S' = \sqrt{|\kappa|^2 - (\Delta\beta'/2)^2}$, $\Delta\beta' = \beta_1 + \beta_{-1} - K_G - 2\alpha$ and α is the real part of the modes' propagation constants.

A.6 CODIRECTIONAL AND CONTRADIRECTIONAL COUPLING BETWEEN SINGLE MODE WAVEGUIDES: GRATING ASSISTED COUPLER

After having illustrated the codirectional coupling between two parallel single mode waveguides and the contradirectional coupling in a single mode waveguide with a periodical sidewall perturbation it is now possible to analyse a case of interest in Chapter 4 and 5: the coupling between two parallel single mode periodically corrugated waveguides. In this section of the appendix the coupled equations describing such a structure will be derived and the calculation of the coupling coefficients discussed. The sketch of the described system is illustrated in Fig. A.7. The two unperturbed waveguides will be always considered having different β and

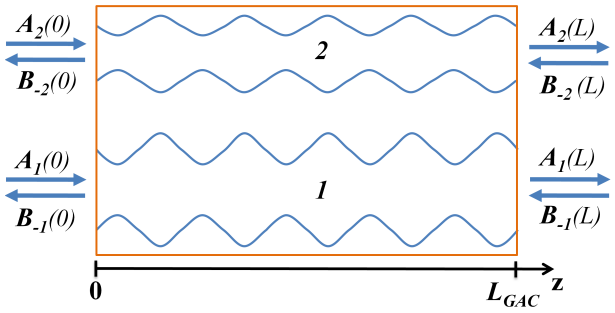

Figure A.7.: Sketch of a grating assisted coupler with the relative complex amplitudes at the four ports.

consequently, as explained in Section A.4, having different width. The two waveguides are assumed to be perturbed by a sinusoidal sidewall corrugation like that illustrated in Section A.3. In the system illustrated in Fig. A.7 an input wave at any port will be coupled to all the other three waves and to itself. These coupling

phenomena can be described by using the CMT (Eq. (A.28) and (A.29)) obtaining the following system:

$$\frac{\partial A_1}{\partial z} = -jA_1\,\kappa_{s11} - jA_2\,\kappa_{s21}\,e^{-j(\beta_2-\beta_1)z} \tag{A.65}$$
$$- j\kappa_{d(-1)1}\,B_{(-1)}\,e^{j(\beta_1+\beta_{(-1)}-\frac{2\pi}{\Lambda})\,z} - j\kappa_{d(-2)1}\,B_{(-2)}\,e^{j(\beta_1+\beta_{(-2)}-\frac{2\pi}{\Lambda})\,z}$$

$$\frac{\partial A_2}{\partial z} = -jA_1\,\kappa_{s21}\,e^{-j(\beta_1-\beta_2)z} - jA_2\,\kappa_{s22} \tag{A.66}$$
$$- j\kappa_{d(-1)2}\,B_{(-1)}\,e^{j(\beta_2+\beta_{(-1)}-\frac{2\pi}{\Lambda})\,z} - j\kappa_{d2(-2)}\,B_{(-2)}\,e^{j(\beta_2+\beta_{(-2)}-\frac{2\pi}{\Lambda})\,z}$$

$$\frac{\partial B_{-1}}{\partial z} = jA_1\,\kappa_{d1(-1)}\,e^{j(\beta_{(-1)}+\beta_1-\frac{2\pi}{\Lambda})\,z} + jA_2\,\kappa_{d2(-1)}\,e^{-j(\beta_2+\beta_{-1})z} \tag{A.67}$$
$$+ j\kappa_{s(-1)(-1)}\,B_{(-1)} + j\kappa_{s(-2)1}\,B_{(-2)}\,e^{-j(\beta_{-1}-\beta_{(-2)})\,z}$$

$$\frac{\partial B_{-2}}{\partial z} = jA_1\,\kappa_{d1(-2)}\,e^{-j(\beta_1+\beta_{-2}-\frac{2\pi}{\Lambda})z} + jA_2\,\kappa_{d2-2}\,e^{-j(\beta_2+\beta_{-2}-\frac{2\pi}{\Lambda})z} \tag{A.68}$$
$$+ j\kappa_{s(-1)(-2)}\,B_{(-1)}\,e^{j(\beta_{-1}-\beta_{(-2)})\,z} + j\kappa_{d(-2)(-2)}\,B_{(-2)}$$

Note that in this situation $\beta_1 = \beta_{-1}$ and $\beta_2 = \beta_{-2}$.

The coupling coefficients present in the obtained coupled system can be divided into four different groups depending on the related coupling process.

- SELF-COUPLING:
  This process represents the coupling of the mode with itself. The perturbation produces a variation of the mode propagation constant. $\kappa_{s11} = \kappa_{s(-1)(-1)} = \kappa_{s1}$ and $\kappa_{s22} = \kappa_{s(-2)(-2)} = \kappa_{s2}$ represent the self-coupling coefficients respectively of the mode of waveguide 1 and of the mode of waveguide 2. Contribution to this coefficient is given by the grating harmonic of order 0 and by the coupled waveguide. An increase in the grating perturbation leads then to an increase of this parameter.

- CODIRECTINAL COUPLING:
  This process represents the coupling of the considered mode with the mode of coupled waveguide propagating in the same direction of the z axis. $\kappa_{s21} = \kappa_{s(-2)(-1)} = \kappa_{21}$ and $\kappa_{s12} = \kappa_{s(-1)(-2)} = \kappa_{12}$ represent the codirectional coupling between the two waveguides. Contribution to this coefficient is given by the gratings harmonic of order 0 and by the coupled waveguide. The more the two waveguides are far apart, the less the coupling strength will be. Having the two waveguides different propagation constants ($\beta_1 \neq \beta_2$) the phase matching condition is not satisfied. The larger the difference between the two

propagation constants (i.e. the more the two waveguides width are different), the smaller the coupling.

- DIRECT CONTRADIRECTINAL COUPLING:
  This process represents the coupling of the considered mode with a mode in the same waveguide but propagating in the opposite direction of the z axis. $\kappa_{d(-1)(1)} = \kappa_{d(1)(-1)} = \kappa_{d1}$ and $\kappa_{d(-2)(2)} = \kappa_{d(2)(-2)} = \kappa_{d2}$ represent the contradirectional coupling between the forward and backward propagating mode in one waveguide, respectively waveguide 1 and waveguide 2. Contribution to this coupling is given by the first order harmonics of the gratings which allows the phase matching condition between the modes. This coupling can be increased mainly by increasing the perturbation of the waveguide where the coupling is acting.

- EXCHANGE CONTRADIRECTINAL COUPLING:
  This process represents the coupling of the considered mode with a mode in the coupled waveguide but propagating in the opposite direction of the z axis. $\kappa_{d(-2)1} = \kappa_{d1(-2)} = \kappa_{d(-1)2} = \kappa_{d2(-1)} = \kappa_{Ex}$, represent the contradirectional coupling between a mode propagating in one direction and a mode propagating in the opposite direction in the other waveguide. Contribution to this coupling is given by the first order harmonics of the gratings which allows the phase matching condition between the modes. This coupling can be increased by reducing the spacing between the waveguides or increasing the perturbation of the waveguides.

In order to analyse how the structure of Fig. A.7 behaves, numerical solvers have to be employed. The scattering matrix of this structure can be easily extracted by solving the mentioned system for all its four inputs, one at a time.

B

TUNABLE BANDWIDTH FILTER

The design, the analysis and the characterization of a novel tunable bandwidth filter has been carried out in Chapter 6. Design and simulation were based on the transfer matrix and the Z-transform approach. In this Appendix the general filter transfer functions will be derived. These functions help to understand the filter behaviour described in Chapter 6.

B.1 TUNABLE BANDWIDTH FILTER TRANSFER FUNCTIONS

As introduced in Section 6.2 we can describe the behaviour of the tunable bandwidth filter through the Z-transform approach by the following general transfer matrix:

$$\begin{bmatrix} Y_1 \\ Y_2 \end{bmatrix} = \begin{bmatrix} H_{11}(z) & H_{12}(z) \\ H_{21}(z) & H_{22}(z) \end{bmatrix} \begin{bmatrix} X_1 \\ X_2 \end{bmatrix}. \tag{B.1}$$

Developing the calculations, the filter transfer functions can be expressed as:

$$H_{11}(z) = \left[c_1 c_2 a^2 H_R(z) - s_1 s_2 \gamma e^{-j\varphi_{mz}} z^{-1} \right], \tag{B.2}$$

$$H_{21}(z) = -j \left[s_2 c_1 a^2 H_R(z) + c_2 s_1 \gamma e^{-j\varphi_{mz}} z^{-1} \right], \tag{B.3}$$

$$H_{12}(z) = -j \left[s_1 c_2 a^2 H_R(z) + c_1 s_2 \gamma e^{-j\varphi_{mz}} z^{-1} \right], \tag{B.4}$$

$$H_{22}(z) = - \left[s_1 s_2 a^2 H_R(z) - c_1 c_2 \gamma e^{-j\varphi_{mz}} z^{-1} \right], \tag{B.5}$$

where

$$H_R(z) = \prod_{i=1}^{2} \frac{ae^{-j\varphi_{ri}}(\rho e^{j\varphi_{ri}} - a\gamma z^{-1})}{(1 - \rho a\gamma e^{-j\varphi_{ri}} z^{-1})}. \tag{B.6}$$

We can now focus on $H_{11}(z)$ and $H_{21}(z)$, the Through and the Cross port transfer functions, when $X_1 = 1$ and $X_2 = 0$ are the conditions at the input of the device. These are in fact the functions of interest in this work. Considering $\varphi_{r1} = -\varphi_{r2} = \varphi_r$ one can then write:

$$H_{11}(z) = \frac{N_{11}(z)}{D_{11}(z)} = \frac{A_{11} + B_{11}z^{-1} + C_{11}z^{-2} + D_{11}z^{-3}}{1 - 2\rho a\gamma \cos(\Delta\varphi/2)z^{-1} + \rho^2(a\gamma)^2 z^{-2}} \tag{B.7}$$

where $\Delta\varphi = \varphi_{r1} - (-\varphi_{r2}) = 2\varphi_r$,

$$A_{11}(z) = c_1 c_2 a^2 \rho^2, \tag{B.8}$$

$$B_{11}(z) = -2\rho a^3 \gamma c_1 c_2 \cos(\Delta\varphi/2) - s_1 s_2 \gamma e^{-j\varphi_{mz}}, \tag{B.9}$$

$$C_{11}(z) = a^3\gamma^2 c_1 c_2 + 2s_1 s_2 \rho a \gamma^2 e^{-j\varphi_{mz}} \cos(\Delta\varphi/2), \tag{B.10}$$

$$D_{11}(z) = -s_1 s_2 \rho^2 a^2 \gamma^3 e^{-j\varphi_{mz}}, \tag{B.11}$$

and

$$H_{21}(z) = -j\frac{N_{21}(z)}{D_{21}(z)} = \frac{A_{21} + B_{21}z^{-1} + C_{21}z^{-2} + D_{21}z^{-3}}{1 - 2\rho a\gamma \cos(\Delta\varphi/2)z^{-1} + \rho^2 a^2\gamma^2 z^{-2}} \tag{B.12}$$

where

$$A_{21}(z) = s_2 c_1 a^2 \rho^2, \tag{B.13}$$

$$B_{21}(z) = -2\rho a^3 \gamma s_2 c_1 \cos(\Delta\varphi/2) + s_1 c_2 \gamma e^{-j\varphi_{mz}}, \tag{B.14}$$

$$C_{21}(z) = a^3\gamma s_2 c_1 - 2s_1 c_2 \rho a \gamma^2 e^{-j\varphi_{mz}} \cos(\Delta\varphi/2), \tag{B.15}$$

and

$$D_{21}(z) = s_1 c_2 \rho^2 a^2 \gamma^3 e^{-j\varphi_{mz}}. \tag{B.16}$$

Consider now a particular case of interest: 3 dB couplers at the input and at the output of our filter (i.e. $s_1 = s_2 = c_1 = c_2 = \sqrt{\frac{1}{2}}$). Under this assumption one can write the numerator and the denominator of the filter transfer functions as:

$$\begin{aligned} N_{11}(z) = {} & a^2\rho^2 \\ & - \left[\gamma e^{-j\varphi_{mz}} + 2\rho a^3 \gamma \cos(\Delta\varphi/2)\right] z^{-1} \\ & + \left[a^3\gamma^2 + 2\rho a \gamma^2 e^{-j\varphi_{mz}} \cos(\Delta\varphi/2)\right] \gamma^2 z^{-2} \\ & - \rho^2 a^2 \gamma^3 e^{-j\varphi_{mz}} z^{-3}, \end{aligned} \tag{B.17}$$

$$\begin{aligned} N_{21}(z) = {} & a^2\rho^2 \\ & + \left[\gamma e^{-j\varphi_{mz}} - 2\rho a^3 \gamma \cos(\Delta\varphi/2)\right] z^{-1} \\ & + \left[a^3\gamma^2 - 2\rho a \gamma^2 e^{-j\varphi_{mz}} \cos(\Delta\varphi/2)\right] \gamma^2 z^{-2} \\ & + \rho^2 a^2 \gamma^3 e^{-j\varphi_{mz}} z^{-3}, \end{aligned} \tag{B.18}$$

$$D_{11}(z) = D_{21}(z) = 1 - 2\rho a \gamma \cos(\Delta\varphi/2) z^{-1} + \rho^2 a^2 \gamma^2 z^{-2}. \tag{B.19}$$

Comparing (B.17) and (B.18) it comes immediately out that a π change of φ_{mz} will swap the two characteristics. Moreover it can be noticed that, considering a real variable $\varphi_X \in [0, 2\pi]$, the poles and zeros of $H_{11}(z, \Delta\varphi = \varphi_X)$ are that of $H_{21}(z, \Delta\varphi = 2\pi - \varphi_X)$ rotated by π respect to the centre of the unit circle. It is then possible to conclude that 3 dB input and output couplers ensures equal performance at both ports of the device.

BIBLIOGRAPHY

[1] "Integrating silicon photonics," *Nature Photonics*, vol. 4, no. 8, pp. 498–499, 2010.

[2] "SAPPHIRE Project Website," http://sapphire.dei.polimi.it/index.html.

[3] R. Essiambre and R. Tkach, "Capacity Trends and Limits of Optical Communication Networks," *Proceedings of the IEEE*, vol. 100, no. 5, pp. 1035–1055, 2012.

[4] D. Miller, "Device Requirements for Optical Interconnects to Silicon Chips," *Proceedings of the IEEE*, vol. 97, no. 7, pp. 1166–1185, 2009.

[5] B. G. Lee, A. Biberman, J. Chan, and K. Bergman, "High-performance modulators and switches for silicon photonic networks-on-chip," *IEEE Journal of Selected Topics in Quantum Electronics*, vol. 16, no. 1, pp. 6–22, 2010.

[6] A. Bianco, D. Cuda, M. Garrich, G. G. Castillo, R. Gaudino, and P. Giaccone, "Optical interconnection networks based on microring resonators," *J. Opt. Commun. Netw.*, vol. 4, no. 7, pp. 546–556, Jul 2012.

[7] Y. Vlasov, "Silicon CMOS-integrated nano-photonics for computer and data communications beyond 100G," *Communications Magazine, IEEE*, vol. 50, no. 2, pp. s67–s72, 2012.

[8] S. Gringeri, B. Basch, V. Shukla, R. Egorov, and T. Xia, "Flexible architectures for optical transport nodes and networks," *Communications Magazine, IEEE*, vol. 48, no. 7, pp. 40–50, 2010.

[9] C. R. Doerr, L. L. Buhl, L. Chen, and N. Dupuis, "Monolithic flexible-grid 1 x 2 wavelength-selective switch in silicon photonics," *Journal of Lightwave technology*, vol. 30, no. 4, pp. 473–478, Feb 2012.

[10] L. Pavesi, "Will silicon be the photonic material of the third millenium?" *Journal of Physics: Condensed Matter*, vol. 15, no. 26, pp. 1169–1196, 2003.

[11] M. Lipson, "Guiding, Modulating, and Emitting Light on Silicon-Challenges and Opportunities," *Journal of Lightwave Technology*, vol. 23, no. 12, pp. 4222–4238, Dec 2005.

[12] B. Jalali, "Can silicon change photonics?" *physica status solidi (a)*, vol. 205, no. 2, pp. 213–224, 2008.

[13] A. Melloni, R. Costa, G. Cusmai, F. Morichetti, and M. Martinelli, "Waveguide index contrast: implications for passive integrated optical components," in *Proceedings of IEEE/LEOS Workshop on Fibres and Optical Passive Components*, Palermo,Italy, Jun. 2005, pp. 246–253.

[14] M. Zuffada, "The industrialization of the silicon photonics: Technology road map and applications," in *Proceedings of the European Solid-State Device Research Conference (ESSDERC)*, 2012, pp. 7–13.

[15] "IMEC website - Silicon Photonics," http://www2.imec.be/be_en/services-and-solutions/silicon-photonics.html.

[16] "Intel Research website - Silicon Photonics at Intel Labs," http://www.intel.com/content/www/us/en/research/intel-labs-silicon-photonics-research.html.

[17] "IBM Research website - Silicon Integrated Nanophotonics," http://researcher.ibm.com/researcher/view_project.php?id=2757.

[18] J. Sun, E. Timurdogan, A. Yaacobi, E. S. Hosseini, and M. R. Watts, "Large-scale nanophotonic phased array," *Nature*, vol. 493, no. 7431, pp. 195–199, Jan 2013.

[19] A. M. Prabhu, A. Tsay, Z. Han, and V. Van, "Extreme Miniaturization of Silicon Add-Drop Microring Filters for VLSI Photonics Applications," *IEEE Photonics Journal*, vol. 2, no. 3, pp. 436–444, Jun. 2010.

[20] P. Dumon, W. Bogaerts, V. Wiaux, J. Wouters, S. Beckx, J. Van Campenhout, D. Taillaert, B. Luyssaert, P. Bienstman, D. Van Thourhout, and R. Baets, "Low-loss soi photonic wires and ring resonators fabricated with deep uv lithography," *Photonics Technology Letters, IEEE*, vol. 16, no. 5, pp. 1328–1330, 2004.

[21] M. Gnan, S. Thoms, D. S. Macintyre, R. M. De La Rue, and M. Sorel, "Fabrication of low-loss photonic wires in silicon-on-insulator using hydrogen silsesquioxane electron-beam resist," *Electronics Letters*, vol. 44, no. 2, pp. 115–116, Jan. 2008.

[22] J. Michel, J. Liu, and L. C. Kimerling, "High-performance Ge-on-Si photodetectors," *Nature Photonics*, vol. 4, no. 8, pp. 527–534, Aug. 2010.

[23] D. Vermeulen, S. Selvaraja, P. Verheyen, G. Lepage, W. Bogaerts, P. Absil, D. V. Thourhout, and G. Roelkens, "High-efficiency fiber-to-chip grating couplers realized using an advanced cmos-compatible silicon-on-insulator platform," *Opt. Express*, vol. 18, no. 17, pp. 18 278–18 283, Aug 2010.

[24] M. Pu, L. Liu, H. Ou, K. Yvind, and J. M. Hvam, "Ultra-low-loss inverted taper coupler for silicon-on-insulator ridge waveguide," *Optics Communications*, vol. 283, no. 19, pp. 3678 – 3682, 2010.

[25] G. T. Reed, G. Mashanovich, F. Y. Gardes, and D. J. Thomson, "Silicon optical modulators," *Nature Photonics*, vol. 4, no. 8, pp. 518–526, 2010.

[26] S. Ibrahim, N. K. Fontaine, S. S. Djordjevic, B. Guan, T. Su, S. Cheung, R. P. Scott, A. T. Pomerene, L. L. Seaford, C. M. Hill, S. Danziger, Z. Ding, K. Okamoto, and S. J. B. Yoo, "Demonstration of a fast-reconfigurable silicon CMOS optical lattice filter," *Optics Express*, vol. 19, no. 14, pp. 13 245–13 256, Jul. 2011.

[27] V. Passaro, F. Magno, and A. Tsarev, "Investigation of thermo-optic effect and multi-reflector tunable filter/multiplexer in SOI waveguides," *Optics Express*, vol. 13, no. 9, pp. 3429–3437, May 2005.

[28] A. H. Atabaki, E. S. Hosseini, A. A. Eftekhar, S. Yegnanarayanan, and A. Adibi, "Optimization of metallic microheaters for high-speed reconfigurable silicon photonics," *Optics Express*, vol. 18, no. 17, pp. 18 312–18 323, Aug 2010.

[29] A. Samarelli, "Micro Ring Resonator in Silicon On Insulator," Ph.D. dissertation, University of Glasgow, 2011.

[30] A. H. Atabaki, A. A. Eftekhar, S. Yegnanarayanan, and A. Adibi, "Sub-100-nanosecond thermal reconfiguration of silicon photonic devices," *Optics Express*, vol. 21, no. 13, pp. 15 706–15 718, Jul 2013.

[31] M. Geis, S. Spector, R. Williamson, and T. Lyszczarz, "Submicrosecond submilliwatt silicon-on-insulator thermooptic switch," *Photonics Technology Letters, IEEE*, vol. 16, no. 11, pp. 2514–2516, Nov 2004.

[32] J. Leuthold, C. Koos, and W. Freude, "Nonlinear silicon photonics," *Nature Photonics*, vol. 4, no. 8, pp. 535–544, Aug 2010.

[33] D. Liang and J. E. Bowers, "Recent progress in lasers on silicon," *Nature Photonics*, vol. 4, no. 8, pp. 511–517, Aug 2010.

[34] R. Nagarajan, M. Kato, J. Pleumeekers, P. Evans, S. Corzine, S. Hurtt, A. Dentai, S. Murthy, M. Missey, R. Muthiah, R. A. Salvatore, C. Joyner, R. Schneider, M. Ziari, F. Kish, and D. Welch, "InP Photonic Integrated Circuits," *IEEE Journal of Selected Topics in Quantum Electronics*, vol. 16, no. 5, pp. 1113–1125, 2010.

[35] M. Hochberg and T. Baehr-Jones, "Towards fabless silicon photonics," *Nature Photonics*, vol. 4, no. 8, pp. 492–494, 2010.

[36] A. Melloni, A. Canciamilla, G. Morea, F. Morichetti, A. Samarelli, and M. Sorel, "Design kits and circuit simulation in integrated optics," in *Integrated Photonics Research, Silicon and Nanophotonics and Photonics in Switching*. Optical Society of America, 2010, p. JTuB24.

[37] A. Melloni and M. Martinelli, "Synthesis of Direct-Coupled-Resonators Bandpass Filters for WDM Systems," *Journal of Lightwave technology*, vol. 20, no. 2, p. 296, Feb. 2002.

[38] C. K. Madsen and J. H. Zhao, *Optical Filter Design and Analysis: A Signal Processing Approach*. New York, NY: John Wiley & Sons, Inc., 1999.

[39] A. M. Prabhu, H. L. Liew, and V. Van, "Generalized parallel-cascaded microring networks for spectral engineering applications," *Journal of the Optical Society of America B*, vol. 25, no. 9, pp. 1505–1514, Sep. 2008.

[40] "EuroPic Project Website," http://europic.jeppix.eu/.

[41] "Paradigm Project Website," http://www.paradigm.jeppix.eu/.

[42] "Helios Project Website," http://www.helios-project.eu/.

[43] D. Melati, F. Morichetti, A. Canciamilla, D. Roncelli, F. Soares, A. Bakker, and A. Melloni, "Validation of the Building-Block-Based Approach for the Design of Photonic Integrated Circuits," *Journal of Lightwave Technology*, vol. 30, no. 23, pp. 3610–3616, 2012.

[44] "ePIXnet Project Website," http://www.epixnet.org/.

[45] "Opsis foundry website," http://opsisfoundry.org/.

[46] "SPLASH Project Website," http://www.st-andrews.ac.uk/physics/splash/.

[47] "Aspic design website," http://www.aspicdesign.com.

[48] M. Gnan, "Photonic wire devices in silicon-on-insulator," Ph.D. dissertation, University of Glasgow, 2007.

[49] A. Canciamilla, "Slow Light Structure for Optical Signal Processing," Ph.D. dissertation, Politecnico di Milano, 2010.

[50] M. Bruel, B. Aspar, and A.-J. Auberton-Hervé, "Smart-cut: A new silicon on insulator material technology based on hydrogen implantation and wafer bonding*1," *Japanese Journal of Applied Physics*, vol. 36, no. Part 1, No. 3B, pp. 1636–1641, 1997.

[51] X.-Q. Feng and Y. Huang, "Mechanics of smart-cut technology," *International Journal of Solids and Structures*, vol. 41, no. 1617, pp. 4299 – 4320, 2004.

[52] F. C. M. J. M. van Delft, "Delay-time and aging effects on contrast and sensitivity of hydrogen silsesquioxane," *Journal of Vacuum Science & Technology B*, vol. 20, no. 6, pp. 2932–2936, 2002.

[53] W. Henschel, Y. M. Georgiev, and H. Kurz, "Study of a high contrast process for hydrogen silsesquioxane as a negative tone electron beam resist," *Journal of Vacuum Science & Technology B*, vol. 21, no. 5, pp. 2018–2025, 2003.

[54] H. Namatsu, T. Yamaguchi, M. Nagase, K. Yamazaki, and K. Kurihara, "Nanopatterning of a hydrogen silsesquioxane resist with reduced linewidth fluctuations," *Microelectronic Engineering*, vol. 41-42, pp. 331–334, 1998.

[55] Y. Vlasov and S. McNab, "Losses in single-mode silicon-on-insulator strip waveguides and bends," *Optics Express*, vol. 12, no. 8, pp. 1622–1631, Apr 2004.

[56] M. Gnan, G. Bellanca, and R. M. De La Rue, "Post-Process Removal of Spurious Fabry-Pérot Oscillations Caused by Cleaved Waveguide-Ends," *Journal of Lightwave Technology*, vol. 27, no. 5, pp. 500–510, Mar 2009.

[57] M. J. Strain, M. Gnan, G. Bellanca, R. M. De La Rue, and M. Sorel, "Retrieval of Bragg Grating Transmission Spectra by Post-process Removal of Spurious Fabry-Pérot Oscillations," *Optics Express*, vol. 17, no. 16, pp. 13 493–13 501, Aug 2009.

[58] V. R. Almeida, R. R. Panepucci, and M. Lipson, "Nanotaper for compact mode conversion," *Optics Letters*, vol. 28, no. 15, pp. 1302–1304, Aug 2003.

[59] C. Ferrari, "VLSI Photonic Devices for All-Optical Signal Processing," Ph.D. dissertation, Politecnico di Milano, 2010.

[60] P. Winzer and R. Essiambre, "Advanced Optical Modulation Formats," *Proceedings of the IEEE*, vol. 94, no. 5, pp. 952–985, 2006.

[61] E. J. Klein, P. Urban, G. Sengo, L. T. Hilderink, M. Hoekman, R. Pellens, P. van Dijk, and A. Driessen, "Densely integrated microring resonator based photonic devices for use in access networks," *Optics Express*, vol. 15, no. 16, pp. 10 346–10 355, Aug 2007.

[62] J. Niehusmann, A. Vörckel, P. H. Bolivar, T. Wahlbrink, W. Henschel, and H. Kurz, "Ultrahigh-quality-factor silicon-on-insulator microringresonator," *Optics Letters*, vol. 29, no. 24, pp. 2861–2863, Dec 2004.

[63] Z. S. Sacks, D. M. Kingsland, R. Lee, and J.-F. Lee, "A perfectly matched anisotropic absorber for use as an absorbing boundary condition," *IEEE Transactions on Antennas and Propagation*, vol. 43, no. 12, pp. 1460–1463, 1995.

[64] S. D. Gedney, "An anisotropic perfectly matched layer-absorbing medium for the truncation of FDTD lattices," *IEEE Transactions on Antennas and Propagation*, vol. 44, no. 12, pp. 1630–1639, 1996.

[65] F. L. Teixeira and W. C. Chew, "General closed-form pml constitutive tensors to match arbitrary bianisotropic and dispersive linear media," *IEEE Microwave and Guided Wave Letters*, vol. 8, no. 6, pp. 223–225, 1998.

[66] N.-N. Feng, G.-R. Zhou, C. Xu, and W.-P. Huang, "Computation of Full-Vector Modes for Bending Waveguide Using Cylindrical Perfectly Matched Layers," *Journal of Lightwave Technology*, vol. 20, no. 11, pp. 1976–1980, Nov 2002.

[67] M. Heiblum and J. Harris, "Analysis of curved optical waveguides by conformal transformation," *IEEE Journal of Quantum Electronics*, vol. 11, no. 2, pp. 75–83, 1975.

[68] P. Bienstman, E. Six, M. Roelens, M. Vanwolleghem, and R. Baets, "Calculation of bending losses in dielectric waveguides using eigenmode expansion and perfectly matched layers," *Photonics Technology Letters, IEEE*, vol. 14, no. 2, pp. 164–166, 2002.

[69] K. Kakihara, N. Kono, K. Saitoh, and M. Koshiba, "Full-vectorial finite element method in a cylindrical coordinate system for loss analysis of photonic wire bends," *Optics Express*, vol. 14, no. 23, pp. 11 128–11 141, Nov 2006.

[70] K. Hiremath, M. Hammer, R. Stoffer, L. Prkna, and J. Čtyroký, "Analytic approach to dielectric optical bent slab waveguides," *Optical and Quantum Electronics*, vol. 37, no. 1-3, pp. 37–61, 2005.

[71] W. Lui, C.-L. Xu, T. Hirono, K. Yokoyama, and W.-P. Huang, "Full-vectorial wave propagation in semiconductor optical bending waveguides and equivalent straight waveguide approximations," *Journal of Lightwave Technology*, vol. 16, no. 5, pp. 910–914, 1998.

[72] F. L. Teixeira and W. C. Chew, "Pml-fdtd in cylindrical and spherical grids," *Microwave and Guided Wave Letters, IEEE*, vol. 7, no. 9, pp. 285–287, 1997.

[73] C. Dellagiacoma, T. Lasser, O. J. F. Martin, A. Degiron, J. J. Mock, and D. R. Smith, "Simulation of complex plasmonic circuits including bends," *Optics Express*, vol. 19, no. 20, pp. 18 979–18 988, Sep 2011.

[74] P. D. Trinh, S. Yegnanarayanan, and B. Jalali, "Integrated optical directional couplers in silicon-on-insulator," *Electronics Letters*, vol. 31, no. 24, pp. 2097–2098, 1995.

[75] L. B. Soldano and E. C. M. Pennings, "Optical multi-mode interference devices based on self-imaging: principles and applications," *Journal of Lightwave Technology*, vol. 13, no. 4, pp. 615–627, 1995.

[76] Y. Li and C. Henry, "Silica-based optical integrated circuits," *IEE Proceedings - Optoelectronics*, vol. 143, no. 5, pp. 263–280, Oct 1996.

[77] A. Melloni, A. Canciamilla, C. Ferrari, F. Morichetti, L. O'Faolain, T. F. Krauss, R. De La Rue, A. Samarelli, and M. Sorel, "Tunable delay lines in silicon photonics: Coupled resonators and photonic crystals, a comparison," *IEEE Photonics Journal*, vol. 2, no. 2, pp. 181–194, Apr. 2010.

[78] A. Driessen, D. H. Geuzebroek, H. J. W. M. Hoekstra, H. Kelderman, E. J. Klein, D. J. W. Klunder, C. G. H. Roeloffzen, F. S. Tan, E. Krioukov, C. Otto, H. Gersen, N. F. van Hulst, and L. Kuipers, "Microresonators as building blocks for vlsi photonics," *AIP Conference Proceedings*, vol. 709, no. 1, pp. 1–18, 2004.

[79] S. Feng, T. Lei, H. Chen, H. Cai, X. Luo, and A. Poon, "Silicon photonics: from a microresonator perspective," *Laser & Photonics Reviews*, vol. 6, no. 2, pp. 145–177, 2012.

[80] W. Bogaerts, P. De Heyn, T. Van Vaerenbergh, K. De Vos, S. Kumar Selvaraja, T. Claes, P. Dumon, P. Bienstman, D. Van Thourhout, and R. Baets, "Silicon microring resonators," *Laser & Photonics Reviews*, vol. 6, no. 1, pp. 47–73, 2012.

[81] B. E. Little, S. T. Chu, H. A. Haus, J. Foresi, and J. P. Laine, "Microring resonator channel dropping filters," *Journal of Lightwave Technology*, vol. 15, no. 6, pp. 998–1005, 1997.

[82] C. K. Madsen and J. H. Zhao, "A general planar waveguide autoregressive optical filter," *Journal of Lightwave Technology*, vol. 14, no. 3, pp. 437–447, 1996.

[83] Q. Xu, B. Schmidt, S. Pradhan, and M. Lipson, "Micrometre-scale silicon electro-optic modulator," *Nature*, vol. 435, pp. 325–327, May 2005.

[84] N. Sherwood-Droz, H. Wang, L. Chen, B. G. Lee, A. Biberman, K. Bergman, and M. Lipson, "Optical 4x4 hitless slicon router for optical networks-on-chip (NoC)," *Optics Express*, vol. 16, no. 20, pp. 15 915–15 922, Sep 2008.

[85] M. T. Wade and M. A. Popović, "Efficient wavelength multiplexers based on asymmetric response filters," *Optics Express*, vol. 21, no. 9, pp. 10 903–10 916, May 2013.

[86] A. Melloni, F. Morichetti, C. Ferrari, and M. Martinelli, "Continuously tunable 1 byte delay in coupled-resonator optical waveguides," *Optics Letters*, vol. 33, no. 20, pp. 2389–2391, Oct 2008.

[87] L. Zhang, J.-Y. Yang, M. Song, Y. Li, B. Zhang, R. G. Beausoleil, and A. E. Willner, "Microring-based modulation and demodulation of DPSK signal," *Optics Express*, vol. 15, no. 18, pp. 11 564–11 569, Sep 2007.

[88] H. L. R. Lira, S. Manipatruni, and M. Lipson, "Broadband hitless silicon electro-optic switch for on-chip optical networks," *Optics Express*, vol. 17, no. 25, pp. 22 271–22 280, Dec 2009.

[89] O. Schwelb, "Transmission, group delay, and dispersion in single-ring optical resonators and add/drop filters-a tutorial overview," *Journal of Lightwave Technology*, vol. 22, no. 5, pp. 1380–1394, 2004.

[90] M. Hammer, K. R. Hiremath, and R. Stoffer, "Analytical approaches to the description of optical microresonator devices," *AIP Conference Proceedings*, vol. 709, no. 1, pp. 48–71, 2004.

[91] A. Melloni, F. Morichetti, and M. Martinelli, "Linear and nonlinear pulse propagation in coupled resonator slow-wave optical structures," *Optical and Quantum Electronics*, vol. 35, no. 4-5, pp. 365–379, 2003.

[92] A. V. Oppenheim, R. W. Schafer, and J. R. Buck, *Discrete Time Signal Processing (2nd Ed.)*. Upper Saddle River, NJ, USA: Prentice-Hall, Inc., 1999.

[93] H. P. Uranus and H. J. W. M. Hoekstra, "Modeling of loss-induced superluminal and negative group velocity in two-port ring-resonator circuits," *Journal of Lightwave Technology*, vol. 25, no. 9, pp. 2376–2384, Sep 2007.

[94] A. C. Turner, M. A. Foster, A. L. Gaeta, and M. Lipson, "Ultra-low power parametric frequency conversion in a silicon microring resonator," *Optics Express*, vol. 16, no. 7, pp. 4881–4887, Mar 2008.

[95] P. P. Absil, J. V. Hryniewicz, B. E. Little, P. S. Cho, R. A. Wilson, L. G. Joneckis, and P.-T. Ho, "Wavelength conversion in GaAs micro-ring resonators," *Optics Letters*, vol. 25, no. 8, pp. 554–556, Apr 2000.

[96] M. J. Strain, P. Orlandi, C. Lacava, F. Morichetti, A. Melloni, P. Bassi, I. Cristiani, and M. Sorel, "Silicon micro-ring resonators with tunable Q-factor for ultra-low power parametric signal generation," in *Conference on Laser and Electro-Optics (CLEO/EUROPE)*, Munich, Germany, 12-16 May 2013.

[97] Z. Zhang, M. Dainese, L. Wosinski, and M. Qiu, "Resonance-splitting and enhanced notch depth in soi ring resonators with mutual mode coupling," *Optics Express*, vol. 16, no. 7, pp. 4621–4630, Mar 2008.

[98] M. R. Watts, J. Sun, C. DeRose, D. C. Trotter, R. W. Young, and G. N. Nielson, "Adiabatic thermo-optic Mach-Zehnder switch," *Optics Letters*, vol. 38, no. 5, pp. 733–735, Mar 2013.

[99] K. Jinguji and M. Oguma, "Optical half-band filters," *Journal of Lightwave Technology*, vol. 18, no. 2, pp. 252–259, 2000.

[100] F. Horst, W. M. Green, S. Assefa, S. M. Shank, Y. A. Vlasov, and B. J. Offrein, "Cascaded Mach-Zehnder wavelength filters in silicon photonics for low loss and flat pass-band WDM (de-)multiplexing," *Optics Express*, vol. 21, no. 10, pp. 11 652–11 658, May 2013.

[101] J. V. Campenhout, W. M. Green, S. Assefa, and Y. A. Vlasov, "Low-power, 2x2 silicon electro-optic switch with 110 nm bandwidth for broadband reconfigurable optical networks," *Optics Express*, vol. 17, no. 26, pp. 24 020–24 029, Dec 2009.

[102] F. Morichetti, R. Siano, A. Boletti, and A. Melloni, "Optical integrated receiver for DQPSK systems," in *Proceedings of 7th International Conference on Transparent Optical Networks*, vol. 2, 2005, pp. 213–216 Vol. 2.

[103] A. H. Gnauck and P. J. Winzer, "Optical phase-shift-keyed transmission," *Journal of Lightwave Technology*, vol. 23, no. 1, pp. 115–130, 2005.

[104] J. K. Doylend, O. Cohen, M. R. Lee, O. Raday, S. Xu, V. Sih, H. Rong, and M. Paniccia, "Tunable ring resonators for silicon raman laser and amplifier applications," vol. 6896, 2008, pp. 68 960Q–68 960Q–9.

[105] W. D. Sacher, W. M. J. Green, S. Assefa, T. Barwicz, H. Pan, S. M. Shank, Y. A. Vlasov, and J. K. S. Poon, "Coupling modulation of microrings at rates beyond the linewidth limit," *Optics Express*, vol. 21, no. 8, pp. 9722–9733, Apr 2013.

[106] W. Green, R. Lee, G. DeRose, A. Scherer, and A. Yariv, "Hybrid ingaasp-inp mach-zehnder racetrack resonator for thermooptic switching and coupling control," *Optics Express*, vol. 13, no. 5, pp. 1651–1659, Mar 2005.

[107] K. Jinguji, N. Takato, A. Sugita, and M. Kawachi, "Mach-zehnder interferometer type optical waveguide coupler with wavelength-flattened coupling ratio," *Electronics Letters*, vol. 26, no. 17, pp. 1326–1327, 1990.

[108] W. M. J. Green, M. J. Rooks, L. Sekaric, and Y. A. Vlasov, "Optical modulation using anti-crossing between paired amplitude and phase resonators," *Optics Express*, vol. 15, no. 25, pp. 17 264–17 272, Dec 2007.

[109] R. Patnaik, V. Vandrasi, C. K. Madsen, A. A. Eftekhar, and A. Adibi, "Comparison of Cascade, Lattice, and Parallel Filter Architectures," *Journal of Lightwave technology*, vol. 28, no. 23, pp. 3463–3469, 2010.

[110] L.-W. Luo, S. Ibrahim, A. Nitkowski, Z. Ding, C. B. Poitras, S. J. B. Yoo, and M. Lipson, "High bandwidth on-chip silicon photonic interleaver," *Optics Express*, vol. 18, no. 22, pp. 23 079–23 087, 2010.

[111] M. S. Rasras, D. M. Gill, S. S. Patel, K.-Y. Tu, Y.-K. Chen, A. E. White, A. T. S. Pomerene, D. N. Carothers, M. J. Grove, D. K. Sparacin, J. Michel, M. A. Beals, and L. C. Kimerling, "Demonstration of a Fourth-Order Pole-Zero Optical Filter Integrated Using CMOS Processes," *Journal of Lightwave Technology*, vol. 25, no. 1, pp. 87–92, Jan. 2007.

[112] C. K. Madsen, "General IIR optical filter design for WDM applications using all-pass filters," *Journal of Lightwave technology*, vol. 18, no. 6, pp. 860–868, Jun. 2000.

[113] H. L. R. Lira, C. B. Poitras, and M. Lipson, "CMOS compatible reconfigurable filter for high bandwidth non-blocking operation," *Optics Express*, vol. 19, no. 21, pp. 20 115–20 121, Oct. 2011.

[114] P. Alipour, A. A. Eftekhar, A. H. Atabaki, Q. Li, S. Yegnanarayanan, C. K. Madsen, and A. Adibi, "Fully reconfigurable compact RF photonic filters using high-Q silicon microdisk resonators," *Optics Express*, vol. 19, no. 17, pp. 15 899–15 907, Aug. 2011.

[115] L. Chen, N. Sherwood-Droz, and M. Lipson, "Compact bandwidth-tunable microring resonators," *Optics Letters*, vol. 32, no. 22, pp. 3361–3363, Nov. 2007.

[116] A. H. Atabaki, B. Momeni, A. A. Eftekhar, E. S. Hosseini, S. Yegnanarayanan, and A. Adibi, "Tuning of resonance-spacing in a traveling-wave resonator device," *Optics Express*, vol. 18, no. 9, pp. 9447–9455, Apr 2010.

[117] M. S. Rasras, K.-Y. Tu, D. M. Gill, Y.-K. Chen, A. E. White, S. S. Patel, A. Pomerene, D. Carothers, J. Beattie, M. Beals, J. Michel, and L. C. Kimerling, "Demonstration of a Tunable Microwave-Photonic Notch Filter Using Low-Loss Silicon Ring Resonators," *Journal of Lightwave Technology*, vol. 27, no. 12, pp. 2105–2110, Jun. 2009.

[118] T. Kominato, Y. Hibino, and K. Onose, "Silica-based finesse-variable ring resonator," *Photonics Technology Letters, IEEE*, vol. 5, no. 5, pp. 560–562, 1993.

[119] B. Little, S. Chu, W. Chen, J. Hryniewicz, D. Gill, O. King, F. Johnson, R. Davidson, K. Donovan, W. Chen, and S. Grubb, "Tunable bandwidth microring resonator filters," in *34th European Conference on Optical Communication (ECOC)*, 2008, pp. 1–2.

[120] W. Green, R. Lee, G. DeRose, A. Scherer, and A. Yariv, "Hybrid InGaAsP-InP Mach-Zehnder Racetrack Resonator for Thermooptic Switching and Coupling Control," *Optics Express*, vol. 13, no. 5, pp. 1651–1659, Mar 2005.

[121] W. D. Sacher, W. M. J. Green, S. Assefa, T. Barwicz, H. Pan, S. M. Shank, Y. A. Vlasov, and J. K. S. Poon, "Coupling modulation of microrings at rates beyond the linewidth limit," *Optics Express*, vol. 21, no. 8, pp. 9722–9733, Apr 2013.

[122] J. K. Doylend, O. Cohen, M. R. Lee, O. Raday, S. Xu, V. Sih, H. Rong, and M. Paniccia, "Tunable ring resonators for silicon Raman laser and amplifier applications," *Proceedings of SPIE*, pp. 68 960 68 960Q 1–9, 2008.

[123] A. Yariv, "Critical coupling and its control in optical waveguide-ring resonator systems," *Photonics Technology Letters, IEEE*, vol. 14, no. 4, pp. 483–485, 2002.

[124] H. Kogelnik and R. V. Schmidt, "Switched directional couplers with alternating $\Delta\beta$," *IEEE Journal of Quantum Electronics*, vol. 12, no. 7, pp. 396–401, 1976.

[125] Y. Silberberg, P. Perlmutter, and J. E. Baran, "Digital optical switch," *Applied Physics Letters*, vol. 51, no. 16, pp. 1230–1232, 1987.

[126] J. Leuthold and C. H. Joyner, "Multimode interference couplers with tunable power splitting ratios," *Journal of Lightwave Technology*, vol. 19, no. 5, pp. 700–707, 2001.

[127] D. A. May-Arrioja, P. LiKamWa, C. Velasquez-Ordonez, and J. Sanchez-Mondragon, "Tunable multimode interference coupler," *Electronics Letters*, vol. 43, no. 13, pp. 714–716, 2007.

[128] J. Yao and M. C. Wu, "Bandwidth-tunable add–drop filters based on micro-electro-mechanical-system actuated silicon microtoroidal resonators," *Optics Letters*, vol. 34, no. 17, pp. 2557–2559, Sep 2009.

[129] M.-C. M. Lee and M. C. Wu, "Variable bandwidth of dynamic add-drop filters based on coupling-controlled microdisk resonators," *Optics Letters*, vol. 31, no. 16, pp. 2444–2446, Aug 2006.

[130] K. E. Grutter, A. Yeh, A. Grine, and M. C. Wu, "An Integrated, Silica-Based, MEMS-Actuated, Tunable-Bandwidth Optical Filter with Low Minimum Bandwidth," in *CLEO: 2013*. Optical Society of America, 2013, p. CTh4F.3.

[131] K. Y. Fong, W. H. P. Pernice, M. Li, and H. X. Tang, "Tunable optical coupler controlled by optical gradient forces," *Optics Express*, vol. 19, no. 16, pp. 15 098–15 108, Aug 2011.

[132] G. Cocorullo, F. G. D. Corte, and I. Rendina, "Temperature dependence of the thermo-optic coefficient in crystalline silicon between room temperature and 550 K at the wavelength of 1523 nm," *Applied Physics Letters*, vol. 74, no. 22, pp. 3338–3340, 1999.

[133] A. Canciamilla, M. Torregiani, C. Ferrari, F. Morichetti, R. M. De La Rue, A. Samarelli, M. Sorel, and A. Melloni, "Silicon coupled-ring resonator structures for slow light applications: potential, imapirments and ultimate limits," *Journal of Optics*, vol. 12, no. 104008 (7pp.), Oct. 2010.

[134] T. Erdogan, "Fiber grating spectra," *Journal of Lightwave Technology*, vol. 15, no. 8, pp. 1277–1294, 1997.

[135] A. Yariv and M. Nakamura, "Periodic structures for integrated optics," *IEEE Journal of Quantum Electronics*, vol. 13, no. 4, pp. 233–253, 1977.

[136] J. Hong and W. Huang, "Coupled-waveguide exchange-Bragg resonator filters: coupled-mode analysis with loss and gain," *Journal of Lightwave Technology*, vol. 11, no. 2, pp. 226–233, 1993.

[137] H.-C. Kim, K. Ikeda, and Y. Fainman, "Tunable Transmission Resonant Filter and Modulator With Vertical Gratings," *Journal of Lightwave Technology*, vol. 25, no. 5, pp. 1147–1151, 2007.

[138] X. Wang, W. Shi, S. Grist, H. Yun, N. A. F. Jaeger, and L. Chrostowski, "Narrow-band transmission filter using phase-shifted bragg gratings in soi waveguide," in *IEEE Photonics Conference (PHO)*, 2011, pp. 869–870.

[139] A. Melloni, M. Floridi, F. Morichetti, and M. Martinelli, "Equivalent circuit of Bragg gratings and its application to Fabry-Pérot cavities," *Journal of the Optical Society of America A*, vol. 20, no. 2, pp. 273–281, Feb 2003.

[140] W. Streifer, D. R. Scifres, and R. Burnham, "Coupling coefficients for distributed feedback single- and double-heterostructure diode lasers," *IEEE Journal of Quantum Electronics*, vol. 11, no. 11, pp. 867–873, 1975.

[141] ——, "Coupled wave analysis of DFB and DBR lasers," *IEEE Journal of Quantum Electronics*, vol. 13, no. 4, pp. 134–141, 1977.

[142] M. J. Strain, "Integrated Chirped Bragg Gratings for Dispersion Control," Ph.D. dissertation, University of Glasgow, 2007.

[143] A. S. Jugessur, J. Dou, J. S. Aitchison, R. M. De La Rue, and M. Gnan, "A photonic nano-Bragg grating device integrated with microfluidic channels for bio-sensing applications," *Microelectronic Engineering*, vol. 86, no. 46, pp. 1488 – 1490, 2009.

[144] A. Kersey, M. A. Davis, H. J. Patrick, M. Leblanc, K. P. Koo, C. G. Askins, M. A. Putnam, and E. J. Friebele, "Fiber grating sensors," *Journal of Lightwave Technology*, vol. 15, no. 8, pp. 1442–1463, 1997.

[145] D. Garthe, R. E. Epworth, W. S. Lee, A. Hadjifotiou, C. P. Chew, T. Bricheno, A. Fielding, H. N. Rourke, S. R. Baker, K. C. Byron, R. S. Baulcomb, S. M. Ohja, and S. Clements, "Adjustable dispersion equaliser for 10 and 20 gbit/s over distances up to 160 km," *Electronics Letters*, vol. 30, no. 25, pp. 2159–2160, 1994.

[146] D. T. H. Tan, K. Ikeda, R. E. Saperstein, B. Slutsky, and Y. Fainman, "Chip-scale dispersion engineering using chirped vertical gratings," *Optics Letters*, vol. 33, no. 24, pp. 3013–3015, Dec 2008.

[147] V. Jayaraman, Z.-M. Chuang, and L. Coldren, "Theory, design, and performance of extended tuning range semiconductor lasers with sampled gratings," *IEEE Journal of Quantum Electronics*, vol. 29, no. 6, pp. 1824–1834, 1993.

[148] U. Glombitza and E. Brinkmeyer, "Coherent frequency-domain reflectometry for characterization of single-mode integrated-optical waveguides," *Lightwave Technology, Journal of*, vol. 11, no. 8, pp. 1377–1384, 1993.

[149] F. Morichetti, A. Canciamilla, and A. Melloni, "Statistics of backscattering in optical waveguides," *Optics Letters*, vol. 35, no. 11, pp. 1777–1779, Jun 2010.

[150] P. Yeh and H. F. Taylor, "Contradirectional frequency-selective couplers for guided-wave optics," *Applied Optics*, vol. 19, no. 16, pp. 2848–2855, Aug 1980.

[151] S. S. Orlov, A. Yariv, and S. V. Essen, "Coupled-mode analysis of fiber-optic add drop filters for dense wavelength-division multiplexing," *Optics Letters*, vol. 22, no. 10, pp. 688–690, May 1997.

[152] K. Ikeda, M. Nezhad, and Y. Fainman, "Wavelength selective coupler with vertical gratings on silicon chip," *Applied Physics Letters*, vol. 92, no. 20, p. 201111, 2008.

[153] D. T. H. Tan, K. Ikeda, S. Zamek, A. Mizrahi, M. P. Nezhad, A. V. Krishnamoorthy, K. Raj, J. E. Cunningham, X. Zheng, I. Shubin, Y. Luo, and Y. Fainman, "Wide bandwidth, low loss 1 by 4 wavelength division multiplexer on silicon for optical interconnects," *Optics Express*, vol. 19, no. 3, pp. 2401–2409, Jan 2011.

[154] D. T. H. Tan, K. Ikeda, and Y. Fainman, "Coupled chirped vertical gratings for on-chip group velocity dispersion engineering," *Applied Physics Letters*, vol. 95, no. 14, p. 141109, 2009.

[155] W. Shi, X. Wang, W. Zhang, L. Chrostowski, and N. A. F. Jaeger, "Contradirectional couplers in silicon-on-insulator rib waveguides," *Optics Letters*, vol. 36, no. 20, pp. 3999–4001, Oct 2011.

[156] W. Shi, X. Wang, C. Lin, H. Yun, Y. Liu, T. Baehr-Jones, M. Hochberg, N. A. F. Jaeger, and L. Chrostowski, "Silicon photonic grating-assisted, contra-directional couplers," *Optics Express*, vol. 21, no. 3, pp. 3633–3650, Feb 2013.

[157] W. Shi, H. Yun, C. Lin, M. Greenberg, X. Wang, Y. Wang, S. T. Fard, J. Flueckiger, N. A. F. Jaeger, and L. Chrostowski, "Ultra-compact, flat-top demultiplexer using anti-reflection contra-directional couplers for CWDM networks on silicon," *Optics Express*, vol. 21, no. 6, pp. 6733–6738, Mar 2013.

[158] H. Qiu, G. Jiang, T. Hu, H. Shao, P. Yu, J. Yang, and X. Jiang, "FSR-free add-drop filter based on silicon grating-assisted contradirectional couplers," *Optics Letters*, vol. 38, no. 1, pp. 1–3, Jan 2013.

[159] D. T. H. Tan, P. C. Sun, and Y. Fainman, "Monolithic nonlinear pulse compressor on a silicon chip," *Nature Communications*, vol. 1, no. 116, 2010.

[160] A. A. Hardy, "A unified approach to coupled-mode phenomena," *IEEE Journal of Quantum Electronics*, vol. 34, no. 7, pp. 1109–1116, 1998.

[161] N. Izhaky and A. Hardy, "Analysis of grating-assisted backward coupling employing the unified coupled-mode formalism," *Journal of the Optical Society of America A*, vol. 16, no. 6, pp. 1303–1311, Jun 1999.

[162] R. R. A. Syms, "Optical directional coupler with a grating overlay," *Appl. Opt.*, vol. 24, no. 5, pp. 717–726, Mar 1985.

[163] A. Muldarisnur, A. Soehianie, A. Iskandar, and M. O. Tjia, "Analysis of asymmetric Bragg-coupler based optical add-drop multiplexer operating on certain phase-matching conditions," *Journal of Applied Physics*, vol. 103, no. 12, pp. 123 110–123 110–11, 2008.

[164] P. Urquhart, "Compound optical-fiber-based resonators," *Journal of the Optical Society of America A*, vol. 5, no. 6, pp. 803–812, Jun 1988.

[165] K. Oda, N. Takato, and H. Toba, "A wide-FSR waveguide double-ring resonator for optical FDM transmission systems," *Journal of Lightwave Technology*, vol. 9, no. 6, pp. 728–736, 1991.

[166] S. Suzuki, K. Oda, and Y. Hibino, "Integrated-optic double-ring resonators with a wide free spectral range of 100 ghz," *Journal of Lightwave Technology*, vol. 13, no. 8, pp. 1766–1771, 1995.

[167] R. Boeck, N. A. Jaeger, N. Rouger, and L. Chrostowski, "Series-coupled silicon racetrack resonators and the vernier effect: theory and measurement," *Optics Express*, vol. 18, no. 24, pp. 25 151–25 157, Nov 2010.

[168] R. Boeck, J. Flueckiger, H. Yun, L. Chrostowski, and N. A. F. Jaeger, "High performance vernier racetrack resonators," *Optics Letters*, vol. 37, no. 24, pp. 5199–5201, Dec 2012.

[169] A. Arbabi, Y. M. Kang, C.-Y. Lu, E. Chow, and L. L. Goddard, "Realization of a narrowband single wavelength microring mirror," *Applied Physics Letters*, vol. 99, no. 9, p. 091105, 2011.

[170] X. Wang, H. Yun, and L. Chrostowski, "Integrated bragg gratings in spiral waveguides," in *CLEO: 2013*. Optical Society of America, 2013, p. CTh4F.8.

[171] A. D. Simard, Y. Painchaud, and S. LaRochelle, "Integrated bragg gratings in spiral waveguides," *Optics Express*, vol. 21, no. 7, pp. 8953–8963, Apr 2013.

[172] S. Zamek, D. T. H. Tan, M. Khajavikhan, M. Ayache, M. P. Nezhad, and Y. Fainman, "Compact chip-scale filter based on curved waveguide bragg gratings," *Optics Letters*, vol. 35, no. 20, pp. 3477–3479, Oct 2010.

[173] J. M. Choi, R. K. Lee, and A. Yariv, "Ring fiber resonators based on fused-fiber grating add-drop filters: application to resonator coupling," *Optics Letters*, vol. 27, no. 18, pp. 1598–1600, Sep 2002.

[174] M. Kulishov, J. Laniel, N. Bélanger, and D. Plant, "Trapping light in a ring resonator using a grating-assisted coupler with asymmetric transmission," *Optics Express*, vol. 13, no. 9, pp. 3567–3578, May 2005.

[175] W. Shi, X. Wang, W. Zhang, H. Yun, C. Lin, L. Chrostowski, and N. A. F. Jaeger, "Grating-coupled silicon microring resonators," *Applied Physics Letters*, vol. 100, no. 12, p. 121118, 2012.

[176] P. Bienstman, "Rigorous and efficient modelling of wavelenght scale photonics circuits," Ph.D. dissertation, Gent University, 2001.

[177] L. Li, "Formulation and comparison of two recursive matrix algorithms for modeling layered diffraction gratings," *Journal of the Optical Society of America A*, vol. 13, no. 5, pp. 1024–1035, May 1996.

[178] N. P. K. Cotter, T. W. Preist, and J. R. Sambles, "Scattering-matrix approach to multilayer diffraction," *Journal of the Optical Society of America A*, vol. 12, no. 5, pp. 1097–1103, May 1995.

[179] T. Wang, Z. Zhang, F. Liu, Y. Tong, J. Wang, Y. Tian, M. Qiu, and Y. Su, "Modeling of quasi-grating sidewall corrugation in SOI microring add-drop filters," *Optics Communications*, vol. 282, no. 17, pp. 3464 – 3467, 2009.

[180] A. Melloni and F. Morichetti, "Tunable photonic circuits: a leap toward system-on-a-chip optical integration," *SPIE Newsroom*, Jun. 2012.

[181] E. J. Norberg, R. S. Guzzon, J. S. Parker, L. A. Johansson, and L. A. Coldren, "Programmable Photonic Microwave Filters Monolithically Integrated in InP-InGaAsP," *Journal of Lightwave technology*, vol. 29, no. 11, pp. 1611–1619, Jun. 2011.

[182] C. Ferrari, A. Canciamilla, F. Morichetti, M. Sorel, and A. Melloni, "Penalty-free transmission in a silicon coupled resonator optical waveguide over the full C-band," *Optics Letters*, vol. 36, no. 19, pp. 3948–3950, Oct 2011.

[183] F. Xia, M. Rooks, L. Sekaric, and Y. Vlasov, "Ultra-compact high order ring resonator filters using submicron silicon photonic wires for on-chip optical interconnects," *Optics Express*, vol. 15, no. 19, pp. 11 934–11 941, Sep 2007.

[184] J. R. Ong, R. Kumar, and S. Mookherjea, "Ultra-high-contrast and tunable-bandwidth filter using cascaded high-order silicon microring filters," *Photonics Technology Letters, IEEE*, vol. 25, no. 16, pp. 1543–1546, 2013.

[185] J. Yao and M. C. Wu, "Bandwidth-tunable add–drop filters based on micro-electro-mechanical-system actuated silicon microtoroidal resonators," *Optics Letters*, vol. 34, no. 17, pp. 2557–2559, Sep. 2009.

[186] Y. Ding, M. Pu, L. Liu, J. Xu, C. Peucheret, X. Zhang, D. Huang, and H. Ou, "Bandwidth and wavelength-tunable optical bandpass filter based on silicon microring-MZI structure," *Optics Express*, vol. 19, no. 7, pp. 6462–6470, Mar. 2011.

[187] A. V. Oppenheim, R. W. Schafer, and J. R. Buck, *Discrete-Time Signal Processing*. New York, NY: Prentice-Hall Signal Processing Series, 1999.

[188] K. Oda, N. Takato, H. Toba, and K. Nosu, "A wide-band guided-wave periodic multi/demultiplexer with a ring resonator for optical FDM transmission systems," *Journal of Lightwave Technology*, vol. 6, no. 6, pp. 1016–1023, Jun. 1988.

[189] Q. Lin, O. J. Painter, and G. P. Agrawal, "Nonlinear optical phenomena in silicon waveguides: modeling and applications," *Optics Express*, vol. 15, no. 25, pp. 16 604–16 644, Dec 2007.

[190] G. Priem, P. Dumon, W. Bogaerts, D. V. Thourhout, G. Morthier, and R. Baets, "Optical bistability and pulsating behaviour in silicon-on-insulator ring resonator structures," *Optics Express*, vol. 13, no. 23, pp. 9623–9628, Nov. 2005.

[191] C. Ferrari, F. Morichetti, A. Canciamilla, M. Sorel, and A. Melloni, "Dynamic compensation of two-photon absorption induced distortions in silicon photonics filters," in *Conference on Lasers and Electro-Optics Europe (CLEO EUROPE/EQEC) and 12th European Quantum Electronics Conference*, May 2011, pp. 1–1.

[192] S.-L. Chuang, "A coupled mode formulation by reciprocity and a variational principle," *Journal of Lightwave Technology*, vol. 5, no. 1, pp. 5–15, 1987.

[193] H. Kogelnik, "2. theory of dielectric waveguides," in *Integrated Optics*, ser. Topics in Applied Physics. Springer Berlin Heidelberg, 1975, vol. 7, pp. 13–81.

[194] J. Adams Stratton, *Electromagnetic Theory*. Mcgraw Hill Book Company, 1941.

[195] W.-P. Huang, "Coupled-mode theory for optical waveguides: an overview," *Journal of the Optical Society of America A*, vol. 11, no. 3, pp. 963–983, Mar 1994.

[196] J. E. Sipe, L. Poladian, and C. M. de Sterke, "Propagation through nonuniform grating structures," *Journal of the Optical Society of America A*, vol. 11, no. 4, pp. 1307–1320, Apr 1994.

[197] A. Yariv and P. Yeh, *PHOTONICS: Optical Electronics in Modern Communications*. New York, NY: Oxford University Press Inc., 2007.

[198] H. G. Winful, "The meaning of group delay in barrier tunnelling: a re-examination of superluminal group velocities," *New Journal of Physics*, vol. 8, no. 6, p. 101, 2006.

[199] A. Yariv and P. Yeh, *Optical Waves in Crystals: Propagation and Control of Laser Radiation*. New York, NY: John Wiley and Sons, inc., 1984.

LIST OF FIGURES

Figure 1.1 PIC design flows: Classical optical design (green arrow) and Building Block based design (High level circuit design, red arrow). 11

Figure 1.2 Sketch of the process sequence employed for SOI devices fabrication. 13

Figure 1.3 (Images taken from [49]) SEM images of fabricated SOI devices: (a) waveguide cross-section with near-vertical sidewall (87°); (b) top-view of the sidewall, showing low LER value (< 1 nm); (c) directional coupler. 14

Figure 1.4 (a) Sketch of the SOI waveguide cross section with the thermo-optic control deposited over the waveguides. The dark green box on top of the silicon waveguide represents the HSQ hard mask that is not removed after the silicon etching process (see Fig. 1.3a). (b) (Image taken from [29]) Optical microscope photograph of the heaters. Red boxes highlight the NiCr high resistivity strips where the heat is generated. . . . 16

Figure 1.5 Setup at Politecnico di Milano: (a) (Image taken from [59]) Schematic of the typical experimental setup employed for the characterization of the devices in the frequency (red links) and time (blue links) domains. Dashed lines indicate electrical control connections. (b) (Image taken from [49]) Photograph of the alignment block of the optical setup showing the two piezo-controlled three-axis nano-positioning stages with tapered lensed fibres and a SOI chip in the middle. 17

Figure 1.6 Setup at Univeristy of Glasgow: (a) Schematic and (b) photographs of the typical experimental setup employed for the characterization of the devices. In (a) dashed lines indicate electrical control connections while dotted lines indicate free space propagation. 19

Figure 2.1 (a) Sketch of the simulation domain. (b) TE modes and first TM mode effective index as a function of the waveguide width w. Electric field components of the first TE mode for $w = 480$ nm: (c) Principal transversal component E_x; (d) E_y; (e) longitudinal component $-jE_z$. 23

Figure 2.2 Cartesian (black arrows) and cylindrical coordinate (green arrows) coordinate system. The red lines define the bent waveguide. The bend modes are calculate on the $z\rho$ cylindrical transversal plane where R is the curvature radius of the bent waveguide. 25

Figure 2.3 Bend losses expressed in dB per 90° bend as a function of the bending radius R. Insets show the real part of the mode principal component E_ρ normalized to its maximum in logaritmic scale. White lines delimit the PML regions. 26

Figure 2.4 (a) Directional coupler with bend-straight input and output sections. (b) Directional coupler with bend-bend input and output sections. 27

Figure 2.5 Simulated (blue trace) and measured (black crosses) K. The red trace has been obtained by fitting the measured results with the CMT analytical equation A.41 obtaining $\kappa = 0.018\ \mu m^{-1}$. Dashed orange traces are simulated by considering $\kappa = 0.017\ \mu m^{-1}$ and $\kappa = 0.019\ \mu m^{-1}$. The inset shows the relative error $((K - K_m)/K)$ between the simulated K and the coupled power fitted from the measurements K_m. 30

Figure 2.6 (a) All-pass and (b) add-drop ring resonator sketch. 31

Figure 2.7 (a) Transmission ($|H|^2$) and (b) phase response of an all-pass RR with $K_r = 0.36$ ($\rho = 0.8$) and FSR=3 nm, varying γ_r. 34

Figure 2.8 (a) Drop ($|H_{13}|^2$) and (b) Through ($|H_{12}|^2$) port transfer functions of a RR add-drop filter with FSR=3 nm, $\gamma_r = 1$ (solid traces) and $\gamma_r = 0.7$ (dash-dotted traces) varying $\rho_1 = \rho_2 = \rho$. 38

Figure 2.9 Sketch of a Mach-Zehnder interferometer. 39

Figure 2.10 $|H_{11}|^2$ (blue trace) and $|H_{21}|^2$ (red trace) of a lossless Mach-Zehnder interferometer with FSR= 1.5 nm. 41

Figure 3.1 (a) Sketch of the TDC cross section.(b) 2D thermal FEM simulation of the silicon TDC cross section. 46

Figure 3.2 Electric field principal component (E_x) of the: (a) First (Symmetric) and (b) Second (Antisymmetric) supermode of the coupler for $P_D = 0$; (c) First and (d) Second supermode of the coupler for $P_D = 25$mW; (e) First and (f) Second supermode of the coupler for $P_D = 50$mW; 48

Figure 3.3 Normalized thermally induced effective index difference versus d for three TDCs with $g = 200$ nm (blue curve), 250 nm (red curve), and 300 nm (black curve). The length of the coupling region L_c is chosen to have $K = 1$ for $P_D = 0$. Heater temperatures T_h refer to the case $d = 0.6\ \mu m$. 49

Figure 3.4 Simulated K versus P_D of four synchronous TDCs with lengths of the coupling region $L_c = 41$ μm (red), 52 μm (blue), 57 μm (orange), and 74 μm (black). The dashed-dotted line show the performance of an asynchronous TDC ($\Delta n = 0.005$) with $L_c = 74$ μm. All the devices have $g = 300$ nm and $d = 0.6$ μm. 50

Figure 3.5 Optical microscope top-view photograph of a silicon TDC embedded in an integrated RR all-pass filter. 51

Figure 3.6 Fitting of RRs normalized transmission characteristic with the analytical model. (a) $K = 0.07$, $\gamma \approx 0.97$. (b) $K = 0.55$, $\gamma \approx 0.98$. 52

Figure 3.7 (a) Wavelength domain response of a RR all-pass filter for increasing power P_D dissipated in the TDC and (b) relative K and Q factor values: overcoupling ($P_D = 0$, $K = 0.7$, blue curve R_1), critical coupling ($P_D = 30.4$ mW, $K = 0.06$, red curve R_2) and undercoupling condition ($P_D = 33.9$ mW, $K = 0.022$, green curve R_3). 53

Figure 3.8 Measured K of four synchronous TDCs with $g = 300$ nm and $L_c = 74$ μm for $d = -0.3$ μm (green circles), 0 μm (blue circles), 0.6 μm (black circles) and 1.5 μm (brown circles). . . . 54

Figure 3.9 Measured K versus P_D of four synchronous TDCs with nominal $K = 1$ (squares, $g = 200$ and 250 nm) and $K = 0.5$ (circles, $g = 200$ and 300 nm). The heater offset is $d = 0.6$ μm. 55

Figure 3.10 Measured (circles) and simulated (solid curves) K versus P_D of three synchronous TDCs with lengths of the coupling region $L_c = 52$ μm (blue), 57 μm (orange), and 74 μm (black). Diamonds and the dashed-dotted line show the performance of an asynchronous TDC ($\Delta n = 0.005$) with $L_c = 74$ μm. All the devices have $g = 300$ nm and $d = 0.6$ μm. 56

Figure 3.11 K versus P_D of the optimized asynchronous TDC ($\Delta n = 0.005$) measured for λ around 1.55 μm (black circles), 1.42 μm (blue circles) and 1.58 μm (red circles) and with $L_c = 74$ μm, $g = 300$ nm and $d = 0.6$ μm. 57

Figure 3.12 Temperature variation ΔT as a function of time of the waveguide closer to the heater (ΔT_1, black circles) and of the waveguide farther from the heater (ΔT_2, red circles) of a TDC with: $L_c = 74$ μm, $g = 300$ nm and $d = 0.6$ μm for $P_D = 34.5$ mW. Note that $\Delta T_1 - \Delta T_2$ (blue circles) represents instead the temperature difference between the two waveguides. ΔT_{90} indicate 90% of the asymptotic (i.e. steady-state) value of the traces. At the right boundary of the figure the asymptotic value of each trace is indicated over the trace itself. 58

Figure 4.1 Bragg grating top view sketch. 60

Figure 4.2 Transmission (T_G, red trace) and reflection (R_G, greentrace) measured spectra of a Bragg grating with: (a) $a = 5$ nm, $L_G = 66.72$ μm; (b) $a = 20$ nm, $L_G = 38.56$ μm. 62

Figure 4.3 Reflection autocorrelation function of a grating with $a = 5$ nm and $L_G = 66.72$ μm. 63

Figure 4.4 Transmission autocorrelation function of a grating with $a = 5$ nm and $L_G = 66.72$ μm. 64

Figure 4.5 Transmission (T_G, red trace) and reflection (R_G, green trace) spectra retrieved with the cavitometric technique of a Bragg grating with: (a) $a = 5$ nm, $L_G = 66.72$ μm; (b) $a = 20$ nm, $L_G = 38.56$ μm. Dashed lines are the results of simulations with the lossless Bragg grating model and the parameters extracted from the fitting procedure. 65

Figure 4.6 Normalized (a) T_G and (b) R_G retrieved spectra (thick black traces) and simulated characteristics (colored traces) of a grating with $a = 5$ nm and $L_G = 66.72$ μm varying I_R. 67

Figure 4.7 Normalized (a) T_G and (b) R_G retrieved spectra (thick black traces) and simulated characteristics (colored traces) of a grating with $a = 20$ nm and $L_G = 38.56$ μm varying I_R. 68

Figure 4.8 Measured (black thick trace) and fitted (light green trace) $\tau_{g_{GR}} - \tau_{g_{W_g}}$ of a grating with $a = 5$ nm and: (a) $L_G = 66.72$ μm; (b) $L_G = 84.32$ μm. Grey scale traces are obtained in both figures through simulations with the lossy Bragg grating model and increasing value of I_R. 69

Figure 4.9 Measured (black thick trace) and fitted (light green trace) $\tau_{g_{GR}} - \tau_{g_{W_g}}$ of a grating with $a = 20$ nm and $L_G = 38.52$ μm. . 70

Figure 4.10 Bragg grating coupling coefficient: measured (black squares) and calculated through the CMT. 71

Figure 4.11 Simulated (a) R_G and (b) $\Delta\lambda_{00}$ as a function of L_G, of a grating with $a = 5$ nm. Blue traces are calculated with the design parameters while red traces are obtained with the ones extracted from the measurements. Insets of both figure show the difference between these two traces. In (b), black circles represent the measured values and grey circles represent the difference between design and measurements. 73

Figure 4.12 Simulated (a) R_G and (b) $\Delta\lambda_{00}$ as a function of L_G, of a grating with $a = 20$ nm. Blue traces are calculated with the design parameters while red traces are obtained with the ones extracted from the measurements. Insets of both figure show the difference between these two traces. In (b) black circles represent the measured values and grey circles represent the difference between design and measurements. 73

Figure 4.13 (a) Schematic diagram of the GAC. (b) Propagation constants of a waveguide with $w_1 = 500$ nm (blue solid trace) and a waveguide with $w_2 = 400$ nm (dark green solid trace). The dash dotted black line represents the grating wavenumber. . . 76

Figure 4.14 (a) Experimental behaviour of a GAC with $w_1 = 500$ nm, $a_1 = 10$ nm and $w_2 = 400$ nm, $a_2 = 8$ nm. The average gap between the two waveguides is $g = 200$ nm and the length of the coupling region is $L_{GAC} = 100$ µm. The period is set to $\Lambda = 320$ nm. (b) GAC behaviour simulated with the coupling coefficients extracted from the measurements and the 2−wave model. 78

Figure 4.15 Measured κ_{Ex} as a function of the GAC gap g for different fabrication runs (marker shape) and a_1, a_2 combinations (marker colour). All the measured GACs had $w_1 = 500$ nm, $w_2 = 400$ nm and $\Lambda = 336$ nm. 80

Figure 4.16 Output characteristics of a GAC with $w_1 = 500$ nm and $w_2 = 400$ nm, $g = 180$ nm, $\Lambda = 336$ nm and: (a) $a_1 = 10$ nm, $a_2 = 8$ nm and $L_{GAC} = 235.2$ µm; (b) $a_1 = 6$ nm, $a_2 = 4$ nm, $g = 180$ nm and $L_{GAC} = 332.64$ µm. 81

Figure 4.17 (a) Measured $\lambda_{B_{Ex}}$ as a function of the GAC gap g for different fabrication runs (marker shape) and a_1, a_2 combinations (marker colour). Different results for the same g, a_1, a_2 and fabrication run refers to devices with different L_{GAC}. (b) $|\rho_X|^2/max(|\rho_X|^2)$ of GACs within the April 2012 fabrication run with $g = 220$ nm, $a_1 = 10$ nm, $a_2 = 8$ nm and varying L_{GAC}. 83

Figure 5.1 (a) Sketch of the GAC-RING geometry. (b) Output spectra of the GAC-RING simulated using the GAC 2−wave model and the scattering matrix method. (c) Sketch of the GAC geometry. (d) Output spectra of the GAC within the GAC-RING of Fig. 5.1a and Fig. 5.1b, simulated using the GAC 2−wave model. 87

Figure 5.2 $\Delta\lambda_{00_{Ex}}$ and $2 \cdot \mathrm{FSR}$ of a RR with $R = 10$ µm and: (a) $w_R = 500$ nm, $w_B = 400$ nm; (b) $w_R = 600$ nm and $w_B = 400$ nm. . . 91

Figure 5.3 SMSR calculated with the RR model (solid traces) and the 2−wave model (circles) for GAC-RINGs with $\kappa = 0.03$ (red) and $\kappa = 0.0015$ (blue), $R = 20$ μm and increasing L_{GAC} 92

Figure 5.4 GAC-RING spectral characteristics simulated with the 2−wave model, for $R = 20$ μm, $\kappa = 0.0015$ μm^{-1} and (a) $kL_{GAC} = 0.36$, (b) $kL_{GAC} = 1.395$ and (c) $kL_{GAC} = 2.16$. Dash-dotted lines represent the input (dark blue trace) and output (light blue trace) GAC spectral behaviour. 92

Figure 5.5 SMSR of GAC-RINGs with (a) $R = 20$ μm and (b) $R = 10$ μm. In both cases $w_R = 500$ nm and $w_B = 400$ nm. 93

Figure 5.6 (a) SMSR and (c) Side Modes Notch Depth as a function of L_{GAC} for GAC-RINGs with $w_R = 500$ nm, $w_B = 400$ nm and $R = 10$ μm. (b) SMSR and (d) Side Modes Notch Depth as a function of L_{GAC} for GAC-RINGs with $w_R = 600$ nm and $w_B = 400$ nm and $R = 10$ μm. 95

Figure 5.7 Central Mode (a) Drop port insertion loss, (b) Through port Notch Depth and (c) Drop port 3 dB bandwidth. All the simulated GAC-RINGs have $w_R = 500$ nm and $w_B = 400$ nm and $R = 10$ μm. 96

Figure 5.8 GAC-RING spectral characteristics simulated with the 2−wave model, for $R = 10$ μm, $\kappa = 0.003$ μm^{-1}, $w_R = 500$ nm, $w_B = 400$ nm, $w_R = 500$ nm, $w_B = 400$ nm, $L_{GAC} = 120$ μm and: (a) $\Delta\lambda_{B_{Ex}} = 0$; (b) $\Delta\lambda_{B_{Ex}} = 1.2$ nm, Central Mode resonance tuned at the intersection between the input and output GAC $|\rho_X|^2$; (c) $\Delta\lambda_{B_{Ex}} = 1.2$ nm, Central Mode resonance tuned at the maximum of the input GAC $|\rho_X|^2$; (d) $\Delta\lambda_{B_{Ex}} = 2.5$ nm; (e) $\Delta\lambda_{B_{Ex}} = 2.5$ nm. Dash-dotted lines represent the input (dark blue trace) and output (light blue trace) GAC spectral behaviour. 98

Figure 5.9 GAC spectral behaviour simulated with: (a) the 2−wave model; (b) the 4−wave model. 99

Figure 5.10 (a) Sketch of the GAC-RING geometry. (b) Spectal behaviour of the GAC-RING simulated with the GAC 4−wave model and the scattering matrix method. 100

Figure 5.11 Spectral behaviour of a GAC-RING with $R = 10$ μm, $w_R = 500$ nm, $w_B = 400$ nm, $\Lambda = 0.336$, $L_{GAC} = 100.8$ and: (a) $g = 180$ nm; (b) $g = 300$ nm. 101

Figure 5.12 Example of a fabricated GACR-RING with heater control over the ring resonator phase. 102

Figure 5.13 Spectral behaviour of a GAC-RING with $R = 10$ μm, $w_R = 500$ nm, $a_R = 6$ nm, $w_B = 400$ nm, $a_B = 4$ nm, $\Lambda = 0.336$, $L_{GAC} = 100.8$ μm, $g = 300$ nm and: (a) $P_D = 0$; (b) $P_D = 0$ and the TM component of the field filtered at the output of the chip; (c) $P_D = 9$ mW and the TM component of the field filtered at the output of the chip; (d) $P_D = 10$ mW and the TM component of the field filtered at the output of the chip. . 104

Figure 5.14 Spectral behaviour of a GAC-RING with $R = 10$ μm, $w_R = 500$ nm, $a_R = 6$ nm, $w_B = 400$ nm, $a_B = 4$ nm, $\Lambda = 0.336$, $L_{GAC} = 100.8$, $g = 300$ nm, $P_D = 6.3$ mW and and the TM component of the field filtered at the output of the chip. . . . 107

Figure 5.15 Spectral behaviour of a GAC-RING with $R = 10$ μm, $w_R = 600$ nm, $a_R = 6$ nm, $w_B = 400$ nm, $a_B = 4$ nm, $\Lambda = 0.336$, $L_{GAC} = 100.8$ μm, $g = 300$ nm and: (a) $P_D = 0$ mW; (b) $P_D = 6.3$ mW. In both experiments the TM component of the field has been filtered at the output of the chip. 109

Figure 6.1 Schematic diagram of the tunable filter architecture. 114

Figure 6.2 (a) Filter Through port intensity transmission for $K_r = 2/3$ (i.e. $\rho = 1/\sqrt{3}$) and different $\Delta\varphi$ as a function of the normalized frequency $\nu = (f - f_0)/\text{FSR}$. (b) Relative pole-zero diagrams where poles and zeroes are represented respectively by crosses and dots. 117

Figure 6.3 (a) Filter Cross port intensity transmission for $K_r = 2/3$ (i.e. $\rho = 1/\sqrt{3}$) and different $\Delta\varphi$ as a function of the normalized frequency $\nu = (f - f_0)/\text{FSR}$. (b) Relative pole-zero diagrams where poles and zeroes are represented respectively by crosses and dots. 118

Figure 6.4 Map of the filter Through port 3 dB bandwidth normalized to the FSR as a function of $\Delta\varphi$ (x axes) and K_r (y axes). 119

Figure 6.5 Map of the (a) filter Off-band Rejection and (b) Shape Factor (color bar and contour lines) for the 3 dB bandwidths obtained for $0 < \Delta\varphi < 2\pi$ (y axes) as a function of K_r (x axes). 120

Figure 6.6 (a) 3 dB bandwidth and (b) Off-band Rejection for $\Delta\varphi = 0$ and $\Delta\varphi = 2\pi$ as a function of K_r (varied between 0.3 and 0.6). (c) Filter Through port normalized intensity transmission for $\Delta\varphi = 0$, $\Delta\varphi = 2\pi$ and $K_r = 0.3$ as a function of ν. 122

Figure 6.7 Map of the Through port 3 dB bandwidth for (a) $\Delta\varphi = 0$ and for (b) $\Delta\varphi = 2\pi$ as a function of K_{c1} and K_{c2}. Note the different scales of the figures. 123

Figure 6.8 Map of the Cross port 3dB bandwidth for (a) $\Delta\varphi = 2\pi$ and for (b) $\Delta\varphi = 0$ as a function of K_{c1} and K_{c2}. Note the different scales of the figures. 124
Figure 6.9 Map of the Through port Off-band Rejection for (a) $\Delta\varphi = 0$, (b) $\Delta\varphi = 2\pi$ and (c) $\Delta\varphi = \pi$ as a function of K_{c1} and K_{c2}. Note the different scales of the figures. 125
Figure 6.10 Map of the Cross port Off-band Rejection for ((a)) $\Delta\varphi = 0$, (b) $\Delta\varphi = 2\pi$ and (c) $\Delta\varphi = \pi$ as a function of K_{c1} and K_{c2}. Note the different scales of the figures. 126
Figure 6.11 (a) Insertion loss, (b) Off-band Rejection, (c) Shape Factor and (d) 3 dB bandwidth as a function of Γ_r for $\Delta\varphi = 0$ (minimum bandwidth), $\Delta\varphi = \pi$ and $\Delta\varphi = 2\pi$ (maximum bandwidth). . 128
Figure 6.12 (a) K_r necessary to obtain the maximally flat passband condition for varying $\Delta\varphi$ at the Through port (blue trace) and at the Cross port (red trace). (b) Filter response for $\Delta\varphi = \pi/2$ and $K_r = 0.26$ (maximally flat passband condition at the Through port). (c) Filter response for $\Delta\varphi = \pi/2$ and $K_r = 0.85$ (maximally flat passband condition at the Cross port). 130
Figure 6.13 Filter Through port (a),(c),(e),(g) τ_n and (b),(d),(f),(h) D_n for: (a),(d) a lossless device; (c),(d) $A = 0$ dB and $\Gamma_r = 0.2$ dB/turn; (e),(f) $A = 0.06$ dB and $\Gamma_r = 0.2$ dB/turn; (g) (h) $A = 0.06$ dB and $\Gamma_r = 1.84$ dB/turn. For all the considered loss conditions, τ_n and D_n simulations where performed for $\Delta\varphi = 0, 0.4\pi, 0.5\pi, \pi, 2\pi$, $K_r = 0.8$, ... 132
Figure 6.14 Filter Through port (a) normalized group delay τ_n and (b) normalized dispersion D_n for $\Delta\varphi = 0, 0.4\pi, 0.5\pi, \pi, 2\pi$, $K_r = 0.7$, $A = 0.06$ dB and $\Gamma_r = 0.2$ dB/turn. 133
Figure 6.15 Optical microscope photograph of a fabricated filter. 133
Figure 6.16 (a) Through and (b) Cross port spectral characteristic tuning from the minimum ($\Delta\varphi = 0$) to the maximum ($\Delta\varphi = 2\pi$) bandwidth condition for a 25 GHz FSR filter with $K_r = 0.79$. At both ports, measured spectra are normalized with respect to the maximum of the filter maximum bandwidth configuration. (c) Measured and simulated 3 dB bandwidth values normalized to the FSR as a function of $\Delta\varphi$ (upper x axis) and of the required RRs power dissipated difference ΔP (lower x axis). 134
Figure 6.17 Through port and Cross port experiment (solid curves) and fitting (dashed curves) for the 25 GHz FSR filter for (a) $\Delta\varphi = 0$ and for (b) $\Delta\varphi = \pi + \pi/25$. 135

Figure 6.18 (a) Through and (b) Cross port spectral characteristic tuning from the minimum ($\Delta\varphi = 0$) to the maximum ($\Delta\varphi = 2\pi$) bandwidth condition for a 200 GHz FSR filter with $K_r = 0.75$. (c) Measured and simulated 3 dB bandwidth values normalized to the FSR as a function of $\Delta\varphi$ (upper x axis) and of the required RRs power dissipated difference ΔP (lower x axis). . 138

Figure 6.19 (a) Central wavelength tuning of a 44 GHz 3 dB bandwidth filter with 200 GHz FSR and (b) corresponding total power dissipated (P_{tot}) versus the frequency shift (Δf). 139

Figure 6.20 Desing versus experiment for the 200 GHz FSR filter for (a) 40GHz 3dB bandwidth configuration and for (b) 100GHz 3dB bandwidth configuration. 140

Figure 6.21 Desing versus experiment for the 25 GHz FSR filter for (a) a 6 GHz 3 dB bandwidth configuration and for (b) a 6 GHz 3 dB bandwidth configuration. 141

Figure 6.22 (a) Cross port and (b) Through port 3 dB bandwidth tuning (i.e. $\Delta\varphi$ from 0 to 2π) of a 100 GHz FSR filter with $K_{r1} = 0.74$ and $K_{r2} = 0.67$. 142

Figure 6.23 (a) Schematic diagram of the tunable filter with tunable coupling sections. The RRs coupling coefficient K_r is illustrated as a function of the dissipated power on the tunable coupler P_{TC}. (b) Filter Cross port characteristic variation due to RRs couplers detuning (i.e. increasing values of P_{TC}) maintaining $\Delta\varphi = 2\pi$ (minimum bandwidth condition). (c) 7 GHz 3 dB bandwidth filter for different values of P_{TC} (and thus K_r) obtained slightly adjusting the value of $\Delta\varphi$ for each case. Insets in (b) and (c) show the Off-band Rejection map of Fig. 6.5a with the red dashed lines to evidence qualitatively the locus of the filter working points. 145

Figure 6.24 Sketch of a WDM system with 12 channels and a fixed grid spaced of Δf_{ch}: (a) Periodically spaced subset of carriers filtered (interleaver function). (b) Single subset of carriers filtered. T and C represents the Through and the Cross port respectively and the filter responses are depicted with a box-like shape. 147

Figure 6.25 (a) 200 GHz filter Through port spectra over 20 nm wavelength span. (b) 3 dB bandwidth and (c) Off-band Rejection variation over the analysed wavelength span for the minimum ($\Delta\varphi = 0$) and the maximum ($\Delta\varphi = 2\pi$) bandwidth condition. 148

Figure 6.26 200 GHz FSR filter (a) Through port characteristic and (b) Cross port characteristic for $\Delta\varphi = 0$ and increasing values of the optical power P_{in} on the chip. 149

Figure 6.27 25 GHz FSR filter (a) Through port characteristic and (b) Cross port characteristic for $\Delta\varphi = 0$ and increasing values of the power on chip P_{in}. 151

Figure 6.28 (a) BER measurements (marks) of a 10 Gbit/s NRZ OOK signal filtered by a 25 GHz FSR device with three different 3 dB bandwidths: 18 GHz (red circles) 10 GHz (green squares) 8 GHz (magenta diamonds). Black triangles show the BER measured after propagation through a 5-mm long silicon waveguide. (b) Eye diagrams for the different conditions. 152

Figure 6.29 Measured (left column) and simulated (central and right column) eye diagrams of a 10 Gbit/s NRZ OOK signal filtered with the 25 GHz filter Cross port haveing 3 dB bandwidth: (a) 18 GHz, (b) 12 GHz and (c) 10 GHz. 153

Figure 6.30 (a) BER measurements (marks) of a 10 Gbit/s NRZ OOK signal filtered by the 200 GHz FSR device with two different 3 dB bandwidths: 173 GHz (red circles) and 23 GHz (green squares). Black triangles show the BER measured after propagation through a $5-$ mm long silicon waveguide. (b) Eye diagrams for the different conditions. 153

Figure A.1 Parallel waveguides schematic, top view. 161

Figure A.2 Corrugated waveguide schematic top view. The waveguide perturbation regions are evidenced in yellow. 161

Figure A.3 (a) Sinusoidally perturbed waveguide (b) Sinusoidally perturbed waveguide top view. Dashed lines represents the average waveguide width. (c) Upper sketch: Sinusoidally perturbed waveguide left sidewall top view. Red and green dashed lines indicate two different positions on the x axis, respectively x_1 and x_{-1}. Lower sketch: $\Delta\varepsilon(x_1, y_0, z)$, red trace and $\Delta\varepsilon(x_{-1}, y_0, z)$, green trace. 165

Figure A.4 Coupled power calculated for four different values of $\Delta\beta/\kappa$ as a function of the longitudinal coordinate z normalized to L_π. Note that L_π is calculated considering the synchronous case (i.e. $\Delta\beta = 0$). 168

Figure A.5 Bragg grating R_G as a function of $\Delta\beta/2\kappa$. 172

Figure A.6 Grating group delay τ_g normalized to the group delay of a straight waveguide τ_0 as a function of $\Delta\beta/2\kappa$. 173

Figure A.7 Sketch of a grating assisted coupler with the relative complex amplitudes at the four ports. 175

LIST OF TABLES

Table 2.1 Straight Waveguide Optical Parameters 22
Table 4.1 Bragg Grating Parameters 66
Table 5.1 Designed and Measured Parameters of the Realized GAC-RINGs 105
Table 6.1 Designed and Measured Parameters of the Realized Tunable Bandwidth Filters 137
Table 6.2 Recent Multi-element Silicon Tunable Filters 143

ACRONYMS

BB Building Block

BER Bit Error Rate

CMT Coupled Mode Theory

DC Directional coupler

DUT Device Under Test

DK Design Kit

Ebeam Electron Beam

EDFA Erbium Doped Fibre Amplifier

FEM Finite Element Method

FSR Free Spectral Range

GAC Grating Assisted Coupler

HSQ Hydrogen SilsesQuioxane

IIR Infinite Impulse Response

LER Line Edge Roughness

MZI Mach-Zehnder Interferometer

PML Perfectly Matched Layers

PIC Photonic Integrated Circuit

RR Ring Resonator

SMSR Side Mode Suppression Ratio

SAPPHIRE Shared Access Platform to PHotonic Integrated REsources

SOI Silicon-on-Insulator

SEM Scanning Electron Microscope

TDC Tunable Directional Coupler

WDM Wavelength Division Multiplexing

ACKNOWLEDGEMENTS

Two countries, three cities, four universities and seven offices after, I think that this thesis owes some to someone ...

First of all to Prof. Paolo Bassi, who gave me the opportunity to follow this path, giving me trust and support from both the scientific and the human side. His guidance has been of key importance for the development of this thesis and my personal growth, especially in the last two years.

I am extremely grateful to Prof. Marc Sorel who allowed me to join the Optoelectronics group at the University of Glasgow. This opportunity and having met him broadened my views.

A special thanks to Prof. Andrea Melloni. The collaboration with him and the time I spent at the Politecnico di Milano has been of fundamental for the development of this dissertation. Every scientific discussion improved my knowledge and my research.

I would also like to acknowledge the project SAPPHIRE for financial support of this work.

In Bologna I had the pleasure to work with Dr. Marco Gnan. Without him, who initiated me to silicon photonics, I would not proably be here writing these sentences.

Thanks to Prof. Gatano Bellanca and to all the helpful discussions we had.

Thanks the invaluable support received form the people of the Photonic Devices Group at the Politecnico di Milano: Prof. Francesco Morichetti, Dr. Antonio Canciamilla and Dr. Carlo Ferrari. Expertise, great ideas and availability: these are, I think, the words than can better describe what have been their impact on this thesis, from the lab to pen and paper.

In Glasgow I had the luck to meet Dr. Michael Strain and Dr. Antonio Samarelli and their undisputed fabrication skills. The results obtained in this thesis owes much to them. Theoretical disscusion were nonetheless important for the successful development of this research project. Remaining in Glasgow I wish to thank for his collaboration also Dr. Philippe Velha. Moreover, I wish to acknowledge all the staff at the James Watt Nanofabrication Centre.

In this city I shared the lab with amazing people: Marco, Vincenzo, Antonio, Michael, Gabor, Piotr. Helpful scientific discussions as well as smiles and jokes contributed a lot to the successful characterization of the devices.

Always in Glasgow, I also met some people that appends to become friends, or really close friends, that I need to acknowledge. Without them Glasgow would not have the same meaning that have now for me and all of them supported me

during this period. Marco, as you wrote in your PhD thesis acknowledgements, you are the first guy I met in Glasgow. From the parties to the lab time, I will have just good memories (and they are a lot. Especially when ....). Felice, another guy 'from Bologna' like me. After few minutes we became friends and I feel lucky for that. Vince, well I already acknowledged you in the lab guys ... but anyway form scientific to trivial discussions it was always and it will always be a pleasure to have a chat with you. Antonio, flatmate, close friend and colleague. And also Irmak, Andrea, Maurizio and Marcos: Thanks to all of you!

In Bologna the impact that the presence of my closest and oldest friends had on this thesis can be hardly described. Antonio, Bojan, Luca, Giorgio, Mario, Francesco, Enrico, Alessando and also whom I don't remember right now because I am going to submit the thesis in 5 minutes. Thanks for your support and friendship.

Thanks to Margherita who accompanied me for the first part of this adventure.

Thanks to my family and especially to (can I be more italian than this?) my mom, the solid ground on which I can always rely.

Thanks to Lucie who still bear my by now famous 'paranoia'.

In conclusion, all the people cited here and all the other ones that I met during these years have contributed to the achievements reached in this thesis and my growth. From the labs and the beers of Glasgow, to the simulations and the wines in 'my' Bologna, passing form the labs and the aperitivi of Milano, friendship, trust, support, help, listening, collaboration, suggestions, laugh, talks ... I just simply owe to them what I am now.